## *Seasonal solar energy storage using thermochemical adsorption for space heating*

ZHOU, JIAN

# Seasonal solar energy storage using thermochemical adsorption for space heating

**Thesis by**

**Jian Zhou**

**In Partial Fulfilment of requirements**
**for the Degree of**
**Doctor of Philosophy (PhD)**


**School of Engineering**

**Durham University**

**Date of Submission:**

**Mar 2023**

# Abstract

Adsorption-based thermochemical heat storage is a long-term thermal energy storage technology that can be used for seasonal solar energy storage and especially for space heating, which has received significant attention. Pure salt as the adsorbent, even though has huge water-adsorption capacity, takes the disadvantage of low thermal conductivity, deliquescence, and swallow problems during cyclic sorption operations, which could finally reduce both the thermal energy storage and the space heating performance. Composite adsorbent, integrating the salt with the porous matrix such as activated carbon and zeolite, could keep the high water-adsorption capacity (energy density) when the porous structure of the matrix providing a more stable form to hold the adsorbed/desorbed adsorbent and to prevent it from agglomeration.

In this project, an efficient adsorption-integrated space heating system has been investigated with the seasonal solar energy storage (SSES) function using the composite adsorbent made by the salt and the zeolite. The water-adsorption space heating system using the composite which could take the advantage like that the water vapour widely spreads in the environment and the zeolite is a popular material for the concrete mixing in the sustainable architecture research.

The composite adsorbent made by salt solutions ($MgSO_4$, LiCl, and LiBr) with different concentrations and various zeolites have been investigated as these salts are easy to obtain and safe for the environment. Moreover, beside the single salt-zeolite composite of MgSO4-zeolite, LiCl and LiBr could form the complex salt(A)-salt(B)-zeolite as LiCl-LiBr-zeolite composite to potentially increase the water-adsorption capacity and thus enhance its space heating and energy storage performance. The manufacturing methodology has been developed according to the practical experimental experience by the author. The prepared composite adsorbent has been experimentally characterized in respect of the surface morphology, thermal-physical properties, porous properties, and adsorption-related characteristics. The involved investigations include Scanning Electron Microscope (SEM) – Energy Dispersive Spectroscope (EDS), Nitrogen Adsorption, X-ray Diffractometer (XRD), and Thermogravimetric Analysis (TGA) - Differential Scanning Calorimetry (DSC). Besides, the adsorption kinetics of the composite adsorbent has been tested by the climate chamber, which could control the adsorption environment of the temperature and the relative humidity. For $MgSO_4$-zeolite, the maximum heat storage density found in the TGA-DSC desorption tests was 481.3 J/g by $MgSO_4$(20%)-4A, while the maximum water

adsorption capacity obtained was 0.1803 g/g by $MgSO_4$(20%)-13X. For LiCl/LiBr-zeolite, the maximum heat storage density, 592.8 J/g, is found in 5%LiCl-5%LiBr-zeolite. The most water adsorption capacity observed in the climatic chamber adsorption experiment is 0.22 g/g (5%LiCl-25%LiBr-zeolite).

As LiCl-LiBr-zeolite has proved its superior water-adsorption capacity as well as the energy density, they are selected as the adsorption composite to be used in the further space heating experiments. An adsorption pipeline reactor has been established to experimentally investigate the air heating effect by using the selected candidates. Moreover, a 1:22.5 scaled house model was printed by a 3D-printer to simulate the condition that the house model is heated by the adsorption heat provided by the tube reactor. The effects of air velocity and relative humidity on the adsorption performance has been examined. The outlet air and room temperature profiles are recorded for analysis. It is found that a flow rate of 15 $m^3$/h and a relative humidity of 70% could lead to the maximum adsorption heat, 434.4 J/g, from the water-adsorption reaction by the composite material, and the highest energy discharge efficiency of 74.3%.

Furthermore, the adsorption-integrated space heating system has been established using the software of TRNSYS. The novel space heating model could collect and store the solar energy under sufficient solar radiation and utilize it to heat the house in the cold seasons. Simulated houses are assumed to be one in Newcastle, UK, and one in Urumqi, China. The gross heat supply by the adsorption-integrated space heating system in Urumqi and in Newcastle is 8862.68 kWh and 6466.39 kWh for the whole space heating seasons, respectively. The results demonstrates that the required room temperature is well kept by the designed space heating system using the composite adsorbent. The system could store the solar thermal energy from 0% of its full storage capacity to 100% during the seasons that the space heating is not required. However, at the end of each space heating season, the heat storage remains 42.85% and 57.00% in Urumqi and Newcastle, respectively. Because after the heat storage capacity is less than 95% of the full capacity, the storage module starts to work simultaneously with the space heating module. When the heat consumption is larger than the heat storage, the storage capacity percentage decreases. After a time, when the heat consumption is less than the heat storage, the storage capacity percentage increases until the end of the space heating season. Thus, the heat storage remains rather than running out. The value of the storage capacity percentage is

dependent on the heat consumption and storage relationships. The extra solar radiation after full storage may be utilized into other functions. Moreover, the COP of the adsorption-integrated space heating system in Newcastle is 20% higher than that in Urumqi.

In a summary, using the composite adsorbent, the adsorption-integrated space heating system is promising to also achieve a high-efficiency and low-environmental impact seasonal solar thermal energy storage system.

## Acknowledgement

This thesis has taken long time to be accomplished as well as the PhD research project. I cherish the time I have spent with both Durham University and Newcastle University.

In the university, I met the best supervision team ever in the world. I would like to thank my supervisors: Prof. Yaodong Wang, Dr. Zhiwei Ma, Dr. Huashan Bao, and Prof. Anthony Paul Roskilly. Without their kind and sincere guidance, the PhD research could not be possible.

I would like to owe my deepest gratitude to my mother, father, and other family members, who have supported me to study overseas. They have taught me a lot beyond learning the professional knowledge. With their continuing encouragement, I now know how to deal with the stress, the pressure, and the failure.

Dr. Pan Wang, my wife, I am grateful that we could meet each other and fall in love. I would love you until the end of my life. Thanks for gifting me my beloved lady and our lovely baby.

Moreover, I would like to share my gratitude to many of my colleagues. The time during which we gathered together and fought for a same dream to be a doctor is very expressive and inspiring. The friendship between us would be forever.

I would also say thanks to the technicians in the laboratory. They have supported me on solving the technical issues to complete the experimental investigations as designed.

# List of publications

[1] **Jian zhou**, Wan Iman Wan Mhod Nazi, Yaodong wang*,Anthony Roskilly, Investigating the impact of building's facade on the building's energy performance-a case study, 10th International Conference on Applied Energy (ICAE2018),22-25 August 2018,Hong kong,CHINA

[2] L.Jiang, A.P. Roskilly, Y.J. Lu, **J. Zhou**, Exploration on a novel sorption thermal energy storage system for electric vehicles, UK energy storage conference, Newcastle, UK, 2018

[3] Wen, Z., **Zhou, J.,** Dong, J. and Zhang, C., 2022. Improvement Measures for Structure System Conversions Caused by Utilising SPMTs to Lift Trusses. In International Conference on Civil Engineering (pp. 11-17). Springer, Singapore.

# List of tables

# List of figures

# Nomenclatures

## Symbols

| | |
|---|---|
| $\tau_D$ | Time when the indoor temperature is within the uncomfortable range of the human body, s |
| $a$ | Activity, - |
| $C_p$ | Specific heat capacity of air, $kJ \cdot kg^{-1} \cdot K^{-1}$ |
| $C_{solution}$ | Mass concentration of the salt solution, % |
| $d$ | Absolute humidity of wet air, g water $\cdot m^{-3}$ air |
| $DRH$ | Deliquescence relative humidity, % |
| $FTC$ | Thermal comfort rate, - |
| $f_w$ | Fugacity of water vapour, $mol \cdot m^{-3}$ |
| $h_{ad}$ | Heat storage density, $kJ \cdot K \cdot m^{-3}$ |
| $K$ | Thermodynamic equiblibrium constant, - |
| $L_{sal}$ | Enthalpy change of the crystallization of salt, kJ |
| $L_w$ | Latent heat of water evaporation from the saturated solution, $kJ \cdot kg^{-1}$ |
| $L_w$* | Evaporation heat, $kJ \cdot kg^{-1}$ |
| $M$ | Total mass of the adsorbent material in the reactor, kg |
| $m_0$ | Dry mass of the adsorbent at the beginning, kg |
| $m_1$ | After-adsorbed mass of the adsorbent at the end, kg |

| | |
|---|---|
| $m_d$ | Mass of the dried matrix, kg |
| $m_g$ | Mass of the dried composite, kg |
| $M_{sal}$ | Molecular mass of salt, $kg \cdot mol^{-1}$ |
| $M_w$ | Molecular mass of water, $kg \cdot mol^{-1}$ |
| $N$ | Water content, mol water $\cdot mol^{-1}$ salt |
| $n_{sal}$ | Molecular number of the salt, mol |
| $N_w$ | Molecular number of water, mol |
| $P_s$ | Saturated water vapor partial pressure, kPa |
| $P_s(T)$ | Partial water vapour pressure in the saturated air at the temperature $T$, kPa |
| $P_v$ | Water vapor partial pressure in the wet air, kPa |
| $P_w$ | Partial pressure of water vapour, kPa |
| $P_w$* | Pressure of water vapour (* indicates pure water), kPa |
| $P_{w,E}$* | Evaporation pressure of pure water, kPa |
| $Q$ | Theoretical adsorption heat released by the adsorbent, $kJ \cdot kg^{-1}$ |
| $Q_E$ | Energy storage density, $kJ \cdot kg^{-1}$ |
| $q_m$ | Mass flow rate of the air, $kg \cdot s^{-1}$ |
| $q_v$ | Volume flow rate of the gas, $m^3 \cdot s^{-1}$ |
| $R$ | Gas constant, $J \cdot K^{-1} \cdot mol^{-1}$ |

| | |
|---|---|
| $RH$ | Relative humidity, % |
| $R_{salt}$ | Mass ratio of the salt in the composite, % |
| $R_w$ | Water adsorption capacity of the adsorbent, kg water $\cdot$ kg$^{-1}$ adsorbent |
| $S°$ | Standard entropy, kJ |
| $T$ | Temperature, K |
| $t$ | Instantaneous time, s |
| $T_i$ | Temperature of the inlet air, K |
| $T_{max}$ | Maximum temperature, K |
| $T_{min}$ | Minimum temperature, K |
| $T_o$ | Temperature of the outlet air, K |
| $t_{total}$ | Total reaction time, s |
| $v$ | Stoichiometric number, - |
| $w_w$ | Water uptake, kg water $\cdot$ kg$^{-1}$ adsorbent |
| $x_{sal}$ | Salt content in the composite, % |
| $\Delta_f H°$ | Standard formation enthalpy, kJ |
| $\Delta_r H°$ | Reaction enthopy change at standard state per mole salt hydrate, kJ |
| $\Delta_r H_w°$ | Reaction enthalpy change at Standard State per mole water reacted, kJ |
| $\Delta_r S°$ | Reaction entropy change at standard state per mole salt hydrate, kJ |

| | |
|---|---|
| $\Delta_r S_w°$ | Reaction entropy change at Standard State per mole water reacted, kJ |
| $\rho_f$ | Density of the dry air, $kg \cdot m^3$ |
| $\varphi_0$ | Absolute humidity of the outlet air, g water/ $m^3$ air |
| $\varphi_i$ | Absolute humidity of the inlet air, g water/ $m^3$ air |

**Abbreviations**

| | |
|---|---|
| 3D | 3 dimensional |
| AA | Activated alumina |
| AC | Activated carbon |
| ACF | Activated carbon fiber |
| At | Attapulgite |
| BET | Brunauer-Emmet-Teller method, also known as nitrogen adsorption |
| BJH | Barrett-Joyner-Halenda theory |
| CF | Carbon foam |
| COP | Coefficient of performance |
| DSC | Differential scanning calorimetry |
| EDS | Electron dispersive spectroscopy |
| EG | Expanded graphite |

| | |
|---|---|
| ERD | X-ray diffractometer |
| EV | Expanded varmiculate |
| MOF | Metal-organic frameworks |
| SEM | Scanning electron microscopy |
| SG | Silica gel |
| SSA | Specific surface area |
| SSES | Seasonal solar energy storage |
| SSTES | Seasonal solar thermal energy storage |
| TCHS | Thermochemical heat storage |
| TES | Thermal energy storage |
| TGA | Themogravimetric analyzer |
| Ze | Zeolite |

# Table of contents

# Chapter 1. Introduction

## 1.1 Background

Energy consumption in buildings has steadily increased in recent years. Fossil fuels are increasingly becoming unviable as an energy source due to the rapidly increasing global population and growing demands of urban construction. Instead, a range of ecologically sound renewable energy sources, such as solar, wind, and biomass energy, are increasingly being developed to supply energy demands [1-3]. This transition to renewable energy is important to slow climate change and reduce the usage of fossil fuel resources. However, at present, there is a mismatch between user demand and the supply of most renewable energy sources. For example, solar energy is an effective alternative to fossil fuels for heating buildings, which is abundant, however it is intermittent and unstable because the solar radiation varies with weather conditions and time of a day [4]. Most of the solar energy supply is in the summer, heating is most needed in the winter when solar energy is less abundant [5]. Therefore, the reasonable utilization of solar energy requires new technologies to realise short to long term heat storage.

Thermal energy storage (TES) can be used to resolve the timing mismatch between solar energy supply and energy demand [6, 7]. There is increasing interest in technically advanced and economical TES systems for applications such as hot water supply and space heating. Among them, thermochemical heat storage (TCHS) systems have many advantages over other types of TES [8, 9]. This method involves storing energy through reversible adsorption processes or chemical reaction; thus, high reaction enthalpies can be used to achieve greater energy storage density, making the system appropriate for large-scale applications. Using this method, the heat loss during the energy storage process is almost zero [3, 10, 11]; in addition, due to controllable gas partial pressure, this technology is capable of heating, cooling and thermal energy storage functions, allowing the conversion of heat within a specific temperature range [12]. Such feature provides more flexibility than traditional heat storage systems. Moreover, long-term seasonal storage for buildings can be achieved by using TCHS because the heat is stored as chemical potential, which does not degrade over time [13-15].

Hygroscopic salts have been extensively investigated as one of the most promising materials for

TCHS applications. These salts have high water adsorption capability and heat storage density [12, 16] and have been identified as suitable thermal storage candidates in the temperature range of 20 to 200 ℃ [17, 18]. Typical hygroscopic salts for TCHS are $CaCl_2$ and $MgCl_2$ [19], LiCl [20] and $MgSO_4$ [21]. In [22], LiCl composites showed higher adsorption capacity, closely followed, in order, by $CaCl_2$ and LiBr composites. By mixing other salts, LiI, $LiNO_3$, LiCl, etc., into the LiBr solution, mixed materials have been developed aiming to improve solubility, corrosion and stability [23], which inspired the development of composite material using mixed salts. Gordeeva et al. [24] found that dual salt composite adsorbents could reduce adsorption hysteresis while having the potential to significantly improve flexibility and operational reliability, and they designed binary LiCl-LiBr systems confined in silica pores as effective materials with predetermined adsorption properties. Entezari et al. [25] discovered that adding a small amount of LiBr to LiCl can improve the adsorption capacity of the binary salt composites by up to 5.5%, using simulations to evaluate the dehumidification performance of the adsorbent.

In practical system applications, deliquescence of hygroscopic salts leads to the leakage of the liquid salty solution and loss of salt, thus reducing the cyclic stability [26]. To improve the usage of hygroscopic salts, researchers have investigated embedding the salts in porous structures, which are used as carriers to immobilize inorganic salts and distribute them uniformly. Furthermore, the porous properties of the carrier increase the surface area of the composite adsorbent – these materials enhance the heat and mass transfer efficiency with increasing surface area [27]. Commonly used porous matrix include silica gel [28], zeolite [29] and expanded graphite [30]. Zeolites are porous materials with good water adsorption capacity and the ability to function at high temperatures, thus forming excellent matrices for composite materials [31]. Thomas et al. [32] developed composite adsorbent by impregnating zeolites with salt solutions and concluded that the impregnation of these salts by zeolite allowed salt deliquescence and water adsorption above the deliquescence humidity, without the problem of leakage and loss of salt. With high salt loading ratio and at high air humidity levels, the heat storage density of composite material can be up to 153% of that of pure zeolite. Gareth et al. [5] developed four zeolite composites impregnated with different mass fractions of $MgSO_4$; their results showed a strong correlation between the microstructure of zeolite and the heat generated by the composite. To avoid deliquescence, the mass concentration of hygroscopic salts in the composites was usually limited to below 35%.

Previous studies on composite adsorbents have focused on characterising small amount of materials [33-35]. These studies have been less further investigated by applying the materials to real practical systems. System design is the key to developing architectural applications for TCHS. In the current study, the deployment of conventional filled beds in energy storage systems suffers from low energy storage density and large volume. Effective ways to solve such problems and reduce potential costs are worth being explored [36]. Addressing this research goal, Calabrese [37] evaluated the performance of foam-based adsorbent materials in open and closed adsorption heat storage applications and pointed out that matrix maintenance of cyclic stability in practical applications is an important issue to be addressed. Xu et al. [38] developed a numerical model to investigate the thermochemical reaction process in a reactor filled with composite adsorbent and calculated the heat transfer between the composite material and water vapour. Li et al. [39] numerically developed a novel multi-layered sieve reactor focusing on the interaction between the composite material and the air in an open system; in addition, they performed a parametric analysis of the inlet temperature, humidity, and air flow rate. Future more, it is expected that the TCHS system will be applied to actual residential heating. A laboratory prototype of a fixed-bed open TCHS reactor developed by Zondag et al. [40] can provide a certain amount of thermal energy for home heating. The system contains 17 $dm^3$ of adsorbent material, which can generate 150W of thermal energy and achieve an effective energy storage density of about 0.5 $GJ/m^3$. Consider time period and material cost constraints when using energy from TCHS systems for home construction. Researchers can use the TRNSYS program to simulate and analyze transient systems. Safa et al. [41] simulated the heating performance of the heat pump system in the TRNSYS environment and found that the coefficient of performance (COP) under different heat source temperatures was 3.05-3.44 during heating. In TRNSYS-EES, Sakellari et al. [42] analyzed the performance of a heating system based on an exhaust air heat pump using simulation. And several strategies have been proposed to keep comfort within a reasonable range.

### 1.2 Aim and objectives

The aim of this PhD project is to develop the thermochemical adsorption technology for space heating, one of the most promising seasonal solar energy storage (SSES) systems. The selected source materials to compose the thermochemical adsorbent include the salts of $MgSO_4$, LiCl, and

LiBr, and the matrix of different zeolites. The specific objectives are summarised as follows:

- Introduce the thermochemical adsorption/desorption mechanics of water sorption with salt. Review the development of the salt and composite materials for water adsorption. Compare their features and point out the scientific research gap, which inspires the author to start this PhD project.
- Develop suitable $MgSO_4$/LiCl/LiBr–zeolite composite adsorbents for space heating applications. Characterize the composite adsorbents in respect of their surface morphology, porous property, thermal-physical characteristics and so on. Experimentally investigate their practical sorption-heating performance.
- Conduct experimental investigation of space heating on a scaled architecture model using the optimal composite adsorbent characterized in the former tests.
- An adsorption-integrated space heating model is established to predict and evaluate the thermochemical adsorption space heating performance. The adsorption-integrated space heating system could store the solar energy in the solar-abundant days and use it in the space heating seasons.
- An optimal choice should be concluded according to the project results, which is feasible in high performance space heating, with the ability to seasonally store the solar energy. Further study directions should be considered referring to the present research experience.

### 1.3 Structure of the thesis

According to the aim and objectives of this PhD project, the structure of the thesis could be therefore organised as follows:

- Chapter 1: The study background is introduced. The objectives are ensured to accomplish the research aim, which is to develop the thermochemical adsorption space heating technology with the seasonal storage ability of solar energy. The structure of the thesis is thus formed corresponding to the specific project objectives.
- Chapter 2: The literature is reviewed in two main respects. One is the thermodynamics of water sorption with salt, and the other is the research and development of the materials for the water sorption. A scientific gap is discovered which inspires the author to conduct the research.
- Chapter 3: The $MgSO_4$-zeolite composite is developed and characterized. The sorption-heating related properties are tested and analysed. The composite adsorbents are also experimentally tested at the constant temperature and relative humidity. The behaviour of

the composite is discussed.

- Chapter 4: The LiCl/LiBr-zeolite composite is manufactured. The surface morphology, porous property, thermal-physical characteristics are tested. The adsorption kinetics of the composite adsorbent is tested in a climate chamber. The sorption-heating performance is analysed.

- Chapter 5: The optimal composite adsorbent is manufactured and filled into a 1/22.5 scaled house model (3D printed in foam concrete). An adsorption pipeline system is first established to provide the heating air to the house model. The space heating experiment is conducted to evaluate the practical performance of the selected composite adsorbent. The experimental data is further used in the numerical simulation. The space heating performance is assessed in respect of scaled experiment and numerical study.

- Chapter 6: The adsorption-integrated space heating system is simulated with the use of TRNSYS. The geometry of the house is the same, while the locations are relatively in Newcastle, UK, and in Urumqi, China. The system is expected to adsorb the solar energy in the warm days and store it to be used in the cold days. Both the space heating and the storage performance of the system is evaluated.

- Chapter 7: The results of each research section are summarized. The optimal thermochemical adsorption composite is therefore concluded. Future studies could be further directed by the existed experience.

# Chapter 2. Literature review

## 2.1 Introduction

With the diminishing of fossil fuels, increasing energy demand and challenge of global warning, more renewable energies and environmental-friendly energy technologies must be deployed. Heating is one of the most energy intensive demands for human. Such as in the UK, energy consumption for space heating increased from 45.1% to 45.7% of the total energy consumed by the entire UK consumption from the year of 2019 to 2021 [43, 44]. About 74.5% of the heat consumed is for space and hot water heating across domestic, industry and service sectors, more than 70% of which is still powered by natural gas [43]. This leads to high carbon emission.

The heating demand is still increasing due to the continuous economic and population growth. Therefore, to reduce the carbon emissions towards a zero-carbon future, it is imperative to maximise the utilisation of renewable energy resources for heating by including direct usage of renewable heat and electrification of heat based on renewable electricity. However, with the intermittent and unstable challenges of renewable energy sources, it is unlikely that the long-term objectives of zero-carbon heating will be met without significant deployment of energy storage capability.

Solar energy is the most important renewable energy source as the amount of solar energy reaching the Earth's surface in one year is about twice as much as that will ever be obtained from all the Earth's non-renewable resources of coal, oil, natural gas, and mined uranium combined [45]. Yet there is only few renewable heating from solar thermal energy. The primary reason for this is the seasonal mismatch between heating demand and solar energy availability. Hence it is strategically important to develop seasonal solar energy storage (SSES) technologies, also known as seasonal solar thermal energy storage (SSTES).

One of the key performance indicators of a SSES system is the volumetric energy density which determines the system volume. Calculated results of some typical thermal energy materials are shown in Fig. 2.1. Some pioneer projects has been conducted between 1996-2008 using water as a SSES material in Germany at community scale [46], and the storage volume ranging from several to more than 50 thousands of cubic meters. Some of these were combined with heat pump

technology. The operational results revealed large heat loss over time and low energy storage density (<50 kWh/m$^3$) of using water for SSES. Using latent heat storage marginally increases the energy storage density, the theoretical value can achieve 58 kWh/m$^3$ (Triacontane, 252 kJ/kg latent heat, 55-95 °C storage temperature, 25% heat loss), which is still not high enough for a desirable compact SSES system, and the potential high heat loss remains unresolved. Sorption energy storage utilises a reversible sorption reaction and takes the advantages of strong physical/chemical bonds to store the energy. This offers higher energy density with minimum loss due to the temperature-independent means of storage. As shown in Fig. 2.1, the energy storage density of a typical physisorption process using zeolite and water as working pair (650 kg/m$^3$ bulk density of zeolite, 0.25 g/g water uptake, only sorption heat is considered) can reach 158 kWh/m$^3$, 4.5 times and 2.7 times as large as that of water and paraffin respectively. Even higher energy storage density can be expected for chemisorption process. Composite material of $CaCl_2$ and silica gel (SG) and water as working pair were experimentally tested with 211 kWh/m$^3$ energy density [47], $SrCl_2$-expanded graphite (EG) composite and ammonia working pair can reach an energy density of 254 kWh/m$^3$ (500 kg/m$^3$ salt packing density). Therefore, the merits and promising potential have encouraged increasing research and development in thermochemical sorption SSES in recent years [48, 49].

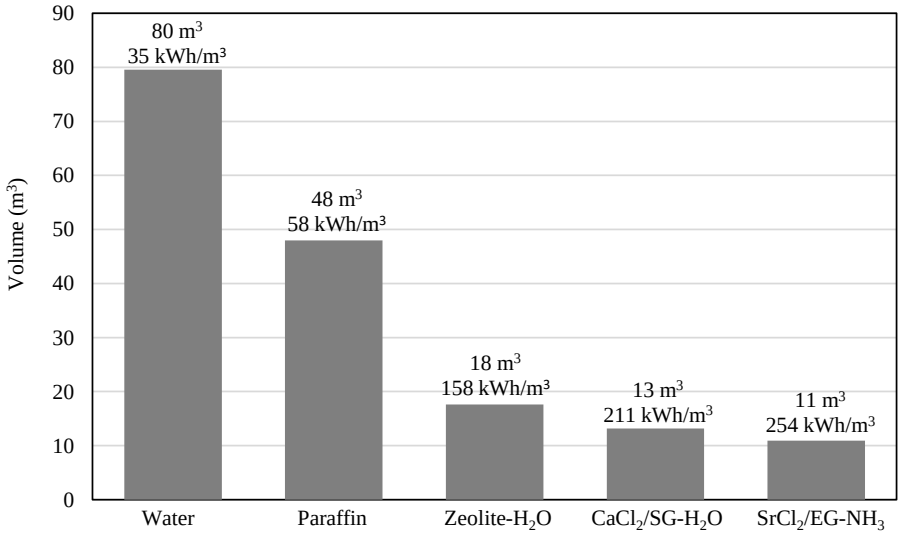


Fig. 2.1 Material volumes required to store 10 GJ heat, water: 55-95 °C storage temperature with 25% heat loss; paraffin (triacontane): 66 °C phase change temperature, 55-95 °C storage temperature with 25% heat loss; zeolite-$H_2O$: 650 kg/m$^3$ bulk density, 0.25 g/g water uptake, no loss of sorption heat; $CaCl_2$/SG-$H_2O$: 211 kWh/m$^3$ storage density [47]; $SrCl_2$/EG-$NH_3$: 500 kg/m$^3$ salt packing density, no loss of sorption heat.

This review summarises the thermodynamic fundamentals and material developments of inorganic salts as water sorption material for thermal energy storage. The literature review mainly consists of two parts. The first part introduces the mechanism of water sorption with salts for thermal energy storage, illustrates the phase equilibrium diagram and deliquescence relative humidity of different salts, then the reaction enthalpy and entropy changes are calculated based on pressure-temperature diagram and standard formation enthalpies and standard entropies, respectively. The second part summarises research and developments of each salt or salt hydrate used for water sorption thermal energy storage. The material issues and salt screening method are discussed first, then the usage of composite material to improve the material performance is introduced, finally the sorption performance some composite materials are summarised.

## 2.2 Thermodynamics of water sorption with salt

### 2.2.1 Mechanism of water sorption with salt for thermal energy storage

The water sorption with salt typically concerns a mono-variant reversible coordination reaction between a salt or its hydrate and water vapour. Because of formation and decomposition of salt hydrate, the adsorption and desorption of water by salt (salt hydrate) are hydration and dehydration. Molecules of water vapour are attracted by metal ions to form coordinate bonds and can be represented by the following equation.

$$M_pX_q.(m+n)H_2O\,[s] + \text{heat} \leftrightarrow M_pX_q.mH_2O\,[s] + nH_2O\,[g] \qquad 2.1$$

A complete energy storage and discharge cycle performs through two phases. Heat is stored by the endothermic dehydration process of the solid $M_pX_q.(m+n)H_2O$, which results into the solid $M_pX_q.mH_2O$ and water vapour. The isolation of the salt and water will effectively store the energy and prevent the heat discharge. The stored heat can be released through exothermic hydration of the solid $M_pX_q.mH_2O$ with the reactive water vapour to form the initial reactant solid. The heat involved in these reactions is the reaction enthalpy associated with hydrogen- and covalent bonding, which is much higher than enthalpy change involved in the latent heat storage and specific heat in the sensible heat storage.

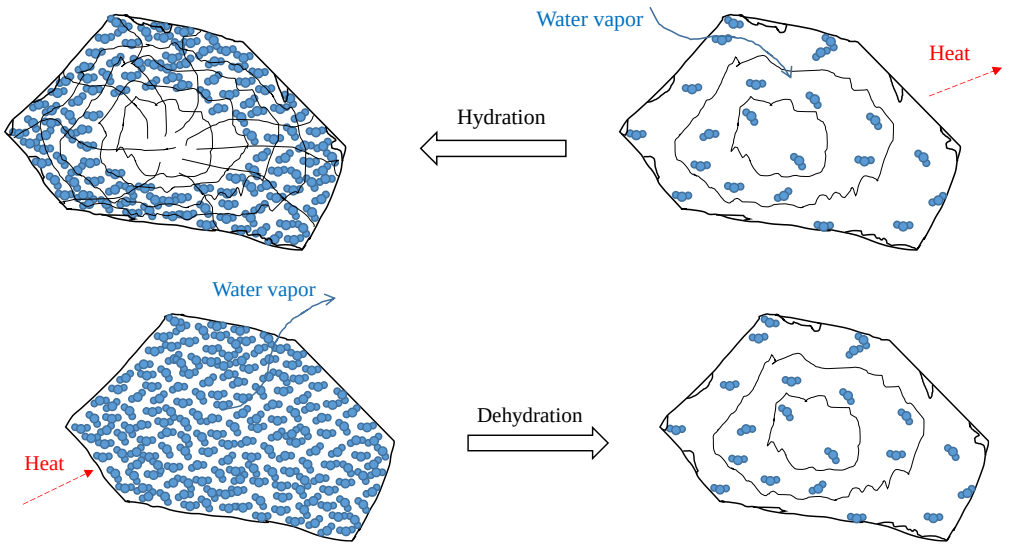


Fig. 2.2 Schematic representation of the dehydration and hydration of salt hydrates occurring at grain scale.

Fig. 2.2 illustrates the hydration and dehydration processes of salt hydrate at grain scale. The dehydration of new salt hydrate will cause morphological changes of the crystal, such as opacity, dimension shrink and cracks, which can be contributed to the density change, the escape of crystalline water and the crystal structure change [50]. The cracks will be used as the water pathway in the hydration stage. However, the newly formed salt hydrate at the outer layer of the crystal will narrow the water vapour pathway and reduce the hydration rate. An inaccessible core area will be eventually formed, indicating the decrease of the hydration / dehydration capacity [51].

Both of closed and open systems, as shown in Fig. 2.3, can be used for thermal energy storage. In a closed system, a condenser / evaporator is used to condense the desorbed water vapour and evaporate the liquid water for adsorption. In such system the pressure of water vapour can be controlled, therefore the desorption / adsorption temperature is correspondingly controlled; on the other way, the desorption / adsorption temperature is limited by available condensation / evaporation temperature. In an open system, water moisture in the air is used for adsorption, and the desorbed water is carried and removed by scrubbing air. Open system is simpler and cheaper, however, the water vapour pressure is determined by the atmospheric condition and uncontrollable, unless a humidifier and a dehumidifier are included in the system.

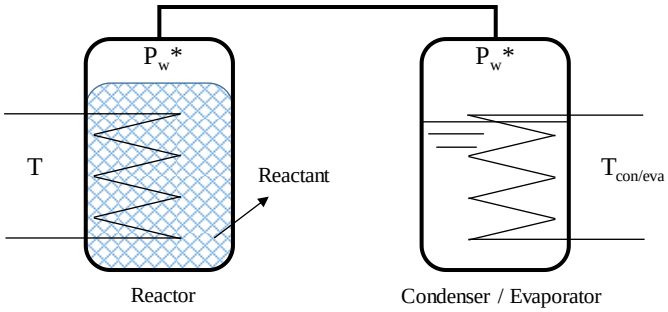


a. Close system

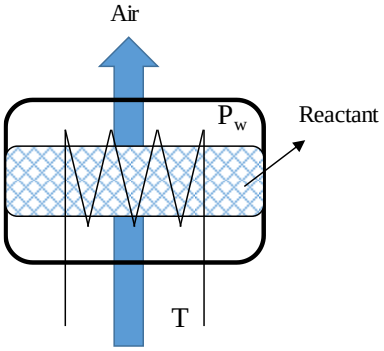


b. Open system

Fig. 2.3 Water sorption system with salts.

### 2.2.2 Sorption phase equilibrium

For a thermodynamic equilibrium process, van't Hoff equation [52] is

$$\ln K = -\frac{\Delta_r H^\circ}{RT} + \frac{\Delta_r S^\circ}{R} \qquad 2.2$$

where $K$ is the thermodynamic equilibrium constant, $\Delta_r H^\circ$ and $\Delta_r S^\circ$ are reaction enthalpy change and entropy change at Standard State ($P^\circ$ = 1 bar) per mole salt hydrate, $R$ is the gas constant, $T$ is the temperature. $K$ can be expressed as

$$K = \prod_i a_i^{v_i} \qquad 2.3$$

where $a$ is the activity ($a \stackrel{\text{def}}{=} \exp\left(\frac{\mu-\mu^\circ}{RT}\right)$), $v$ is the stoichiometric number, subscript $i$ indicates different reactants or products. Therefore, for the water-salt sorption process given in Eq. 2.1, the following expression for the thermodynamic constant can be obtained

$$K = \frac{a_{\mathrm{M_pX_q}.m\mathrm{H_2O}} \cdot a_{\mathrm{H_2O}}^{n}}{a_{\mathrm{M_pX_q}.(m+n)\mathrm{H_2O}}} \qquad 2.4$$

With an approximation of zero compressibility, the activity of pure solid phase is close to unit except for very high pressure. Hence

$$K \approx a_{\mathrm{H_2O}}^{n} = \left(\frac{f_w}{P^\circ}\right)^n \approx \left(\frac{P_w}{P^\circ}\right)^n \qquad 2.5$$

where $f_w$ and $P_w$ are the fugacity and pressure of water vapour respectively. The approximation in above equation is the consideration of water vapour as ideal gas.

Considering a closed sorption system as shown in Fig. 2.3.a with reactant and product only, the following equation is given to correlate the reaction temperature and pressure under equilibrium state

$$\ln\frac{P_w^*}{P^\circ} = -\frac{\Delta_r H_w^\circ}{RT} + \frac{\Delta_r S_w^\circ}{R} \qquad 2.6$$

where $P_w$* denotes the pressure of water vapour (the superscript * indicates pure water), $\Delta_r H_w^\circ$ and $\Delta_r S_w^\circ$ are reaction enthalpy change and entropy change at Standard State per mole water reacted. $\Delta_r H_w^\circ$ and $\Delta_r S_w^\circ$ depend on temperature only. The equilibrium *P*-*T* data of some salt hydrates have been gathered and illustrated in Appendix. A. The lines of ln$P_w$* (bar) *vs* $-1/T$ (K) were found to be almost linear, and were fitted by Eq. 2.6 to obtain the corresponding enthalpy change $\Delta_r H_w^\circ$ and entropy change $\Delta_r S_w^\circ$, the results are listed in Tab. 2.1. It should be mentioned that the obtained values of $\Delta_r H_w^\circ$ and $\Delta_r S_w^\circ$ are not for one specific temperature but for a certain temperature range because of the linearity of ln$P_w$* (bar) *vs* $-1/T$ (K) lines.

For an open sorption system, Eq. 2.6 should be re-written to

$$\ln\frac{P_w}{P^\circ} = -\frac{\Delta_r H_w^\circ}{RT} + \frac{\Delta_r S_w^\circ}{R} \qquad 2.7$$

where $P_w$ is the partial water vapour pressure in atmospheric air ($P_{air}$ = 1.01325 bar).

Because of the involvement of air, it is more convenient to use *RH*-*T* diagram to illustrate the reaction equilibrium, as exemplified in Fig. 2.4 by $MgSO_4$-$H_2O$ system. The equilibrium $P_w$*-*T* data in a closed sorption system can be transferred to *RH*-*T* data in an open system and vice versa by using the Eq. 2.8.

$$RH = \frac{P_w}{P_s(T)} = \frac{P_w^*}{P_s(T)} \qquad 2.8$$

where $P_s(T)$ is the partial water vapour pressure in the saturated air at the temperature of $T$.

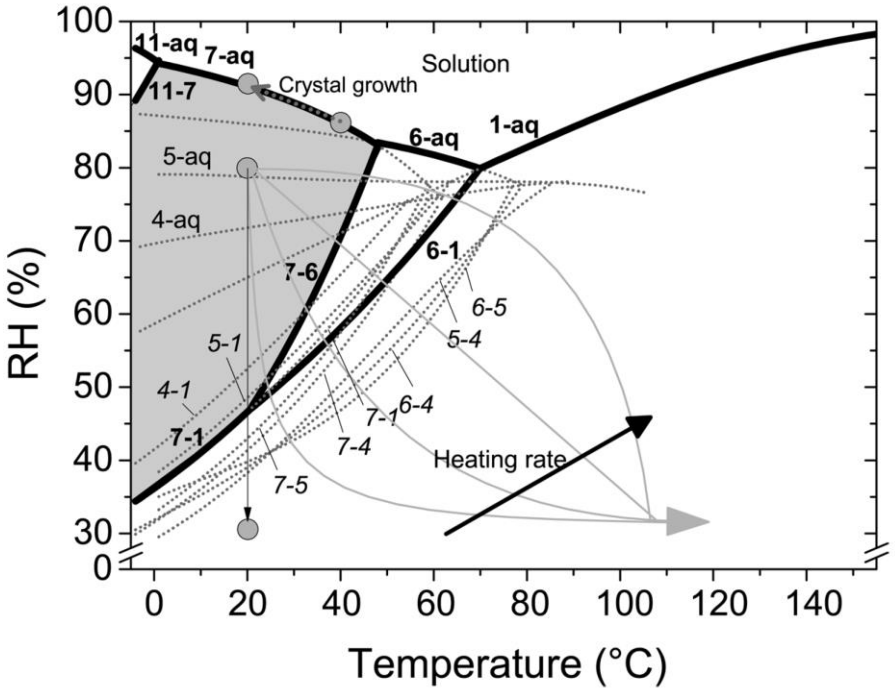


Fig. 2.4 Example of equilibrium *RH-T* diagram of $MgSO_4$ hydrate [53].

Tab. 2.1 Enthalpy and entropy changes of salt-water sorption.

| | ln*P*-*T* method | | | | | Calculated based on standard quantities (at 25 °C) | |
|---|---|---|---|---|---|---|---|
| | $\Delta_r H_w°$ (kJ·mol$^{-1}$) | $\Delta_r S_w°$ (J·mol$^{-1}$·K$^{-1}$) | $T_{min}$ (°C) | $T_{max}$ (°C) | Ref | $\Delta_r H_w°$ (kJ·mol$^{-1}$) | $\Delta_r S_w°$ (J·mol$^{-1}$·K$^{-1}$) |
| $MgCl_2$-6/4$H_2O$ | 57.845 | 136.630 | 4 | 185 | Carling 1981 [54] | 58.197 | 137.775 |
| | | | | | Kipouros and Sadoway 1987 [55] | | |
| | | | | | Kuznik et al. 2015 [56] | | |
| | | | | | Ferchaud 2016 [50] | | |
| | | | | | N'Tsoukpoe et al. 2016 [57] | | |
| $MgCl_2$-4/2$H_2O$ | 67.118 | 144.791 | 30 | 186 | Kipouros and Sadoway 1987 [55] | 67.817 | 146.775 |
| | | | | | Kuznik et al. 2015 [56] | | |
| | | | | | Ferchaud 2016 [50] | | |
| | | | | | N'Tsoukpoe et al. 2016 [57] | | |
| $MgCl_2$-4/2$H_2O$ | 63.156 | 135.699 | 20 | 132 | Carling 1981 [54] | | |
| $MgCl_2$-2/1$H_2O$ | 68.665 | 138.870 | 77 | 252 | Kipouros and Sadoway 1987 [55] | 71.272 | 146.125 |
| | | | | | Ferchaud 2016 [50] | | |
| $MgCl_2$-1/0$H_2O$ | 81.368 | 135.032 | 182 | 377 | Kipouros and Sadoway 1987 [55] | 83.492 | 141.245 |
| $MgSO_4$-7/6$H_2O$ | 58.322 | 161.271 | 4 | 185 | Chou and Seal 2003 [58] | 59.892 | 164.925 |
| | | | | | Donkers et al. 2015 [53] | | |
| | | | | | Kuznik et al. 2015 [56] | | |
| | | | | | Ferchaud 2016 [50] | | |
| | | | | | N'Tsoukpoe et al. 2016 [57] | | |

| | | | | | | | |
|---|---|---|---|---|---|---|---|
| $MgSO_4$-7/6$H_2O$ | 62.425 | 172.171 | 10 | 70 | Bertsch et al. 2009 [59] | | |
| $MgSO_4$-6/1$H_2O$ | 53.716 | 144.821 | 0 | 70 | Chou and Seal 2007 [60]<br>Donkers et al. 2015 [53]<br>N'Tsoukpoe et al. 2016 [57] | 55.162 | 144.485 |
| $MgSO_4$-6/1$H_2O$ | 56.081 | 146.669 | 4 | 185 | Bertsch et al. 2009 [59]<br>Kuznik et al. 2015 [56]<br>Ferchaud 2016 [50] | | |
| $MgSO_4$-7/1$H_2O$ | 52.779 | 142.450 | −4 | 21 | Donkers et al. 2015 [53] | 55.950 | 147.892 |
| $MgSO_4$-6/4$H_2O$ | 53.457 | 144.890 | 0 | 65 | N'Tsoukpoe et al. 2016 [57] | 53.382 | 144.725 |
| $MgSO_4$-1/0$H_2O$ | 77.768 | 154.970 | 111 | 180 | Ferchaud 2016 [50] | 75.382 | 154.025 |
| $MgSO_4$-6/0$H_2O$ | 58.558 | 146.662 | 4 | 186 | Kuznik et al. 2015 [56] | 58.532 | 146.075 |
| $CaCl_2$-6/4$H_2O$ | 46.990 | 116.338 | 0 | 186 | Kuznik et al. 2015 [56]<br>N'Tsoukpoe et al. 2016 [57] | 57.332 | 153.865 |
| $CaCl_2$-4/2$H_2O$ | 47.768 | 115.513 | 4 | 83 | Fujioka and Suzuki 2013 [61]<br>N'Tsoukpoe et al. 2016 [57] | 61.532 | 155.985 |
| $CaCl_2$-4/2$H_2O$ | 58.709 | 149.689 | 25 | 45 | Collins and Menzies 1936 [62] | | |
| $CaCl_2$-2/1$H_2O$ | 47.532 | 106.530 | 17 | 176 | Roozeboom 1889 [63]<br>Lannung 1936 [64]<br>Fujioka and Suzuki 2013 [61]<br>N'Tsoukpoe et al. 2016 [57] | 51.882 | 117.325 |
| $CaCl_2$-1/0$H_2O$ | 42.911 | 80.208 | 4 | 186 | Fujioka and Suzuki 2013 [61]<br>Kuznik et al. 2015 [56] | 71.582 | 158.738 |

| | | | | | | | |
|---|---|---|---|---|---|---|---|
| | | | | | N'Tsoukpoe et al. 2016 [57] | | |
| $CaCl_2$-2/(1/3)$H_2O$ | 60.277 | 134.762 | 104 | 174 | Molenda et al. 2013 [65] | 59.280 | 134.950 |
| $CaCl_2$-(1/3)/0$H_2O$ | 68.703 | 147.565 | 125 | 191 | Molenda et al. 2013 [65] | 73.992 | 153.437 |
| $Na_2S$-9/5$H_2O$ | 55.374 | 148.240 | 0 | 50 | Boer 2003 [66] | 55.032 | 148.550 |
| $Na_2S$-5/2$H_2O$ | 63.238 | 150.119 | 15 | 83 | Mauran et al. 2008 [67] | 54.382 | 149.125 |
| $Na_2S$-2/0$H_2O$ | 72.188 | 171.678 | 5 | 83 | N'Tsoukpoe et al. 2016 [57] | 74.782 | 170.525 |
| $SrBr_2$-6/1$H_2O$ | 67.287 | 155.761 | 0 | 160 | Mauran et al. 2002 [68] | 58.122 | 143.625 |
| | | | | | Lahmidi et al. 2006 [69] | | |
| | | | | | Michel et al. 2012 [70], 2014 [71] | | |
| | | | | | Courbon et al. 2017 [72] | | |
| $SrBr_2$-6/1$H_2O$ | 61.022 | 155.312 | 20 | 88 | Collins and Menzies 1936 [62] | | |
| | | | | | Mauran et al. 2008 [67] | | |
| | | | | | N'Tsoukpoe et al. 2016 [57] | | |
| $SrBr_2$-6/1$H_2O$ | 57.926 | 124.044 | 5 | 186 | Kuznik et al. 2015 [56] | | |
| $SrBr_2$-1/0$H_2O$ | 71.819 | 124.965 | 5 | 186 | Kuznik et al. 2015 [56] | 71.982 | 143.925 |
| $SrBr_2$-1/0$H_2O$ | 71.894 | 143.871 | 84 | 120 | N'Tsoukpoe et al. 2016 [57] | | |
| $CuSO_4$-5/3$H_2O$ | 56.373 | 150.708 | 2 | 47 | Ferchaud 2016 [50] | 55.852 | 149.275 |
| $CuSO_4$-5/3$H_2O$ | 70.115 | 196.887 | 10 | 60 | Bertsch et al. 2009 [59] | | |
| $CuSO_4$-5/3$H_2O$ | 55.321 | 147.606 | 25 | 95 | Collins and Menzies 1936 [62] | | |
| $CuSO_4$-3/1$H_2O$ | 57.241 | 150.322 | 8 | 116 | Collins and Menzies 1936 [62] | 57.422 | 151.175 |
| | | | | | Ferchaud 2016 [50] | | |
| $CuSO_4$-3/1$H_2O$ | 75.176 | 209.466 | 10 | 65 | Bertsch et al. 2009 [59] | | |

| | | | | | | | |
|---|---|---|---|---|---|---|---|
| $LiCl\text{-}1/0H_2O$ | 57.682 | 135.014 | 14 | 100 | Yu et al. 2014 [73] | 62.152 | 145.315 |
| $LiCl\text{-}1/0H_2O$ | 63.004 | 150.091 | 22 | 60 | Thakker et al. 1968 [74] | | |
| $LiBr\text{-}1/0H_2O$ | 69.057 | 143.707 | 41 | 140 | Yu et al. 2014 [73] | 69.549 | 153.495 |
| | | | | | Zhao et al. 2016 [75] | | |
| $LiBr\text{-}1/0H_2O$ | 66.208 | 138.473 | 98 | 150 | Clayton et al. 1980 [76] | | |
| $Na_2SO_4\text{-}10/0H_2O$ | 52.388 | 145.269 | 1 | 32 | Steige and Asmussen 2008 [77] | 52.200 | 144.583 |
| | | | | | Donkers et al. 2015 [78] | | |
| $Na_2S_2O_3\text{-}5/0H_2O$ | 55.243 | 145.799 | 4 | 185 | Kuznik et al. 2015 [56] | 55.168 | 145.425 |
| $CaSO_4\text{-}2/0H_2O$ | 104.207 | 288.359 | 4 | 185 | Kuznik et al. 2015 [56] | 52.442 | 145.125 |
| $CuCl_2\text{-}2/0H_2O$ | 58.088 | 143.562 | 26 | 142 | Polyachenok et al. 2009 [79] | 58.782 | 159.360 |
| $CuCl_2\text{-}2/1H_2O$ | 58.397 | 156.759 | 15 | 65 | Derby and Yngve 1916 [80] | | |
| $K_2CO_3\text{-}1.5/0H_2O$ | 63.645 | 157.218 | 24 | 100 | N'Tsoukpoe et al. 2016 [57] | 63.635 | 156.972 |
| $KOH\text{-}2/1H_2O$ | 59.929 | 154.489 | 15 | 35 | N'Tsoukpoe et al. 2016 [57] | 60.282 | 155.425 |
| $CaBr_2\text{-}6/4H_2O$ | 60.279 | 148.646 | 20 | 40 | N'Tsoukpoe et al. 2016 [57] | | |
| $CaBr_2\text{-}2/1H_2O$ | 65.462 | 133.811 | 70 | 120 | N'Tsoukpoe et al. 2016 [57] | | |
| $CaBr_2\text{-}1/0H_2O$ | 81.673 | 158.720 | 104 | 120 | N'Tsoukpoe et al. 2016 [57] | | |
| $Li_2SO_4\text{-}1/0H_2O$ | 57.876 | 142.707 | 17 | 57 | Ferchaud 2016 [50] | 57.192 | 140.325 |
| $Li_2SO_4\text{-}1/0H_2O$ | 55.437 | 136.716 | 114 | 132 | Campbell 1943 [81] | | |
| $LiNO_3\text{-}0.5/0H_2O$ | 61.047 | 144.695 | 30 | 70 | Thakker et al. 1968 [74] | | |
| $LiOH\text{-}1/0H_2O$ | 56.416 | 145.151 | 30 | 50 | Thakker et al. 1968 [74] | 61.262 | 160.415 |
| $ZnSO_4\text{-}7/6H_2O$ | 57.638 | 161.000 | 10 | 25 | Bonnell and Burridge 1935 [82] | 58.472 | 163.725 |
| $ZnSO_4\text{-}7/6H_2O$ | 57.151 | 159.308 | 0 | 38 | Hoffler et al. 2018 [83] | | |

| | | | | | | | |
|---|---|---|---|---|---|---|---|
| $ZnSO_4$-6/5$H_2O$ | 55.415 | 152.943 | 10 | 25 | Bonnell and Burridge 1935 [82] | | |
| $ZnSO_4$-6/1$H_2O$ | 53.540 | 146.142 | 0 | 52 | Hoffler et al. 2018 [83] | 52.776 | 143.805 |
| $FeSO_4$-7/6$H_2O$ | 54.218 | 149.101 | 10 | 25 | Bonnell and Burridge 1935 [82] | | |
| $FeSO_4$-7/4$H_2O$ | 53.074 | 145.361 | 21 | 48 | Chou et al. 2002 [84] | 53.305 | 146.558 |
| $Ca(NO_3)_2$-4/3$H_2O$ | 60.738 | 161.237 | 20 | 42 | Ewing 1927 [85] | 52.512 | 132.725 |
| $Ca(NO_3)_2$-4/2$H_2O$ | 53.119 | 134.673 | 20 | 39 | Ewing 1927 [85] | 53.967 | 135.875 |
| $Ca(NO_3)_2$-4/0$H_2O$ | 53.075 | 131.879 | 20 | 30 | Ewing 1927 [85] | 56.667 | 143.325 |
| $Ca(NO_3)_2$-3/2$H_2O$ | 55.801 | 140.232 | 20 | 51 | Ewing 1927 [85] | 55.422 | 139.025 |
| $Ca(NO_3)_2$-2/0$H_2O$ | 59.540 | 151.350 | 20 | 51 | Ewing 1927 [85] | 59.367 | 150.775 |
| $SrCl_2$-6/2$H_2O$ | 54.660 | 145.858 | 0 | 65 | Collins and Menzies 1936 [62] | 54.632 | 145.625 |
| | | | | | N'Tsoukpoe et al. 2016 [57] | | |
| $SrCl_2$-2/1$H_2O$ | 59.287 | 142.710 | 24 | 100 | N'Tsoukpoe et al. 2016 [57] | 59.382 | 142.825 |
| $SrCl_2$-2/1$H_2O$ | 59.523 | 149.928 | 25 | 130 | Collins and Menzies 1936 [62] | | |
| $SrCl_2$-1/0$H_2O$ | 66.041 | 131.712 | 80 | 120 | N'Tsoukpoe et al. 2016 [57] | 66.082 | 131.675 |
| $Sr(OH)_2$-8/1$H_2O$ | 62.558 | 169.356 | 23 | 43 | Mauran et al. 2008 [67] | 56.382 | |
| $BaCl_2$-2/1$H_2O$ | 59.501 | 157.882 | 25 | 102 | Collins and Menzies 1936 [62] | 57.712 | 152.825 |
| $BaCl_2$-1/0$H_2O$ | 76.776 | 184.803 | 50 | 130 | Collins and Menzies 1936 [62] | 60.182 | 145.605 |
| $BaBr_2$-2/1$H_2O$ | 59.315 | 154.814 | 25 | 108 | Collins and Menzies 1936 [62] | 56.082 | |
| $BaBr_2$-1/0$H_2O$ | 58.033 | 122.305 | 50 | 130 | Collins and Menzies 1936 [62] | 69.082 | |
| $Ba(OH)_2$-8/1$H_2O$ | 44.978 | 112.601 | 21 | 38 | Mauran et al. 2008 [67] | 57.282 | |

### 2.2.3 Deliquescence relative humidity

In some cases of high water vapour pressure (closed system) or high relative humidity of air (open system), the reaction between solid salt or salt hydrate and water vapour results in liquid salt solution rather than solid hydrate. This is deliquescence process, the corresponding threshold of relative humidity is called deliquescence relative humidity (*DRH*), as expressed in the following equations [48]

$$\text{Salt/Salt hydrate (s)} + H_2O\ (g) \leftrightarrow \text{Salt hydrate (s) for } RH < DRH \qquad 2.9$$

$$\text{Salt/Salt hydrate (s)} + H_2O\ (g) \leftrightarrow \text{Salt solution (l) for } RH \geq DRH \qquad 2.10$$

The *DRH* in open system or the deliquescence water vapour pressure in closed system is the equilibrium *RH* or equilibrium pressure of the system consisting of liquid solution, water vapour and solid salt (or salt hydrate). As shown Fig. 2.4, the *DRH* of $MgSO_4$ hydrate is at the boundary line of salt hydrates and solution. The deliquescence water vapour pressure equals to the water vapour pressure above saturated salt solution. Some other reported *DRH* of some salts has been summarized in Appendix. B.

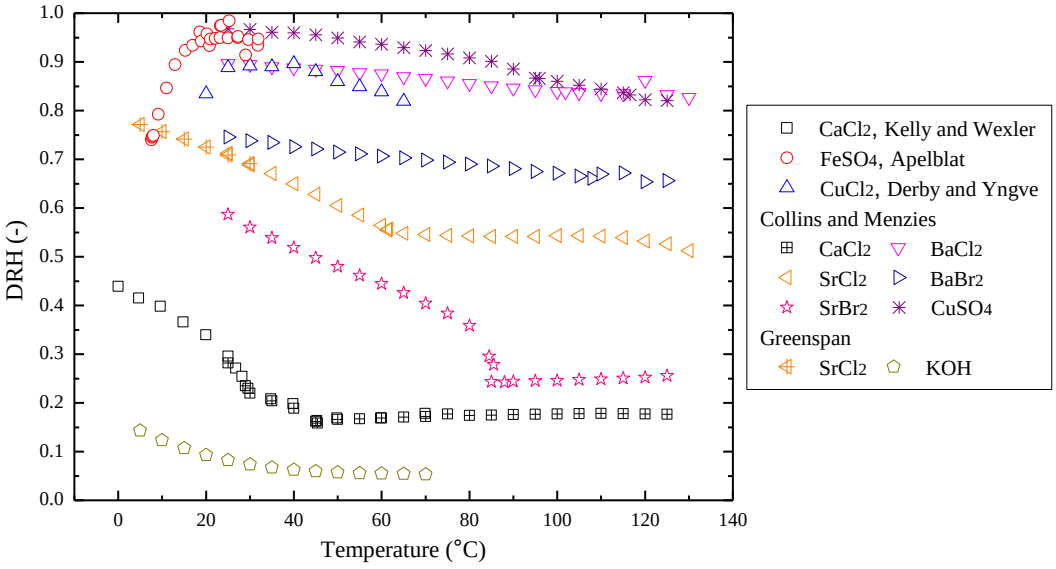


Fig. 2.5 *DRH* with temperature of $CaCl_2$, $FeSO_4$, $CuCl_2$, $CaCl_2$, $BaCl_2$, $SrCl_2$, $BaBr_2$, SrBr, $CuSO_4$, and KOH.

*DRH* is predictable. Assuming the solubility of the interest salt, $M_pX_q$, is $n_{sal}$ mole per mole water at the interested temperature, to maintain the saturation state, the evaporation of 1 mole water from the saturated solution will result in the crystallization

of $n_{sal}/(1-nn_{sal})$ mole of salt or salt hydrate ($M_pX_q.nH_2O$) depending on temperature. The following thermodynamic equilibrium equation has been derived by Denbigh [86] for binary solution in contact with vapour phase of solvent and solid phase of solute

$$\frac{d\ln P_w}{dT} = \frac{L_w + \frac{n_{sal}}{1-nn_{sal}} L_{sal}}{RT^2} \quad 2.11$$

where $P_w$ is the water vapour pressure, $L_w$ is the latent heat of water evaporation from the saturated solution, $L_{sal}$ is the enthalpy change of the crystallization of salt or salt hydrate from the solution. The evaporation of pure liquid water follows the Clausius-Clapeyron equation as

$$\frac{d\ln P^*_{w,E}}{dT} = \frac{L^*_w}{RT^2} \quad 2.12$$

where $P_{w,E}$* is the evaporation pressure of pure water, $L_w$* is the evaporation heat. Considering the following equation given by [87]

$$L_w - L^*_w \ll \frac{n_{sal}}{1-nn_{sal}} L_{sal} \quad 2.13$$

the following expression for *DRH* can be obtained

$$\frac{d\ln DRH}{dT} = \frac{d\ln \frac{P_w}{P_s(T)}}{dT} = \frac{d\ln \frac{P_w}{P^*_{w,E}(T)}}{dT} \approx \frac{\frac{n_{sal}}{1-nn_{sal}} L_{sal}}{RT^2} \quad 2.14$$

$$DRH(T) = DRH(T_0)\exp\left(\frac{\frac{n_{sal}}{1-nn_{sal}} L_{sal}}{R}\left(\frac{1}{T} - \frac{1}{T_0}\right)\right) \quad 2.15$$

where the tiny difference between the evaporation pressure of pure water, $P_{w,E}$*($T$), and the partial water vapour pressure in a saturated air, $P_s(T)$, is ignored [52]. The above equation has been validated by Kelly and Wexler [87] with various salt hydration / dehydration reactions.

### 2.2.4 Sorption enthalpy and entropy changes

Besides using the equilibrium pressure-temperature lines, the sorption enthalpy and entropy changes can also be determined by using the standard formation enthalpy ($\Delta_f H°$) and standard entropy ($S°$) of reactants and products [88], by using the following equations

$$\Delta_{\mathrm{r}}H_w^\circ = \Delta_{\mathrm{f}}H^\circ\{\mathrm{H_2O\ [g]}\} + \frac{\Delta_{\mathrm{f}}H^\circ\{\mathrm{M_pX_q}.m\mathrm{H_2O\ [s]}\}}{n} - \frac{\Delta_{\mathrm{f}}H^\circ\{\mathrm{M_pX_q}.(m+n)\mathrm{H_2O\ [s]}\}}{n} \quad 2.16$$

$$\Delta_{\mathrm{r}}S_w^\circ = S^\circ\{\mathrm{H_2O\ [g]}\} + \frac{S^\circ\{\mathrm{M_pX_q}.m\mathrm{H_2O\ [s]}\}}{n} - \frac{S^\circ\{\mathrm{M_pX_q}.(m+n)\mathrm{H_2O\ [s]}\}}{n} \quad 2.17$$

The values of these standard thermodynamic properties at 25 °C have been tabulated in [88]. Using these data, enthalpy and entropy changes at 25 °C can be calculated, the results are given and compared to those obtained based on $\ln P_{\mathrm{w}}^*$ (bar) *vs* $-1/T$ (K) curves in Tab. 2.1.

Considering the only slightly change of $\Delta_{\mathrm{r}}Cp^\circ$ within a short temperature range, the following equations can be used to extend the standard enthalpy and entropy changes to other temperatures [88].

$$\left(\frac{\partial \Delta_{\mathrm{r}}H_w^\circ}{\partial T}\right)_P = \Delta_{\mathrm{r}}Cp^\circ \quad 2.18$$

$$\Delta_{\mathrm{r}}H_w^\circ(T_2) - \Delta_{\mathrm{r}}H_w^\circ(T_1) \approx \Delta_{\mathrm{r}}Cp^\circ(T_1)\cdot(T_2 - T_1) \quad 2.19$$

$$\left(\frac{\partial \Delta_{\mathrm{r}}S_w^\circ}{\partial T}\right)_P = \frac{\Delta_{\mathrm{r}}Cp^\circ}{T} \quad 2.20$$

$$\Delta_{\mathrm{r}}S_w^\circ(T_2) - \Delta_{\mathrm{r}}S_w^\circ(T_1) \approx \Delta_{\mathrm{r}}Cp^\circ(T_1)\cdot ln\frac{T_2}{T_1} \quad 2.21$$

The extension of reaction enthalpy and entropy changes on pressure can follow the following relationships between *H* and *S* against *P* at constant *T* [88].

$$\left(\frac{\partial H}{\partial P}\right)_T = V - T\left(\frac{\partial V}{\partial T}\right)_P \quad 2.22$$

$$\left(\frac{\partial S}{\partial P}\right)_T = -\left(\frac{\partial V}{\partial T}\right)_P \quad 2.23$$

For condensed phase, the change of *H* and *S* with pressure *P* can be ignored [88].

### 2.2.5 Heat capacity of salt hydrates

The heat capacity of salt hydrate was believed to obey thermodynamic solvate difference rule [89]. Heat capacities of 85 salt hydrates were gathered to determine the value of the constant in thermodynamic solvate difference equation. As shown in Fig. 2.6, the difference between heat capacity of salt hydrates and anhydrous salt generally

increases linearly with the hydration number. The determined equation is given as follows.

$$Cp^{\circ}\{M_pX_q.nH_2O\ [s]\} - Cp^{\circ}\{M_pX_q\ [s]\} = 42.8n \qquad 2.24$$

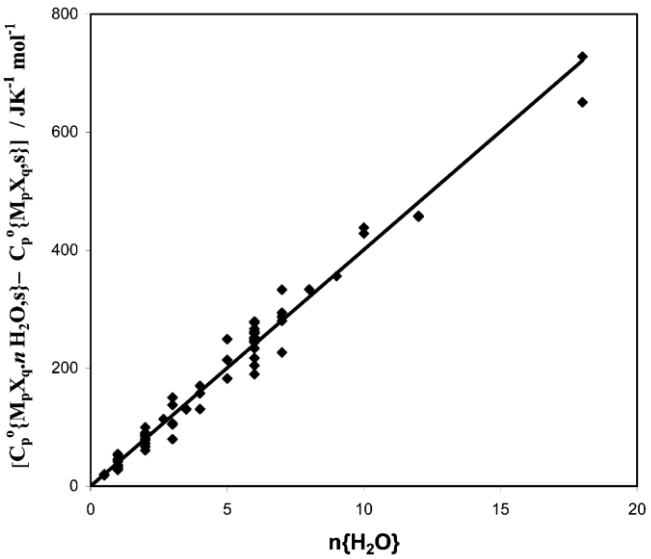


Fig. 2.6 Heat capacity differences of salt hydrates and anhydrous salts *vs* moles of water [89].

## 2.3 Research and developments of salts and composite materials for water sorption

### 2.3.1 Material issues and salt screening

Extensive research has been carried out on using salt-water sorption for the purpose of thermal energy storage. Among hundreds of salts those can form hydrates, $CaCl_2$, LiCl, $MgSO_4$, $MgCl_2$, $SrBr_2$, $Na_2S$, LiBr, $K_2CO_3$, $Na_2SO_4$, $CuCl_2$, $SrCl_2$, $CuSO_4$, $Al_2(SO_4)_3$, $FeSO_4$, $Li_2SO_4$, $ZnSO_4$, $Ca(NO_3)_2$, $LiNO_3$, $MgCO_3$ and LiOH etc. have been ever studied, mainly because of one or more of the reasons of high energy storage density, achievable desorption temperature using waste or renewable heat and suitable adsorption temperature to deliver certain heating purpose. A good salt hydrate for water sorption thermal energy storage should have good chemical, physical and economic properties. Tab. 2.2 lists some criteria of suitable salt hydrates [90, 91].

Theoretical energy densities and the sorption temperature of salt-water sorption for thermal energy storage are most often focused, which have been summarized in Tab. 2.3. The volumetric energy densities based on hydrate with higher hydration number

are ranged from 0.40 to 2.64 GJ/$m^3$ which are 111.1 kWh/$m^3$ to 733.3 kWh/$m^3$. The sorption temperature is calculated with the condition of 1.2 kPa water vapour pressure corresponding to air temperature at 20 °C and relative humidity of 50%. The sorption temperature is in the range of 14-196 °C, a careful selection is needed considering available heat source temperature and requirement of heat release temperature.

Tab. 2.2 Selected criteria of salt-water sorption materials for thermal energy storage.

| Physical properties | Chemical properties | Economic properties |
|---|---|---|
| Low molar volume | High uptake of water | Low cost |
| Small volume change | High reaction enthalpy change | Commercially available |
| Good heat and mass transfer | Relatively low desorption temperature | |
| High thermal conductivity | High reaction rate | |
| Higher melting temperature than desorption temperature | Suitable sorption temperature | |
| High deliquescence vapour pressure | High sorption power | |
| Reaction compound easy to handle | Reactions completely reversible without secondary reactions | |
| | Non-reactive to $O_2$ | |
| | Non-toxic | |
| | Non-flammable/explosive | |
| | Non-corrosive | |

Besides high desorption temperature, low adsorption temperature, low energy storage density and safety issues, other potential existing issues of the application of salt-water sorption for thermal energy storage should also be solved:

- Low deliquescence water vapour pressure (or *DRH*). As introduced in Section 2.2.3, some salts have low deliquescence water vapour pressure so that they are easy to form aqueous solution of salt during the hydration process. This is an undesired effect since it reduces the porosity of the material and slows the vapour transport, leading to the deteriorating performance in multi-cycles. This deliquescence, however, can be accepted in the case of certain technique has been applied to avoid the leakage and vapour channel blockage.
- Low solid-liquid phase change temperature (melting temperature). The solid-liquid phase change can happen to almost all salt hydrates, such like $CaCl_2.6H_2O$ at 29 °C and $MgCl_2.6H_2O$ at 117 °C [92] at atmospheric pressure. This phase change temperature is the upper limit of the dehydration temperature to avoid the occurrence

of liquid.

- Chemical instable. The used salt hydrate should be chemically stable within the lifespan, e.g. 15 years. Some salts tend to be oxidised in air environment which should be avoided for open system; decomposition of salt hydrates to unwanted reactants should be avoided, such like $MgCl_2.2H_2O$ and $MgCl_2.H_2O$ can decompose to MgOHCl (solid), HCl (vapour) and $H_2O$ (vapour) at certain temperature level (> 130 °C [40, 93, 94]).
- Low thermal power. The thermal power in and out of the storage system is dominated by reaction kinetics. Slow reaction leads to bulky system or higher desorption temperature or lower adsorption temperature to satisfy the required input/output thermal power.

N'Tsoukpoe et al. [91] have conducted the screen of salt-water sorption materials for thermal energy storage application from 125 salts. The first 45 salts were screened out based on material safety data sheet and experience. The second screen was conducted based on hydration/dehydration cyclical tests using TGA and some calculations to determine the energy storage density etc., 17 salts were obtained. These promising salts were finally validated by TGA again and evaluated considering practical applications. Eventually, $SrBr_2.6H_2O$ and $LaCl_3.7H_2O$ were considered as the most promising salt hydrate disregarding an economic analysis. From 563 salt hydrates, Donkers et al. [49] selected 25 promising candidates with the filter of at least 1.3 $GJ/m^3$ energy density, a hydration temperature of 50 °C or higher (12 mbar water vapour pressure) and dehydration temperature below 120 °C (20 mbar water vapour pressure); then considering the aspects of energy density, volume variation, hydration/dehydration temperature, melting point, deliquescence vapour pressure, price, safety, and hydration/dehydration kinetics, $K_2CO_3$ stood out despite the relative low energy density, while $MgCl_2$ was considered as another candidate as long as the deliquescence and HCl-outgassing can be avoided. More information of these salt hydrates will be detailed reviewed in the following sections.

Tab. 2.3 Theoretical energy densities and sorption temperatures of different salt-water sorption materials.

| | Hydrate with higher hydration number | | | Hydrate with lower hydration number | | | Sorption temperature with 1.2 kPa water pressure (20 °C, 50%) |
|---|---|---|---|---|---|---|---|
| | Density [a] | Specific energy density | Volumetric energy density | Density [a] | Specific energy density | Volumetric energy density | |
| | kg $m^{-3}$ | kJ $kg^{-1}$ | GJ $m^{-3}$ | kg $m^{-3}$ | kJ $kg^{-1}$ | GJ $m^{-3}$ | °C |
| $MgCl_2.6/4H_2O$ | 1590 | 572.50 | 0.91 | 1650 | 695.81 | 1.15 | 59.96 |
| $MgCl_2.4/2H_2O$ | 1650 | 810.83 | 1.34 | 1900 | 1033.42 | 1.96 | 96.01 |
| $MgCl_2.2/1H_2O$ | 1900 | 543.03 | 1.03 | 2020 | 629.43 | 1.27 | 116.20 |
| $MgCl_2.1/0H_2O$ | 2020 | 737.35 | 1.49 | 2330 | 876.85 | 2.04 | 195.47 |
| $MgSO_4.7/6H_2O$ | 1680 | 242.99 | 0.41 | 1720 | 262.15 | 0.45 | 23.53 |
| $MgSO_4.6/1H_2O$ | 1720 | 1207.24 | 2.08 | 2580 | 1993.01 | 5.14 | 30.89 |
| $MgSO_4.7/1H_2O$ | 1680 | 1361.99 | 2.29 | 2580 | 2425.79 | 6.26 | 29.55 |
| $MgSO_4.6/4H_2O$ | 1720 | 467.31 | 0.80 | 2010 | 554.81 | 1.12 | 20.69 |
| $MgSO_4.1/0H_2O$ | 2580 | 544.71 | 1.41 | 3010 | 626.23 | 1.88 | 121.61 |
| $MgSO_4.6/0H_2O$ | 1720 | 1537.19 | 2.64 | 3010 | 2917.52 | 8.78 | 46.67 |
| $CaCl_2.6/4H_2O$ | 1710 | 523.40 | 0.90 | 1840 | 626.42 | 1.15 | 27.31 |
| $CaCl_2.4/2H_2O$ | 1840 | 672.31 | 1.24 | 1840 | 837.08 | 1.54 | 45.79 |
| $CaCl_2.2/1H_2O$ | 1840 | 352.90 | 0.65 | 2240 [b] | 402.18 | 0.90 | 63.19 |
| $CaCl_2.1/0H_2O$ | 2240 [b] | 554.89 | 1.24 | 2190 | 644.96 | 1.41 | 92.67 |
| $Na_2S.9/5H_2O$ | 1430 | 916.52 | 1.31 | 1590 | 1309.36 | 2.08 | 23.53 |
| $Na_2S.5/2H_2O$ | 1590 | 970.42 | 1.54 | 1737 [c] | 1430.18 | 2.48 | 19.11 |
| $Na_2S.2/0H_2O$ | 1737 [c] | 1311.12 | 2.28 | 1856 | 1916.42 | 3.56 | 87.30 |
| $SrBr_2.6/1H_2O$ | 2440 | 817.40 | 1.99 | 3880 | 1094.77 | 4.25 | 48.74 |
| $SrBr_2.1/0H_2O$ | 3880 | 271.17 | 1.05 | 4260 | 290.91 | 1.24 | 124.86 |
| $CuSO_4.5/3H_2O$ | 2290 | 447.39 | 1.02 | 2670 | 522.84 | 1.40 | 26.77 |
| $CuSO_4.3/1H_2O$ | 2670 | 537.54 | 1.44 | 3350 | 646.58 | 2.17 | 32.09 |
| $LiCl.1/0H_2O$ | 1760 | 1028.85 | 1.81 | 2090 | 1466.06 | 3.06 | 67.87 |
| $LiBr.1/0H_2O$ | 2680 | 663.22 | 1.78 | 3510 | 800.79 | 2.81 | 92.07 |
| $Na_2SO_4.10/0H_2O$ | 1470 | 1620.16 | 2.38 | 2690 | 3674.99 | 9.89 | 14.41 |
| $Na_2S_2O_3.5/0H_2O$ | 1760 | 1111.45 | 1.96 | 2340 | 1744.65 | 4.08 | 29.36 |
| $CaSO_4.2/0H_2O$ | 2300 | 609.18 | 1.40 | 2990 | 770.40 | 2.30 | 14.88 |
| $CuCl_2.2/0H_2O$ | 2510 | 689.62 | 1.73 | 3400 | 874.43 | 2.97 | 26.29 |
| $K_2CO_3.1.5/0H_2O$ | 2180 | 577.68 | 1.26 | 2430 | 690.62 | 1.68 | 55.01 |
| $KOH.2/1H_2O$ | 1780 | 654.25 | 1.16 | 1960 | 813.25 | 1.59 | 40.22 |
| $KOH.1/0H_2O$ | 1960 | 1110.54 | 2.18 | 2120 | 1467.10 | 3.11 | 165.99 |
| $Li_2SO_4.1/0H_2O$ | 2090 | 446.96 | 0.93 | 2230 | 520.19 | 1.16 | 49.49 |
| $LiOH.1/0H_2O$ | 1530 | 1459.89 | 2.23 | 1450 | 2558.08 | 3.71 | 37.25 |
| $ZnSO_4.7/6H_2O$ | 1950 | 203.35 | 0.40 | 2072 [d] | 216.95 | 0.45 | 18.22 |
| $ZnSO_4.6/1H_2O$ | 2072 [d] | 979.07 | 2.03 | 3370 | 1470.52 | 4.96 | 18.83 |
| $FeSO_4.7/4H_2O$ | 1900 | 575.21 | 1.09 | 2290 | 714.01 | 1.64 | 17.33 |
| $Ca(NO_3)_2.4/3H_2O$ | 1910 | 222.37 | 0.42 | 2039 [c] | 240.73 | 0.49 | 36.36 |
| $Ca(NO_3)_2.4/2H_2O$ | 1910 | 457.06 | 0.87 | 2150 | 539.35 | 1.16 | 39.13 |
| $Ca(NO_3)_2.4/0H_2O$ | 1910 | 959.85 | 1.83 | 2490 | 1381.37 | 3.44 | 41.20 |
| $Ca(NO_3)_2.3/2H_2O$ | 2039 [c] | 254.07 | 0.52 | 2150 | 276.94 | 0.60 | 41.81 |
| $Ca(NO_3)_2.2/0H_2O$ | 2150 | 593.31 | 1.28 | 2490 | 723.59 | 1.80 | 43.11 |
| $SrCl_2.6/2H_2O$ | 1960 | 819.64 | 1.61 | 2710 | 1123.21 | 3.04 | 26.09 |
| $SrCl_2.2/1H_2O$ | 2710 | 305.22 | 0.83 | 2920 | 336.36 | 0.98 | 57.19 |
| $SrCl_2.1/0H_2O$ | 2920 | 374.32 | 1.09 | 3100 | 416.85 | 1.29 | 118.79 |
| $BaCl_2.2/1H_2O$ | 3110 | 236.26 | 0.73 | 3320 | 255.07 | 0.85 | 30.96 |
| $BaCl_2.1/0H_2O$ | 3320 | 265.98 | 0.88 | 3940 | 288.99 | 1.14 | 56.54 |

[a] Densities of salt hydrates are from [95] except with specific reference.

[b] [96]; [c] Extrapolated by available densities of parent salt and other salt hydrates; [d] [97].

### 2.3.2 Solution to the degradation and deliquescence - composite

As has been described, the issue of deliquescence of pure salt hydrate can result in degradation of salt-water sorption after several cycles. Using porous host matrix and impregnating salt into the micro pores can be an effective solution to solve the deliquescence and degradation problem. The porous structure of the host matrix allows the existence of certain amount of liquid without the problems of leakage, agglomeration and blockage of the vapour channel. The commonly used porous host matrixes include zeolite (Ze), silica gel (SG), activated carbon (AC), activated carbon fiber (ACF), activated alumina (AA), expanded vermiculate (EV), carbon foam (CF), expanded graphite (EG) and attapulgite (At) etc. Very recently metal-organic frameworks (MOF) material was used as host matrix.

During the fabrication process of composite material, the host matrix is normally dried first and is then soaked into salty solution for salt impregnation. The water will be removed by drying. Repeating the impregnation and drying processes can result in higher salt content [98]. The chemical nature of the host matrix, the mass ratio of the salt and the synthesis processes open new opportunities for adjusting the properties and performance of the composite sorbent material.

Aristov [99] described the mechanism of the water sorption process of $CaCl_2$-SG composite, as shown in Fig. 2.7. Solid $CaCl_2$ particles inside the host matrix adsorb water vapour and become $CaCl_2$ hydrate ($CaCl_2.2H_2O$), while the porous structure of the host matrix provides the flow channels for the vapour; because of the deliquescence, the solid salt hydrate gradually transfers to aqueous solution as more and more water vapour is captured; the liquid $CaCl_2$ solution captures more water vapour through absorption process and finally the solution fills all the pores of the host matrix. The water vapour hydrated by the solid $CaCl_2$ was believed only about 10-15% of the total water uptake, most of the water was captured by liquid absorption which was about 80% of the total, while the physical adsorption by the porous host matrix only accounted for 3-5%. This was confirmed by Zhang et al. [100] through a STA test on LiCl-EV composite, 83.0%-88.3% of the total water uptake was by liquid absorption by LiCl solution, 9.8%-10.2% was hydrated by LiCl to form hydrate, and other 1.9%-6.8% was adsorbed by EV.

Nevertheless, the potential leakage of liquid from the host matrix is still the most

damaging issue. Gordeeva and Aristov [101] suggested the following three ways to alleviate this shortcoming: (a) proper selection of salt mass ratio; (b) anchoring the salt cations to the surface of the matrix; (c) cover the composite surface with liquid proof but vapour penetrable coating.

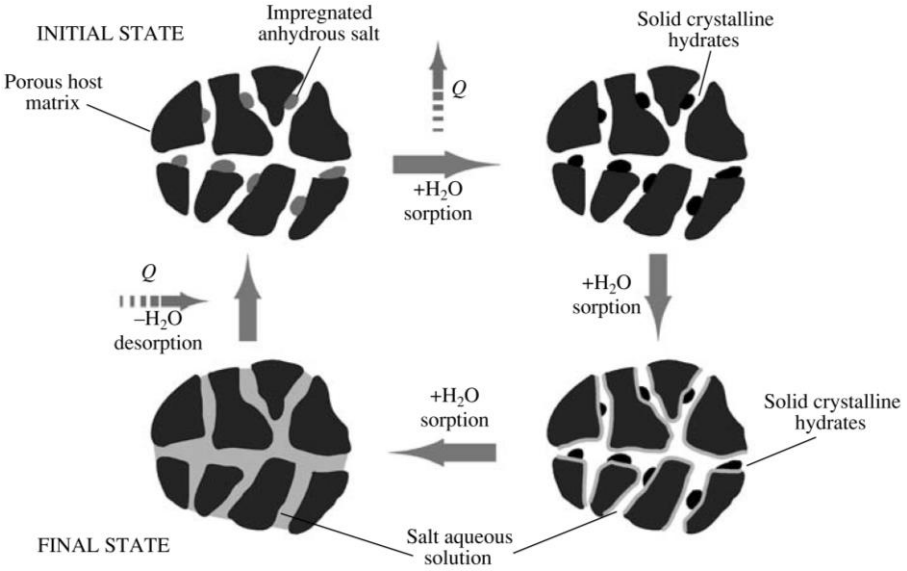


Fig. 2.7 Water sorption mechanism of $CaCl_2$ impregnated in silica gel [99].

The salt content is a key factor dominating the overall water uptake and the storage density of the composite material. Generally, higher salt content leads to better performance of the composite material, however, the narrower water vapour channel should be considered as the disadvantage of using higher salt content. 15 wt% salt content was selected as the maximum value by [102] since the authors believed higher salt content can cause the problem of surface crust of the porous host matrix which blocked the water vapour flow channel.

Ye et al. [103] tested influence of impregnation period (18-96 hours) and $CaCl_2$ solution concentration (5-55 wt%) on $CaCl_2$ content in the composite using ACF as matrix. 18 hours was found enough to allow the penetration of salty solution into the ACF; the salt content in the composite increased rapidly with the used solution concentration when the concentration is less than 22.5 wt% and reached constant value at about 40 wt%.

The impregnated salts will certainly occupy a fraction of the pores of the host matrix, the total pore volume before and after salt impregnation was compared in [104]. About

21% and 15% volume reduction were found after impregnating $CaCl_2$ into silica gel and activated carbon with mesoporous pores; for zeolite which has microporous pores, the impregnation damages the material structure and only 2% pore volume reduction was noticed; for vermiculite which has macropores, the impregnation led to an average pore volume reduction of 72% and no evidence of damage to pore structure was notice. Microporous matrix like zeolite was found to be not suitable as host matrix due to the inferior salt dispersion and the block of micropores by the salt particles, this deteriorated the water vapour transfer and resulted in lower water uptake comparing to that of pure zeolite [105].

The energy densities of various salt-porous matrix composite materials have been measured by Aristov et al. [106] by using DSC. The used salts included LiBr, $CaCl_2$ and $MgCl_2$ while the used matrix included silica gel, aerogel, alumina and Sibunit. The results showed that the total desorption energy almost linearly increased with increasing water uptake (kg/kg dry composite) despite of the salt and matrix types. The obtained average heat of desorption was 2.62 kJ/g $H_2O$ (47 kJ/mol) for different composites, which is close to the evaporation heat of water from diluted salty solutions.

MOF materials have been tried and compared by Permyakova et al. [107] as host matrix of $CaCl_2$. Hydrophilic MOF materials were found not suitable as salt host matrix due to their low desorption efficiency. Mesoporous and amphiphilic MOFs, such as MIL-100(Fe) and MIL-101(Cr), were validated as the suitable MOF materials which can bear high salt contents and exhibited high cyclical stability.

Other novel techniques like coating or encapsulating salt material by porous shell have also employed to form a composite material. The method has drawn intensive attention on encapsulating inorganic phase change material in recent years, but only a couple of tries have been made on sorption material. A core-shell structure is formed by this method. Core salt material is protected by a shell material with water vapour permeability, then the deliquescence and absorption process are allowed without liquid leakage. Gaeini et al. [108] used spraying drying method to encapsulate $CaCl_2$ with ethyl cellulose shell, the salt content can reach 80%. Shkatulov et al. [109] used modified sol-gel method to encapsulate LiCl, $SrBr_2$ and $CaCl_2$, the shell was silica, and the salt content reached 45%, 59% and 50% respectively for the three salts. Wei et al.[110] coated $CaCl_2$ by using coal tars so that carbon shell was formed. The salt

content was in the range of 65-89%.

### 2.3.3 $CaCl_2$ Composite

Calcium chloride ($CaCl_2$) is one of the most used chemicals in many thermal engineering applications. It is an easily and cheaply commercially available salt hydrate because large quantities are produced as by-product of numbers of industrial processes. That makes it very appealing for many applications particularly for those need large quantities such like seasonal thermal energy storage applications.

$CaCl_2$ is a highly hygroscopic salt and can take up 6 water molecules as crystalline hydrates, including the salt hydrate $CaCl_2.H_2O$, $CaCl_2.2H_2O$, $CaCl_2.4H_2O$ and $CaCl_2.6H_2O$. If all six moles of water can be involved in the hydration, the energy storage density of this salt hydrate can achieve its maximum value of 750 kWh/$m^3$ [111]. Nevertheless, this potential of desirable high energy density is hardly fully utilised. While the hydration from anhydrous ($CaCl_2$) to dihydrate ($CaCl_2.2H_2O$) is generally used, higher hydrates $CaCl_2.4H_2O$ and $CaCl_2.6H_2O$ melt at around 45.3 °C and 28-30 °C [111], respectively, and consequently form an aqueous solution which must be avoided. Otherwise, porous host matrix must be used to eliminate the inefficient vapour transport, sluggish kinetics and reduced water uptake. Jabbari-Hichri et al. [112] reported that after a complete dehydration performed up to 300 °C using TG–DSC the rehydration under humid gas flow ($RH$ = 0.28) for 16 hours only regained 2.6 water molecules. That indicated a loss of around 37% of potential performance in heat storage and was attributed to the swelling and agglomeration during the dehydration process. To address the above issues, the majority of the research on $CaCl_2$ water sorption for thermal energy storage used composite material. There has been a good number of works investigating $CaCl_2$-host matrix composites based on different porous materials, probably including all the types those have been ever reported, for the applications of adsorption refrigeration / heat pump, desiccant cooling / dehumidification, phase change material and energy storage etc.

The hydration of $CaCl_2$ is a stepwise process at constant temperature or constant water vapour pressure, e.g. either forming the salt hydrate or not. When using composite material, the allowance of the existing of liquid solution confined in the pore of host matrix leads to a bivariant sorption process that depends on both temperature and water vapour pressure, as exemplified by $CaCl_2$-SG composite as shown in Fig. 2.8 [113]. As

shown in the figure, the water content (*N*, mol water per mol salt, this is also hydration number of hydrate) increases rapidly with the decrease of temperature at a constant water vapour pressure $P_w$, and the curve shifts to the higher temperature side as the increase of $P_w$, which indicates higher water content can be achieved at higher $P_w$ at constant temperature. The two plateaus indicate the formation of $CaCl_2.0.33H_2O$ and $CaCl_2.2H_2O$. Above the plateau of $CaCl_2.2H_2O$, the formed $CaCl_2.4H_2O$ was believed to coexist with the salt solution or completely melt into liquid state, therefore the water content increased with the decreasing temperature and can be larger than the maximum hydration number of $CaCl_2$ (6 as in $CaCl_2.6H_2O$). Similarly, Janchen et al. [114] reported stepwise change of water uptake by $CaCl_2$-At composite as the increase of water vapour pressure, and detected the formation of solid $CaCl_2.2H_2O$ and $CaCl_2.4H_2O$ by X-ray diffraction (XRD). The formation of $CaCl_2.6H_2O$ was observed when using high salt content in the composite by Aristov et al. [115] using $CaCl_2$-EV composite with 57.3% salt content and Ye et al. [103] using $CaCl_2$-ACF composite with 58.6% salt content. However, these step changes were not always detected.

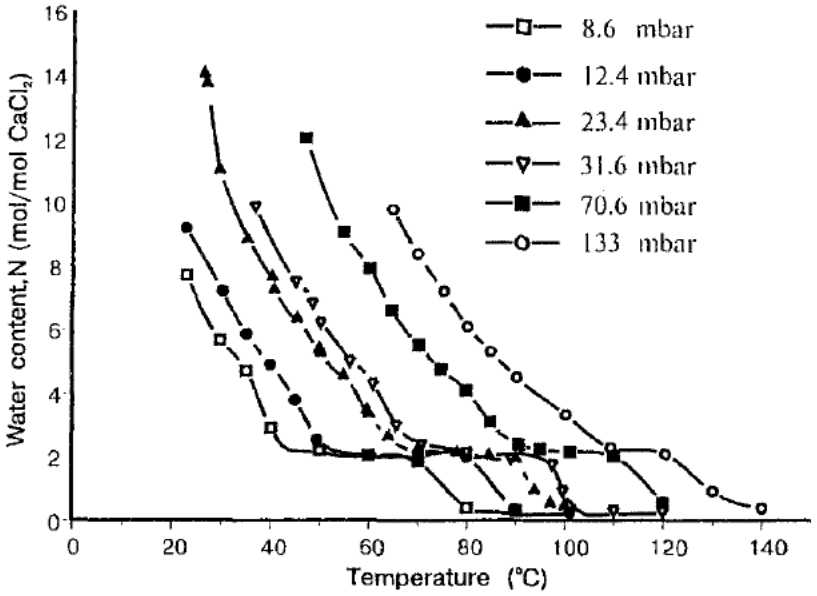


Fig. 2.8 $CaCl_2$-SG water sorption isobars [113].

The bivariant hydration process dependent on temperature and water vapour pressure can be described as a monovariant process by correlating the water content *N* and the relative humidity *RH*. *N vs RH* of different $CaCl_2$ composites have been summarized in

Fig. 2.9. The figure also shows the profiles of pure $CaCl_2$ hydration process to be compared with composite materials. Since not all the referred publications presented the data of *N* and *RH* directly, some of the water contents were calculated based on the equation $N = \frac{w_w}{x_{sal}} \frac{M_{sal}}{M_w}$, where $w_w$ is the water uptake (g water / g dry composite), $x_{sal}$ is the salt content in the composite (g salt / g dry composite), $M_{sal}$ *and* $M_w$ are the molecular mass (g/mol) of salt and water respectively. As shown in the figure, many results show the existing of solid hydrate, $CaCl_2.2H_2O$, indicated by the plateau around $N = 2$ when $RH < 0.2$. The formation of $CaCl_2.2H_2O$ in composite materials is noticed to start from a lower *RH* than that of pure salt material. $CaCl_2$ hydrate with higher hydration number was less observed. After *RH* is larger than about 0.2, the sorption process is completely a liquid absorption process attributing to the low *DRH* of $CaCl_2$ (*DRH* < 0.2 when temperature is higher than 35 °C). Thereafter most of the reported composite materials have their *N vs RH* curves follow the pure salt absorption *N vs RH* curve, which is determined by the solubility of the salt at different relative humidity conditions. When the salt content in the composite is relatively low, the water amount adsorbed by the host matrix can be relatively large, thus the water content calculated based on the amount of $CaCl_2$ can be very high, such as the cases of using FeKIL2 [116] (7% salt content) and WSS [117] (2.2% salt content).

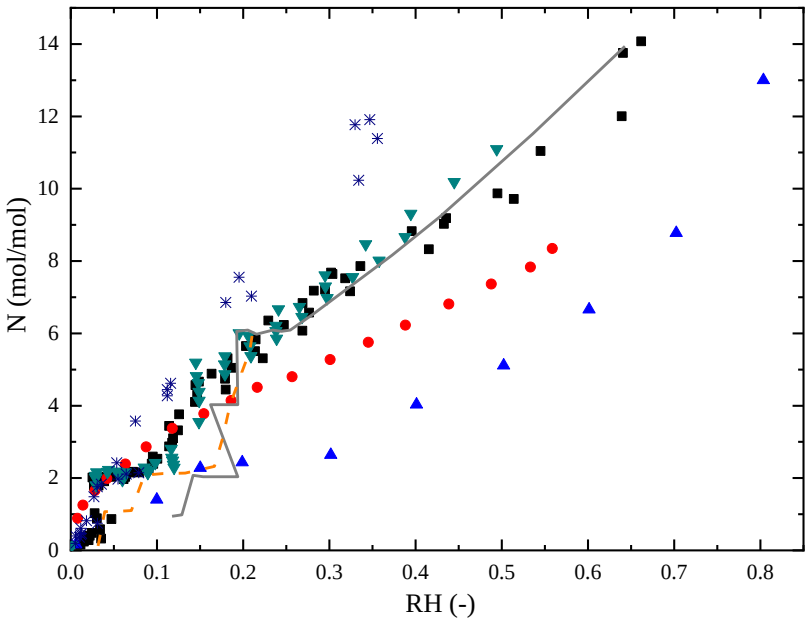


■ $x_{sal}$ = 33.7% [113] ; ● $x_{sal}$ = 21.7% [118]; ▲ $x_{sal}$ = 35% [119]; ▼ $x_{sal}$ = 43% [47] [120]; ✳ $x_{sal}$ = 17-33% [105].

Fig. 2.9 *N vs RH* of $CaCl_2$-SG composite.

Grey solid curve and orange dash curve are of pure $CaCl_2$ reported by [113] and [117] respectively.

The reported maximum water uptakes of $CaCl_2$ composite is in the range of 0.1-2.2 g/g and generally increases with salt content and relative humidity but with apparent exceptions such as reported by [108, 121]. More than half of the reported composites (about 60 composites) had water uptakes higher than 0.5 g/g and about 20% of these composites had water uptakes higher than 1.0 g/g. However, it should be noticed that almost all these high water uptakes (>1.0 g/g) were obtained with high relative humidity (> 0.8), then the success of using $CaCl_2$ composite material lies more on creating high relative humidity environment than using high salt content.

The sorption heat of $CaCl_2$ composites per mole water vapour are summarized in Fig. 2.10. As shown in the figure, the sorption heat decreases drastically with water content $N$ when $N$ is less than 2, which is agree with the reaction enthalpy change of $CaCl_2$ hydrates as given in Tab. 2.1. Thereafter, the sorption heat seems to be a constant value when $N$ is higher than 2, at around 45.0 kJ/mol water which is close to water condensation / evaporation heat in liquid $CaCl_2$ solution (47.0 kJ/mol) [113]. It was generally believed that solid hydrates were formed when $N \leq 2$ which has stronger bound force between salt and water molecules, and $CaCl_2$ aqueous solution was formed when $N > 2$ and the solution confined in meso- and/or macro-pores of matrixes does not change its water sorption properties compared to the bulk solution [113].

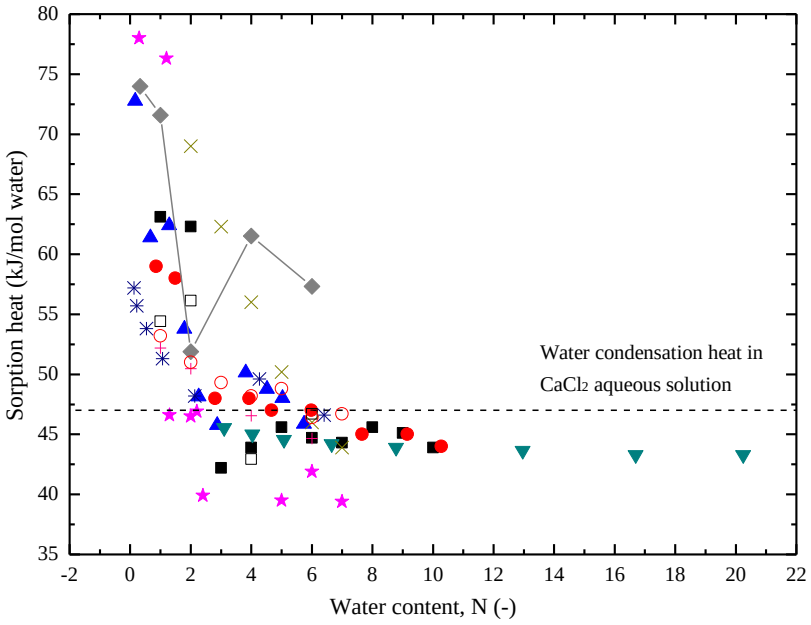


■ SG, $x_{sal}$ = 33.7% [113] ; ● SG, $x_{sal}$ = 33% [105]; ▲ At, $x_{sal}$ = 30% [114]; ▼ SG, $x_{sal}$ = 35% [119]; ✳ Xerogel, $x_{sal}$ = 28.9% [122]; ★ EV, $x_{sal}$ = 57.3% [115]; × SG, $x_{sal}$ = 21.7% [118]; + Pure salt [108]; □ Encapsulated salt [108]; ○ MCM-41, $x_{sal}$ = 37.7% [99]; ◆ Reaction enthalpy changes from Tab. 2.1.

Fig. 2.10 Sorption heats of $CaCl_2$ composites

The energy densities of $CaCl_2$ composites are dependent on the salt content in the composite and the relative humidity of the air. As summarized in Fig. 2.11, the energy densities are scattered in the large range of few hundreds to 3000 kJ/kg composite (based on dry composite mass), and higher salt content and higher relative humidity generally lead to larger specific energy density. Volumetric energy densities were less reported. The highest volumetric energy density was 1.2 GJ/m$^3$ reported by [108], however the used host matrix, vermiculite, and the high salt content 86%, led to overhydrate and leakage of liquid; the encapsulated salt was believed to have the high cyclical stability, however the volumetric energy density was only 0.4 GJ/m$^3$ due to the low bulk density of the material.

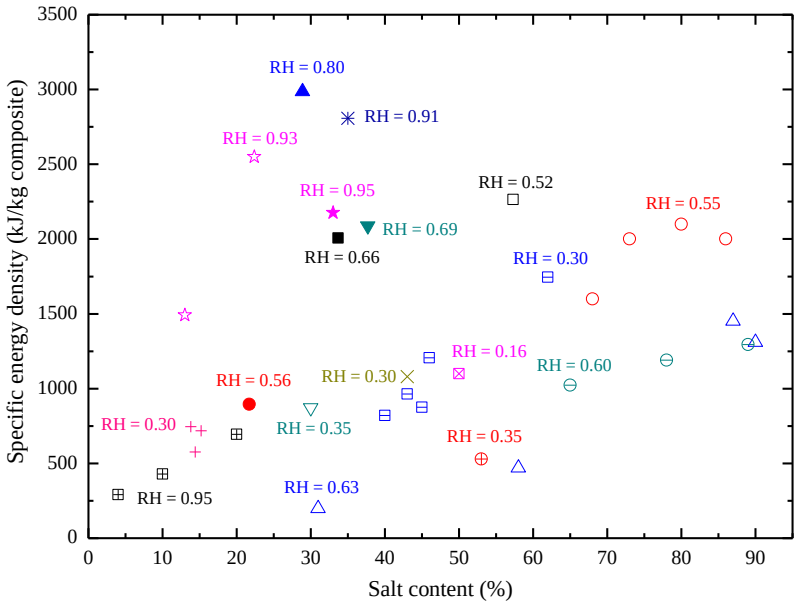


■ SG [113] ; ● SG [118]; ▲ Xerogel [122]; ▼ MCM-41 [123]; ✳ SG [119]; ★ SG [105]; × SG [47]; ┼ SG, alumina, bentonite [102]; ☐ EV [115]; ○ Ve, EG, ethyl cellulose encapsulated [108]; △ ACF, EG [121]; ▽ At [114]; ☆ WSS [117]; ⊞ PHTS [124]; ⊕ MWCNT [125]; ⊟ MOF [107]; ⊖ Carbon encapsulation [110]; ⊠ Silica encapsulation [109].

Fig. 2.11 Specific energy densities of $CaCl_2$ composites

### 2.3.4 LiCl Composite

LiCl has extraordinary solubility in polar solvent and is a highly hygroscopic salt. It is widely used in liquid desiccant technology [126]. There are also studies using absorption / desorption process of LiCl aqueous solutions for thermal energy storage [127]. Because of the low *DRH*, it is essential to use host matrix to allow the existence of liquid when using LiCl sorption for thermal energy storage.

Similar to that of $CaCl_2$ composite, the hydration process of LiCl-host matrix composite involves three mechanisms, porous matrix adsorption, solid salt hydration, and salty solution absorption. As a high hygroscopic salt, the deliquescence occurs at very low relative humidity, 10-11%. As summarised in Fig. 2.12, at relative humidity lower than 10%, the formation of LiCl monohydrate was detected in some composite materials, but was not shown in many others especially those with low salt content. This can be attributed to the well distribution of salt inside pores of host matrix and the adsorption of the porous host matrix. Once deliquesce happens, the water content, *N*, increases rapidly with the increasing relative humidity. The formed liquid LiCl solution will be

constrained within the host matrix, ideally without leakage.

Because of the existence of liquid absorption, the water content, *N*, can be very high, e.g. up to 25, especially when the salt content is low. Many experimental results of *N vs RH* of LiCl composite materials follow the profile of pure LiCl salt. However, more results having lower water content than that of pure LiCl salt at the same relative humidity are noticed. This is probably caused by the mass transfer limitation of the composite material.

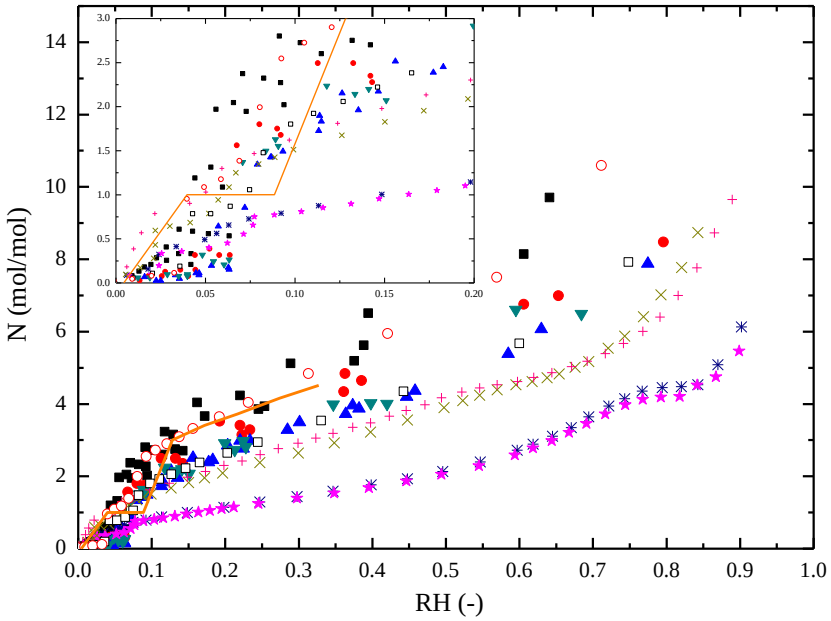


■ SG, $x_{sal}$ = 11.4% [128]; ● SG, $x_{sal}$ = 24% [128]; ▲ SG, $x_{sal}$ = 35.1% [128]; ▼ SG, $x_{sal}$ = 43.6% [128]; ✳ SG (type B), $x_{sal}$ = 36% [129]; ★ SG (type C), $x_{sal}$ = 39% [129]; × SBA-15, $x_{sal}$ = 32% [130]; + MCM-41, $x_{sal}$ = 24% [130]; □ SG 636, $x_{sal}$ = 21% [131]; ○ SG 646, $x_{sal}$ = 25.7% [131].

Fig. 2.12 *N vs RH* of LiCl composite materials, orange curve is of pure LiCl reported by [132].

Because of the easy deliquescence, the water uptake of LiCl-host matrix composites can be much higher than the pure hydration process of LiCl. The reported maximum water uptake ranges from 0.2 g/g to 2.2 g/g and generally increases with salt content and relative humidity. Around half of the study cases have the water uptake higher than 1.0 g/g. While the use of conventional host matrix materials, such as SG, EV, AA and AC can lead to water uptake up to 1.0 g/g, some newly reported novel porous materials resulted in extraordinary high water uptakes. Using hollow carbon sphere (carbon

encapsulation) [133] as host matrix led to high water uptake around 2.2 g/g. The use of MOFs as host matrix, including MIL-101(Cr) [132] and MIL-101(Fe) [134] also led to high water uptake of 1.03-1.88 g/g and 0.75-2.03 g/g respectively. Moreover, it seems relative humidity has less impact on water uptake of LiCl composite materials comparing to those of $CaCl_2$ composite materials, the water uptakes can reach high value even at low and medium relative humidity.

The sorption heat of LiCl-SG composite decreases as increasing water content [131], which was around 64 kJ/mol water when $N$ = 0.1 mol/mol attributed to the water adsorption by silica gel and decreased exponentially from 50 to 44 kJ/mol at $N$ = 3-7 mol/mol indicating the formation of LiCl aqueous solution [131]. Similar conclusion was achieved by Grekova et al. for LiCl-EV composite [135] and LiCl-MWCNT composite [125], the hydration heat was 61 kJ/mol water and 64 kJ/mol water respectively when $N$ = 0-1 mol/mol, then decreased gradually to around 56 kJ/mol water and 54 kJ/mol water as the increase of $N$. Nevertheless, the hydration heat in LiCl-At composite was found increasing with increasing water uptake from 42 to 50 kJ/mol water [136], the sorption behaviour was believed to be different from that of zeolite and silica gel.

Some studies evaluated the energy storage densities of LiCl composite materials based on two different operational scenarios, daily storage (DS) and seasonal storage (SS) [125, 135, 137-139]. The two scenarios had the same sorption temperature at 35 °C but different water vapor pressure (or relative humidity) at 873 Pa (corresponding to 5 °C water evaporation and 0.155 RH at 35 °C of air) for DS and 1228 Pa (corresponding to 10 °C water evaporation and 0.218 RH at 35 °C of air) for SS. In these studies, the largest specific energy density is 2600 kJ/kg (corresponding to 253 kWh/$m^3$ considering 350 kg/$m^3$ packing density) achieved by LiCl-EV composite with 59% salt content for SS using 85 °C desorption temperature [135].

### 2.3.5 $MgSO_4$ Composite

Magnesium sulphate ($MgSO_4$) does not occur in the nature in anhydrous form, only as hydrates. The dominant natural occurring magnesium sulfates on earth are epsomite ($MgSO_4 \cdot 7H_2O$), hexahydrate ($MgSO_4 \cdot 6H_2O$) and kieserite ($MgSO_4 \cdot H_2O$), are contained in the form of stable solid phases or in aqueous solution. The magnesium sulfates with 2, 3, 4, and 5 mol $H_2O$, and other non-stoichiometric hydrates are

considered to be metastable [140].

The hydration / dehydration processes of $MgSO_4$ hydrates are complicated [53, 141]. Though the deliquescence only appears in high relative humidity, evidence showed that liquid appeared during the hydration process at lower relative humidity (or water vapour pressure) [142]. On the other side, the kinetic of the hydration is hindered as the formed hydrates block the water vapour diffusion channel in the salt crystals [53]. In addition, the considerable volume expansion further reduces the accessibility of the anhydrous phase to the water vapour. Hence the using host matrix composite was believed to be necessary for a reliable thermal energy storage system. Besides the conventional used host matrix like zeolite [143-148] and silica gel [99], other matrix including porous glass material [142, 149], polymer [150, 151] and cellular foam [152, 153] etc. have been tried.

Many researches have been published about using zeolite as host matrix for $MgSO_4$, however, the conclusions are not consistent on whether more water would be adsorbed by composite material comparing to that by zeolite only. Whiting et al. [146] tested $MgSO_4$-Ze composite as potential thermal energy storage material using different types of zeolites, including Na-13X, Mordenite, Na-Y and H-Y (details please refer to the original paper). The majority of the studied composites with different salt contents had lower water uptake than that of zeolite only. $MgSO_4$-Ze composites have also been characterized by Mahon et al. [147]. $MgSO_4$-13X composite was found having lower water uptake and sorption heat as increasing salt content, and the authors believed that there was no hydration of the salt in the composite. However, the measured sorption heat of $MgSO_4$-Ze Y composite clearly showed the hydration / dehydration of salt and the sorption heat was enlarged by 129% and 56% comparing to that of pure zeolite Y according to the measurements by DSC and 200 g sample cyclical test respectively. Nevertheless, the hydration / dehydration of $MgSO_4$ impregnated in zeolite 13X was evidenced by TG-DSC tests by Xu et al. [144], the water uptake was slighter higher than that of pure zeolite 13X and the sorption heat was nearly the sum of adsorption heat of pure zeolite 13X and hydration heat of $MgSO_4$. Another research [148] obtained 4.8-52.4% water uptake increase of $MgSO_4$-13X composite with 3.22-10.48% salt content comparing to that using pure zeolite 13X.

The dehydration and hydration heats of the transformation between $MgSO_4.6H_2O$ and

$MgSO_4$ have been determined by TG-DSC measurement [154], the dehydration heat was about 2.1 ± 0.1 GJ/m$^3$ while the hydration can deliver about 1.8 ± 0.1 GJ/m$^3$ at the condition of 25 °C and 2.3 kPa water vapour pressure. However, at 50 °C and 2.1 kPa water pressure, the salt can hardly hydrate which could be a big problem for the usage of $MgSO_4$ for seasonal heat storage. Lower hydration heat of 0.76 GJ/m$^3$ ($MgSO_4.H_2O$ to $MgSO_4.6H_2O$) was reported in [94] by using TG-DSC measurement at 1.3 kPa water vapour pressure, which was only 45% of the energy stored from the dehydration reaction ($MgSO_4.6H_2O$ to $MgSO_4.H_2O$). It was surmised due to the amorphization of the material during the hydration reaction as part of the stored heat may be converted in energy to modify the material structure when the water molecules were introduced again in the molecular structure. The low heat release may also be assigned to textural changes which influences the measurement conditions, or caused by experimental artefacts of the DSC measurement.

The specific energy density of $MgSO_4$-Ze composite was measured based on both micro- and macro- calorimetry experiments in [143], both experiments gave about 648 kJ/kg specific energy density with the salt content of 15%; the volumetric density was 0.5976 GJ/m$^3$ (166 kWh/m$^3$) determined by the mirco-calorimetry test, which was 27% higher than the theoretical density of pure zeolite 13X (131 kWh/m$^3$). The study also confirmed that the composite material can keep the high energy density at least within three cycles. However, the study [146] showed the non-positive effect of using $MgSO_4$-Ze composite than using zeolite only on both sides of water uptake and energy density. For example, the specific energy density reduced from about 920 kJ/kg of Zeolite 13X only to 731 kJ/kg of $MgSO_4$-13X composite with 15% salt content. The composites with other three zeolites and 15% salt contents had the energy densities of 1090 kJ/kg (Na-Y), 867 kJ/kg (H-Y) and 507 kJ/kg (MOR), while the pure host matrix had energy densities of 978 kJ/kg, 822 kJ/kg and 522 kJ/kg respectively. It was revealed that large pore volume of the host zeolite must be maintained to get high sorption heat. The authors attributed this performance reduction to the formation of partially hydrated $MgSO_4 \cdot xH_2O$ in amorphous form which had much lower heat in hydration / dehydration.

Larger volumetric energy density was also found when using $MgSO_4$-glass composite than that of the host matrix material [149], and the volumetric energy density increased with reducing glass pore size due to the larger surface area to volume ratio which helped

the overcome of the kinetic hindrance of the hydration reaction occurred in bulk salt and in the host matrix with large pore size. The largest specific and volumetric energy densities among the tested composite materials were 620.8 kJ/kg and 0.556 GJ/$m^3$ respectively when using the lower pore size glass, Vycor 7930 (pore size 7 nm), with 0.15 g/g salt content.

Kallenberger et al. [150, 151] reported the highest salt content in composite material up to 80-90% (of $MgSO_4.1.25H_2O$) by using a special polymerization process. The developed $MgSO_4$-polymer composite had a specific energy density of 1080 kJ/kg at the condition of 30 °C and 81% RH at the first hydration cycle, and the energy density increased to about 1228 kJ/kg after 5 cycles, which was attributed to the reorganization of the hydrate crystals. Within 40 sorption cycles in a climatic chamber, the water uptake of the developed composite material stayed almost constant; while the water uptake and energy density of the hydration measured in the calorimeter increased after 40 hydration / dehydration cycles, this was explained by the higher accessibility of the salt within the composite after some cycles.

The specific energy densities of different $MgSO_4$-host matrix composites are summarized in Fig. 2.13. As seen in the figure, all the studies used composite materials with less than 40% salt content, with only one exception of 67.4% (80% $MgSO_4.1.25H_2O$). The specific energy densities are scattered between 210 kJ/kg and 1395.0 kJ/kg without apparent trend. The highest value was obtained by using $MgSO_4$-EG-AC composite with 1:1 ratio of EG:AC and 36.6% salt content, the desorption heat of which was 1395 kJ/kg for fresh material but reduced to 1320.0 kJ/kg after 10 cycles.

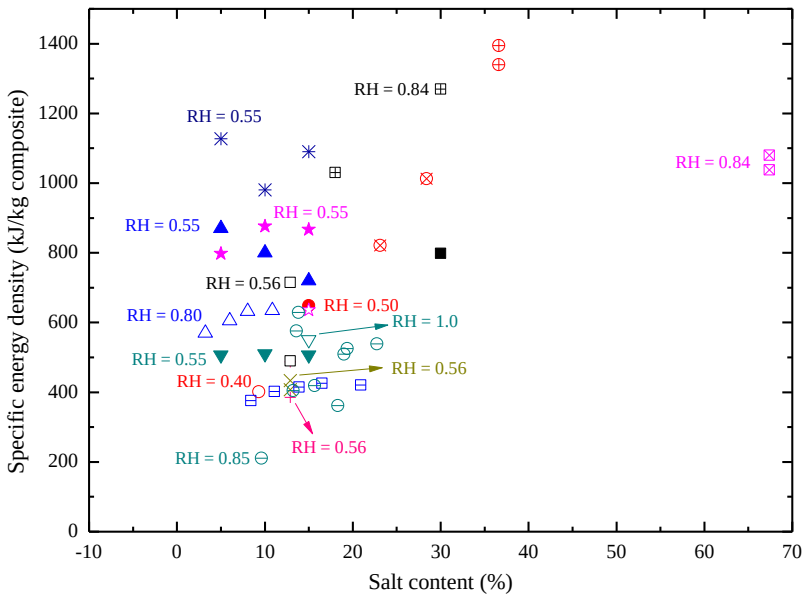


■ SG [155]; ● Ze [143]; ▲ Ze Na–X [146]; ▼Mordenite [146]; ✳ Ze Na–Y [146]; ★ Ze H–Y [146]; × Ze 13X [147]; ＋ Ze 13X + Binder [147]; □ Ze Y + Binder [147]; ○ Ze 13X [145]; △ Ze 13X [148]; ▽Ze 13X [144]; ☆ Ze 13X [156]; ⊞ AC [157]; ⊕ EG-AC [158]; ⊟ AA [156]; ⊖ Glass [149]; ⊠ Polymer [150, 151]; ⊗ Cellulose foam [153].

Fig. 2.13Specific energy densities of $MgSO_4$ composites.

### 2.3.6 $MgCl_2$ Composite

Magnesium chloride hexahydrate ($MgCl_2 \cdot 6H_2O$, also known as the mineral bischofite) shows promising characteristics for domestic application of heat storage, either through phase change [159, 160] or thermochemical sorption, regarding low cost, easy availability, high energy density, higher temperature lift and faster reaction rate compared to that of magnesium sulphate hydrates, probably owe to the less complex structure of $MgCl_2$ hydrates with almost no meta-stable isomers [161]. Its main disadvantage is thermal decomposition and instability.

Similar to $CaCl_2$ and LiCl, the $MgCl_2$ salt and hydrates are hydroscopic and may turn into a solution at ambient condition, which induces structure changes like grain agglomeration and clogging in the packed bed, leading to the reduction in thermal performance over cycles. Moreover, over-hydration were noticed by Zondag et al. [162] when using $MgCl_2$ in both closed and open water sorption reactors, a solid layer was formed and the pressure drop of the air flow increased. Therefore using porous host matrix is necessary for $MgCl_2$ to be used as thermal energy storage material.

The hydration and dehydration heats of $MgCl_2 \cdot 2/4H_2O$ and $MgCl_2 \cdot 4/6H_2O$ were

measured by TG-DSC by Ferchaud et al. [94]. It was found that the hydration heats were 13% and 21% lower than the dehydrations heats. The authors recommended a minimum temperature of 40 °C during hydration reaction to avoid over-hydration of $MgCl_2 \cdot 6H_2O$ under a water vapour pressure of 1.3 kPa, and obtained a total energy density of 1.41 GJ/m$^3$ (903.8 kJ/kg), which was 84% of the measured dehydration heat. This deduction was attributed to the textural changes in the materials and the heat losses to the gas.

The specific energy densities of different $MgCl_2$-host matrix composites are summarized in Fig. 2.14. As seen in the figure, the specific energy densities are scattered between 310 kJ/kg and 1370 kJ/kg without apparent trend. All the studies used composite materials with less than 32% salt content, with only one exception of 80-90% salt content achieved by using polymerization method [151], this high salt content led to specific energy densities of 1295 kJ/kg and 844 kJ/kg at relative humidity at 0.30 and 0.20 respectively, corresponding to 1.27 GJ/m$^3$ and 0.59 GJ/m$^3$.

Similar to studies of $MgSO_4$-Ze composites in [146], Whiting et al. [163] measured the sorption heat of $MgCl_2$-Ze composites using four different zeolites, Na-X, MOR, Na-Y and H-Y. In overall, $MgCl_2$-Ze composite offered superior hydration heat comparing to $MgSO_4$-Ze composite due to the lower *DRH* and the unblocked zeolite pores during hydration of $MgCl_2$. It was believed that there was a balance on the salt content in zeolite Na-X and the accessibility of the salt, this led to the highest sorption heat of $MgCl_2$-Ze Na-X composite occurred at the salt content of 5%. Further increase of salt content led to the reduction of sorption heat, even lower than the sorption heat of Na-X. Among the four zeolites, $MgCl_2$-Ze MOR composite offered the largest improvement on hydration heat in comparison to host matrix only (916 kJ/kg of composite (15% salt content) comparing to 506 kJ/kg of Ze MOR), which was due to the increasing water uptake. Taking the advantage of large pore volume of Na-Y, $MgCl_2$-Ze Na-Y composite with 15% salt content had the highest sorption heat in all study cases in [163], 1173 kJ/kg composite. Nevertheless, in another study [164], the specific energy density of $MgCl_2$-Ze 13X composite with 22% salt content was 1386 kJ/kg composite which was 2.26 times as large as that of zeolite 13X (604 kJ/kg).

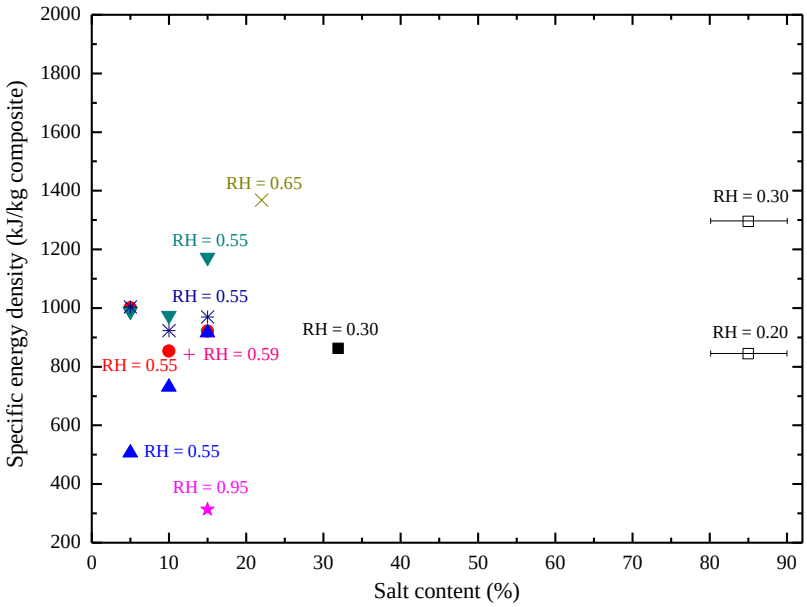


■ SG [120]; ● Ze Na-X [163]; ▲ Ze MOR [163]; ▼ Ze Na-Y [163]; ✳ Ze H-Y [163]; ★ Ze 13X [165]; × Ze 13X [164]; ＋ Ze Na-X [166]; □ Polymer [151].

Fig. 2.14 Specific energy densities of $MgCl_2$ composites

### 2.4 Thermal energy storage applications

Many studies related to reactor design and operation conditions to improve the adsorption and desorption performance of salt hydrate heat storage have been reported. The salt hydrate sorption reactor design was generally suitable for a lot of applications from the space heating to energy storage in respect to its high energy density. Hawwash et al. [167] examined both cylindrical and conical reactors. They numerically investigated on different sizes of the reactors by altering the inlet-to-outlet area ratio (AR) during the $MgCl_2 \cdot 6H_2O$ desorption. Kant et al. [168] developed a three-dimensional numerical model (Fig. 2.15) for the $K_2CO_3$ adsorption and desorption. It was demonstrated that the reactor geometry can significantly affected the sorption reaction and heat transfer in the bed. By shrink the heat exchanger size up could improve the heat transport as well as the reaction rate. A mesoporous honeycomb was manufactured by filling $CaCl_2$/LiCl into the siliceous shale to experimentally investigate on an open system, as shown in Fig. 2. 16 [169]. The result demonstrated that the storage composite exhibited a high energy density. It was also observed that the adsorption rate has significantly affect the outlet temperature of air medium. The composite with LiCl showed an energy density of 180 $MJ/m^3$. Moreover, it kept stable

when regenerated at 80 °C or a high adsorption.

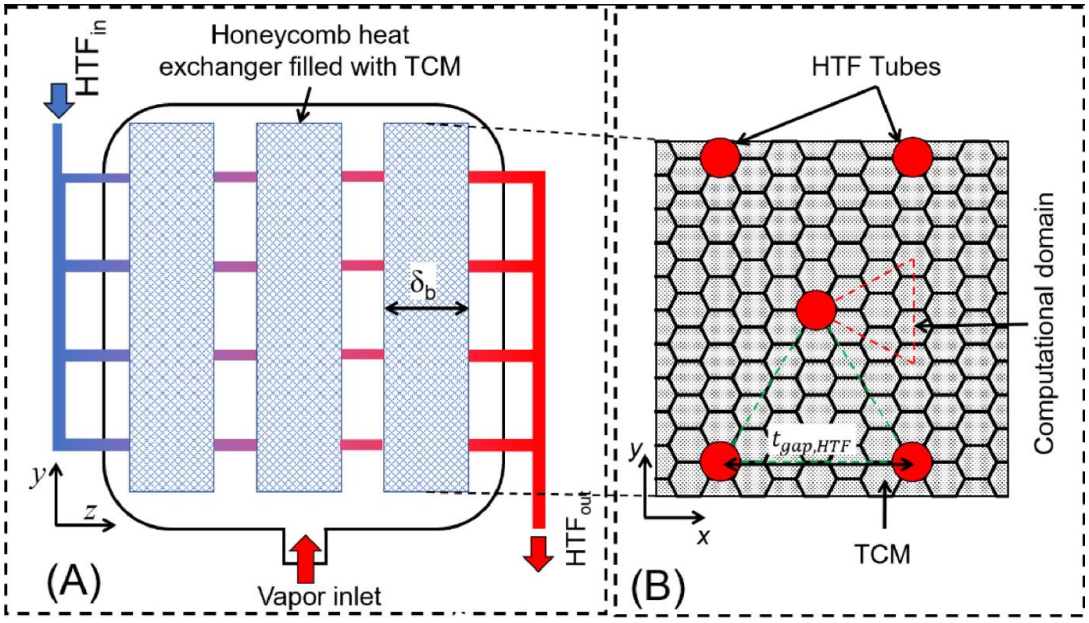


Fig. 2.15 Geometric diagram of the bed and computational domain in respect of (a) the whole thermal energy storage system, (b) side view of heat exchanger [168]

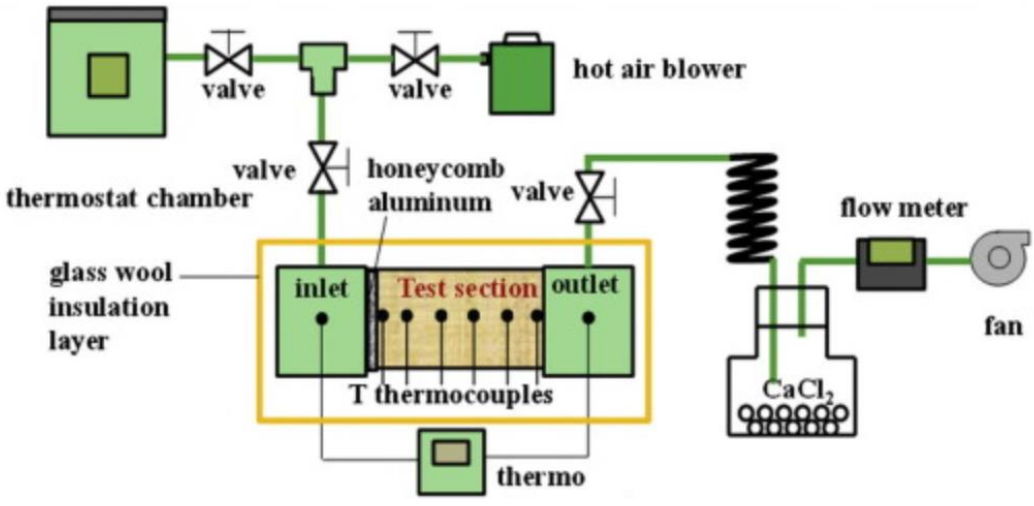


Fig. 2.16 Illustration of the thermal energy storage system [169].

## 2.5 Conclusion

Hygroscopic salt composite is regarded as one of the most promising solutions for the application which could store the solar thermal energy in the radiation-abundant days and provide heating effect in the space heating season. This review summarises the thermodynamic fundamentals and material developments of inorganic salts as water sorption material for thermal energy storage. The literature review mainly consists of two parts. The first part introduces the mechanism of water sorption with salts for thermal energy storage, illustrates the phase equilibrium diagram and deliquescence relative humidity of different salts, then the reaction enthalpy and entropy changes are calculated based on pressure-temperature diagram and standard formation enthalpies and standard entropies, respectively. The second part summarises research and developments of each salt or salt hydrate used for water sorption thermal energy storage. The material issues and salt screening method are discussed first, then the usage of composite material to improve the material performance is introduced, finally the sorption performance of some composite materials is summarised, as well as some of the thermal energy storage applications using the composite materials. It is worth noting that, when zeolite is impregnated with salt, it can block pores and reduce the specific surface area of the zeolite. As a result, the heat storage density of the zeolite may be relatively reduced after impregnation with salt. However, the heat storage density of zeolite is lower than that of salt initially. Considering salt and zeolite's different characteristics and behaviours, the overall heat storage density can be increased when combined. This non-linear relationship arises due to the combined effects of reduced zeolite heat storage density and salt's inherently higher heat storage density.

# Chapter 3. $MgSO_4$-zeolite composites

## 3.1 Introduction

According to the literature review, space heating using seasonal stored solar energy could potentially use the water-salt sorption technology, which could be safe (no poison), cheap (water is widely accessed), and stable (thermochemical adsorbed sorbent could be stored in long time scale). However, pure salt-water adsorption suffers from the low thermal conductivity and reduced mass transport during adsorption (swallow and expansion could happen in the adsorption process and thus block the water vapour transfer). In this chapter, $MgSO_4$ is selected as the water adsorption salt, while the matrix is the zeolite. Using the mixture of the $MgSO_4$-zeolite is expected to resolve the problems found when using pure salt as the adsorbent. Moreover, their thermal-physical characteristics should be specified as they could determine the water adsorption heating performance.

## 3.2 Methodology

### 3.2.1 Manufacturing $MgSO_4$-zeolite

Zeolites 3A, 4A, 5A, 10X and 13X, five representatives among normally used zeolite in industry were selected as porous host matrixes, provided by Henan Qingquan Environmental Protection Technology Co., LTD. The salt, $MgSO_4$, has the purity of 99.9%, was provided by Sinopharm Chemical Reagent Co. LTD. It was selected for its high energy density, stability, easy-access, and no poison.

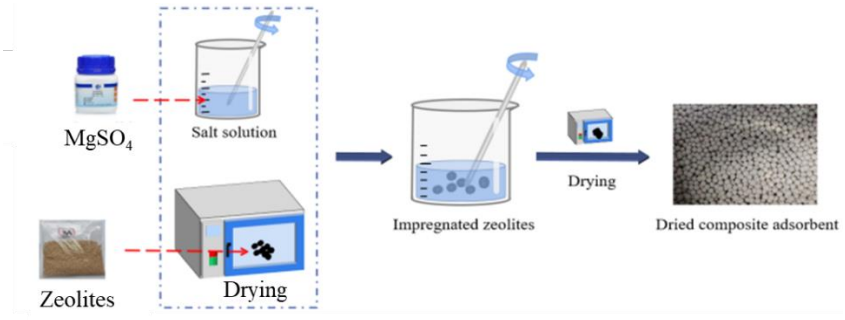


Fig. 3.1 The manufacturing process of $MgSO_4$-zeolite composites.

The composite materials were manufactured by infiltrating method as presented in Fig.

3.1. The porous host matrix was firstly dried then was immersed into the salt solution with a certain concentration, and the wet matrix was dried after its pores were filled with the solution. The salt percentage is low due to the crystallization issue happened during using high concentration solution. One approach to improve the impregnation process is by increasing the immersion temperature. This technique effectively enhances the dissolution rate of salt, allowing for better penetration and impregnation of zeolite. By raising the temperature, the overall impregnation process can be accelerated and made more efficient. In addition, vacuum impregnation can be employed to enhance the adsorption of zeolite to salt. Creating a vacuum environment facilitates the penetration of salt into the pores of zeolite, resulting in improved adsorption and a stronger bond between the two materials. Furthermore, surface treatment of zeolite offers another avenue for enhancing the adsorption process. By modifying the pore size distribution and porosity of zeolite through surface treatments, the interaction between zeolite and salt can be optimized. This leads to an improved adsorption capacity and a more effective impregnation process.

Tab. 3.1 The specification of the prepared heat storage composite.

| No. | $C_{solution}$ | Type of zeolite | $R_{salt}$ |
|---|---|---|---|
| 1 | - | 3A | 0% |
| 2 | - | 4A | 0% |
| 3 | - | 5A | 0% |
| 4 | - | 10X | 0% |
| 5 | - | 13X | 0% |
| 6 | 10% | 3A | 3.01% ± 0.05% |
| 7 | 10% | 4A | 2.94% ± 0.05% |
| 8 | 10% | 5A | 2.79% ± 0.05% |
| 9 | 10% | 10X | 2.76% ± 0.05% |
| 10 | 10% | 13X | 2.66% ± 0.05% |
| 11 | 20% | 3A | 3.91% ± 0.05% |
| 12 | 20% | 4A | 5.03% ± 0.05% |
| 13 | 20% | 5A | 5.06% ± 0.05% |
| 14 | 20% | 10X | 5.81% ± 0.05% |
| 15 | 20% | 13X | 3.63% ± 0.05% |

The detailed process is as follows:

**Pre-treatment:** Soak the 3A, 4A, 5A, 10X, and 13X zeolites in deionized water for 12 hours to remove impurities in the pore of the zeolite.

**Drying:** Heat the 3A, 4A, 5A, 10X, and 13X zeolite in an oven at 300 °C for 12 hours.

**Infiltration:** Immerse 3A, 4A, 5A, 10X, and 13X zeolite in the $MgSO_4$ solution with the mass concentration, $C_{solution}$, of 10% and 20%, for 24 hours. Mechanical stirring was used to guarantee the sufficient mixing until no bubbles appeared on the zeolite surfaces.

**Drying:** After 24 h immersion, the composite spheres were filtered out and then moved into a nylon mesh bag for draining off. Allow them to stand for 4 h. Dehydrate the salt-zeolite composite at 300 ℃ for 12 hours.

Finally, the composite sorption material was obtained and stored in the sealed container. The mass ratio of the salt in the composite, $R_{salt}$, is expressed in Eq. 3.1,

$$R_{salt}=\frac{m_g - m_d}{m_g} \quad 3.1$$

where $m_g$ is the gross mass of the dried composite material, and $m_d$ is the dry mass of the host matrix. The information of the prepared composite material is listed in Tab. 3.1, including the measurement error.

### 3.2.2. $N_2$ isothermal adsorption（BET）

The pore volume and pore size distributions of the samples were examined by the nitrogen adsorption/desorption method, utilizing an automatic surface and pore size analyser (BET, Micromeritics APSP2460). Before sending into the analyser, the samples were degassed at 250 °C for 2 h. The $N_2$ isotherm adsorption was performed at 77 K. Pore size distribution and SSA (specific surface area) were calculated using the BJH (Barrett-Joyner-Halenda) theory and the BET (Brunauer-Emmet-Teller) equation. The pore volume and pore size distributions can be determined according to the adsorption isotherm curves.

### 3.2.3. Scanning Electron Microscope – Energy Dispersive Spectrometer (SEM-EDS)

Scanning electron microscopy (SEM, ZEISS, Sigma300) was used to observe the surface morphology of the manufactured salt-zeolite composite, as the salt can either fill in the zeolite pores or adhere on the surface. Electron dispersive spectroscopy (EDS) was used to obtain the elemental distribution (salt distribution) conditions of the manufactured composite materials.

### 3.2.4. X-Ray Diffractometer (XRD)

The phase composition analysis of the composite adsorbents after water adsorption were carried out by employing X-ray diffractometer (XRD, Rigaku,SmartLab SE). The scanning speed was set to 0.01°/s, and the scanning angle is 3-80° (2θ). The radiation source utilized in the test was the Cu target Ka1 ray with the wavelength of 0.15406

nm.

### 3.2.5. Thermogravimetric Analyzer – Differential Scanning Calorimetry (TGA-DSC)

The TGA-DSC (TGA5500 – TAQ2000) was used to measure the water adsorption capacity as well as the heat storage density of the salt-zeolite composites. The composite after adsorption (25 ℃ and 60% RH) was heated at a rate of 5 °C/min from 25 ℃ to 300 ℃.

### 3.2.6 Adsorption performance at constant temperature and humidity

The adsorption experiment was conducted to get the water adsorption capacity of the composite materials, in which a small amount of composite adsorbent was placed inside a constant temperature and relative humidity environment provided by a climatic chamber. The climatic chamber (Tianjin Hongnuo Instrument Co., Ltd.) can adjust and maintain the temperature and relative humidity of its enclosed environment for the adsorbents. It has a forced air circulation mechanism by a ventilation fan to provide a uniform temperature and relative humidity condition. Due to the continuous long adsorption time for the adsorbent to achieve the equilibrium, an electrical scale was used inside the climatic chamber to retrieve the mass data versus the uninterrupted reaction time, which was recorded by the data logger. Besides, to alleviate the vibration that may influence the accuracy, the scale was located at the bottom of the chamber with the shockproof foam. The air flow direction was also directed to avoid disturbing the scale. Due to the humidity controlling in the chamber, condensed water can be formed in the container which could lead to the wrong reading of the adsorbent mass. To solve this problem, the mass of an empty container was monitored inside the climatic chamber as a reference to obtain a condensed water mass data and therefore a relatively precise mass reading of the adsorbent. Additionally, water adsorbing sponges were adhered in the inner walls of the chamber in case of the condensed water dropping.

$MgSO_4$ composites with different mass ratios were place into the climatic chamber and tested under various temperatures (25 ℃, 35 ℃, 45 ℃, 55 ℃) and relative humidity (60%, 70%, 80%, 90%) conditions. The water adsorption capacity of the adsorbent, $R_w$, is calculated based on the retrieved mass at the beginning-dry mass of the adsorbent,

$m_0$, and at the end-adsorbed mass of the adsorbent, $m_1$.

$$R_w = \frac{m_1 - m_0}{m_0} \quad 3.2$$

The theoretical adsorption heat released by the adsorbent, $Q$, can be calculated by the heat storage density, $h_{ad}$, and the dry mass of the composite sorbent, $m_0$. The practical heat storage density can be obtained through the TGA-DSC tests mentioned above.

$$Q = m_0 \cdot h_{ad} \quad 3.3$$

Each experiment was repeated for three times to eliminate the random error. The results in Section 3.3 took only the average results of the tree-time tests. Some obviously abnormal data is removed before averaging.

## 3.3 Results and discussion

### 3.3.1 SEM-EDS

The $MgSO_4$-zeolite composites were prepared by the impregnation methodology stated above, and the surface morphology was observed by SEM with the magnification ratios of 2000 and 20000. Fig. 3.2 exhibited the SEM photos of the composites: $MgSO_4$-3A/4A/5A/10X/13X with solution concentrations of 10% and 20% (during composite making process) at the magnification of 2000 times. As shown in the figure, with using higher concentration $MgSO_4$ solution, the composite surface presented severer crystallization phenomenon. For example, the net shape with fibres in Fig. 3.2.b, the cracked rock like shape in Fig. 3.2.d and Fig. 3.2.h, or the thin needles figure in Fig. 3.2.f. It should be noted that even though higher solution concentration impregnation may stand for higher adsorption capacity as the loaded $MgSO_4$ theoretically increases, the mass transfer may be constrained due to the crystallization issue on the surface of composite adsorbent.

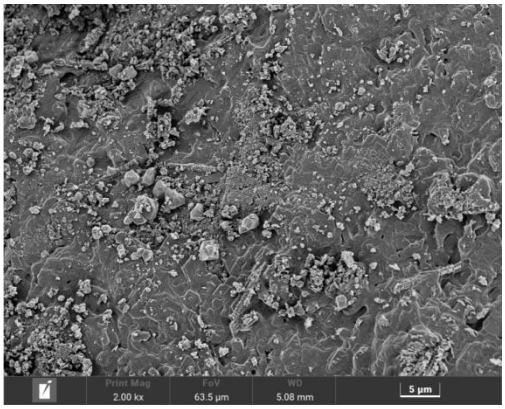


a. $MgSO_4$(10%)-3A

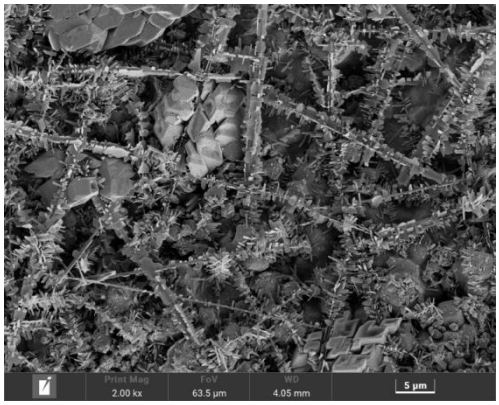


b. $MgSO_4$(20%)-3A

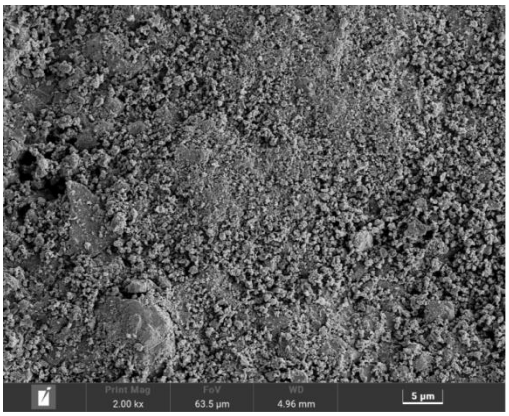


c. $MgSO_4$(10%)-4A

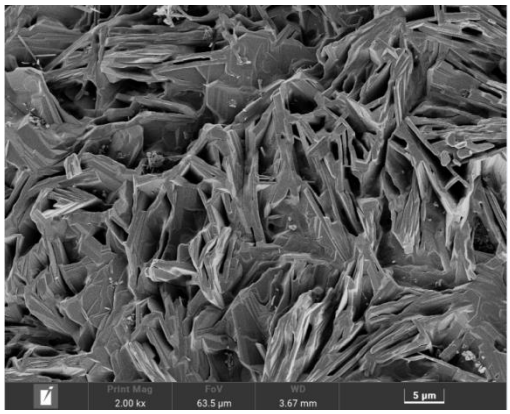


d. $MgSO_4$(20%)-4A

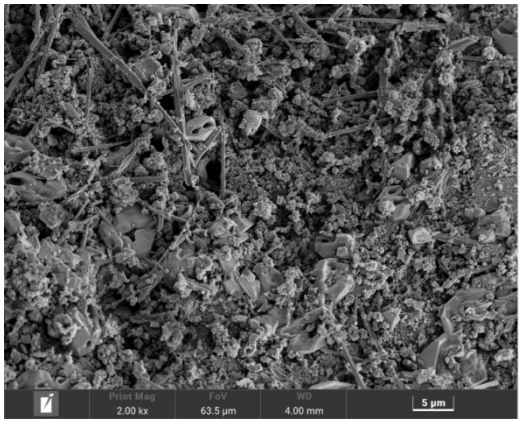


e. $MgSO_4$(10%)-5A

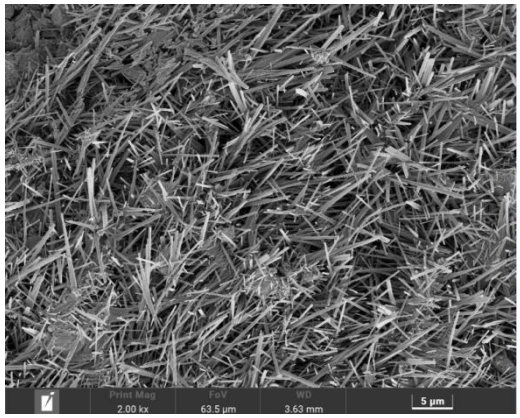


f. $MgSO_4$(20%)-5A

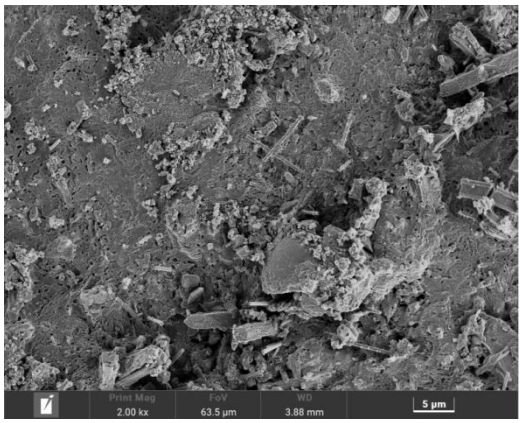


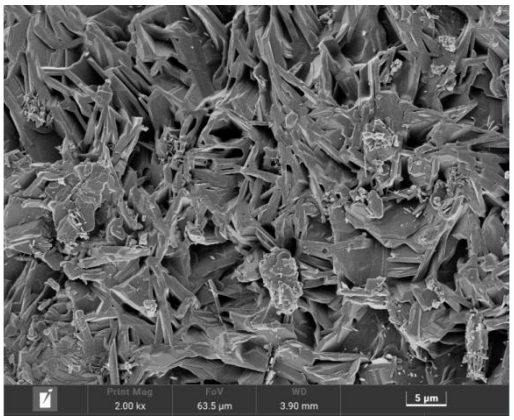

g. $MgSO_4$(10%)-10X

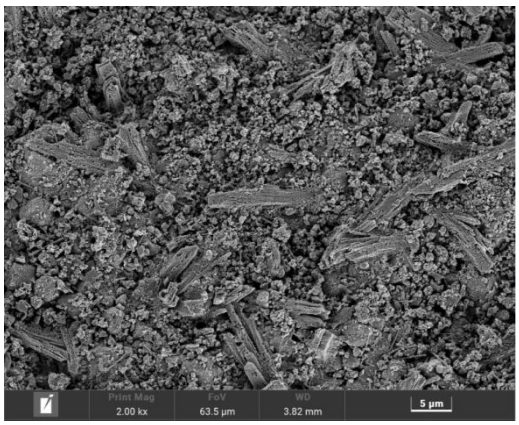


h. $MgSO_4$(20%)-10X

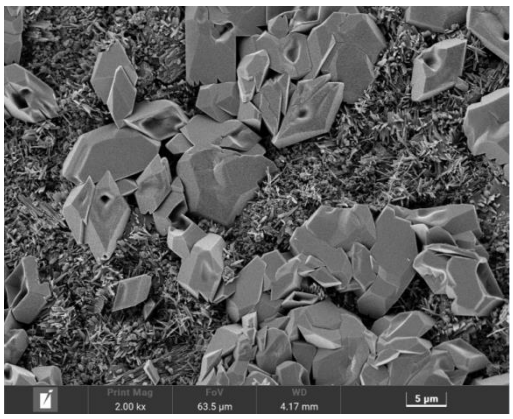


i. $MgSO_4$(10%)-13X

j. $MgSO_4$(20%)-13X

Fig. 3.2 SEM photos of the composites with different solution concentrations at the magnification of 2000 times

Higher magnification of 20000 times photos was taken for EDS analysis. Fig. 3.3 presented the Mg and S element mapping of the composite adsorbents, using $MgSO_4$(10%)-3A as the representative. These $MgSO_4$ distribution photos were further analysed for the salt covering percentage of the manufactured composites.

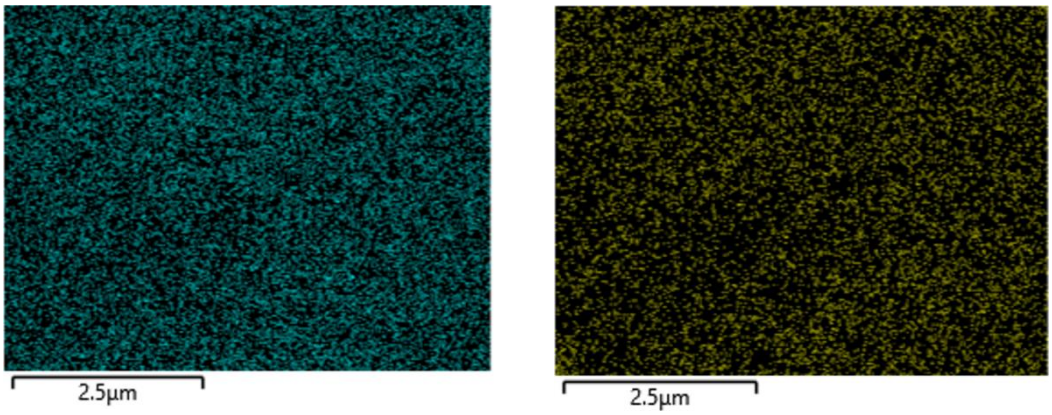


a. Mg

b. S

Fig. 3.3 Element mapping of $MgSO_4$(10%)-3A

Fig. 3.4 displayed the contents of $MgSO_4$ in the prepared composite sorbents, which demonstrated that higher impregnation concentration resulted in the higher content of $MgSO_4$ covering the surfaces of composite zeolite samples. The highest $MgSO_4$ content (74.75% over the whole detected sample surface) was observed to be with the

utilization of 3A type zeolite, infiltrated by 20% $MgSO_4$ solution. The smallest covered surface was found to be with $MgSO_4$(10%)-10X (45.66% sample surface covered by $MgSO_4$). Theoretically, $MgSO_4$(20%)-3A would be the optimal candidate in terms of highest water adsorption capacity with the most load of $MgSO_4$ per unit surface area. However, the crystallization issue found in SEM photos might constrain the actual adsorption capacity as the mass transfer might be constrained.

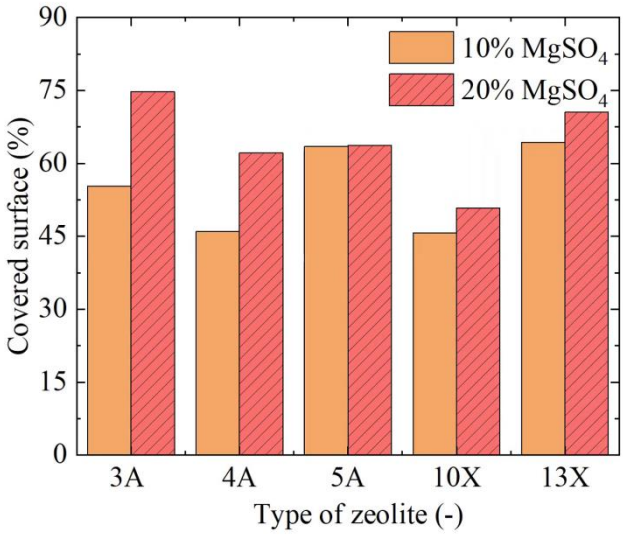


Fig. 3.4 Covered surface by $MgSO_4$ in the prepared composite sorbents.

### 3.3.2 BET

Fig. 3.5 illustrated the $N_2$ adsorption/desorption curve of the various prepared composite materials. The results showed high consistence with type I for $N_2$ sorption, which was based on the IUPAC definition. They were also in good accordance with the porous material, for instance, the activated carbon and the common zeolites [170]. According to the $N_2$ sorption curves, essential porous characteristics, for example, the pore volume, surface area, and average pore diameter, of the tested samples were determined.

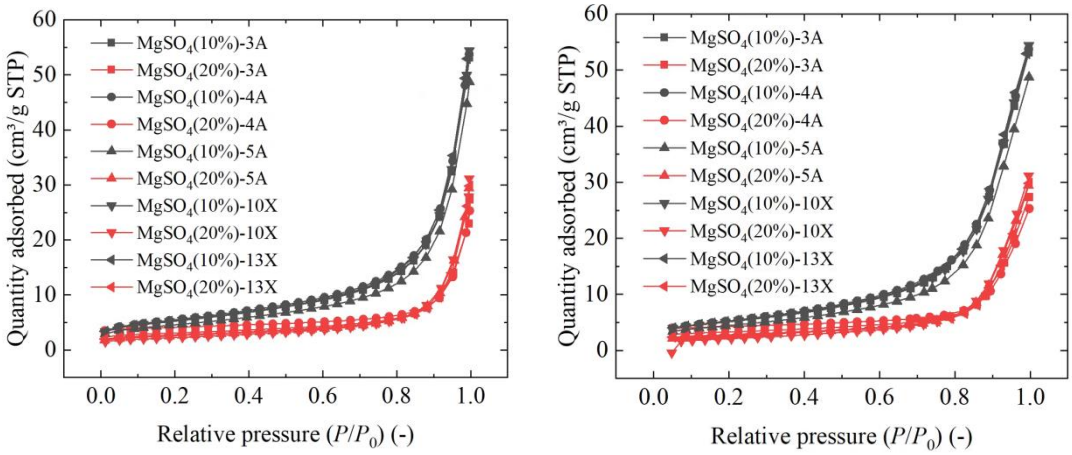


a. Adsorption b. Desorption

Fig. 3.5 Isothermal $N_2$ adsorption/desorption curves.

Fig. 3.6 presented the pore size distributions corresponding to $N_2$ adsorption/desorption. It was demonstrated that the impregnation concentration could affect the pore volume of the porous composite. When the used concentration of $MgSO_4$ solution was higher, the pore volume distributed on the same pore diameter was reduced, which can result into the smaller $H_2O$ vapor transport channel and thus negatively influence on the mass transfer and sorption performance. The adsorption average pore diameter of the measured samples ranged from approximately 13 nm ($MgSO_4$(20%)-4A) to 25 nm ($MgSO_4$(20%)-10X). The desorption average pore diameter varied from about 9 nm ($MgSO_4$(20%)-4A) to 17 nm ($MgSO_4$(20%)-10X). Even though a tail was found in $MgSO_4$(10%)-13X, the result might be susceptible as BET test was designed for pores ranging within a diameter less than 50 nm.

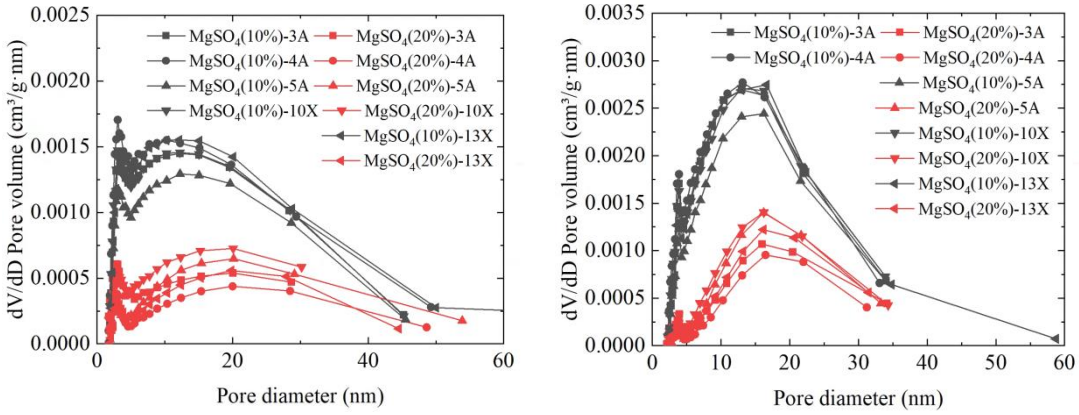


a. Adsorption b. Desorption

Fig. 3.6 Pore size distribution

Fig. 3.7 displayed the surface areas of the various sorbents versus the pore width. It was discovered that with the infiltration concentration increasing, the distributed surface area on a certain pore width was obviously decreased. A decreased SSA means less active area for adsorption and thus lower water adsorption capability. Moreover, the composite surface area was mainly contributed by the pores with width of around 10 nm.

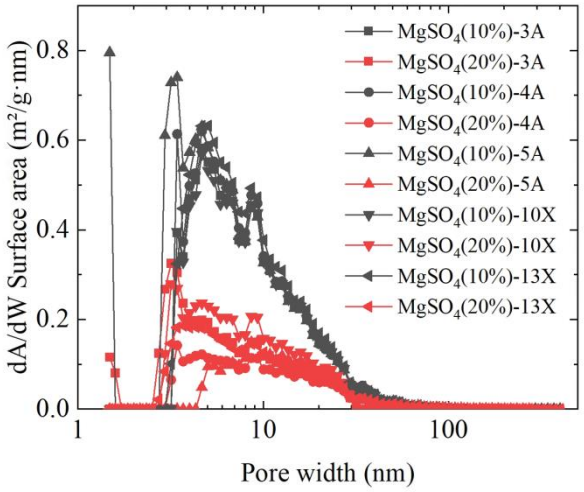


Fig. 3.7 The surface area versus the pore width.

Tab. 3.2 The essential porous characteristics of the composite $MgSO_4$(10%/20%)-zeolites(3A/4A/5A/10X/13X).

| Composite | Surface Area ($m^2/g$) | Pore volume ($cm^3/g$) | Adsorption/desorption average pore diameter (nm) |
|---|---|---|---|
| $MgSO_4$(10%)-3A | 18.28 | $8.22x10^{-2}$ | 17.68/13.87 |
| $MgSO_4$(20%)-3A | 11.10 | $4.23x10^{-2}$ | 15.19/10.30 |
| $MgSO_4$(10%)-4A | 19.17 | $8.32x10^{-2}$ | 17.02/13.49 |
| $MgSO_4$(20%)-4A | 13.41 | $3.92x10^{-2}$ | 13.20/9.02 |
| $MgSO_4$(10%)-5A | 15.99 | $7.54x10^{-2}$ | 18.55/14.37 |
| $MgSO_4$(20%)-5A | 9.08 | $4.55x10^{-2}$ | 19.49/13.82 |
| $MgSO_4$(10%)-10X | 18.48 | $8.42x10^{-2}$ | 17.87/13.86 |
| $MgSO_4$(20%)-10X | 7.84 | $4.82\ x10^{-2}$ | 24.35/16.72 |
| $MgSO_4$(10%)-13X | 18.49 | $8.19\ x10^{-2}$ | 17.49/14.33 |
| $MgSO_4$(20%)-13X | 9.66 | $4.61x10^{-2}$ | 18.95/12.42 |

Tab. 3.2 listed the essential porous properties. It was found that the surface area, pore volume, and the adsorption/desorption average pore diameter were all reduced with the solution concentration increasing, which indicated that the active adsorption area decreased, and the mass transfer would be therefore restrained. It was revealed that 10% increment of the $MgSO_4$ solution concentration resulted in a maximum decrease of surface area, 10.64 $m^2/g$, obtained from the 10X-based material, or a maximum decrease of the pore volume, 0.044017 $cm^3/g$, retrieved from the 4A-based composite.

### 3.3.3 XRD

After water adsorption, the formed $MgSO_4 \cdot xH2O$ was detected by XRD to estimate the hydration number. The adsorption condition is at the temperature of 25 °C, and the relative humidity of 60%. Fig. 3.8 displayed the XRD results of fully absorbed 3/4/5A and 10/13X composites with infiltrated $MgSO_4$.

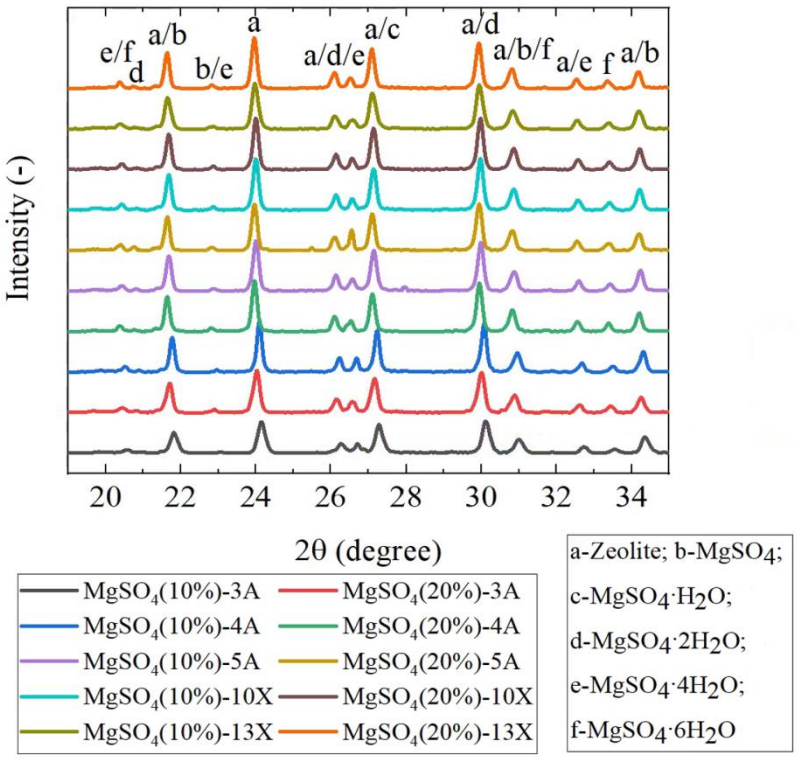


Fig. 3.8 XRD results of fully water-adsorbed $MgSO_4$-zeolite composites.

Except for the diffraction signals of zeolites, $MgSO_4$ hydrates, and anhydrous $MgSO_4$, no other peak signals were observed in the XRD patterns, which indicated an excellent chemical stability and compatibility between the water molecules, zeolites and

infiltrated $MgSO_4$. The diffraction peaks of hydrated $MgSO_4$ salt, for instance, $MgSO_4 \cdot H_2O$, $MgSO_4 \cdot 2H_2O$, $MgSO_4 \cdot 4H_2O$, and $MgSO_4 \cdot 6H_2O$ were evidently observed for almost all samples. It revealed that even though the adsorption process reached equilibrium, low-water-content hydrates still existed. This is due to that part of the pores in the sorbents were blocked as the SEM-EDS results showed, which constrained the water mass transfer for the high-water-content hydrates formation. Furthermore, no $MgSO_4 \cdot 7H_2O$ diffraction peaks were detected, potentially due to the instability and easy dehydration at the room temperature of this hydrates. The results were consistent with the reported literature [171].

### 3.3.4 TGA-DSC

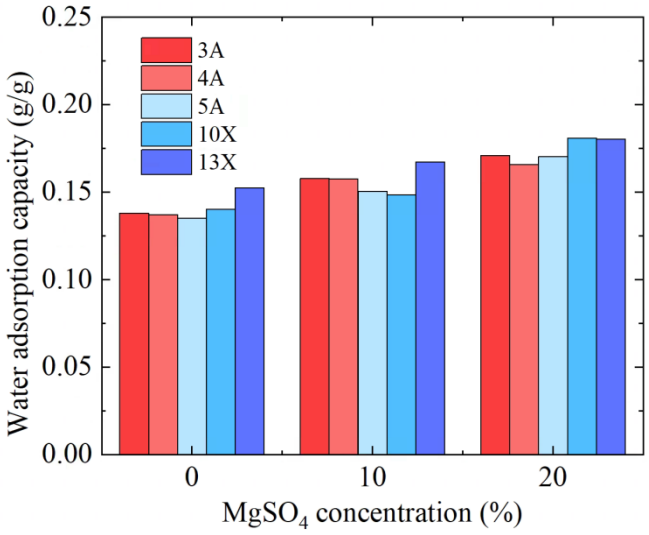


Fig. 3.9 Water adsorption capacity measured by TGA.

Fig. 3.9 showed the TGA test results of the $MgSO_4$-zeolites having adsorbed vapor at the temperature of 25 °C and the humidity of 60%. The water adsorption capacity of the composite adsorbents using 20% $MgSO_4$ concentration during impregnation is generally higher than that of using solution with 10% concentration during impregnation and pure zeolites. $MgSO_4$-13X composites presented higher water adsorption capacity than others. The maximum water adsorption capacity obtained from the tests was 0.1803 g/g by $MgSO_4$(20%)-13X.

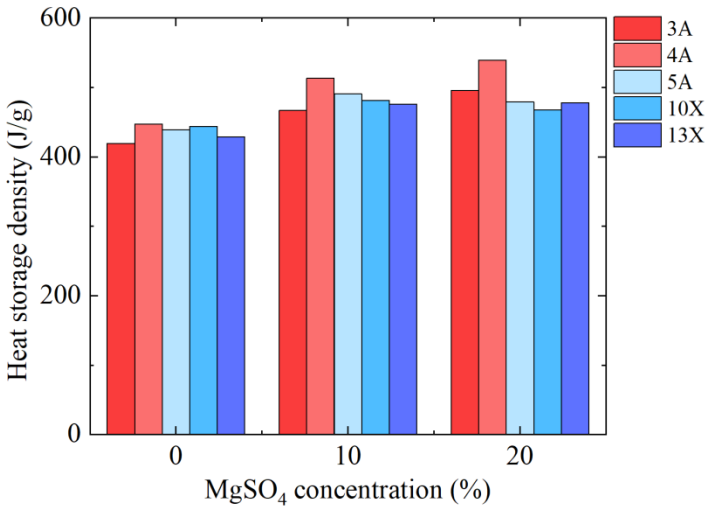


Fig. 3.10 The DSC result of manufactured adsorbent.

Fig. 3.10 showed the results of the DSC tests of the composite materials having adsorbed the vapor at the temperature of 25 °C and the relative humidity of 60%. Similarly, composites impregnated within higher concentration solution displayed with higher heat storage density, while the zeolite of 4A always presented the highest heat storage density among other candidates. The maximum heat storage density found in the test was 481.3 J/g by $MgSO_4$(20%)-4A.

### 3.3.5 Adsorption at constant temperature and relative humidity

At the temperature of 25 °C and the relative humidity of 60%, adsorption process of various adsorbents is illustrated in Fig. 3.11. As the nature of the sorption reaction, the adsorption rate is high at the beginning and reduced with time. Finally, the adsorption tends to be completed at the time of around 24 hours, with the mass change no larger than 0.1% in an hour. For the reference group, zeolite 3A and 4A have the highest sorption rate and water adsorption capacity. For composite materials made from 10% $MgSO_4$ solution, $MgSO_4$-3A and $MgSO_4$-13X have the highest reaction rate and water uptake capacity. Using 20% $MgSO_4$ solution, 3A-$MgSO_4$ presents both the highest adsorption rate and the largest water adsorption capacity. A maximum water adsorption capacity is found to be 0.179 g/g for the reference group, 0.207 g/g for the ones using 10% salt solution, and 0.197 g/g for those using 20% salt solution. The embedded salt improves the water adsorption capacity, but excess addition can reduce the mass transfer in the adsorption process thus confines the adsorption rate/capacity. Based on

these experimental tests, the optimum composite material is determined to be 3A or 13X zeolite with using 10% $MgSO_4$ solution in the manufacture process.

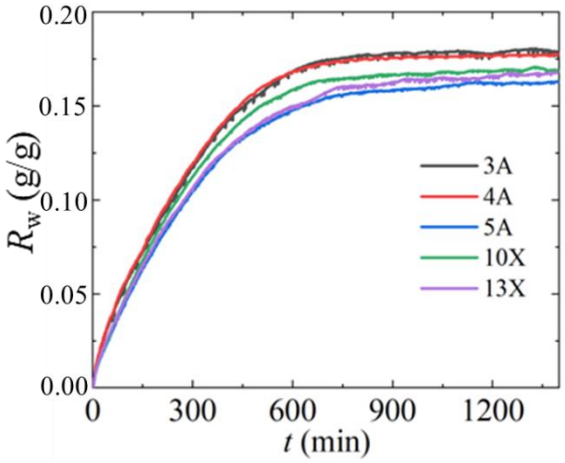


a. Water adsorption capacity of reference groups

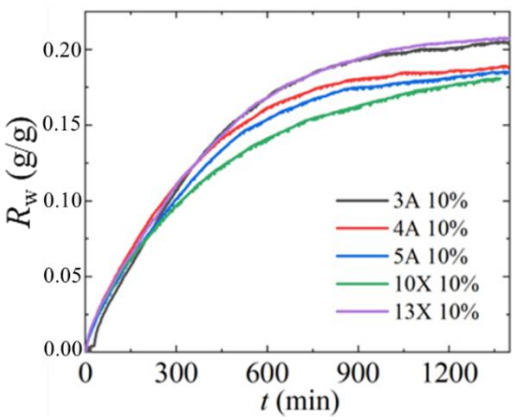


b. Water adsorption capacity of composite material using 10% solution

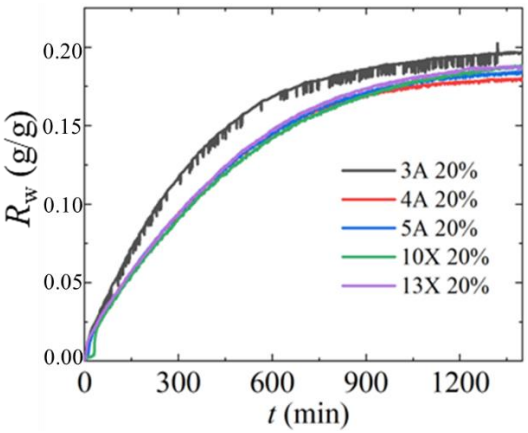


c. Water adsorption capacity of composite material using 20% solution

Fig. 3.11 Adsorption performance of various materials at 25 °C and 60% relative humidity.

The composite of 3A-$MgSO_4$ made by using 20% $MgSO_4$ solution is selected to do the adsorption test at different temperatures as the high concentration $MgSO_4$ impregnation can provide more reactants and the 3A type zeolite showed an optimal performance in Fig. 3.11. The results are plotted in Fig. 3.12. The water adsorption capacity tends to grow as temperature increasing, and the equilibrium time is reduced. However, temperature higher than 45 °C has limited improvement as 55 °C and 45 °C adsorption results show similar shape as the initial stage. Only 10 °C increment from 35 °C to 45 °C can raise huge improvement of the adsorption process, which provides an

operation strategy for practical application. The curve of 55 °C indicates that this high temperature may results in water desorption in some extend. The maximum water adsorption capacity is 0.238 g/g, found in the 45 °C sorption test.

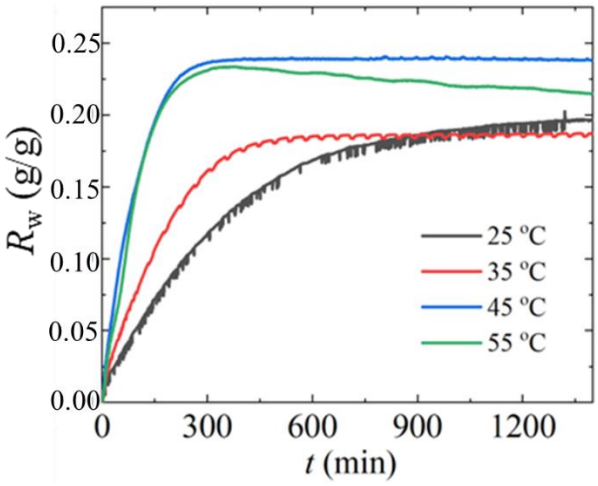


Fig. 3.12 Water adsorption capacity of the 3A-$MgSO_4$ composite at temperatures ranging from 25 °C to 55 °C and 60% relative humidity.

This composite was also tested under different humidity as exhibited in Fig. 3.13. The water adsorption capacity increases but only slightly as increasing relative humidity. Given 90% relative humidity, the maximum water adsorption capacity is observed to be 0.219 g/g.

Compared with the desorption results TGA tests, interestingly, 20% $MgSO_4$ infiltration resulted in lower water adsorption capacity than that of 10% $MgSO_4$ impregnation. The reason might be that the tested composites still had hydrated $H_2O$ (with lower hydration number) before entering the climatic chamber, while in TGA part or all this hydrated $H_2O$ could be removed because of the used high heating temperature (300 °C) which was counted in the water adsorption capacity.

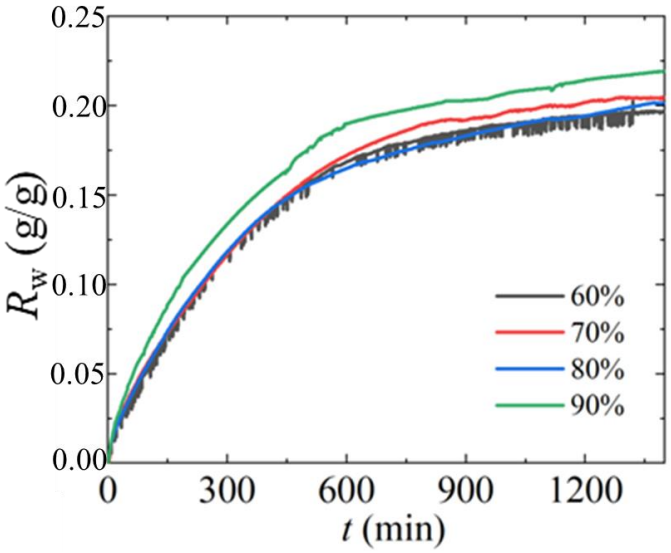


Fig. 3.13 Water adsorption capacity of the selected composite, given the humidity ranging from 60% to 90% (Temperature = 25 °C).

### 3.4. Conclusion

In this chapter, different types of the $MgSO_4$-zeolite composite adsorbents for the application of seasonal thermal energy storage were manufactured and characterised. These characterisations can help to explain the adsorption-heating performance difference in further applications and to discover the selection criteria for desired adsorption heat storage material.

SEM-EDS results showed that the using of high solution concentration in the impregnation process could lead to high salt covering which can increase the water adsorption capacity. It also revealed that the crystallization issue can be resulted by the high concentration, which may negatively influence on sorption mass transfer.

BET results revealed that the adsorption average pore diameter of the measured samples ranged from approximately 13 nm ($MgSO_4$(20%)-4A) to 25 nm ($MgSO_4$(20%)-10X) and the desorption average pore diameter varied from about 9 nm ($MgSO_4$(20%)-4A) to 17 nm ($MgSO_4$(20%)-10X). It was also discovered that with the impregnation concentration increasing, the distributed surface area on a certain pore width was obviously decreased. Moreover, the composite surface area was mainly contributed by the pores with width of around 10 nm.

XRD results demonstrated that the diffraction peaks of hydrated $MgSO_4$ salt, for instance, $MgSO_4 \cdot H_2O$, $MgSO_4 \cdot 2H_2O$, $MgSO_4 \cdot 4H_2O$, and $MgSO_4 \cdot 6H_2O$ were evidently

observed for almost all samples. It revealed that even though the adsorption process reached equilibrium, low-water-content hydrates still existed.

The maximum heat storage density found in the TGA-DSC desorption tests was 231.3 J/g by $MgSO_4$(20%)-4A. The maximum water adsorption capacity obtained from the tests was 0.1803 g/g by $MgSO_4$(20%)-13X.

Constant temperature-humidity adsorption results suggested that the composite adsorbents manufactured with a salt solution at concentration of 10% and the zeolite of 3A and 13X are the most promising ones for the space heating application.

# Chapter 4. LiCl/LiBr-zeolite composites

## 4.1 Introduction

In Chapter 3, the author studied the adsorption/heating related properties of the MgSO4-zeolite composite, as well as the adsorption-heating performance. In this chapter, the LiCl/LiBr would be experimentally investigated towards the similar tests to those in Chapter 3. Besides, the different salts of LiCl and LiBr could be integrated into one composite and then function together to adsorb water vapour and provide heating effect.

## 4.2 Methodology

### 4.2.1 Manufacturing LiCl/LiBr-zeolite

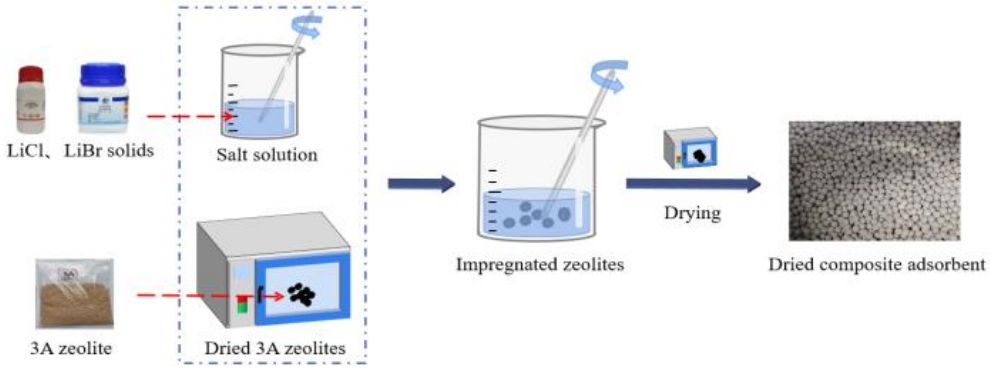


Fig. 4.1 The manufacturing process of LiCl/LiBr-zeolite composites.

Fig. 4.1 presents the manufacturing process of LiCl/LiBr-zeolite composites, as similar to that in Section 3.2.1. The materials used in this study mainly included zeolite, anhydrous lithium chloride (LiCl), anhydrous lithium bromide (LiBr), and deionized water. The details of the materials are presented in Tab. 4.1. $S_{BET}$ is the specific surface area (SSA) using BET method, while $V_p$ is the pore volume, and $d_a$ is average pore diameter.

Tab. 4.1 Raw material information.

| Material | Parameter | Manufacturer |
|---|---|---|
| 3A Zeolite | $S_{BET}$ =382 $m^2/g$, $V_p$ = 0.29 cm3/g, $d_a$ = 9.6 nm | Henan Qingquan Environmental Protection Technology Co., LTD |
| LiCl | Assay>99% | Sinopharm Chemical Reagent Co. LTD |
| LiBr | Assay>99% | Sinopharm Chemical Reagent Co. LTD |

The final mass ratios of the salt versus the dried composite, $R_{salt}$, are listed in Tab. 4.2.

Tab. 4.2 The ingredient with various ratios of the manufactured composite.

| Group | 1 | 2 | 3 | 4 | 5 | 6 | 7 | 8 | 9 | 10 | 11 | 12 | 13 | 14 |
|---|---|---|---|---|---|---|---|---|---|---|---|---|---|---|
| $C_{LiCl}$ (%) | 5 | 10 | 15 | - | - | - | - | - | 5 | 5 | 5 | 5 | 5 | - |
| $C_{LiBr}$ (%) | - | - | - | 5 | 10 | 15 | 20 | 25 | 5 | 10 | 15 | 20 | 25 | - |
| $R_{salt}$ (%) | 2.31 | 4.00 | 6.31 | 1.06 | 1.96 | 4.52 | 5.51 | 7.52 | 1.38 | 1.74 | 3.29 | 5.45 | 6.83 | 0.00 |

### 4.2.2 Composite characterization

Similar characterizations has been conducted on the manufactured composite. The pore volume and pore size distributions of the samples were examined by the nitrogen adsorption/desorption method, utilizing an automatic surface and pore size analyser (BET, Micromeritics APSP2460). Scanning electron microscopy (SEM, ZEISS, Sigma300) was used to observe the surface morphology of the manufactured salt-zeolite composite, as the salt can either fill in the zeolite pores or adhere on the surface. Electron Dispersive Spectroscopy (EDS) was used to obtain the elemental distribution (salt distribution) conditions of the manufactured composite materials. The phase composition analysis of the composite adsorbents after water adsorption were carried out by employing X-ray diffractometer (XRD, Rigaku,SmartLab SE). The TGA-DSC (TGA5500 – TAQ2000) was used to measure the water adsorption capacity as well as the heat storage density of the salt-zeolite composites. The detailed settings are the same in Section 3.2.

### 4.2.3 Adsorption performance at constant temperature and humidity

The prepared LiCl/LiBr/LiCl-LiBr with 3A zeolite composites were tested in a constant temperature and humidity chamber (climatic chamber, model: HWS-50B, Tianjin Hongnuo Instrument Co., Ltd). The settings are the same with that in Section 3.2.6.

## 4.3 Results and discussion

### 4.3.1 Pore volume, pore size distribution, and surface area (BET).

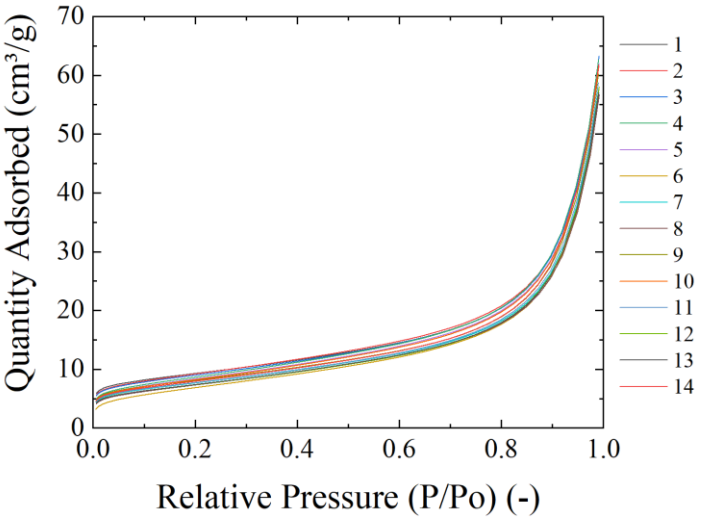


a. Isothermal adsorption curve

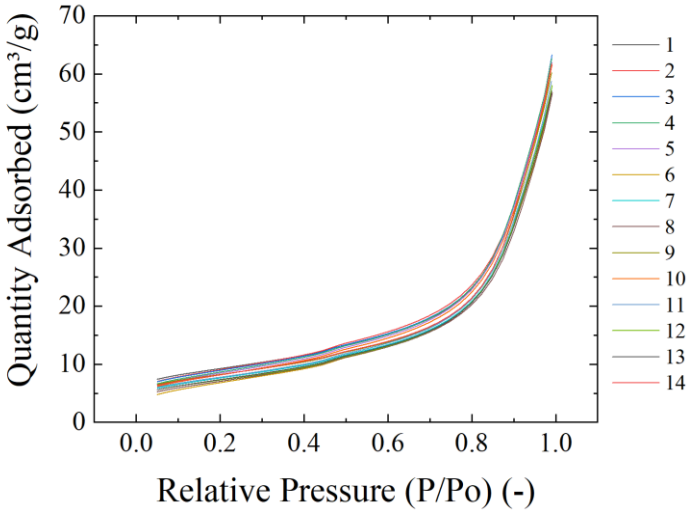


b. Isothermal desorption curve

Fig. 4.2 Isothermal adsorption/desorption curves of LiCl/LiBr-zeolite composite

Fig. 4.2.a and Fig. 4.2.b show the isothermal adsorption and desorption curves, respectively, whose results were highly consistent with type I $N_2$-ad/desorption in IUPAC definition. They proved good accordance with other porous materials such as the activated carbon. Corresponding to these two adsorption and desorption curves, significant porous characteristics such as the pore size distribution, the pore volume, and the surface area can be therefore obtained. These properties are listed in Tab. 4.3.

Tab. 4.3 The essential porous characteristics of the composite adsorbents

| Group | Surface Area ($m^2/g$) | Pore volume ($cm^3/g$) | Adsorption/desorption average pore diameter (nm) |
|---|---|---|---|
| 1 | 31.88 | $6.48 \times 10^{-2}$ | 8.09/9.53 |
| 2 | 31.90 | $6.42 \times 10^{-2}$ | 7.95/9.37 |
| 3 | 31.10 | $6.47 \times 10^{-2}$ | 8.22/9.70 |
| 4 | 30.16 | $7.72 \times 10^{-2}$ | 8.49/10.02 |
| 5 | 29.17 | $6.37 \times 10^{-2}$ | 8.55/10.23 |
| 6 | 24.39 | $5.78 \times 10^{-2}$ | 9.08/10.90 |
| 7 | 26.70 | $5.95 \times 10^{-2}$ | 8.76/10.50 |
| 8 | 25.70 | $5.73 \times 10^{-2}$ | 8.69/10.42 |
| 9 | 28.11 | $6.22 \times 10^{-2}$ | 8.74/10.41 |
| 10 | 28.76 | $6.35 \times 10^{-2}$ | 8.65/10.21 |
| 11 | 26.90 | $6.07 \times 10^{-2}$ | 8.89/10.53 |
| 12 | 25.67 | $5.88 \times 10^{-2}$ | 9.00/10.84 |
| 13 | 25.83 | $5.83 \times 10^{-2}$ | 8.86/10.63 |
| 14 | 27.73 | $6.36 \times 10^{-2}$ | 9.02/10.71 |

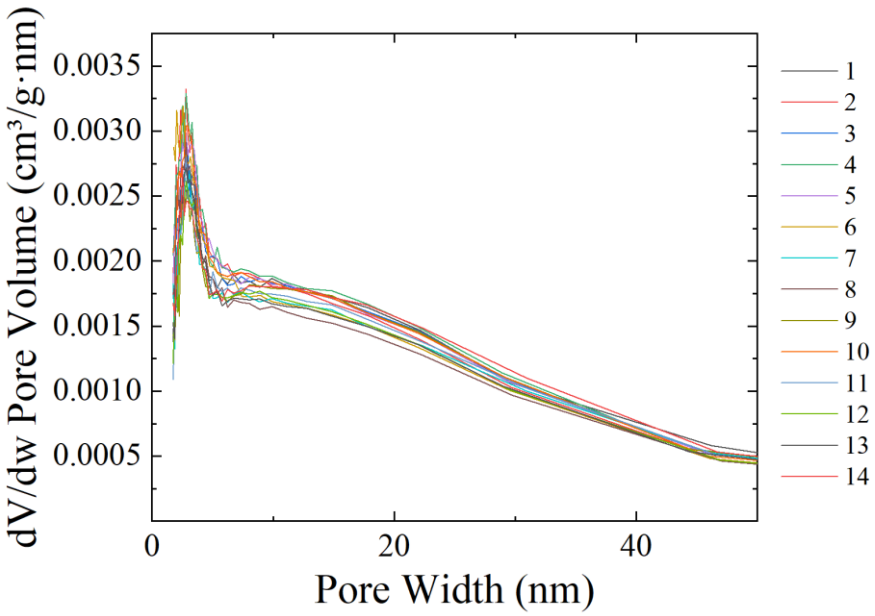


a. Adsorption pore volume *vs.* pore width

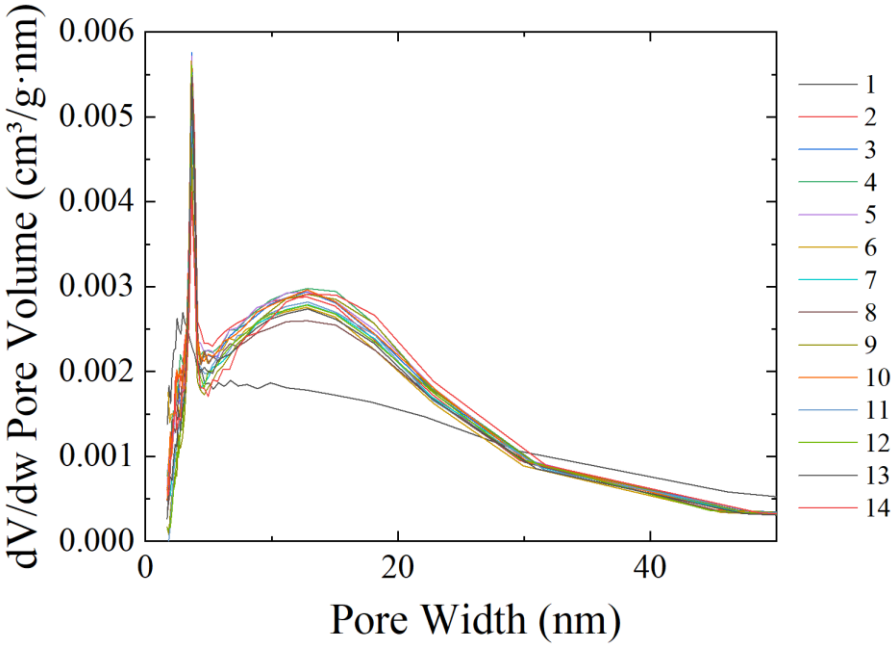


b. Desorption pore volume *vs.* pore width

Fig. 4.3 Adsorption/desorption pore volume *vs.* pore wideth of LiCl/LiBr-zeolite composite.

Fig. 4.3.a and Fig. 4.3.b are the pore volume analysis versus different pore width. A large-enough pore volume sustains the active space for $H_2O$ vapor to transport in and out during the sorption process. Otherwise, the small void phase can result in the constrained mass transfer of water sorption. All tested samples had a similar trend which increase rapidly at the begin and tend to be stable towards the end. They all have a peak pore volume approximately at the pore width of 5-7 nm, implying that the most

pore sizes are distributed among this range. The results demonstrate that the impregnation of $Li^+$ salts into the zeolite changes the mesoporous properties of the porous matrix in a very limited way. According to the results, the maximum pore volume, 7.72 x $10^{-2}$ $cm^3/g$, is found in Group 4, 5% LiBr-zeolite. The smallest pore volume, 5.73 x $10^{-2}$ $cm^3/g$, is found in Group 8, 25% LiBr-zeolite. The average pore diameter calculated based on the desorption curve is always larger than that retrieved by the adsorption curves. The maximum average pore diameter is 9.08 nm and 10.90 nm (15% LiBr-zeolite) for $N_2$ adsorption and desorption tests, respectively, while the minimum average pore diameter is 7.95 nm and 9.37 nm (10% LiCl-zeolite) separately for adsorption and desorption. The results also reveal that the pore volume or the average pore diameter can be probably reduced by the increased solution concentration. Although high solution concentration theoretically provides more salt reactants for water adsorption, it can also restrain the water sorption by sacrificing some of the mesoporous mass transport channels in the support structures, which indicates a balance between the LiCl/LiBr loads in the composite and the pore volume should be carefully maintained to accomplish an optimal sorption heat storage material.

Fig. 4.4.a-c present the surface area results retrieved from BET tests versus the pore width for Group 1-14, separately displayed by the impregnation solution type. Some huge fluctuations between the pore width from about 5 nm to 15 nm may demonstrated that lots of pores were distributed in this range but not evenly. A sharper peak in the surface area illustration represents the more distribution toward the corresponding pore width, i.e. more pores were within the pore width and contributed to more share in the material gross surface area. The trend is still clear that the most surface area is contributed by the pores within a width of 4-25 nm, and a peak can be found between 5-7 nm. The largest surface area, 31.90 $m^2/g$, is found in Group 2, 10% LiCl-zeolite, while the smallest is discovered in Group 6, 15% LiBr-zeolite. Similarly, to the pore volume results, the high concentration can potentially reduce the surface area of the porous structure, which can result in the decreased active sites for the water adsorption to be carried out and thus the negatively influenced sorption performance.

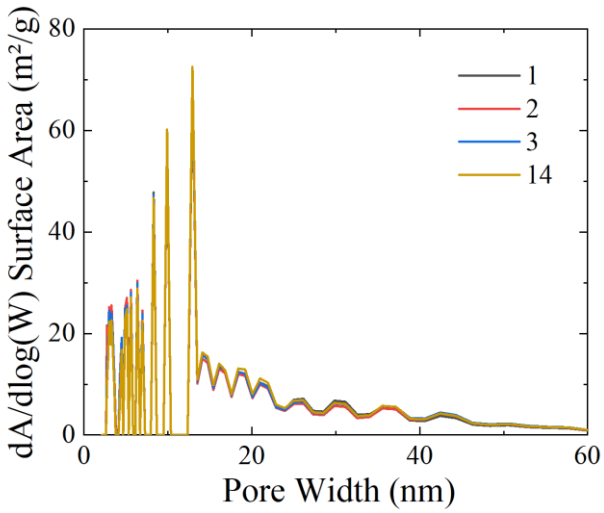


a. Surface area of LiCl-zeolite *vs* pore width

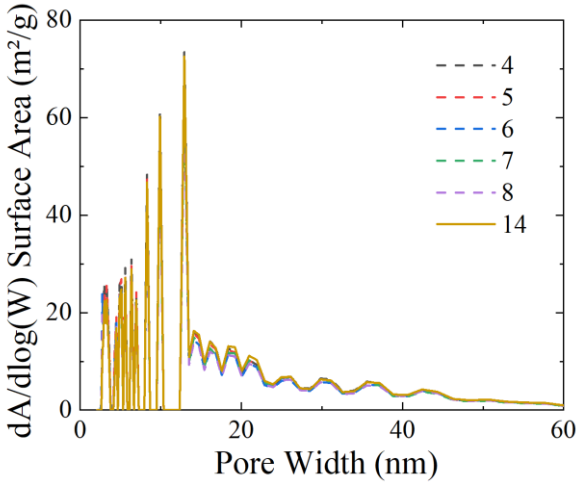


f. Surface area of LiBr-zeolite *vs* pore width

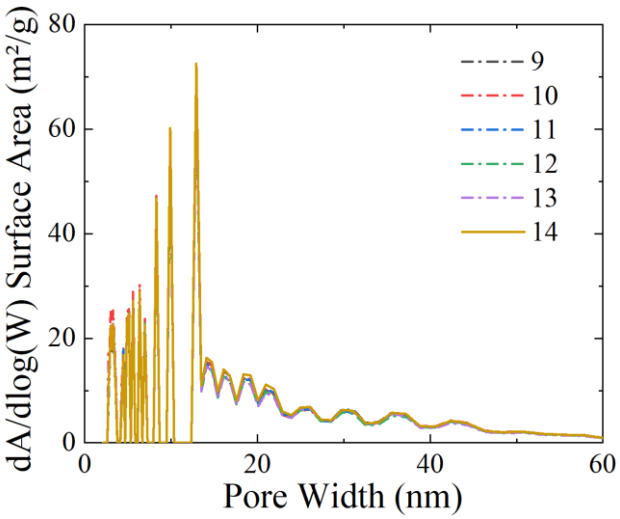


g. Surface area of LiCl-LiBr-zeolite *vs* pore width

Fig. 4.4 BET results of the prepared composite adsorbents.

### 4.3.2 Surface morphology and surface salt distribution (SEM-EDS)

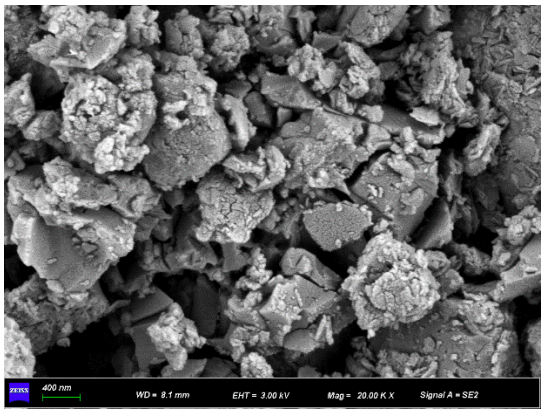


a. 5% LiCl

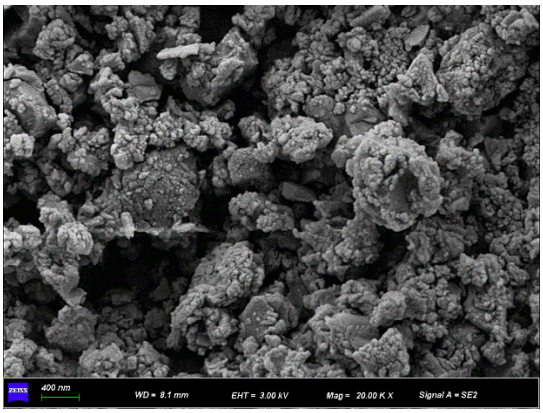


b. 10% LiCl

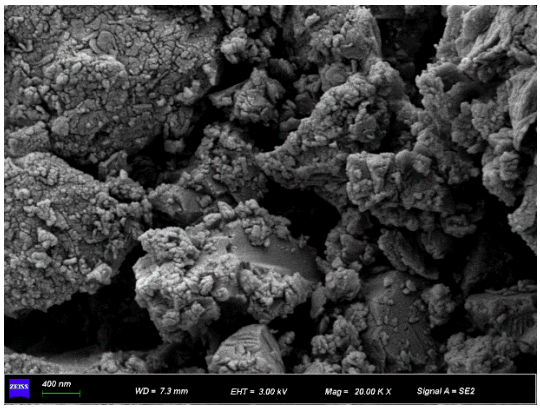


c. 15% LiCl

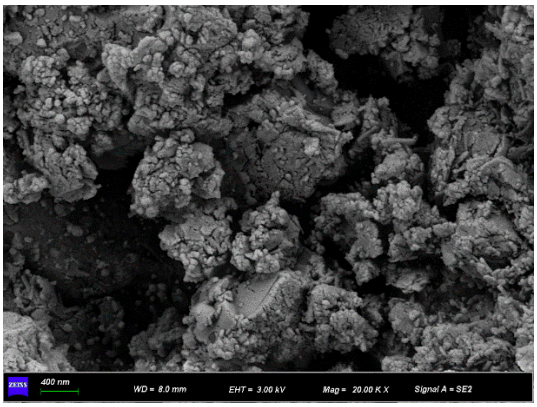


d. 5% LiBr

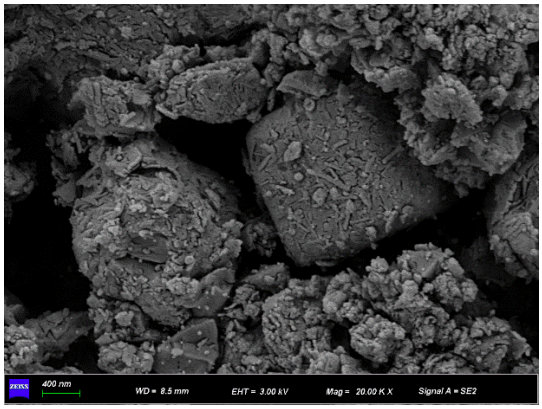


e. 10% LiBr

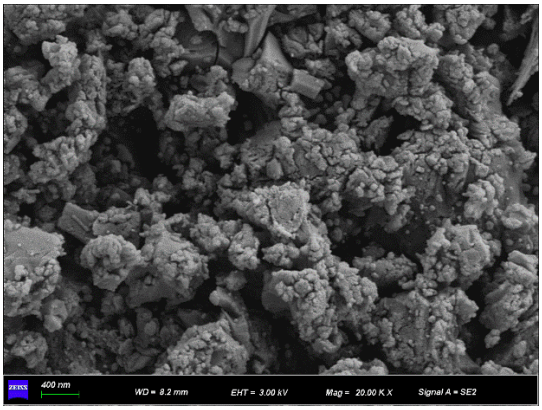


f. 15% LiBr

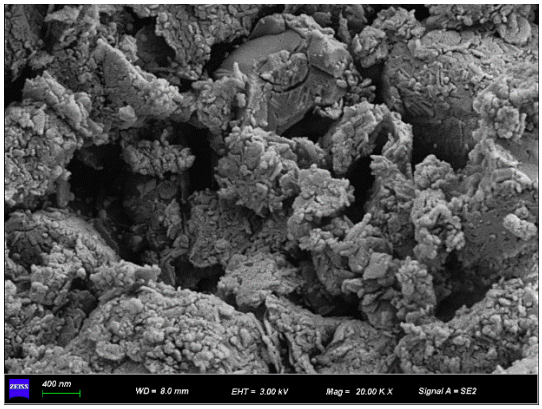


g. 20% LiBr

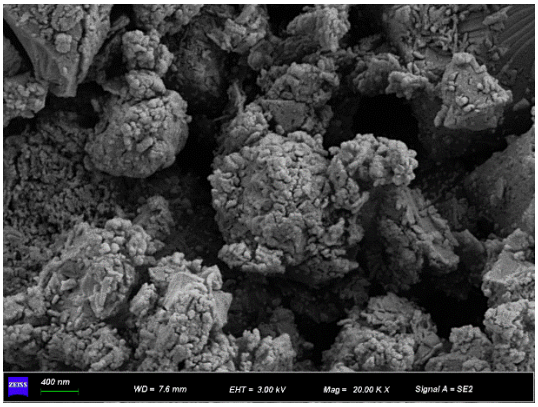


h. 25% LiBr

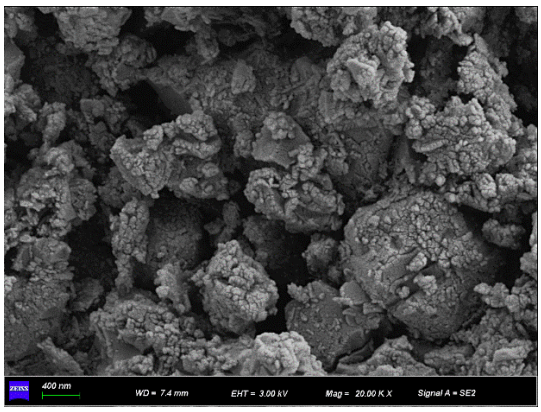


i. 5% LiCl + 5% LiBr

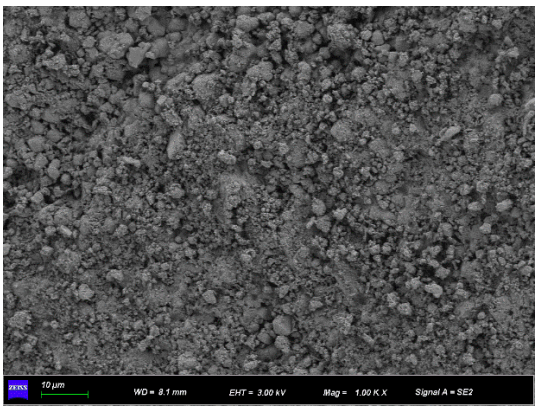


j. 5% LiCl + 10% LiBr

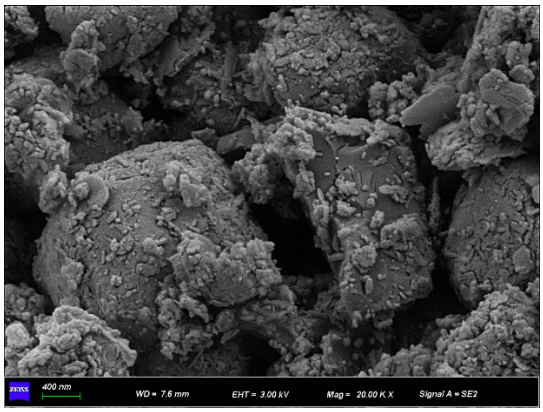


k. 5% LiCl + 15% LiBr

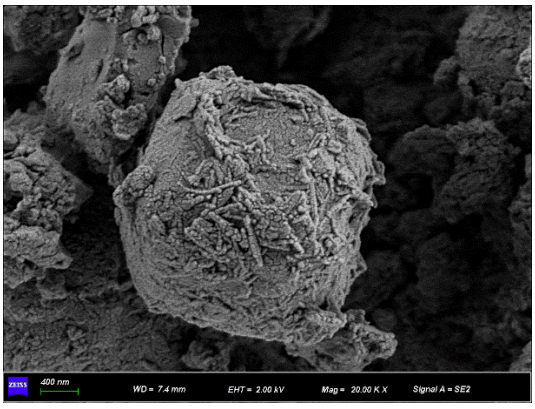


l. 5% LiCl + 20% LiBr

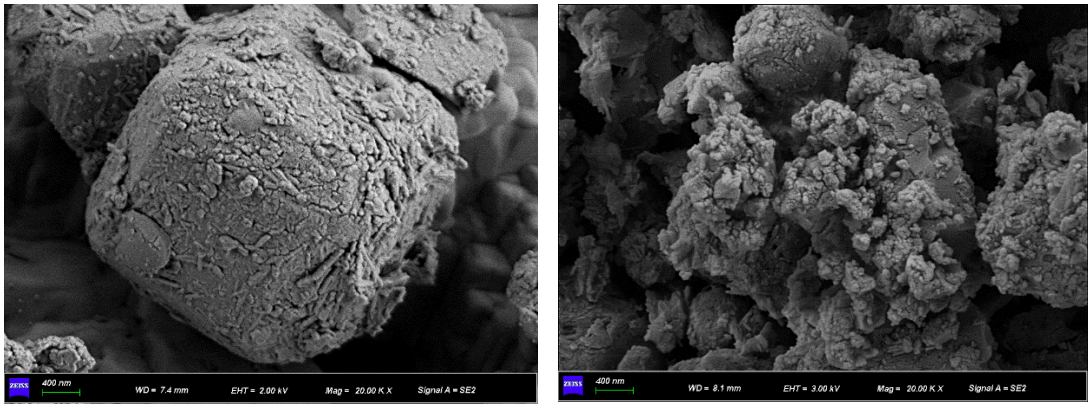


m. 5% LiCl + 25% LiBr o. no salt

Fig. 4.5 SEM photos of the manufactured composite with different solution concentrations.

Fig. 4.5 showed the surface morphologies of all prepared composite samples, given a magnification of 20,000x. The layer-structured matrix is the zeolite basement, and the outer powdery structure is the salt. The salt of magnesium sulphate crystallizes in the form of needle-shape in some of the figures. As shown in Fig. 4.5.o, pure 3A zeolite exhibits a porous structure as fissures and pores can be clearly observed all over the sample photo. The matrix shape of the 3A zeolite seems like graininess with a small portion of flakes. Other photos in Fig. 4.5 displayed the prepared salt-zeolite composite adsorbents. With the increase of the salt mass ratio, for instance, compared Fig. 4.5.a and Fig. 4.5.b, the surface and the pores in the 3A zeolite were loaded with more salt particles. The more salt loads mean the more potentially water adsorption capacity, which can theoretically enhance the heat storage density of the composite adsorbent. However, the excess loading can result in the issues such as the salt agglomeration presented in Fig. 4.5.c, which can cause severe problem as the crystallized salt can constrain the mass transfer for the water to be adsorbed. It should be noted that to achieve a high heat storage density, a balance should be found between the high salt loads and the sacrificed flow channels for vapour transport.

Fig. 4.6 displayed the EDS results scanning the corresponding 20,000x SEM photos. Fig. 4.6.a presented the mapping of the element Br as an example, while Fig. 4.6.b was that of the element Cl. The element mappings were similar, and thus only two of them were exhibited in this paper. The different colours of green and red respectively represented the element Br and Cl, whose covering area can be analysed for the element or salt coverage of the sample surface.

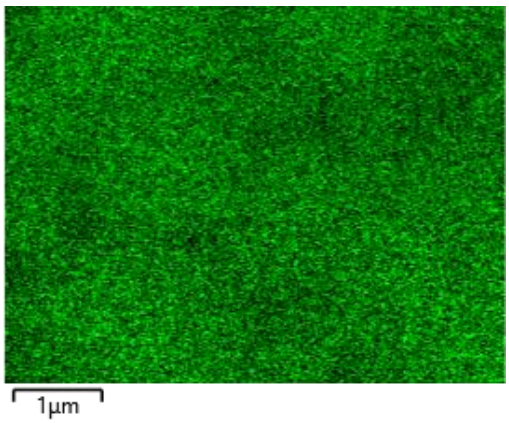


a. Br mapping of 5% LiCl +5% LiBr composite

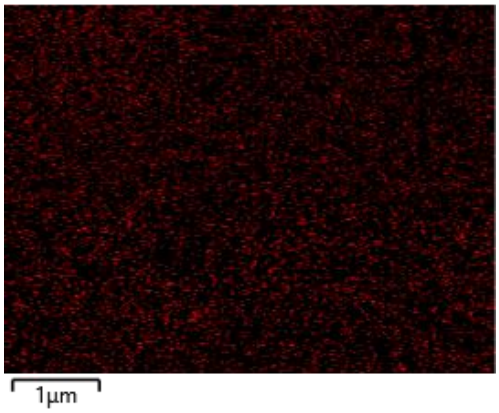


b. Cl mapping of 5% LiCl +5% LiBr composite

Fig. 4.6 Element mapping of Cl and Br in LiCl/LiBr-zeolite composite

Fig. 4.7 was the element coverage on the tested composite adsorbents. Although these measurements seemed semi-quantitative, it was evidence to prove that higher solution concentration can lead to a higher salt content in the composite surface or even demonstrated the potential of that in the material volume. However, the increment of the salt content in the final adsorbent can be smaller than that made of the lower solution concentration as the impregnation process between the ions in the solution and the pores who can hold the salt may be constrained by the too high concentration. Again, the EDS results showed that the highest concentration of LiBr or LiCl solution may not be an optimal choice for making better composite adsorbent. The surface coverage, 47.23%, scanning the composited impregnated by the 20% LiBr, was found to maximum among all candidates.

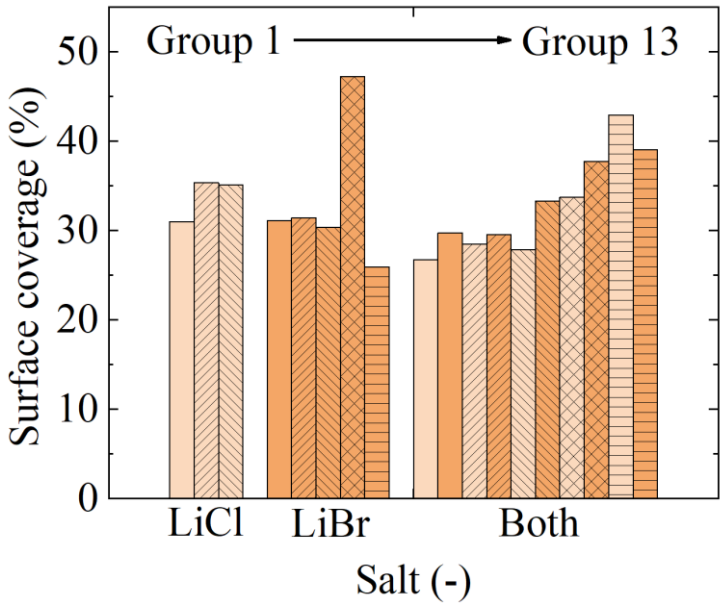


Fig. 4.7 Element mapping results

**4.3.3 Theoretical water adsorption capacity and heat storage density (TGA-DSC)**

Fig. 4.8 displays the water adsorption capacity results of the manufactured composite adsorbents from the TGA tests. The maximum water uptake capacity, 0.16 g/g, is discovered in Group 1, 5% LiCl-zeolite, while the minimum value, 0.10 g/g, is observed in Group 13, 5%LiCl-25%LiBr-zeolite. For the results of LiCl-zeolite composites, the lowest water adsorption capacity is found in 10% LiCl-zeolite, which corresponds to the most surface area and the maximum average pore diameter group. It may refer to the mistakes taken during manufacture that the salt load is low in Group 2 and thus the water adsorption capacity is lower than that of the other two concentrations. For LiBr-zeolite, the results demonstrate that the lowest LiBr solution concentration enables the highest water adsorption and thus a maximum adsorption heat. It can be found in this case, the reduction of mesoporous channels for the water vapour transfer can affect more significant on the water uptake than the potentially more salt loads by using higher LiBr solution concentrations. Moreover, the pure zeolite even has higher water adsorption capacity than 5%LiCl-20/25%LiBr-zeolite. It means these two groups benefits nothing from these high concentration infiltrations due to the less mass transport channels and smaller average pore diameters. For LiCl-LiBr-zeolite composites, it has the same trend with that of LiBr-zeolite.

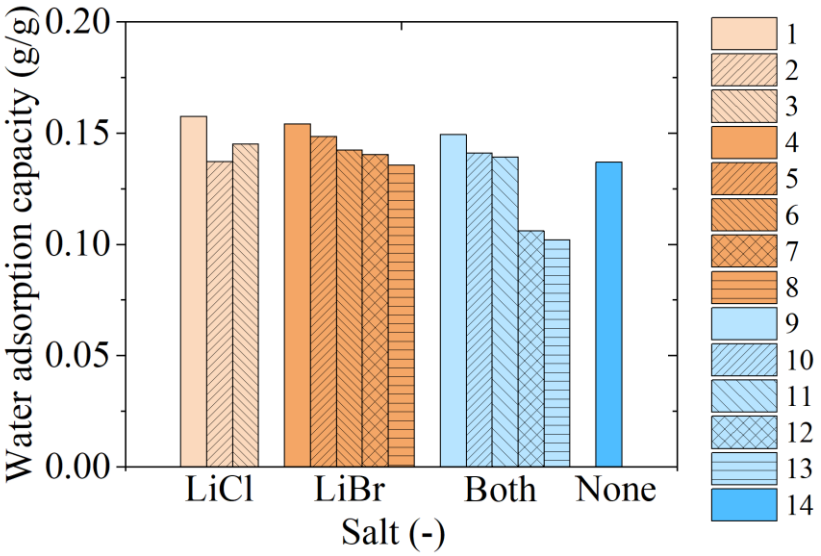


Fig. 4.8 Water adsorption capacity obtained by TGA tests.

Fig. 4.9 shows the DSC test results revealing the desorption heat (heat storage density) of the various adsorbent samples. The maximum heat storage density, 592.8 J/g, is found in Group 9, 5%LiCl-5%LiBr-zeolite, while the minimum heat storage density, 404.7 J/g, is discovered in Group 8, 25% LiBr-zeolite. Interestingly, for LiCl-zeolite, the heat storage density decreases with the solution concentration increasing. Even though the water adsorption capacity of Group 2, 10% LiCl-zeolite, is low, its heat storage density is higher than that of Group 3, 15% LiCl-zeolite. This may be due to that the varied porous structure may affect the hydration bound formation processes. For LiBr-zeolite, 10% and 15% solution concentrations have similar performance toward the heat storage density aspect, 472.0 J/g and 472.7 J/g, respectively. It reveals that a higher solution concentration may potentially raise the salt loads (the water adsorption capacity), however, the increased solution concentration can also affect the mass transfer process of the water adsorption process thus affect the hydration bond formation and result in the lower heat storage density. Besides, all LiCl-LiBr-zeolite groups present better performance than LiCl/LiBr-zeolite, due to the more complicated hydration bond formation conditions, even the water adsorption capacity may not be higher than those composites made with single salt.

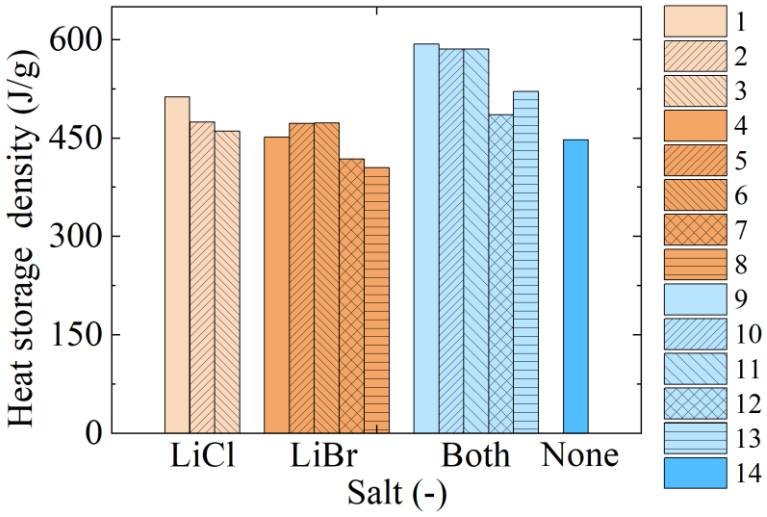


Fig. 4.9 Heat storage densities obtained by DSC tests.

### 4.3.4 Analysis of physical properties of composites (XRD).

Fig. 4.10 is the XRD results showing the various hydrate composition phases of the manufactured composite adsorbents which have completed their water adsorption. The peaks show similar shape but the different signal intensity within LiCl-zeolite, LiBr-zeolite, and LiCl-LiBr-zeolite, their own groups, also consistent with the 3A zeolite XRD profiles. For the LiCl-zeolite composite, three potential hydrates are found, $LiCl{\cdot}H_2O$, $LiClO_3{\cdot}0.25H_2O$, and $LiClO_4{\cdot}3H_2O$. The increased concentration of LiCl solution raises the peaks of $LiClO_3{\cdot}0.25H_2O$ indicating the augment of this composition phase content, as exhibited in Fig. 4.10.a. For the adsorbent with LiBr, the peaks of $LiBr{\cdot}H_2O$, $LiBr{\cdot}2H_2O$, and $LiBrO_3{\cdot}H_2O$ are observed as presented in Fig. 4.10.b. No special fluctuations are found exclude a very strong signal b ($LiBr{\cdot}2H_2O$) in LiBr-zeolite using 25% solution concentration. For the hybrid composite LiCl-LiBr-zeolite, all these peaks mentioned above are observed, while the peaks of $LiClO_3{\cdot}0.25H_2O$ and $LiBrO_3{\cdot}H_2O$ seem stronger than other candidates. The stronger signal indicates the higher share of corresponding hydrate.

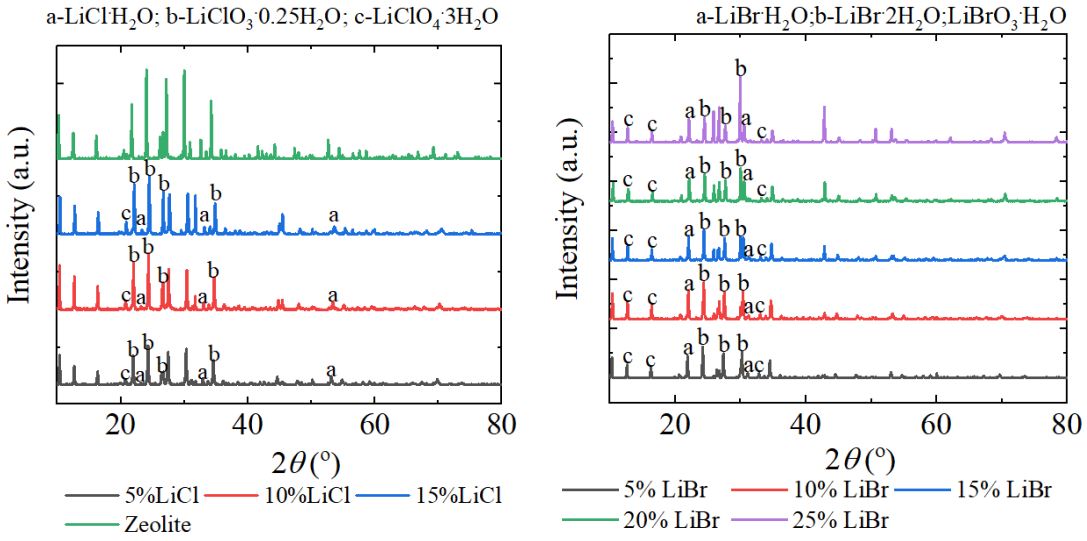


a. LiCl-zeolite, zeolite

b. LiBr-zeolite

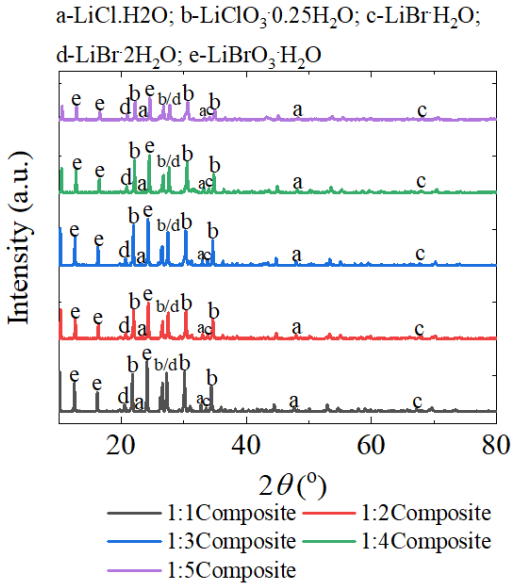


c. LiCl-LiBr-zeolite

Fig. 4.10 XRD results of the manufactured composites

### 4.3.4 Water uptake of composite materials in climatic chamber

The composite adsorbent was placed in the climatic chamber (T/H chamber) for water adsorption. An automatically recording electronic balance was used to measure the continuous weight change of the samples during the experiment with an accuracy of ±0.01 g. The achievement of the adsorption equilibrium is defined as when the weight difference reaches less than 5% in two consecutive 60-minute intervals. The total adsorption time was 24 hours.

The kinetic curves of water adsorption of different adsorbents at 25 °C and 60% relative humidity are shown in Fig. 4.11.a. In the illustration, 14 adsorbent groups are further divided into 4 categories, solid line for LiCl-zeolite, dash line for LiBr-zeolite, dot line for LiCl-zeolite, and dash dot for 3A zeolite. For the adsorption tests carried out on LiCl-zeolite, the 15% LiCl-zeolite obviously has the fastest adsorption kinetics with water, as well as the highest water adsorption capacity after 24 h. In this category, the adsorption rate increase when the impregnated solution concentration increases. For the LiBr-zeolite-water adsorption, before 240 min, the fastest adsorption was found in 10% LiBr-zeolite. Between 240 min to 765 min, 5% LiBr-zeolite adsorbs waster at the fastest rate. In the range of 765 min to 1022 min, 20% LiBr-zeolite has the fastest water adsorption. After 1022 min, the green dash line locates the highest part among all LiBr-zeolite in the figure, representing the highest adsorption rate as well as the water adsorption capacity. For the composite made by mixed salt solution, before 770 min, 5%LiCl-5%LiBr-zeolite takes the outstanding performance as it is the most rapid adsorbent working with water, while after 770 min, 5%LiCl-25%LiBr-zeolite shows the maximum adsorption rate among all mixed salt-zeolite composite. Considering all groups in one competition, before 112 min, 112-295 min, 295-765 min, 765-1022min, 1022-1308 min, and after 1308 min, the optimal one is group 5 (10% LiBr), group 3 (15% LiCl), group 4 (5% LiBr), group 7 (20% LiBr), group 8 (25% LiBr), and group 13 (5% LiCl-25% LiBr). According to the different adsorption performance in the various period, rational strategy to manage the adsorption operation can be made.

Fig. 4.11.b illustrates the corresponding final water adsorption capacity after 24 h for each group. With the solution concentration increasing, the water adsorption capacity grows except for group 12 (5% LiCl-20% LiBr), which may be caused by the experimental errors. The bare 3A zeolite shows higher water adsorption capacity than all samples solely made by LiCl solution. The maximum water uptake observed in the climatic chamber adsorption experiment is 0.22 g/g (5%LiCl-25%LiBr-zeolite), while the minimum value is 0.14 g/g, found in 5% LiCl-zeolite samples.

It should be noticed that the balance integrated with TGA has higher accuracy compared to that used in the climate chamber, as the condensed water at the surrounded walls in the chamber is hard to control.

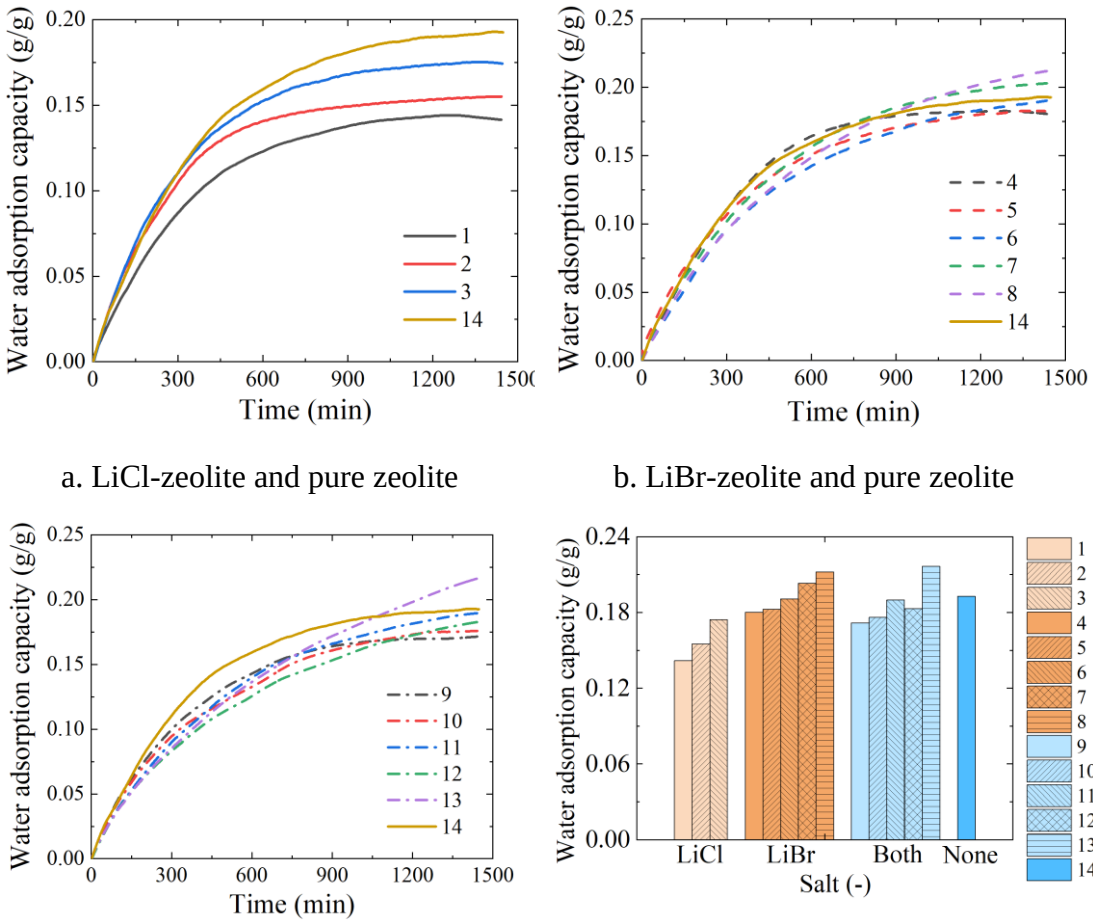


a. LiCl-zeolite and pure zeolite

b. LiBr-zeolite and pure zeolite

c. LiCl-LiBr-zeolite and pure zeolite

d. final water adsorption capacity

Fig. 4.11 Water adsorption performance in the climatic chamber (a/b/c - adsorption kinetics; d – water adsorption capacity).

### 4.4. Conclusion

In this study, the composite thermochemical adsorbent materials of LiCl-zeolite, LiBr-zeolite, and LiCl+LiBr-zeolite were characterised. The main findings are summarized as follows:

- The higher solution concentration favours the more loadings of the salt onto the 3A zeolite, however too high solution concentration may raise the problem of blockage of mass transfer channels of water adsorption and thus limit the heat storage capacity of the adsorbent. Both SEM and BET tests results can support this finding. The framework structure of 3A zeolite remained well after impregnation.

- XRD results show five possible hydration bonds in the totally adsorbed composite: $LiCl{\cdot}H_2O$, $LiClO_3{\cdot}0.25H_2O$, and $LiClO_4{\cdot}3H_2O$ for LiCl impregnated samples, and $LiBr{\cdot}H_2O$, $LiBr{\cdot}2H_2O$, and $LiBrO_3{\cdot}H_2O$ for LiBr infiltrated adsorbents.

- The maximum heat storage density, 592.8 J/g, is found in Group 9, 5%LiCl-5%LiBr-zeolite. The most water adsorption capacity observed in the climatic chamber adsorption experiment is 0.22 g/g (5%LiCl-25%LiBr-zeolite). The highest water adsorption capacity found in TGA tests is 0.16 g/g, in Group 1, 5% LiCl-zeolite.

# Chapter 5. Thermochemical house heating experiment

## 5.1 Introduction

The thermochemical solar energy storage material of the experimentally examined salt-zeolite composite is used in the practical space heating house model experiment. The house model was scaled by 1/22.5.

## 5.2 Methodology

### 5.2.1 LiCl-LiBr-zeolite

The complex LiCl-LiBr-zeolite composite is employed as the solar energy storage material in the space heating experiment. The manufacturing process and the source company has been recorded in Chapter. 4. Tab. 5.1 lists the mass ratios of the LiCl and LiBr in the composite preparation.

Tab. 5.1 The ingredient with various ratios of the manufactured composites

| Group | Z0 | Z5 | Z10 | Z15 | Z20 | Z25 |
|---|---|---|---|---|---|---|
| Salt concentration | 0wt% | 5wt% | 10wt% | 15wt% | 20wt% | 25wt% |
| LiCl:LiBr mass ratio | - | 1:1 | 1:2 | 1:3 | 1:4 | 1:5 |

The samples were imaged using a Sigma 300 model scanning electron microscope (SEM) as shown in Fig. 5.1, at a magnification of 20,000x. High-concentration salt solutions are also susceptible to crystallisation, which may limit the material's mass transfer capacity. It is therefore essential to identify the optimum concentration of salt solution used for manufacturing the composite adsorption material.

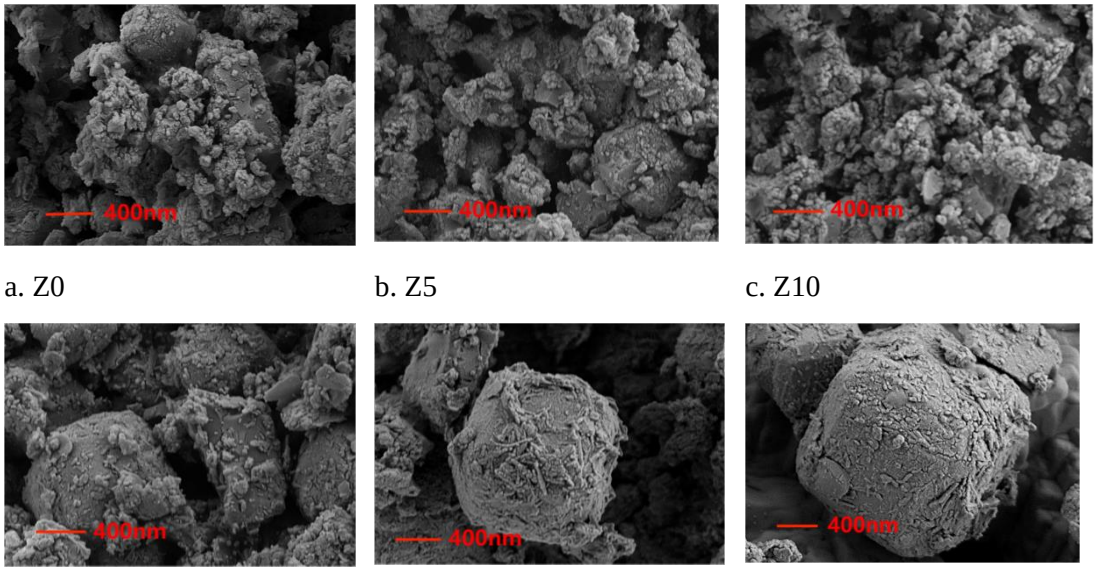


a. Z0 b. Z5 c. Z10

d. Z15 e. Z20 f. Z25

Fig. 5.1 SEM photos of the composites with different solution concentrations at the magnification of 2000 times: (a)Z0; (b)Z5; (c)Z10; (d)Z15; (e)Z20; (f)Z25.

The pore volume and pore size distribution of the materials were examined using a fully automatic surface and pore size analyzer (BET, Micromeritics APSP2460) using nitrogen adsorption-desorption experiments are listed in Tab. 5.2.

Fig. 5.2.a and Fig. 5.2.b show the pore volume versus different pore widths. Although a high salt concentration theoretically provides more reactants for water adsorption, it also limits water adsorption by sacrificing some mesoporous mass transport channels in the support structure. This suggests that the balance between LiCl/LiBr loading and pore volume in the composite should be carefully maintained to accomplish an optimal thermochemical thermal storage material.

Tab. 5.2 The essential porous characteristics of the manufactured composite adsorbents

| Group | Surface Area ($m^2/g$) | Pore volume ($cm^3/g$) | Adsorption/desorption average pore diameter (nm) |
|---|---|---|---|
| Z0 | 27.73 | $6.36 \times 10^{-2}$ | 9.02/10.71 |
| Z5 | 28.11 | $6.22 \times 10^{-2}$ | 8.74/10.41 |
| Z10 | 28.76 | $6.35 \times 10^{-2}$ | 8.65/10.21 |
| Z15 | 26.90 | $6.07 \times 10^{-2}$ | 8.89/10.53 |
| Z20 | 25.67 | $5.88 \times 10^{-2}$ | 9.00/10.84 |
| Z25 | 25.83 | $5.83 \times 10^{-2}$ | 8.86/10.63 |

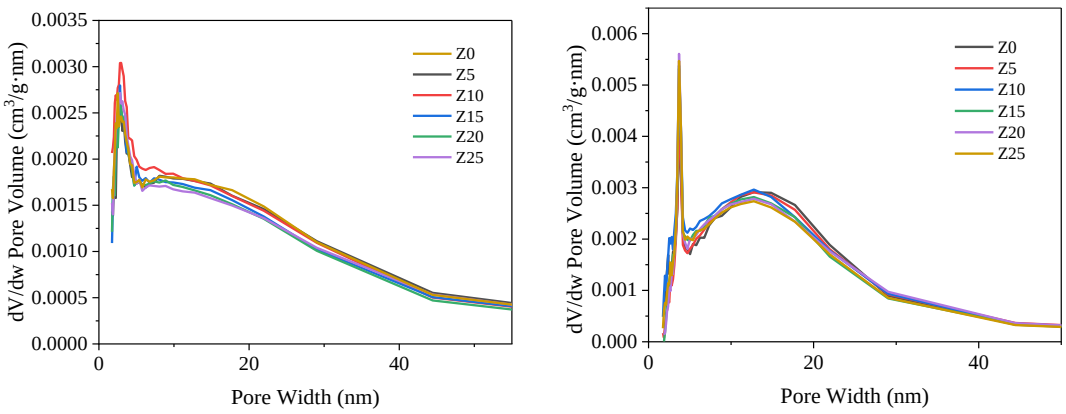


a. Adsorption b. Desorption

Fig. 5.2 Pore volume vs. pore width of the prepared composite adsorbents by BET.

Differential scanning calorimetry (DSC) were performed on Z0 to Z25. Using a simultaneous thermal analyser, with $N_2$ selected as the test atmosphere. The experimental temperature conditions were set to increase from 30 °C to 300 °C, the heating rate was 5 °C/min, and the experimental time was 1 h. The heat flow was recorded throughout the process. The DSC curves of the endothermic dehydration process of each group of samples are shown in Fig. 5.3.a The theoretical heat storage density of the composite heat storage material is obtained by integrating the curve inland in a certain range, and plotted in Fig. 5.3.b. Sample Z0 exhibites a heat storage density of 447.1 J/g; however, in all instances, the heat storage density of the composites are higher than that of the pure zeolite. This effect is due to the contribution of salt to the water absorption capacity, thereby increasing its thermal storage density. The most significant thermal storage density is recorded in Z5 (32.6% higher than Z0). Although no positive correlation was identified between the heat storage density of the composite adsorbent and the salt solution concentration, a higher solution concentration may nonetheless hinder mass transfer during water adsorption, thus resulting in a lower heat storage density. Therefore, samples Z5, Z10 and Z15 can be used as the three ‘ideal’ samples for the analyses in this study because their heat storage densities do not markedly differ.

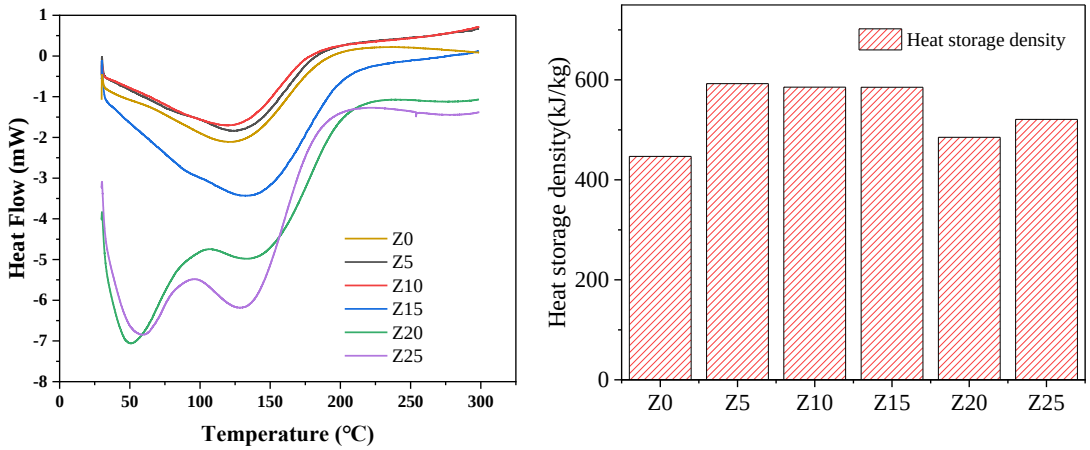


a. Heat flow curve b. Heat storage density.

Fig. 5.3 DSC results of the prepared composite adsorbents.

The adsorption rate and capacity of water vapour have significantly impact on the energy storage capacity of LiCl-LiBr-zeolite adsorption systems. The adsorption tests were conducted in a constant temperature and humidity chamber (climatic chamber) under a temperature of 25 °C and relative humidity (RH) levels of 60%, 70%, 80%, and 90% to analyse the adsorption kinetics. The mass change of the adsorbent samples over 24 hours was measured by using an electronic balance. The water uptake kinetics of samples are depicted in Fig. 5.4. When the weight difference is below 5% in two consecutive 60 min intervals, adsorption equilibrium was deemed to have been achieved.

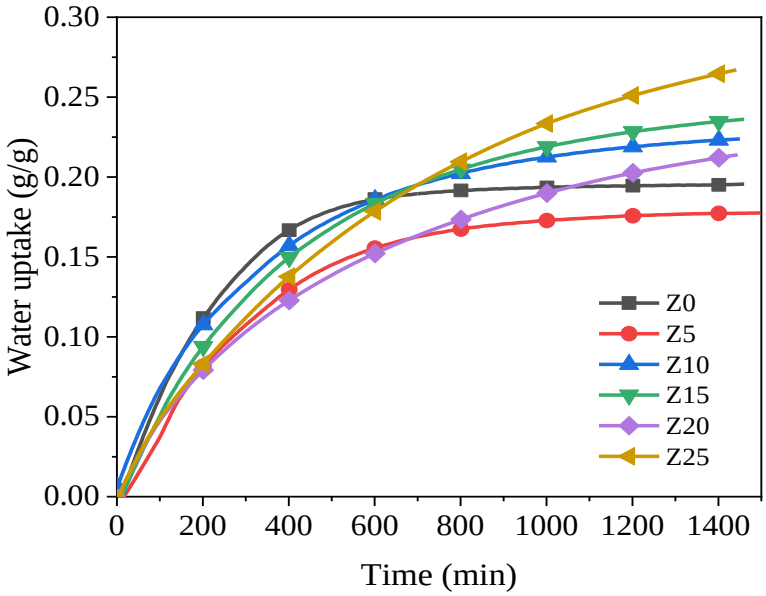


Fig. 5.4 Water adsorption kinetics of samples with different composites.

The pure zeolite, Z0, exhibits high adsorption rate at the early adsorption stage, reaching a maximum value of 0.18 g/g after 600 minutes of adsorption at 25 °C and 80% RH, as shown in Fig. 5.4. Comparing to Z0, Z5 performs more poorly as an adsorbent with lower adsorption rate and capacity, which is due to its low salt content and partially blocked water transfer channels. Higher salt content adsorbents take longer to achieve equilibrium, suggesting that the water transfer channels were blocked more significantly with increasing salt content; however, the adsorption rate are larger at late stage of adsorption and the final adsorption capacity is also promoted. In contrast, samples Z10, Z15 and Z25 demonstrate reasonable adsorption rates and capacities. However, sample Z20 did not show a similar linear growth pattern, which is due to that under the conditions of the salt concentration impregnated by Z20, the salt swells upon hydration, leading to the blockage of the zeolite pore channels. This self-clogging effect is detrimental to the water adsorption behaviour of the material. In particular, For sample Z25, the zeolite's pores were much filled with salt, thus, this sample exhibited a lower sorption rate than Z10 and Z15 until 700 minutes due to the corresponding significant mass transfer barrier; thereafter due to the strong water adsorption capacity of salt, the overall adsorption rate is higher. Finally, the adsorption capacity of Z10, Z15 and Z25 are 0.22 g/g, 0.24 g/g and 0.27 g/g, respectively. Z15 always maintains a high adsorption rate and has a high adsorption capacity when the adsorption equilibrium is reached.

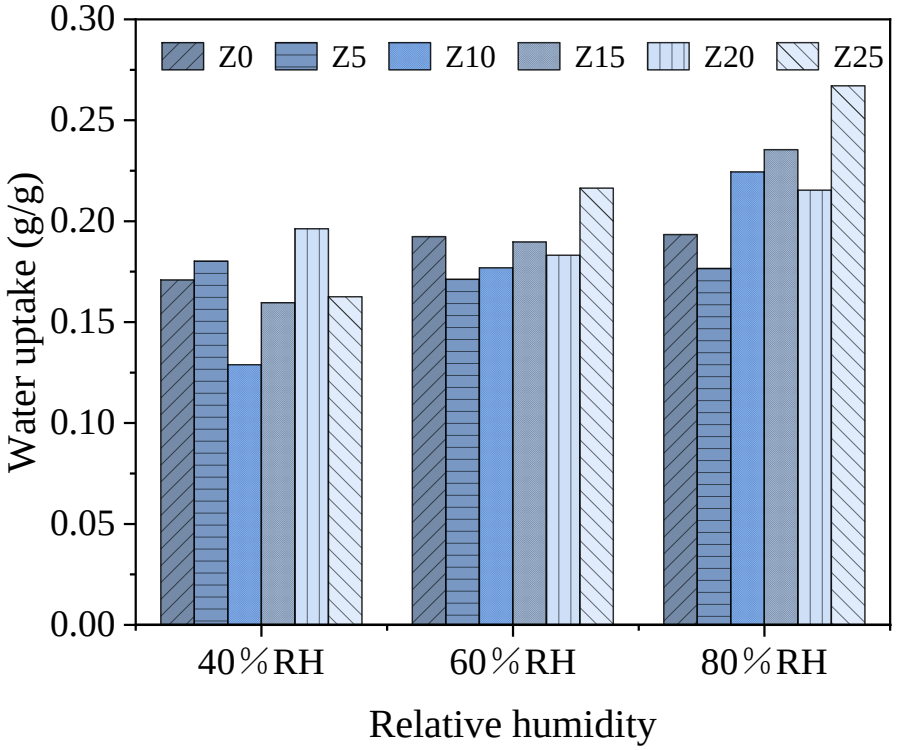


Fig. 5.5 Water adsorption capacity with different relative humidifies.

The RH significantly impacts the equilibrium adsorption capacity of every sample. Fig. 5.5 shows the adsorption capacity of the samples after reaching equilibrium at 40%, 60% and 80% RH. The overall pattern indicates that high RH encourages wate vapour adsorption, thus increasing the adsorption capacity of all samples. This occurs because the increased RH elevates the water vapour pressure difference between the water vapour in the air and the equilibrium water vapour pressure of the adsorbent material, which facilitates the effective diffusion of water vapour into the adsorbent. Another significant factor is that salt deliquescence in a high-humidity environment reduces zeolite micropore blockage, which is advantageous for increasing water adsorption. Nevertheless, the swelling of salt hydration occurs at the same relative humidity conditions, which may lead to the clogging of zeolite pores still exists.

### 5.2.2 Adsorption of LiCl-LiBr-zeolite in a tube reactor

The investigation of the adsorption kinetics of the samples revealed that Z15 had both a high water adsorption rate and capacity. Further DSC studies show the heat storage

density of Z15 is up to 585.3 J/g, which is 30.9% higher compared to Z0. On this basis, sample Z15 was selected as the optimal composite adsorbent for lab-scale open system experiment.

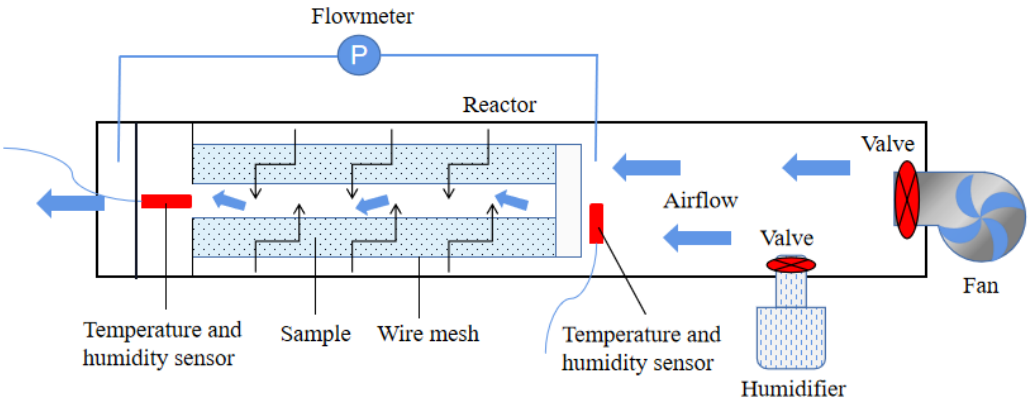


a. Schematic diagram of the tube reactor configuration

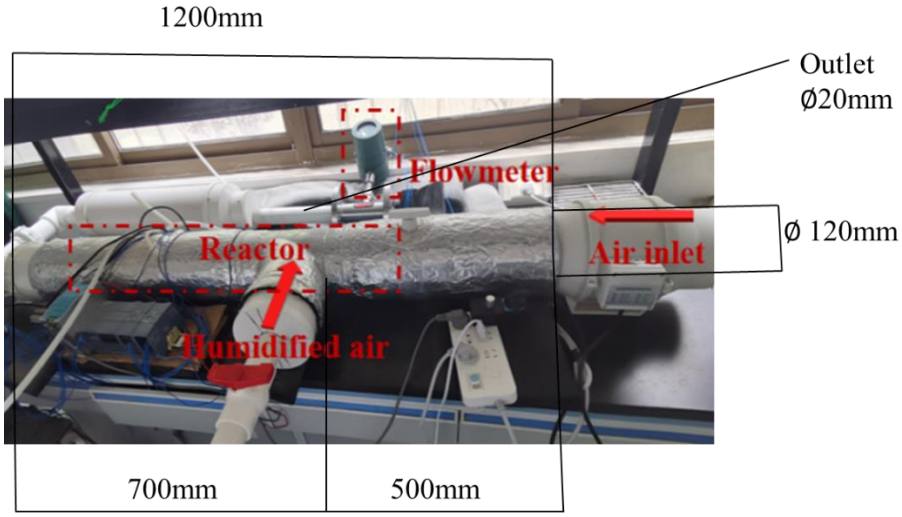


b. Photo of the adsorption pipeline system

Fig. 5.6 Adsorption experimental pipeline diagram

Fig. 5.6.a shows a schematic diagram of a reaction system, while Fig. 5.6.b is the photo of the thermochemical heat storage reaction system, which comprises a pipe with a valve, a fan, a humidifier, and a reactor. The reactor is placed inside the hollow cylindrical pipe that houses the entire apparatus. The rightmost side of the pipe is connected to an inclined flow booster pipe fan. In addition, the humidifier is connected to the inlet air duct. Later in Section 5.2.4, the adsorption pipeline will be used to integrated with the scaled house model as a heat source.

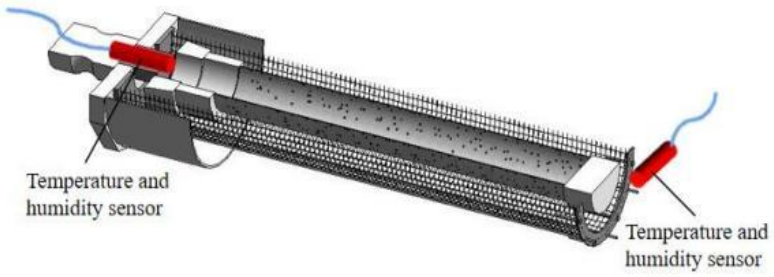


Fig. 5.7 Cross-sectional area of the tube.

The layout of the reactor is shown in Fig. 5.7. The wire mesh container containing the composite adsorbent Z15 is covered with a metal disc-shaped covering. To achieve a more thorough and uniform adsorbent reaction, the reactor is fitted with a thin tube with perforations in the centre shaft. In total, 3 kg of Z15 adsorbent was placed inside the reactor. During the experiment, the pipes were covered in aluminium foil insulation foam to minimize heat loss to the exterior. Temperature and humidity sensor (A-Pt100) were installed at the inlet and outlet of the reactor to measure the temperature and humidity of the air. To assess the volume of air passing through the pipe, a gas flow meter was installed at the end of the pipe.

- **Experimental procedures**

In this study, the air flow rate and relative humidity were chosen as the main variables for investigation; thus, to examine the impacts of both on the thermal storage performance of the composite salt, orthogonal experiments were configured with airflow rates of 5 $m^3$/h, 10 $m^3$/h, 15 $m^3$/h and 20 $m^3$/h and humidity levels of 60%, 70%, 80% and 90% RH.

3 kg of LiCl/LiBr-zeolite composite thermal storage material was placed in the reactor, and the fan and humidifier were adjusted to ensure that the experimental conditions were within the predetermined ranges. Overall, the adsorption reaction procedure for the composite material takes 12 to 20 hours to complete. In the initial stage of the reaction, the outlet temperature rises at a certain rate and then begins to fall after reaching its peak. The temperature curve subsequently tends to slowly level off and return to the inlet temperature, indicating the reaction's completion. The adsorption material in the reactor was heated in an oven following each experiment, totally

dehydrated, and then cooled in preparation for the following experiment.

- **Energy density calculation**

For the thermochemical heat storage system, the energy density is a crucial indicator to evaluate the performance of the composite salt heat storage, which can be calculated by the following equation. Since the humidity data measured by the temperature and humidity sensor is 0%–100% RH, the water vapor partial pressure $P_v$ in the wet air can be obtained by the following Equation 5.1 [54]:

$$P_v = \varphi P_s \tag{5.1}$$

$P_s$ is the saturated water vapor partial pressure [54], and the absolute humidity $d$ of wet air can be expressed as:

$$d = 0.622 \frac{P_v}{P - P_v} \tag{5.2}$$

The enthalpy $H$ of wet air can be calculated from Equation 5.3 [181]:

$$H=1{,}006t+d(2501+1{,}805t) \tag{5.3}$$

The energy storage density $Q_E$ can be calculated by Equation 5.4 [55]:

$$Q_E = \frac{\int_0^{t_d} \rho_f q_v (H_{exit} - H_{inlet})\, dt}{M} \tag{5.4}$$

$\rho_f$ is the density of the dry air, $q_v$ is the volume flow rate of the gas, $M$ is the total mass of the adsorbent material in the reactor, this experiment uses $M$ = 3 kg.

### 5.2.3 3D-printed 1:22.5 house model

A house model with size of 1：22.5 equivalently scaled down (300 mm×400 mm×300 mm) was printed by a foundry sand 3D printer (KOCEL AJS 2500A) in this study. Using powder materials (quartz sand, ceramist sand, etc.) materials, the thermal conductivity of the walls and roof can approach that of an actual house. Fig. 5.8 shows the construction process of the house model. The house drawing was generated by Revit software, which was then fed into the 3D printer. As work proceeds, the first layer of fine sand was premixed with the binder and distributed over the build platform surface. Adhesive was then sprayed over the area of the build platform for each slice (cross-

section) of the model to be printed. Additional areas were covered by loose sand and compacted by a coater. After completing a layer of plane, the platform moved vertically by a set distance (layer thickness). The above printing process was repeated until all slices of the house model were completely printed.

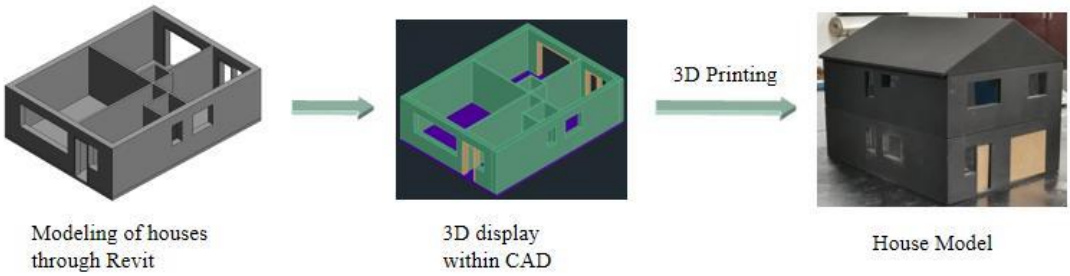


Fig. 5.8 The construction process of the 1:22.5 house model using 3D printing.

Fig. 5.9 shows the first (Fig. 5.9.a) and second floor (Fig. 5.9.b) plans of the 3D printed house. Each room was numbered for ease of follow-up research. The first number represents the floor, the second number corresponds to the room number in each floor, and the letters "a" and "b" are used to distinguish the different locations of the thermohydrometer probe testing in the same room (at the floor and at the ceiling, respectively), for example, room 12b represents the location of the thermohydrometer probe at the ceiling in the second room on the first floor.


a. First floor b. Second floor

Fig. 5.9 Photo of the different floors in the 1:22.5 house model.

Insulation cotton was pasted on the outer surface of the house, as shown in Fig. 5.10, to reduce the heat release to the ambient.

Fig. 5.10 3D printed house model with insulation cotton.

### 5.2.4 Seasonal solar energy storage house heating system

The current work aimed to experimentally investigated a seasonal heat storage unit for space heating, the working principle is shown in Fig. 5.11. When it is expected to be used in practice, the solar collector can be used for charging. It is also possible to use nighttime electric energy as the management of the power consumption side, which makes the power consumption more balanced and achieves the effect of shaving peaks and filling valleys. Space heating is achieved based on the temperature of the reusable outlet air. For discharge mode, the reactor releases all heat of adsorption to heat the gas stream, and space heating is achieved by the hot gas stream.

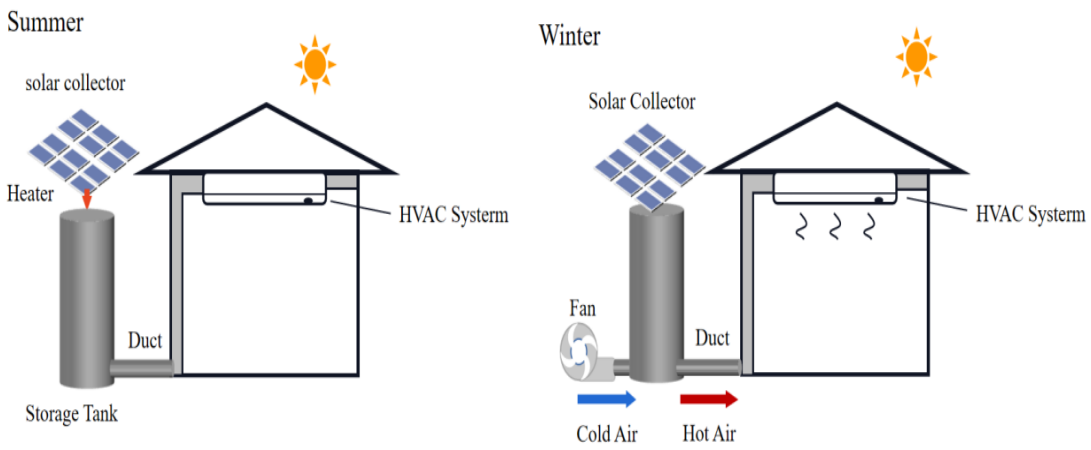


a. Summer: dehydration using solar b. Winter: Hydration providing heat

Fig. 5.11 Schematic of the open STES system functioning

Fig. 5.12 shows a schematic diagram of the entire setup integrating the scaled house and the adsorption pipeline system. 3 kg of LiCl/LiBr-zeolite composite adsorbent was filled the reactor. To make the material reaction more uniform and complete, the air flow was forced following radial direction of the reactor made by two layers of mesh tubes.

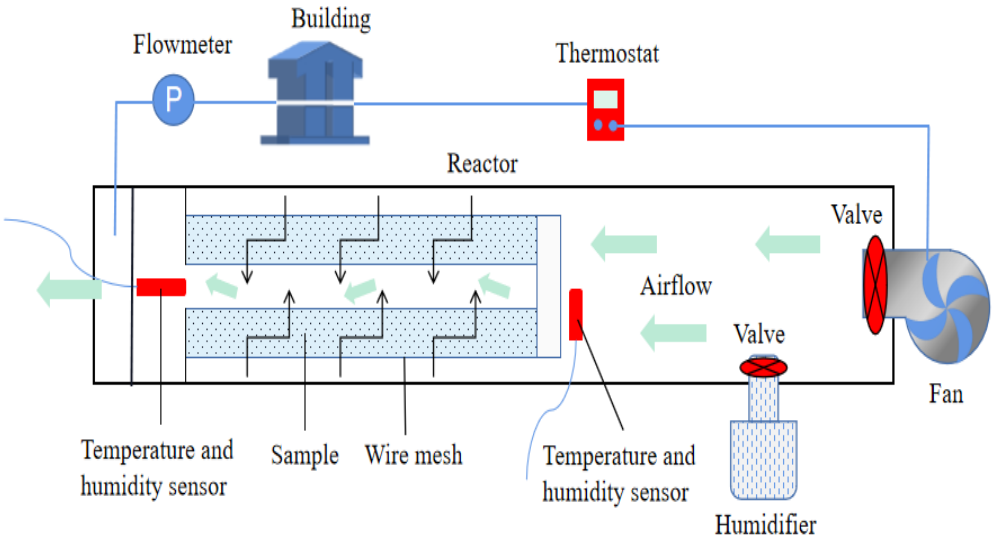


Fig. 5.12 Entire setup integrating the scaled house and the adsorption pipeline.

Fig. 5.13 is the photo of the combined house and adsorption pipeline.

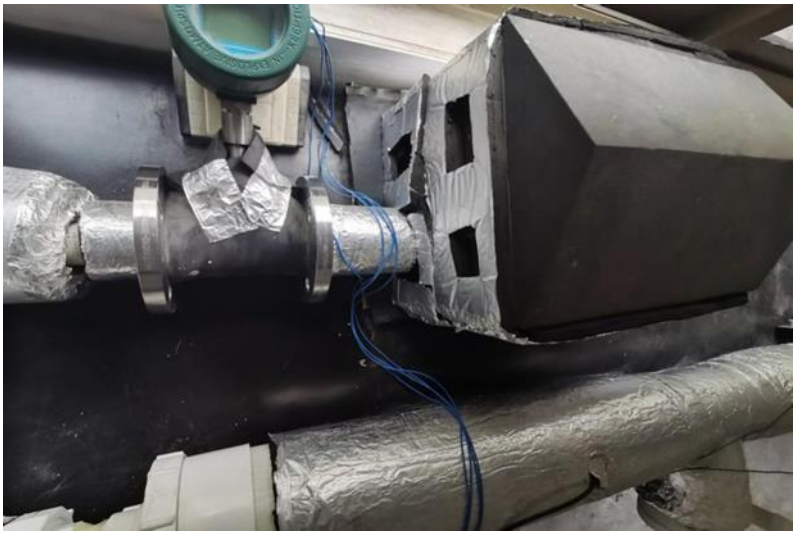

Fig. 5.13 Photo of the combined house with the adsorption pipeline.

The ventilation duct was with the with a diameter of 20 mm, inletting through Room 11a, ground floor. Al foil was used as the insulation of the ventilation duct.

A high temperature thermohydrometer (A-Pt100) was used for measuring temperature and humidity (with an accuracy of ±0.3°C and ±0.1% RH) of the inlet and outlet air. An adjustable industrial humidifier is used to increase the relative humidity (70-90%) of the inlet air. The air flow at the outlet of adsorption reactor was measured by a flow meter (HSTL-FY01). Since the experimental test rig was located in a natural space, the flow rate and temperature and humidity of air were checked every 30 minutes, and the fan and humidifier were fine-tuned accordingly in order to control the air flow and relative humidity more accurately.

Pt100 temperature sensor was placed inside each room of the house model to record temperature changes. To reduce heat loss in the experiment, both the pipes and the house were insulated. The fan was on/off controlled by using a temperature controller based on the temperature in room 11a. The power supply to the fan was cut-off once the room temperature reached the set point. According to the EU heating (ref) requirements, the indoor temperature range was set at 19℃-25 ℃. When the temperature exceeded 25°C, the fan is powered off, and the doors and windows were closed to reduce heat loss. When the room temperature was lower than 19℃, the fan started again.

It is worth noting that the material reacted immediately in contact with moist air.

Therefore, the moist air flow rate and relative humidity of the air passed into the pipeline were brought to the desired experimental conditions before the reactor containing the composite adsorbent was loaded into the pipeline.

This experiment investigated the effect of air flow rate and relative humidity on the performance of the heat release by adsorption. Orthogonal experiments were set up with air flow rates of 5 $m^3$/h, 10 $m^3$/h, and 15 $m^3$/h and relative humidity of 70%, 80%, and 90%. After heat release, the used adsorbent material was fully desorbed at 200 °C by using an oven.

Considering the requirement for precise control in this study, the flow rate and humidity of the air in the pipeline were observed every 30 minutes.

Based on the air temperature and humidity sensor, the instantaneous water uptake $x_t$ , total water uptake $x_{total}$, the dimensionless adsorption rate $X$, and the adsorption heat were calculated and used to evaluate the heating performance of the reactor. The equations used are given as follows [31]:

$$x_t = \int_0^t q_m \left( d_i - d_o \right) dt \tag{5.5}$$

$$x_{total} = \int_0^{t_{total}} q_m \left( d_i - d_o \right) dt \tag{5.6}$$

$$X = x_t / x_{total} \tag{5.7}$$

$$Q = \int_0^{t_{total}} q_m C_p \left( T_o - T_i \right) dt \tag{5.8}$$

Among them, $t$ and $t_{\text{total}}$ represent the instantaneous time and the total reaction time, respectively, $\varphi_{\text{i}}$ and $\varphi_0$ represent the absolute humidity of the inlet and outlet air, respectively, and $q_m$ is the mass flow rate of the air. $T_{\text{i}}$ and $T_{\text{o}}$ represent the temperature of the inlet and outlet air, respectively, and $C_p$ represents the specific heat of air.

To further evaluate the thermal performance of the room, the temperature rise $\Delta T$, the effective time $t$ and the thermal comfort rate $FTC$ are selected as evaluation indicators [32]. The larger the temperature rise, the longer the effective reaction time and the better the thermal performance of the room. The formula for calculating thermal comfort rate $FTC$ is as follows [32]:

$$FTC = \frac{P - \tau_D}{P} \qquad 5.9$$

$\tau_D$ is the time when the indoor temperature is within the uncomfortable range of the human body, and $P$ is a given time. According to the EU requirements, the design temperature range for heating in winter is 19-25°C.

## 5.3 Results and discussion

### 5.3.1 Adsorption in a tube reactor

For each of the four relative humidity levels, Fig. 5.14 illustrates the impact of various air flow rates on the exit air temperature. All the temperature differential variations initially climb rapidly and then slowly decline until the temperature rise becomes close to zero. The final temperature increase reduces to zero at the point of which the adsorbent is saturated, the stored heat is completely released, and the reaction is over. The rate of temperature rise increases with increasing air flow rate, with the recorded temperature rise rate at a flow rate of 5 $m^3$/h noticeably lower than the other measured flow rates. Since the air flow rate affects the rate of moisture transfer and the low air flow rate limits the process of mass and heat transfer between the wet air and the adsorbent [56]. However, the effective reaction time of the material becomes shorter at low flow rate conditions. The reaction time decreases consistently with increasing flow rate under conditions of 60% RH. The adsorbent still tends to have a shorter reaction time at high flow rates when the air has an RH of 70% or below, however, as the relative humidity rises, this difference becomes less noticeable at flow rates of 10 $m^3$/h, 15 $m^3$/h, and 20 $m^3$/h.

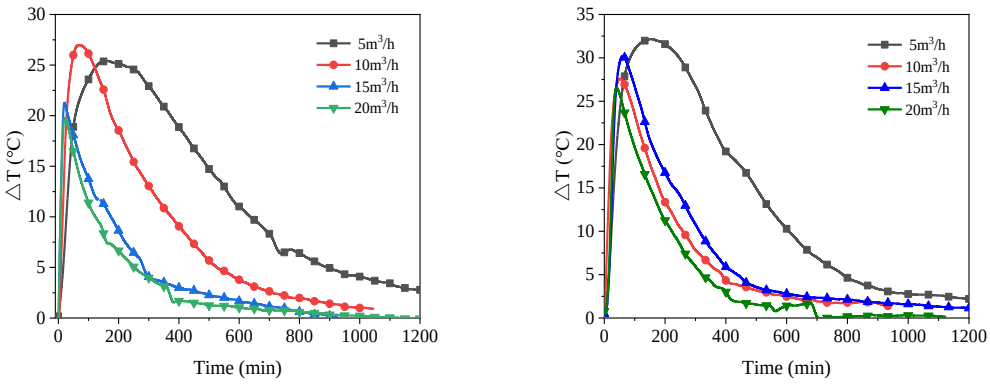

a. 60%RH

b. 70%RH

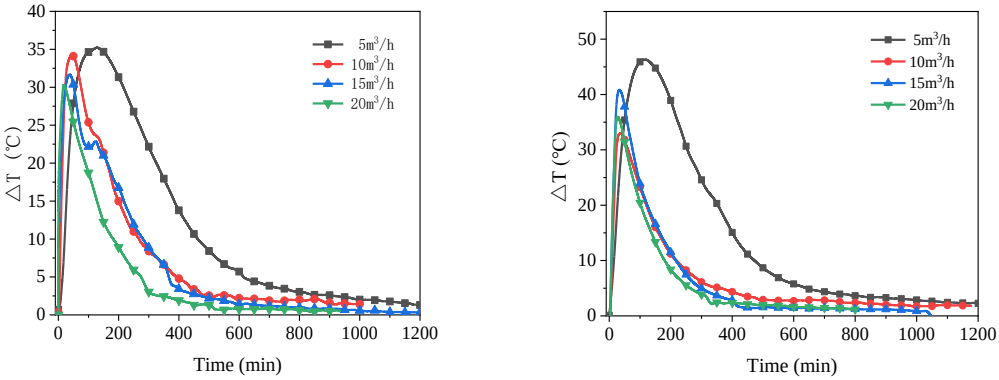


c. 80%RH

d. 90%RH

Fig. 5.14 Air temperature rises with time for different air flow rates at four air relative humidity.

As the results from Fig. 5.15, the maximum temperature difference increases as the relative humidity increases. The air temperature increased by 84.1%, 28.1%, 93.3%, and 79.8%, respectively, when the relative humidity was elevated from 60% to 90%. Similarly, when more humid air flowed through the reaction pipeline, the rate of temperature rise of the air at the initial stage was higher. This behaviour was especially noticeable at a flow rate of 5 $m^3$ /h. This is because high relative humidity of wet air provides more water to the adsorbent, which accelerates the hydration reaction of the material driving the heat generation. This causes the increase in temperature rise value and rate.

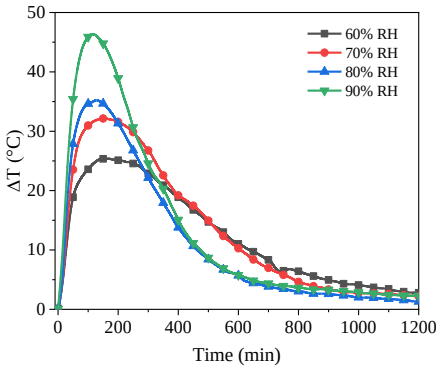


a. 5 $m^3/h$

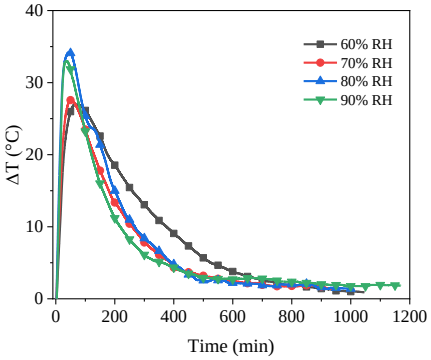


b. 10 $m^3/h$

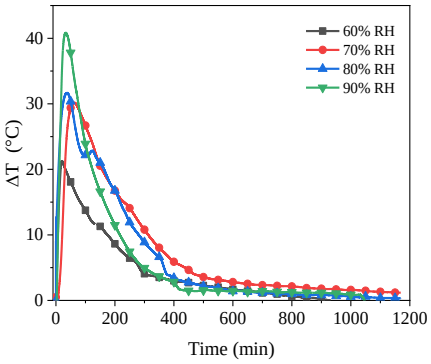


c. 15 $m^3/h$

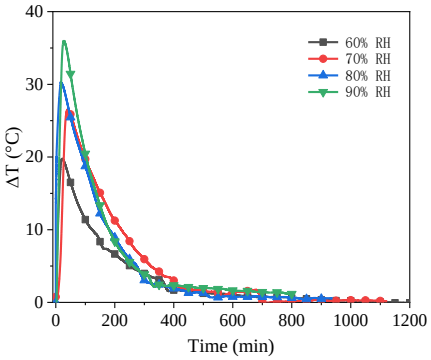


d. 20 $m^3/h$

Fig. 5.15 Air temperature rises with time for different air relative humidity at four air flow rates.

For each group of experiments, the energy storage density was calculated and plotted in Fig. 5.16. It can be seen from the experimental results that the maximum temperature difference and the temperature rise rate have a positive correlation trend with the gas flow rate and relative humidity. However, energy storage density does not have such a law. From the formula, it shows that the energy storage density is not only related to the maximum temperature difference, but also to the effective reaction time. In addition, it cannot be ignored that in the same room temperature environment, the heat loss under different experimental conditions is different. The higher the flow rate, the more heat is lost through the pipe, metal reactor. In this experiment, the composite material has the highest heat release value of 434.4 J/g when the gas flow rate is 15 $m^3/h$ and the relative humidity is 70%, and its energy discharge efficiency is 74.3%. The heat storage density measured by DSC is relative larger than that measured in this section. The

composite sample tested in DSC is under the full adsorption condition (25 °C and 60% RH), and 300 °C is high enough to desorb all water. The test in this section using air with different volume flow rates under the given adsorption time is not enough to enable the full adsorption of the composite. Moreover, the integrated TGA-DSC has a more precise operation environment, compared to the inevitable thermal runaway in the tube reactor. It also decreases the air increase temperature and results in the reduction of the energy density.

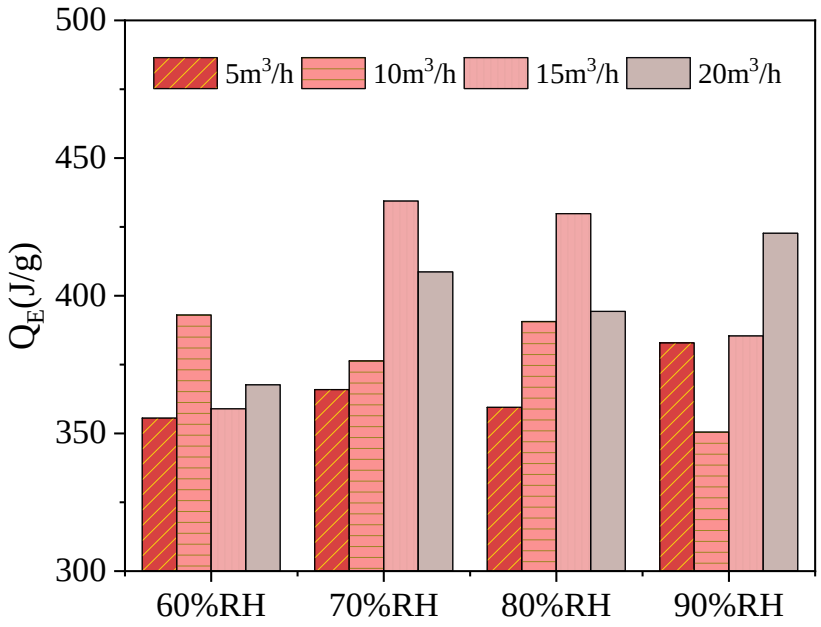


Fig. 5.16 Energy storage density with different experimental conditions.

To get the cyclic performance, the adsorbent material was subjected to ten cycles of adsorption/desorption under experimental conditions with an air flow rate of 15 m$^3$/h and a relative humidity of 70%. Fig. 5.17 shows the variation of the outlet temperature with time. The rate of temperature increase decreases with the number of cycles.

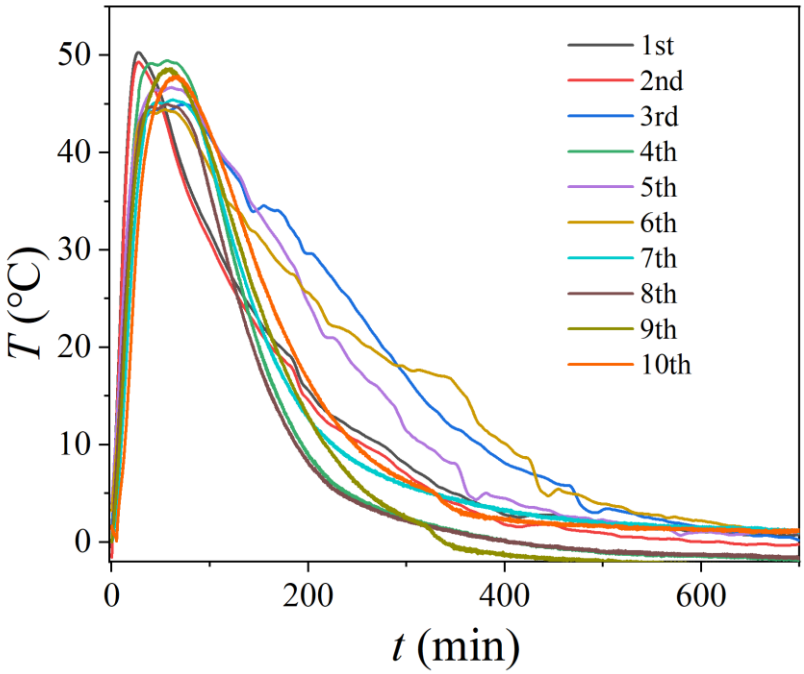


Fig. 5.17Air temperature rises with time for cyclic experiments.

Fig. 5.18 shows the variation of the energy storage density for the ten cycling experiments, and although they decreased significantly in the first three trials, the decrease slowed down in the subsequent studies, with a final rate of change of only 0.17%. This indicates that while certain microstructure changes do occur in the composite adsorption material during cycling, these changes become smaller and smaller as the number of cycles increases. Cycling experiments show that this material can be recycled for a long time in cross-season heat storage.

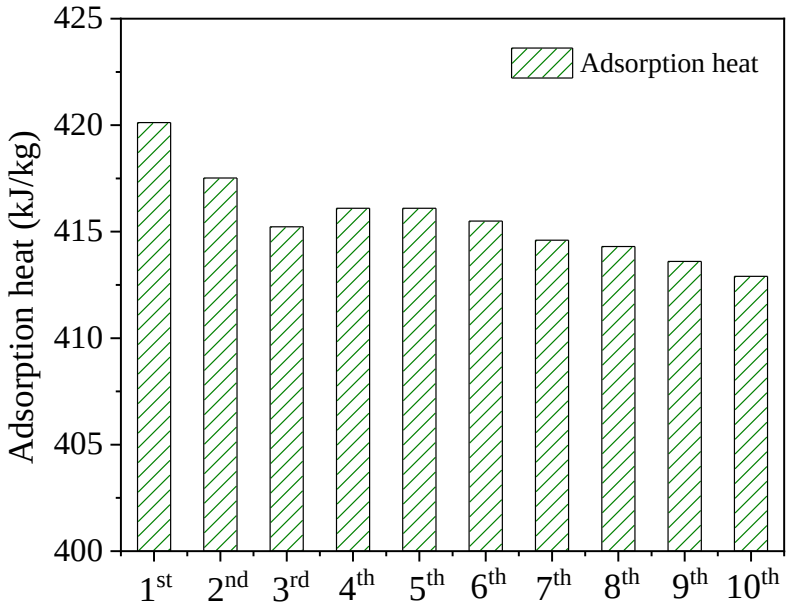


Fig. 5.18 Energy storage density for cyclic experiments.

### 5.3.2 Space heating in 1:22.5 house model

Fig. 5.19 shows the experimental results of adsorption process with inlet air at 10 °C, 70% relative humidity and flow rate of 15 $m^3$/h. Changes in relative humidity ($\varphi_i$, $\varphi_0$, $\Delta\varphi$) and changes in temperature ($T_i$, $T_0$, $\Delta T$) at the inlet and outlet of the reaction tube are shown. The water content of the inlet air was maintained at 10.2 g/kg (corresponding to a relative humidity $\varphi_i$ of approximately 70%), as shown in Fig. 5.19.a. The outlet air is very dry at the beginning of the reaction. As the adsorption reaction progressing, the relative humidity of the outlet air increased and was close to that of the inlet air after 800 min.

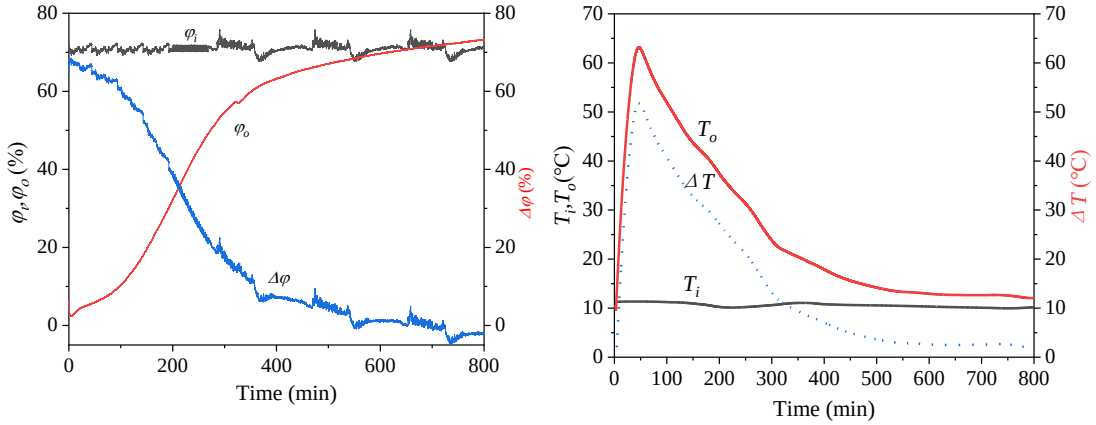


a. Relative humidity b. Air temperature

Fig. 5.19 Sorption performance of the reactor with inlet air at 10 °C, 70% RH, $q_v$ = 15 $m^3$/h.

As shown in Fig. 5.19.b, the outlet air temperature is rapidly heated to 60.4 °C within 50 min due to large amount of adsorption heat released by water adsorption. After reaching the peak temperature, $\Delta T$ started to decrease, and the temperature of the inlet and outlet air also approached after 800 min, indicating the completion of the adsorption.

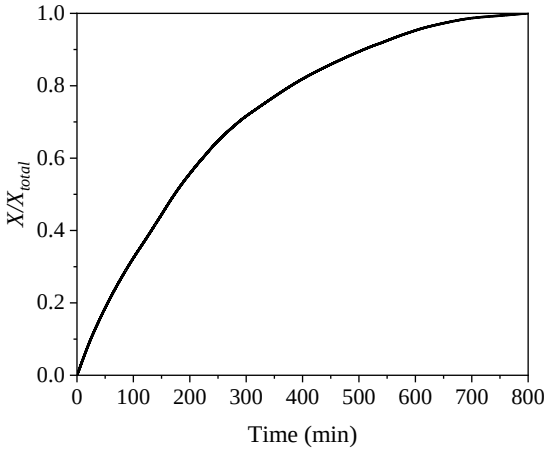


Fig. 5.20 Adsorption rate under the condition of 70% RH, $q_v$ = 15 m$^3$/h.

Further, under this operating condition, Fig. 5.20 shows the adsorption rate as a function of time. When moist air flows through the reactor, the composite adsorbent undergoes rapid physical adsorption (by zeolite) and hydration reactions (by salt). In the initial stage of adsorption, the amount of water uptake increases significantly; due to the time-dependent feature of adsorption kinetics, the adsorption rate decreases with the progress of the reaction.

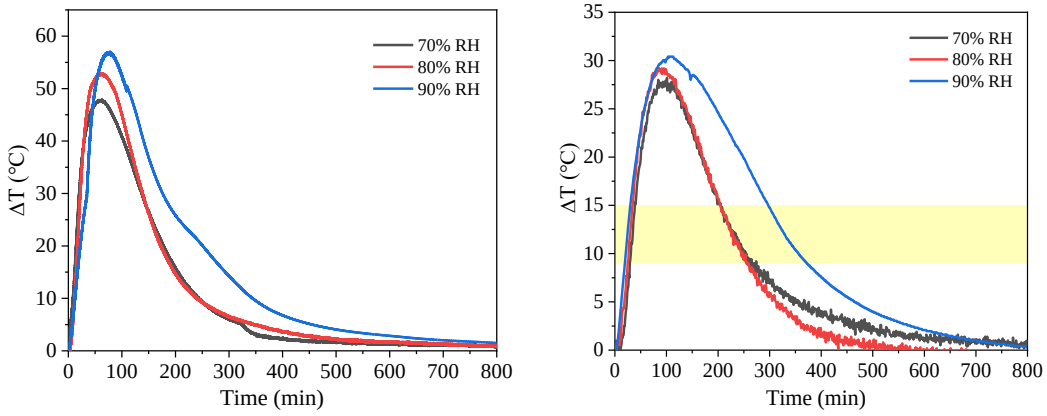


a. air passing through reactor b. room 11a

Fig. 5.21Temperature lift results with 60% RH, 70% RH and 80% RH and flow rate of 5 m$^3$/h.

The relative humidity of the air affects the heat release performance of the composite adsorbent. The adsorption performance of the reactor was studied at room temperature, $q_v$ =5 $m^3$/h, and relative humidity of 70%, 80% and 90%. Fig. 5.21.a shows the changes of temperature lift of air by using different inlet relative humidity of air. Moist air with high relative humidity provides higher pressure difference which drives the adsorption, accelerating the hydration reaction that the heat generation. It can be seen from the figure that the temperature lift increases with the increase of relative humidity. As shown in Fig. 5.21.a, when the relative humidity is 90%, the total heat released by adsorption process reaches 480.92 kJ/kg, which is 33.56% and 26.4% higher than 70% and 80%, respectively.

Fig. 5.21.b shows the temperature change of the room 11a. The overall trend is like that of Fig. 5.21.a, it still maintains the law that the higher the relative humidity, the larger the temperature lift. For space heating, it is necessary to consider the comfort range of the environment. The yellow area in Fig. 5.21.b is in the range of 9°C-15°C, which represents the comfort zone.

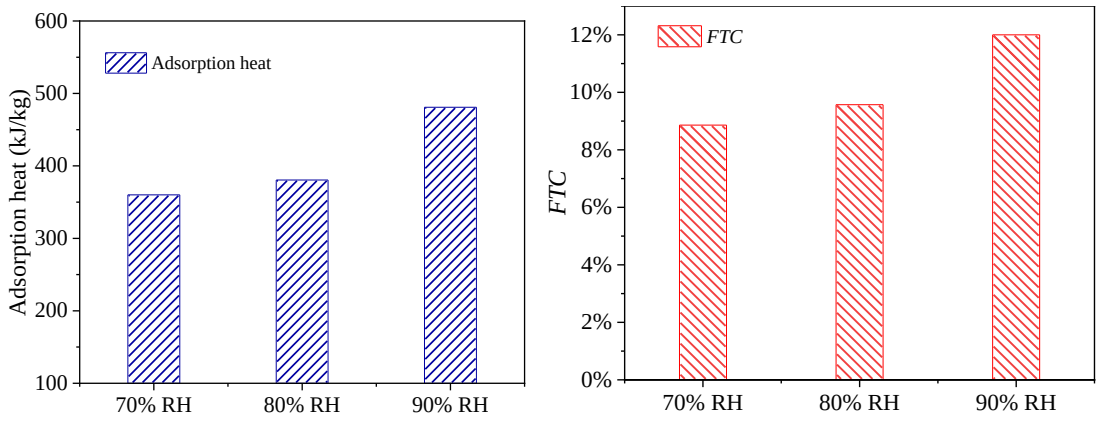


a. adsorption heat b. FTC

Fig. 5.22 The comparison of the adsorption heat and FTC for the room 11a, with 60% RH, 70% RH and 80% RH and flow rate of 5 $m^3$/h.

The effectiveness of heat release for space heating was evaluated by calculating the thermal comfort rate, as plotted in Fig. 5.22.b. The results show that under the experimental conditions, when the humidity is 90%, the thermal comfort rate *FTC* is

up to 12%.

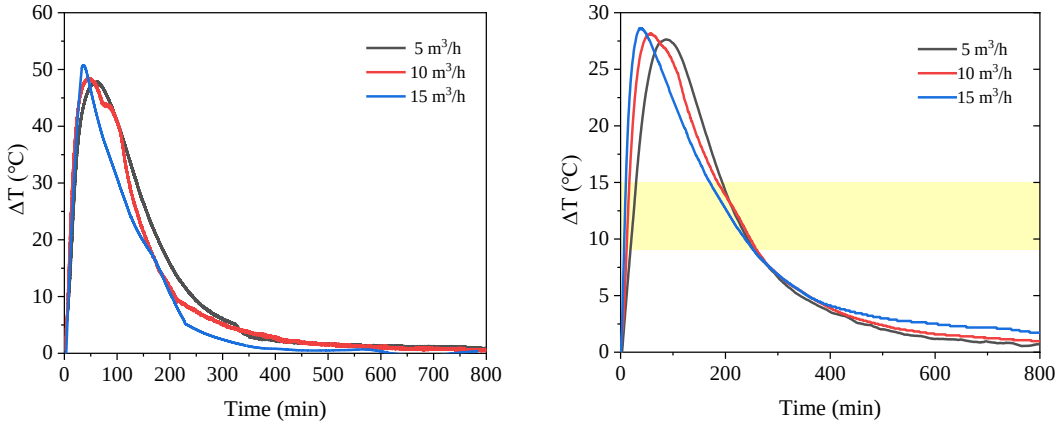


a. air passing through reactor b. room 11a

Fig. 5.23 Temperature lift of the air and room 11a with 70% RH and flow rates of 5 $m^3$/h, 10 $m^3$/h and 15 $m^3$/h.

Air flow rate is another important parameter that affects output temperature and adsorption heat release. In this experiment, the effect of four different air flow rates of 5 $m^3$/h, 10 $m^3$/h and 15 $m^3$/h on the adsorption performance was investigated at room temperature, and 70% relative humidity. Fig. 5.23.a shows the temperature lift of air at different flow rate. The increase of air flow rate leads to the increase of mass and heat transfer between moist air and adsorbent, thus increases the adsorption rate and the temperature lift of the air, correspondingly the effective reaction time is shortened.

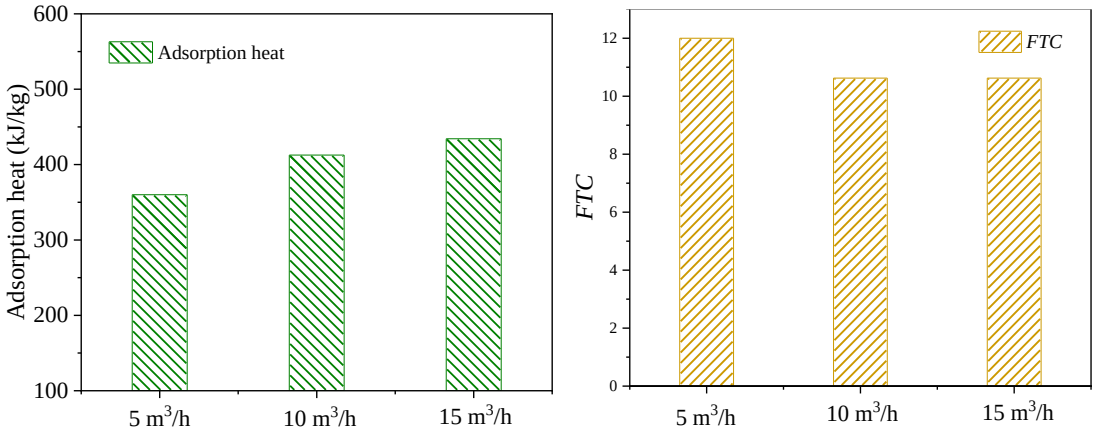


(a) (b)

Fig. 5.24 The comparison of (a) total adsorbed heat for the reactor and (b) FTC for the room 11a under 5 $m^3$/h, 10 $m^3$/h and 15 $m^3$/h at 70% RH.

Nevertheless, the effects are less apparent comparing to using different relative humidity. Fig. 5.24.a shows that the total adsorption heat increases with the increase of the flow rate. The main reason is that the gas with a large flow rate provides more water per unit time, while the reaction time is reduced, and the heat loss caused by other factors is correspondingly reduced. The overall trend of the room 11a is similar to that of the air passing through reactor. With the increase of the air flow rate, the temperature lift becomes larger. The flow rate of 15 m/s leads to the highest temperature lift, however, it decreases faster than the other two flow rate. Fig. 13(b) shows a maximum *FTC* of 12% at 5 $m^3$/h.

### 5.3.3 Heating in different rooms

Taking the experimental conditions of air flow rate of 15 $m^3$/h and relative humidity of 70% as an example, the temperature lift of each room after hot air is introduced into the house model is shown in Fig. 5.25. The heating of the room by the hot air is delayed with the path distance, and the temperature lift peak is also affected by it. The room 11a, which is directly connected to the pipeline outlet, is the first to be heated up and has the greatest temperature rise. In contrast, the room 23a which is furthest from the hot air inlet began to heat up after 26 minutes, and the temperature lift is 56.9% lower than that of the first room. They all returned to room temperature after 800 min, indicating that there was heat loss in the process of hot air passing through each room, but the effective time for which they are heated followed the reaction time of the material. In addition. It is found that the temperature rise curve of 12b is higher than that of 12a (rooms 12a and 12b represent the bottom and top of the second room on the first floor, respectively), indicating that the hot air is easy to flow upward. Through the above analysis, we can consider that in the actual house construction, each room should be set with hot air openings to reduce the heat loss on the path, and the openings should be set in the lower part of the room to improve air circulation.

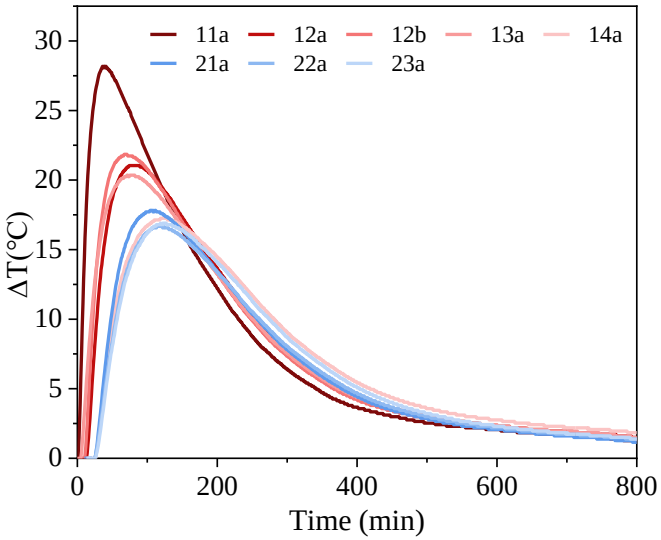


Fig. 5.25 The temperature lift at each room test point varies at flow rate of 15 $m^3$/h, relative humidity of 70% RH.

As a summary, it can be found that the effective utilization rate of heat released by adsorption process to the space heating is not high without suitable controlling. For such reason, a temperature sensor was replaced inside the room 11a with a temperature controller to simulate the actual heating control of the house in winter.

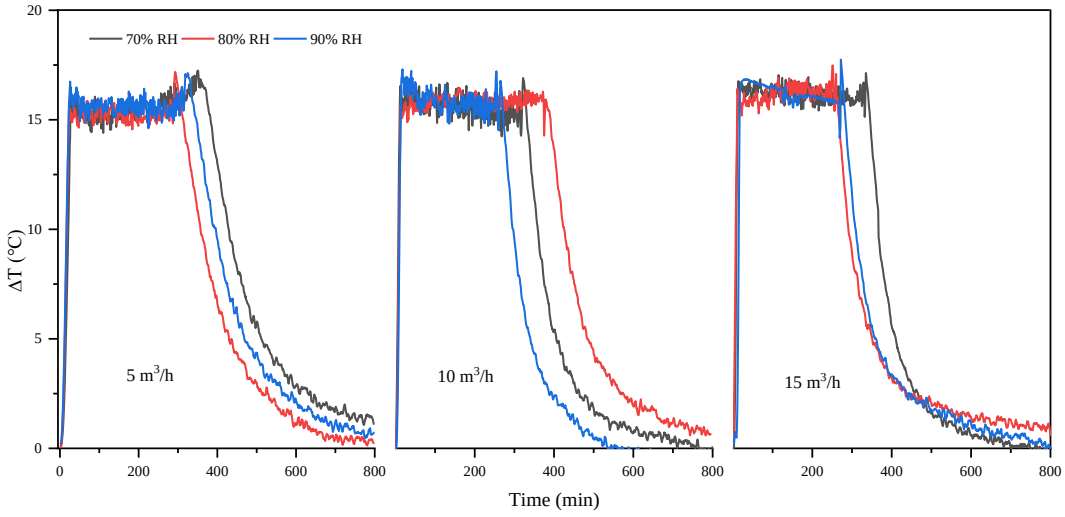


Fig. 5.26 The air temperature lift in room 11a with temperature controller under different air flow rates and relative humidities.

Fig. 5.26 shows the temperature rise of room 11a under different experimental conditions. At the initial stage of the adsorption reaction, the temperature lift increases linearly to about 18°C, and then fluctuates between 12 °C and 18 °C, which leads to a

room temperature of 19-25 °C. The room temperature is then effectively controlled by the temperature controller, and the heat release from adsorption process is reasonably used for space heating, which reflects on the temperature change fluctuations among the platform at approximately 15-16 °C. From the figure, the continuous performance of the adsorption reaction heat supply under different experimental conditions can be visually compared. After this temperature plateau period, the temperature begins to drop, indicating the reaction of the material is progressing to completion. In particular, when the air flow rate is 15$m^3$/h and the air relative humidity is 90%, the initial temperature rise peaks corresponding to the three different flow rates are all larger than the temperature rise peaks when the relative humidity is 70% and 80%. It reveals that under the high relative humidity and inlet air volume flow rate could accelerate the adsorption reaction, as the first process of temperature rapidly increases to lead the curve almost perpendicular to the x-axis. Moreover, more water is adsorbed by the sorbent, and more heat is released to the air to heat the room, at the start. However, when the relative humidity is 90%, the effective reaction time is not the longest, indicating that under this experimental condition, the material reacts too fast, and the continuous heating effect is poor. Fig. 5.26 can intuitively see the length of the temperature plateau period, which represents the heating capability of the material reaction.

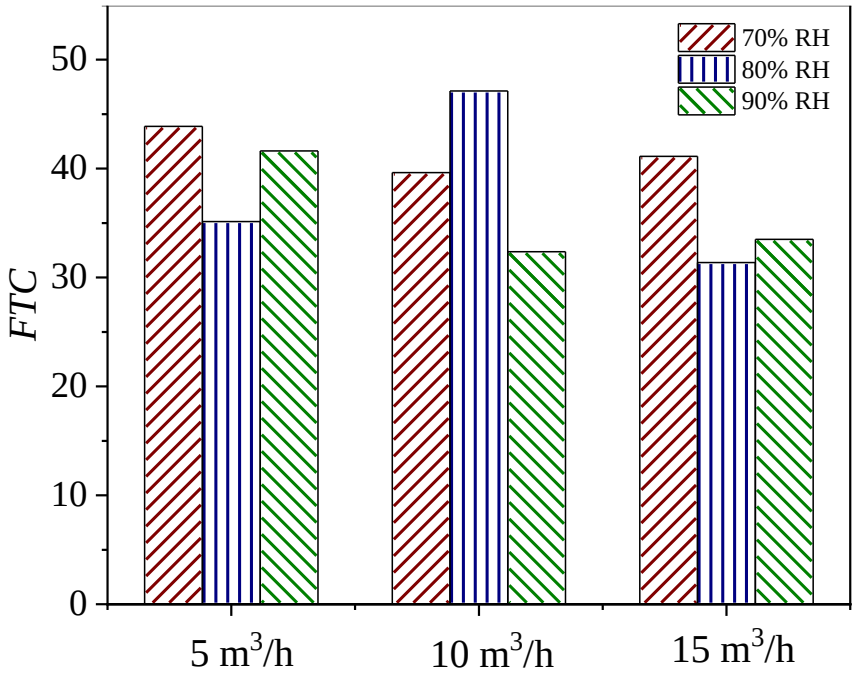


Fig. 5.27 The comparison of FTC for the room 11a controlled by the temperature controller under different air flow rate and relative humidity conditions.

The comfort rate of room 11a under each condition is calculated and plotted in Fig. 5.27. Room 11a has the highest FTC of 47.13% when the air flow rate is 10 $m^3$/h and the relative humidity is 80%. The lowest FTC occurs at a flow rate of 15 $m^3$/h and relative humidity of 90%, which is 31.32% lower than the highest. It should be mentioned that the FTC can be significantly improved by using another batch of adsorption material/reactor once the temperature plateau is finished.

### 5.4 Conclusion

In this chapter, a LiCl/LiBr–zeolite composite adsorbent was developed. Subsequently, it was applied to a lab-scale reaction unit for experimental study. To further evaluate the actual effect of TCHS system applied to the house. The main conclusions are as follows:

- The different salt concentrations resulted in different adsorption capacities and thermal storage properties. Under the same experimental conditions, sample Z15 shows the best composite adsorbent.
- In the pipeline-level adsorption heat storage experiments, the temperature rise rate at the outlet of the pipeline is influenced by the flow rate and humidity of the gas passing through. The studied composite adsorbent exhibited its highest heat release of 434.4 J/g at a gas flow rate of 15 $m^3$/h and an RH value of 70%, achieving an energy discharge efficiency value of 74.3%.
- The decrease in temperature and heat release at the pipe outlet showed a slowing down trend with the number of cycling experiments, and the composite adsorbent has good periodicity and stability.
- The outlet relative humidity and air temperature reflects that the fastest adsorption at the begin and the decreased adsorption rate along with the time evolution, similar to the pipe-line adsorption experiment.
- The increased temperature by adsorption-heating inclines with the relative humidity increment. When the relative humidity is 90%, the total heat released by adsorption process reaches the maximum of 480.92 kJ/kg, which is 33.56% and 26.4% higher than 70% RH and 80% RH, respectively. The corresponding thermal

comfort rate *FTC* is up to 12%.

- The higher air flow rate could also increase the adsorption-heating effect, as the peak temperature lift positively grows due to the enhanced heat and mass transfer. The flow rate of 15 $m^3$/s leads to the highest temperature lift with a maximum FTC of 12% at 5 $m^3$/h.

- A temperature controller is required to achieve an effectively controlled room temperature and reasonably released adsorption heat for space heating. Room 11a has the highest FTC of 47.13% when the air flow rate is 10 $m^3$/h and the relative humidity is 80%. FTC can be significantly improved by using extra batch of adsorption material/reactor.

# Chapter 6. Simulation of thermochemical house heating

## 6.1 Introduction

The adsorption technology is integrated with the space heating system for the house application. The novel adsorption-integrated space heating system could store the solar energy in the warm days and transfer it into thermal energy to provide heating effect to the users, even across several seasons. This chapter simulates the novel adsorption-integrated seasonal solar energy storage space heating system by the software of TRNSYS to evaluate the space heating and the storage performance of the innovative technology. A simplified pre-simulation of using TRNSYS to model another space heating model is recorded in Appendix. C for interest.

The simulation software is TRNSYS (Transient System Simulation Program), which was first developed by the University of Wisconsin-Madison in United States of America. It is a professional simulation software for solar energy systems separating the whole system into several sub-projects. Each sub-project is independent for a certain module, such as the solar concentration or the pump. According to the technological processes of the system, different sub-modules could be integrated in order and function as it should be in the practical operation. Moreover, this software highly presents flexibility, as the users could utilize their self-developed modules with the open TRNSYS source code provided.

## 6.2 House model

The thermochemical house heating using solar energy was simulated as located in either Newcastle (at the North-east of United Kingdom) or Urumqi (at the North-west of People's Republic of China) as separately depicted in Fig. 6.1. The novel adsorption-heating integrated technology would be employed in the houses located in these typical areas.


a. Newcastle upon Tyne, UK b. Urumqi, China

Fig. 6.1 The location of Newcastle and Urumqi.

Fig. 6.2 presents the single house researched in this chapter as in both areas the same house geometry was used. The house separately stands without any attached architectures. It owns two floors and one garret with a triangle shape roof.

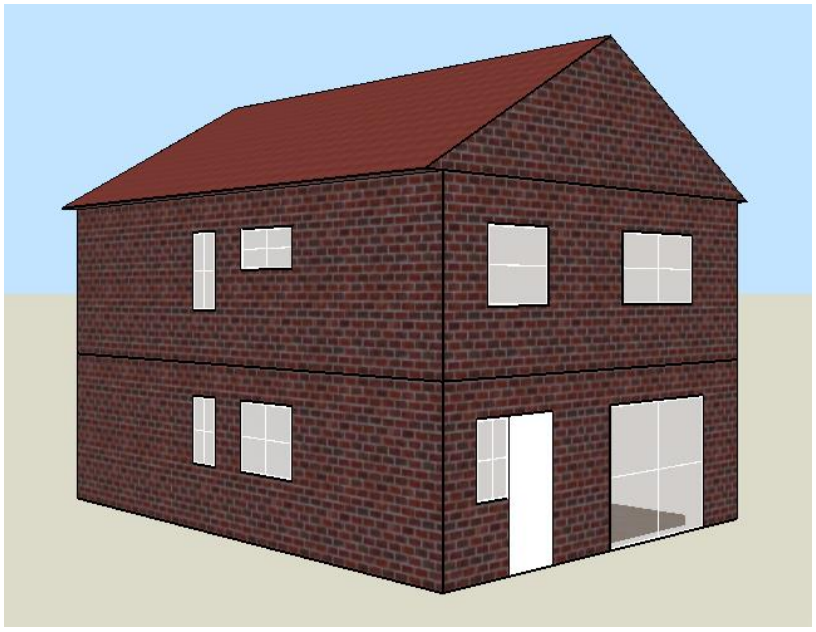

Fig. 6.2 Schematic diagram of the researched house.

Fig. 6.3 is the configuration of the first-floor layout, while Fig. 6.4 is the second-floor layout. The composition of the attic was ignored as this part normally served as a storage space without temperature requirement.

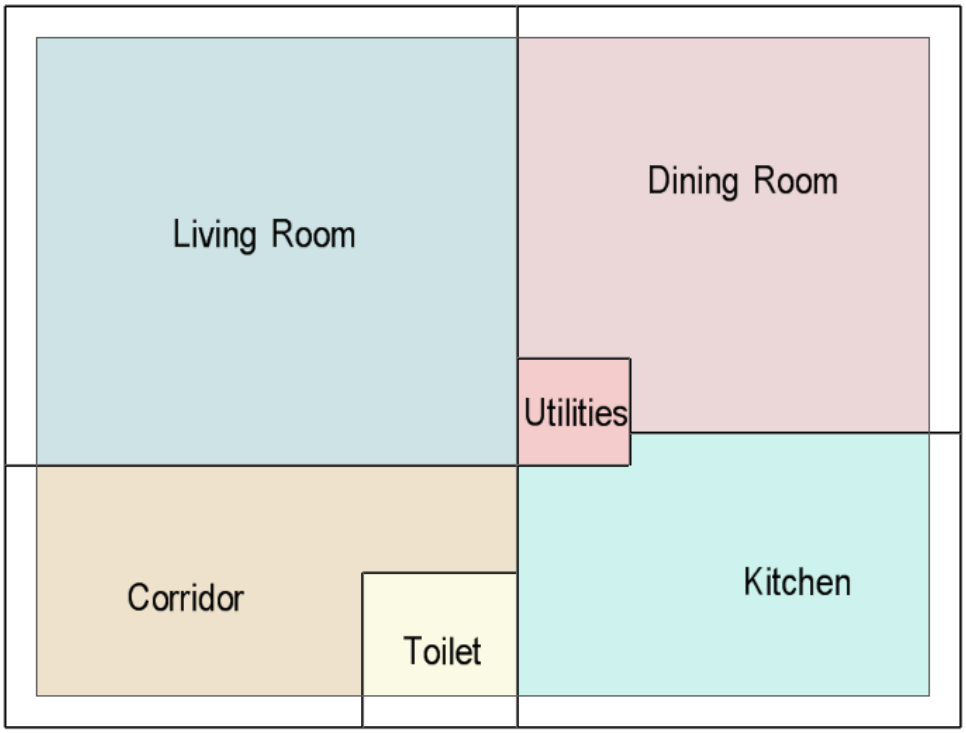


Fig. 6.3 The layout of the first floor.

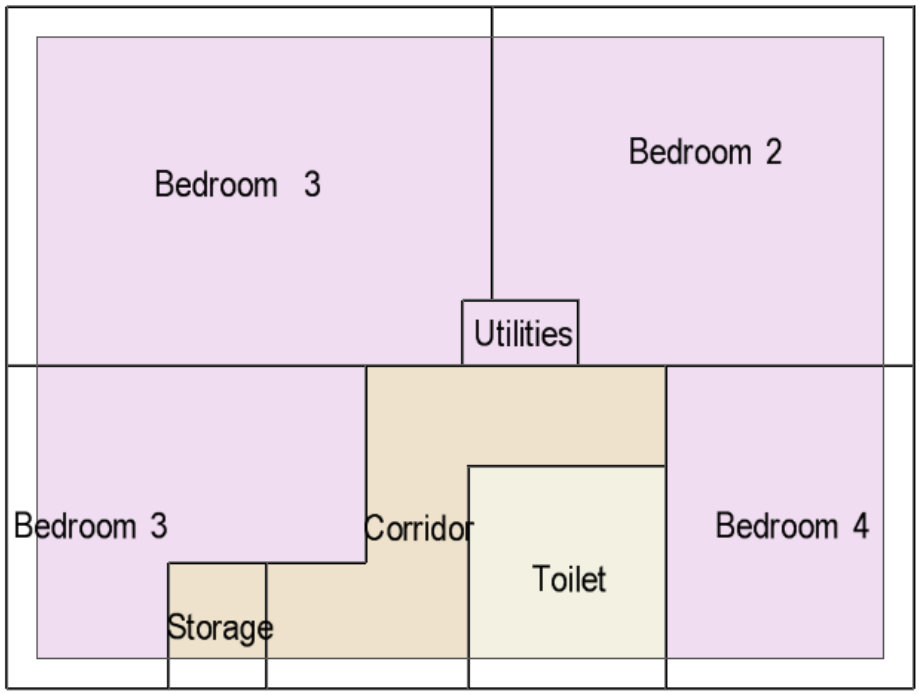


Fig. 6.4 Configuration of the second floor.

The specification of the house layout is listed in Tab. 6.1. The property has overall dimensions of 6.75 m × 8.95 m, and the building area of the house is approximately 120.80 m2. The usable floor area of the Conventional House is calculated to be 90 m2. Both the ground floor and the first floor have a storey height of 2.55 m. The external walls have a thickness of 300 mm, while the internal walls are 100 mm thick.

Tab. 6.1 Specification table of the house layout.

| Floor | Room | Area/$m^2$ | Volume/$m^3$ | Heating |
|---|---|---|---|---|
| 1st | Living | 17.78 | 40.00 | Y |
| | Corridor | 8.16 | 18.37 | N |
| | Dining | 13.51 | 30.39 | Y |
| | Kitchen | 9.17 | 20.64 | N |
| | Storage 1 | 1 | 2.25 | N |
| | Toilet 1 | 1.74 | 3.91 | N |
| 2nd | Bedroom 1 | 14.44 | 33.2 | Y |
| | Bedroom 2 | 11.96 | 27.52 | Y |
| | Bedroom 3 | 7.49 | 17.22 | Y |
| | Bedroom 4 | 6.24 | 14.34 | Y |
| | Toilet 2 | 4.08 | 9.39 | Y |
| | Corridor | 5.49 | 12.63 | N |
| | Storage 2 | 0.92 | 2.11 | N |
| | Storage 3 | 0.74 | 1.7 | N |
| Roof | Storage 4 | 56.36 | 59.77 | N |

## 6.3 Simulation parameters

Without specific clarification, the parameters are designed within the general condition or calculation to achieve the required heating demand.

### 6.3.1 Thermal parameters

Tab. 6.2 Heat transfer properties of the house model in different areas. adapted from[182]

| Location | Outer wall $W/m^2K$ | Roof $W/m^2K$ | House-land thermal resistance $m^2K/W$ | Window heat transfer coefficient $W/m^2K$ | Window solar heat gain coefficient |
|---|---|---|---|---|---|
| Urumqi | 0.3 | 0.2 | 4 | 1.4 | 0.59 |
| Newcastle | 0.54 | 2.693 | 4 | 2.21 | 0.59 |

The heat transfer properties are listed in Tab. 6.2. The vacuum tube air solar collector

has been set with the parameters presented in Tab. 6.3. It should be noted that the mounting angle of the collector in Newcastle is 65°, while the direction of the device is towards the South. The mounting angle of the collector in Urumqi is 54° and towards the South as well. The mounting angle was determined by their geometric information of the latitude, to enable a maximum solar radiation exposure.

Tab. 6.3 The thermal parameters of the vacuum tube air solar collector. adapted from[172]

| Transient efficient intercept | First order heat loss coefficient $W/m^2k$ | Second order heat loss coefficient $W/m^2k^2$ | Collector area $m^2$ |
|---|---|---|---|
| 0.7 | 2.0 | 0.0083 | 30.96 |

The space heating is required from the first day of the October to the last day in the April in Newcastle, UK, while that is needed from 5th October to 20th April in Urumqi, China. The temperature requirement of the room is listed in Tab. 6.4.

Tab. 6.4 The room temperature requirement in Newcastle and in Urumqi.

| Room | Time | | Require room temperature ℃ |
|---|---|---|---|
| Living | Workday | 20:00~23:00 | 21℃±1℃ |
| | | Other | 16±1℃ |
| | Weekend | 9:00~23:00 | 21℃±1℃ |
| | | Other | 16±1℃ |
| dining | Workday | 20:00~23:00 | 21℃±1℃ |
| | | Other | 16±1℃ |
| | Weekend | 9:00~23:00 | 21℃±1℃ |
| | | Other | 16±1℃ |
| Bedroom | Workday | 20:00-9:00 | 21℃±1℃ |
| | | Other | 16±1℃ |
| | Weekend | 20:00-9:00 | 21℃±1℃ |
| | | Other | 16±1℃ |
| Toilet | Workday | 20:00~23:00 | 21℃±1℃ |
| | | Other | 16±1℃ |
| | Weekend | 9:00~23:00 | 21℃±1℃ |
| | | Other | 16±1℃ |

### 6.3.2 Internal turbulence parameters

The internal conditions including the population density, device power density and illumination power density could interfere with the thermal environment of the building, and the internal disturbance parameters are set as shown in Tab. 6.4.

Tab. 6.5 Internal disturbance parameters used in the house heating modelling, adapted from [172].

| Room | Population density person/$m^2$ | Illumination power density W/$m^2$ | Device power density W/$m^2$ |
|---|---|---|---|
| Bedroom 1 | 0.09 | 5 | 3 |
| Bedroom 2 | 0.13 | 5 | 3 |
| Bedroom 3 | 0.43 | 5 | 3 |
| Bedroom 4 | 0.16 | 5 | 3 |
| Living | 0.17 | 5 | 5 |
| Dining | 0.64 | 5 | — |
| Kitchen | 0.34 | 5 | 12 |
| Toilet 1 | 2 | 5 | — |
| Toilet 2 | 0.88 | 5 | — |
| Corridor | — | 5 | — |
| Storage 1 | — | — | — |
| Storage 2 | — | — | — |
| Storage 3 | — | — | — |
| Storage 4 | — | — | — |

The occupation or function timetable is summarized towards the people (Tab. 6.4), illumination (Tab. 6.5), and the other device (Tab. 6.6).

Tab. 6.6 The occupation or function timetable of the people in house, adapted from [172].

| Room | Time | | | | | | | | | | | |
|---|---|---|---|---|---|---|---|---|---|---|---|---|
| | 1 | 2 | 3 | 4 | 5 | 6 | 7 | 8 | 9 | 10 | 11 | 12 |
| Bedroom | 1 | 1 | 1 | 1 | 1 | 1 | 0.5 | 0.25 | 0 | 0 | 0 | 0 |
| Living | 0 | 0 | 0 | 0 | 0 | 0 | 0 | 0 | 0 | 0 | 0 | 0 |
| Kitchen | 0 | 0 | 0 | 0 | 0 | 0 | 1 | 1 | 1 | 0 | 0 | 0 |
| Dining | 0 | 0 | 0 | 0 | 0 | 0.25 | 1 | 1 | 0.25 | 0 | 0 | 0 |
| Toilet | 0 | 0 | 0 | 0 | 0 | 0.25 | 1 | 1 | 0.25 | 0 | 0 | 0 |
| Corridor | 0 | 0 | 0 | 0 | 0 | 0 | 1 | 1 | 1 | 0 | 0 | 0 |
| Storage | 0 | 0 | 0 | 0 | 0 | 0 | 0 | 0 | 0 | 0 | 0 | 0 |
| Room | Time | | | | | | | | | | | |
| | 13 | 14 | 15 | 16 | 17 | 18 | 19 | 20 | 21 | 22 | 23 | 24 |
| Bedroom | 0 | 0 | 0 | 0 | 0 | 0 | 0 | 0 | 0 | 0.25 | 0.75 | 1 |
| Living | 0 | 0 | 0 | 0.5 | 0.5 | 1 | 1 | 1 | 1 | 0.67 | 0 | 0 |
| Kitchen | 0 | 0 | 0 | 0 | 0 | 0 | 0.2 | 0.2 | 0.2 | 0.2 | 0 | 0 |
| Dining | 0 | 0 | 0 | 0 | 0 | 0.5 | 1 | 1 | 0.3 | 0 | 0 | 0 |
| Toilet | 0 | 0 | 0 | 0 | 0 | 0.5 | 1 | 1 | 0.3 | 0 | 0 | 0 |
| Corridor | 0 | 0 | 0 | 0 | 0 | 0 | 0.2 | 0.2 | 0.2 | 0.2 | 0 | 0 |
| Storage | 0 | 0 | 0 | 0 | 0 | 0 | 0 | 0 | 0 | 0 | 0 | 0 |

Tab. 6.7 The occupation or function timetable of the illumination devices in house, adapted from [172].

| Room | Time | | | | | | | | | | | |
|---|---|---|---|---|---|---|---|---|---|---|---|---|
| | 1 | 2 | 3 | 4 | 5 | 6 | 7 | 8 | 9 | 10 | 11 | 12 |
| Bedroom | 0 | 0 | 0 | 0 | 0 | 0 | 1 | 1 | 1 | 0 | 0 | 0 |
| Living | 0 | 0 | 0 | 0 | 0 | 0 | 0 | 0 | 0 | 0 | 0 | 0 |
| Kitchen | 0 | 0 | 0 | 0 | 0 | 0 | 1 | 1 | 1 | 0 | 0 | 0 |
| Dining | 0 | 0 | 0 | 0 | 0 | 1 | 1 | 1 | 1 | 0 | 0 | 0 |
| Toilet | 0 | 0 | 0 | 0 | 0 | 1 | 1 | 1 | 1 | 0 | 0 | 0 |
| Corridor | 0 | 0 | 0 | 0 | 0 | 0 | 1 | 1 | 1 | 0 | 0 | 0 |
| Storage | 0 | 0 | 0 | 0 | 0 | 0 | 0 | 0 | 0 | 0 | 0 | 0 |
| Room | Time | | | | | | | | | | | |
| | 13 | 14 | 15 | 16 | 17 | 18 | 19 | 20 | 21 | 22 | 23 | 24 |
| Bedroom | 0 | 0 | 0 | 0 | 0 | 0 | 0.2 | 0.2 | 0.2 | 0.2 | 0 | 0 |
| Living | 0 | 0 | 0 | 1 | 1 | 1 | 1 | 1 | 1 | 1 | 0 | 0 |
| Kitchen | 0 | 0 | 0 | 0 | 0 | 0 | 1 | 1 | 1 | 1 | 0 | 0 |
| Dining | 0 | 0 | 0 | 0 | 0 | 1 | 1 | 1 | 1 | 0 | 0 | 0 |
| Toilet | 0 | 0 | 0 | 0 | 0 | 1 | 1 | 1 | 1 | 0 | 0 | 0 |
| Corridor | 0 | 0 | 0 | 0 | 0 | 0 | 1 | 1 | 1 | 1 | 0 | 0 |
| Storage | 0 | 0 | 0 | 0 | 0 | 0 | 0 | 0 | 0 | 0 | 0 | 0 |

Tab. 6.8 The occupation or function timetable of the other devices in house, adapted from [172].

| Room | Time | | | | | | | | | | | |
|---|---|---|---|---|---|---|---|---|---|---|---|---|
| | 1 | 2 | 3 | 4 | 5 | 6 | 7 | 8 | 9 | 10 | 11 | 12 |
| Bedroom | 0.07 | 0.07 | 0.07 | 0.07 | 0.07 | 0.07 | 0.53 | 1 | 0.53 | 0.07 | 0.07 | 0.07 |
| Living | 0.06 | 0.06 | 0.06 | 0.06 | 0.06 | 0.06 | 0.06 | 0.06 | 0.06 | 0.06 | 0.06 | 0.06 |
| Kitchen | 0.07 | 0.07 | 0.07 | 0.07 | 0.07 | 0.07 | 1 | 1 | 1 | 0.07 | 0.07 | 0.07 |
| Dining | 0 | 0 | 0 | 0 | 0 | 0 | 0 | 0 | 0 | 0 | 0 | 0 |
| Toilet | 0.06 | 0.06 | 0.06 | 0.06 | 0.06 | 0.29 | 1 | 1 | 0.29 | 0.29 | 0.29 | 0.29 |
| Corridor | 0 | 0 | 0 | 0 | 0 | 0 | 0 | 0 | 0 | 0 | 0 | 0 |
| Storage | 0 | 0 | 0 | 0 | 0 | 0 | 0 | 0 | 0 | 0 | 0 | 0 |
| Room | Time | | | | | | | | | | | |
| | 13 | 14 | 15 | 16 | 17 | 18 | 19 | 20 | 21 | 22 | 23 | 24 |
| Bedroom | 0.07 | 0.07 | 0.07 | 0.07 | 0.3 | 0.53 | 0.77 | 1 | 1 | 0.77 | 0.3 | 0.07 |
| Living | 0.06 | 0.06 | 0.06 | 0.53 | 0.53 | 1 | 1 | 1 | 1 | 0.69 | 0.06 | 0.06 |
| Kitchen | 0.07 | 0.07 | 0.07 | 0.07 | 0.07 | 0.07 | 0.25 | 0.25 | 0.25 | 0.25 | 0.07 | 0.07 |
| Dining | 0 | 0 | 0 | 0 | 0 | 0 | 0 | 0 | 0 | 0 | 0 | 0 |
| Toilet | 0.29 | 0.29 | 0.29 | 0.29 | 0.29 | 0.53 | 1 | 1 | 0.34 | 0.34 | 0.06 | 0.06 |
| Corridor | 0 | 0 | 0 | 0 | 0 | 0 | 0 | 0 | 0 | 0 | 0 | 0 |
| Storage | 0 | 0 | 0 | 0 | 0 | 0 | 0 | 0 | 0 | 0 | 0 | 0 |

### 6.3.3 Other device parameters

The parameters used in the fan is shown in Tab. 6.8.

Tab. 6.9 The parameters of the fan.

| City | Fan type | Volume flow rate $m^3/h$ | Power kW |
|---|---|---|---|
| Newcastle | Heat collection fan | 1115 | 0.19 |
| | Blower | 1000 | 0.17 |
| Urumqi | Heat collection fan | 1115 | 0.19 |
| | Blower | 2000 | 0.34 |

The adsorption device has the energy storage capacity of 3600 kWh and 6550 kWh in Newcastle and Urumqi, respectively.

The vacuum tube thermal collector is set as exhibited in Tab. 6.9.

Tab. 6.10 Other parameters set in the vacuum tube thermal collector.

| Name | Value | Unit |
|---|---|---|
| Number in series | 1 | - |
| Collector area | 30.96 | $m^2$ |
| Fluid specific heat | 1.2 | kJ/kg·K |
| Efficiency mode | 1 | - |
| Flow rate at test conditions | 36 | Kg/hr·$m^2$ |
| Logical unit of file containing biaxial IAM data | 45 | - |

The heat adsorption, heat generation, and energy storage modules are set with parameters shown in Tab. 6.10, Tab. 6.11 and Tab. 6.12, respectively.

Tab. 6.11 The heat adsorption parameter in the adsorption system.

| Term | Value | Unit |
|---|---|---|
| Inlet fluid temperature | 20.0 | °C |
| Inlet flow rate | 10000.0 | kg/hr |
| Control function | 1 | - |
| Set point temperature | 50 | °C |
| Overall loss coefficient | 0.0 | kJ/hr·K |
| Boiler efficiency | 0.7 | Fraction |
| Temperature of surroundings | 30 | °C |

Tab. 6.12 The heat generation parameter in the adsorption system.

| Term | Value | Unit |
|---|---|---|
| Inlet fluid temperature | 20.0 | °C |
| Inlet flow rate | 10000.0 | kg/hr |
| Control function | 1 | - |
| Set point temperature | 20 | °C |
| Overall loss coefficient | 0.0 | kJ/hr·K |
| Temperature of surroundings | 20 | °C |

Tab. 6.13 The energy storage parameter in the adsorption system.

| Term | Value | Unit |
|---|---|---|
| Mode | 1 | - |
| Cell energy capacity | 4250 | kWh |
| Cells in parallel | 1 | - |
| Cells in series | 1 | - |
| Charging efficiency | 1 | - |

### 6.3.4 Climate parameters

Climate parameters used in this study employed the TMY (Typical Meteorologic Year) climate data, which method was first proposed by NREL (National Renewable Energy Laboratory) and Sandia National Laboratory in 1981. The TMY model requires that the TMM (Typical Meteorological Month) should be selected from the long-term historical records using mathematical statistical method, and then the TMY could be therefore formed by 12 of this TMM. It should be noted that using the TMY model, a simulated climate year was retrieved with each climate month suiting the typical target area, rather than using an extreme climate. This also made TMY model a representative climate database for the corresponding location in the annual content.

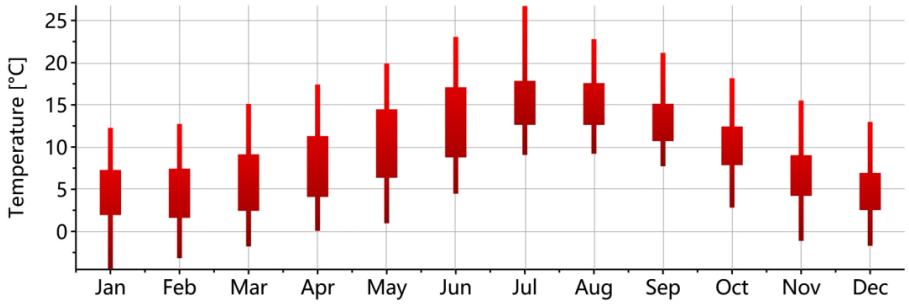


Fig. 6.5 Outdoor dry-bulb temperature in Newcastle.

Fig. 6.5 exhibits the outdoor dry-bulb temperature in Newcastle. The average outdoor dry-bulb temperature in Newcastle is 9.2 °C, and the lowest outdoor temperature is -4.3 °C in January. The maximum outdoor temperature is 26.65 °C in July.

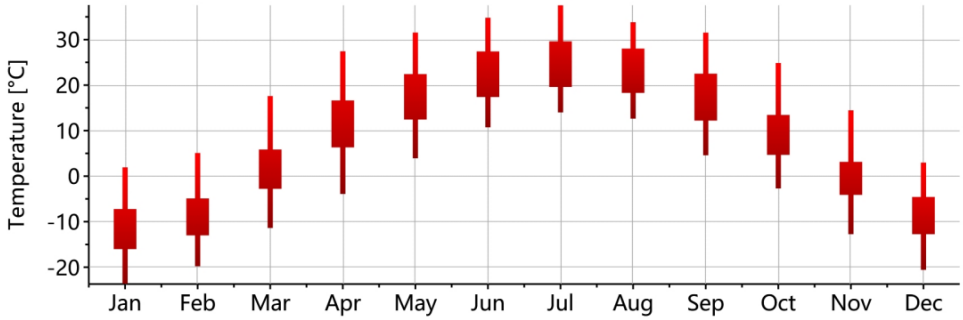


Fig. 6.6 Outdoor dry-bulb temperature in Urumqi.

Fig. 6.6 presents the outdoor dry-bulb temperature in Urumqi. The average outdoor temperature is 8 °C. The minimum and maximum outdoor dry-bulb temperature in Urumqi are -23.5 °C and 37.5 °C, respectively in January and in July.

## 6.4 TRNSYS modelling

### 6.4.1 Geometry import

A geometry model of the simulated house was established by the TRNSYS insert (Trn3d) in the software of SketchUp 2018 as shown in Fig. 6.7. The geometry model was then employed in the TRNbuild module in TRNSYS. The user interface was presented in the Appendix. D, if interested. The information includes the construction materials (concrete, cement mortar and so on), constructive wall category (outer wall, roof, and so on), window, function/occupation timetable, inner heat source, room geometry (room area, room volume, outer wall area, and so on). The Appendix. D presented the parameters setting corresponding to the information in Tab. 6.1 to Tab. 6.6.

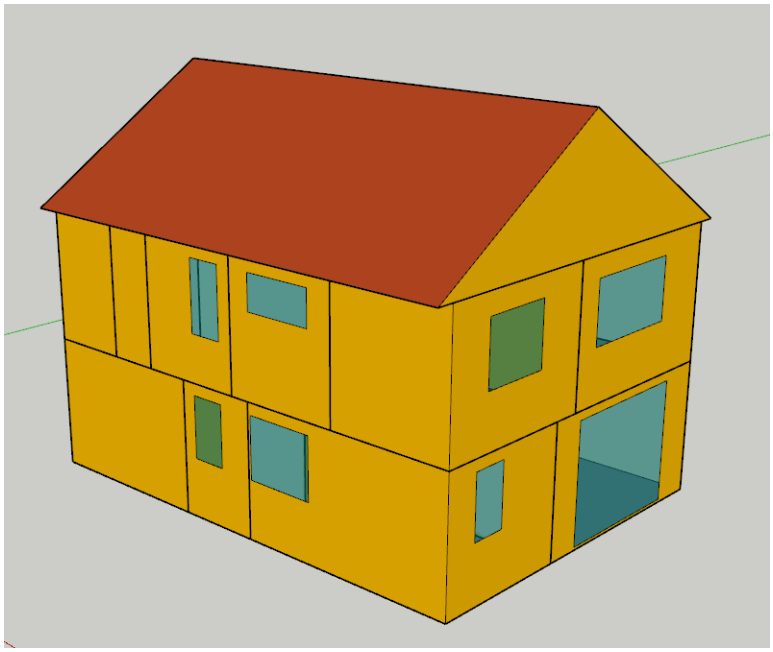

Fig. 6.7 Geometry model of the simulated house, drawn by SketchUp 2018.

### 6.4.2 Modules and subsystems

Fig. 6.8 expressed the TRNSYS building heat load calculation model. It was a part of the thermal simulation system. More details were provided later.

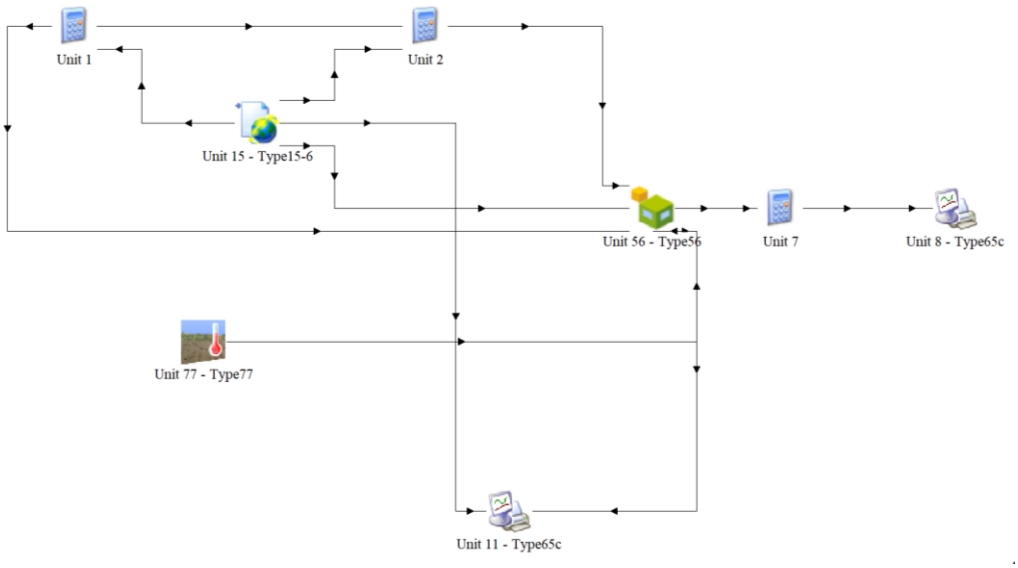


Fig. 6.8 The building heat load calculation model using TRNSYS.

The related modules utilized in the solar-adsorption space heating system are shown in Tab. 6.13.

Tab. 6.14 The related modules utilized in the solar-adsorption space heating system.

| No. | Module | Function | External file |
|---|---|---|---|
| 1 | Type56 | To simulate the thermal processes in the building | House geometry file |
| 2 | Type15-2 | To read the TMY data in the form of TM2 | Climate data |
| 3 | Type77 | To simulate the contact surface temperature between the house and the land | None |
| 4 | Equa | To define the calculation equation, the calculation controlling signal, the statistical energy consumption, or to define the value of the variable | None |
| 5 | Type14h | To define the schedule/timetable | None |
| 6 | Type14k | To define the space heating period | None |
| 7 | Type33e | To solve the absolute humidity by the local atmospheric pressure, dry-bulb temperature, relative humidity and so on | None |
| 8 | Type165b | To switch the controlling module on/off | None |
| 9 | Type71 | Vacuum pipe thermal accumulator | None |
| 10 | Type146 | To simulate the fixed-frequency fan and calculate the fan energy consumption | None |
| 11 | Type1246 | To calculate the adsorbed heat of the adsorption devices | None |
| 12 | Type47a | To analyze the stored energy of the adsorption device | None |
| 13 | Type659 | To simulate the exothermic process in the adsorption device | None |
| 14 | Type752h | To simulate the water-adsorption process in the adsorption device | None |
| 15 | Type754h | To simulate the water supply process in the adsorption device | None |
| 16 | Type698 | To control the room temperature | None |
| 17 | Type648 | Combined air valve | None |
| 18 | Type24 | To count the accumulative thermal energy consumption and energy consumption | None |
| 19 | Type65c | To export the data and image | Export Excel file |
| 20 | Type64a | To count the monthly energy consumption, operational cost, cooling and heating power | Export text file |

The established TRNSYS is presented in Fig. 6.9.

This house heating model in TRNSYS has five main subsystems, including the thermal simulation system of the building, the thermal accumulation system of the thermal collector, the adsorption system, the heating system, and the controlling system.

- **The thermal simulation subsystem of the building**

The weather module (Type15-2), architecture module (Type56), land temperature calculation module (Type77), and the module of Equa constitute the thermal simulation of the desired architecture. The TMY data is read by the weather module, and the solar radiation and external temperature and humidity towards different building surfaces are therefore calculated and led into the architecture module. The example of sending the data from the weather module to the architecture module is presented in Appendix. D. The land surface temperature is used to calculate the heat loss between the land and the building by the land temperature calculation module. The heat transfer between the building and the environment is determined by the architecture module. Moreover, during this period, some other data including the room temperature and humidity are also obtained.

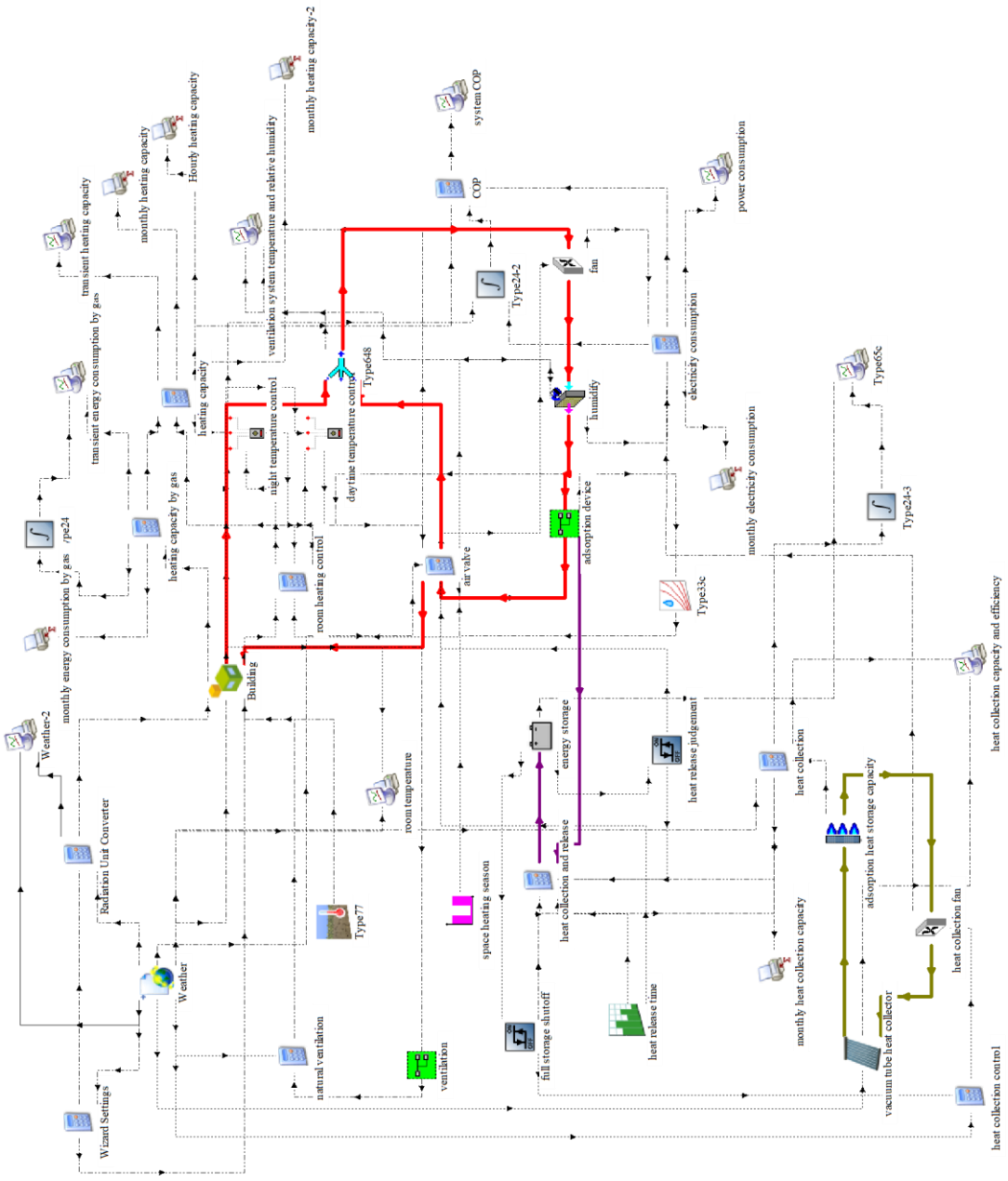


Fig. 6.9 The schematic diagram of the developed house heating model in TRNSYS.

- **The thermal accumulation subsystem of the thermal collector**

The thermal accumulation system of the thermal collector is composed of the weather module (Type15-2), the vacuum tube thermal collector (Type71), the thermal collection fan (Type 146), and the adsorption device heat consumption module (Type1246). The weather module sends the data including the outer dry-bulb temperature, zenith angle of the sun, solar azimuth, the radiation intensity of the inclined surfaces and so on to the vacuum tube thermal collector module. The thermal collection fan (Type146) also sends the air data into the vacuum tube thermal collector (Type71). After the thermal

accumulation of the thermal collector, the air with the increased temperature is send to the heat adsorption module (Type1246) in the adsorption system. The heat is transferred to the part in the adsorption system and the air is therefore cooled to a lower temperature. The air is then returned to the thermal collection fan and reheated to fulfil the thermal collection circulation.

- **The adsorption subsystem**

Simplification has been carried out to simulate the adsorption, heat storage, heat adsorption and water adsorption processes happened in the adsorption device, as no existed adsorption device module in the TRNSYS software. The whole adsorption subsystem includes the heat adsorption module (Type1246), the energy storage module (Type47a), the heat generation module (Type659), and the water vapour adsorption module (Type752h). The outlet air temperature of Type1246 is 20°C, according to the experimental investigation. This module could calculate the adsorption heat by the inlet air volume flow rate and temperature. The adsorption heat is stored in the energy storage module (Type47a), and the accumulative adsorption heat is calculated. The returned air of the room is send to the ultrasonic humidifier through the return fan to increase the relative humidity to 70%. Then the wetter air flows into the adsorption system. After being heated, the air is forced to the room. The heat generation module (Type659) in the adsorption system has the outlet air temperature of 50 °C, according to the experimental record. The thermal supply from the energy storage module (Type47a) is calculated by Type659.

- **The heating subsystem**

The system which proves heat to the building mainly consists of the return fan module (Type146), humidifying module (Type754h), the heat release module (Type659) and moisture adsorption module (Type752h) in the adsorption device, the fan valve module (Equa), and the return fan valve module (Type648). During space heating process, the return fan is working, and the outlet air temperature of the adsorption device is 50 °C. The hot air is shunted by the fan valve to each room. The room temperature will be controlled at a desired temperature by the controlling system.

- **The controlling subsystem**

Modules of Type14k, Type165b, Type698, and Equa construct the controlling

subsystem. The controlling tasks include the thermal collection system controlling, the energy storage and release controlling of the adsorption device, the space heating controlling, and the ventilation controlling.

The thermal collection system controlling need to switch on the thermal collection fan and the energy storage when the collector surface receives the direct solar radiation intensity higher than 100 kJ/hm$^2$ and the energy storage module is still able to store more. Otherwise, the thermal collection fan should be turned off, and the vacuum tube thermal collector stopped thermal collection processes. This controlling is realized by Equa.

The energy storage and release controlling will start the energy charging mode when less than 95% of the maximum thermal storage capacity is stored. The thermal energy is stored until the direct solar radiation intensity is less than 100kJ/hm$^2$. When the space heating is required and the energy storage percentage is higher than 0.5%, the energy storage module is controlled to release the heat. However, when either the energy storage percentage is less than 0.1% or the space heating is not desired, the heat release is stopped. In this controlling, Type165b and Equa are employed.

The heating controlling system uses module of Type698. It monitored all room temperatures. During the space heating dates, if the room temperature is 1 °C less than the required room temperature, the output signal of the heating controlling module is 1, and the fan valve will be open to send the hot air into the typical room. The output signal will be 0 if the room temperature is 1 °C higher than the required one, and the fan valve to the room will be switched off. During this process, the excess air will be returned by the return valve to the heating source.

The ventilation controlling will open the window to cool the room to less than 22 °C when the room temperature is higher than 24 °C. When the room temperature is lower than 22 °C, the window is controlled to be closed by the ventilation controlling system.

## 6.5 Results and discussion

### 6.5.1 Heat supply analysis

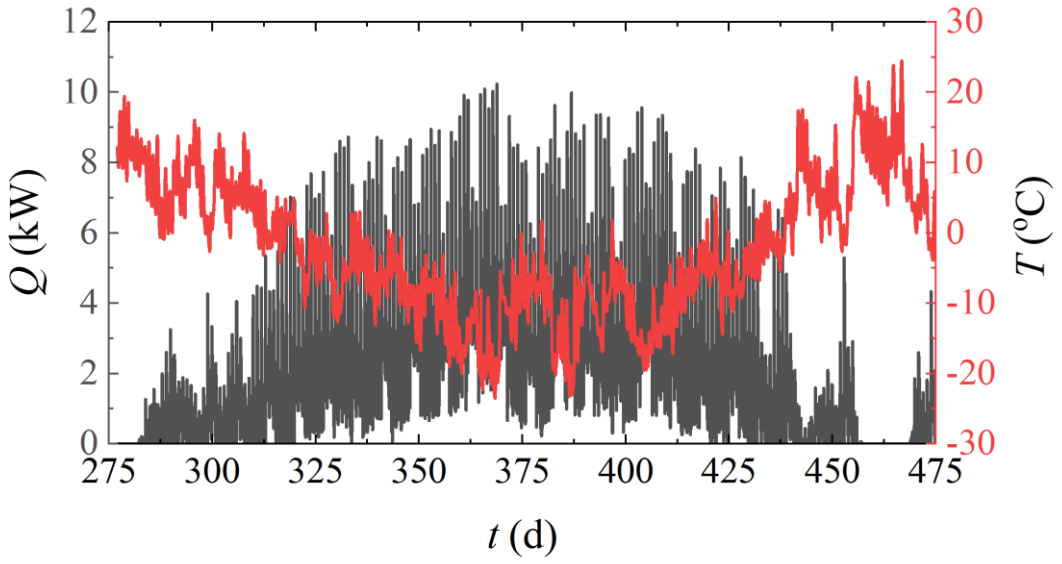


Fig. 6.10 The timely heat supply in Urumqi.

Fig. 6.10 presented the heat supply during the whole space heating season. The maximum heat supply amount is 10.23 kW by the adsorption-integrated space heating system. With the outer temperature decreasing, the heat supply increases. Moreover, the heat load has relatively large fluctuations, which could be contributed by the room temperature controlling process. If the required room temperature is decreased, the heat supply could be reduced as well.

Tab. 6.15 is the monthly heat supply in Urumqi. The minimum heat supply, 99.88 kWh, is discovered in April, which is because of the highest outer average temperature, 11.8 °C. The maximum heat supply, 2442.91 kWh, is found in January, which is led by the lowest outer average temperature, -12.4 °C. The gross heat supply in the space heating season is 8862.68 kWh.

Tab. 6.15 Monthly heat supply in Urumqi.

| Month | Monthly heat supply kWh | Monthly average temperature ℃ |
|---|---|---|
| October | 283.77 | 9 |
| November | 1185.37 | -0.7 |
| December | 2173.65 | -9.4 |
| January | 2442.91 | -12.4 |
| February | 1824.22 | -9.2 |
| March | 852.87 | 1.2 |
| April | 99.88 | 11.8 |

The room temperature is drawn in Fig. 6.11, which demonstrates that the room temperature is well kept in the required room temperature. It also reveals that this adsorption-integrated space heating system is feasible for place where takes the advantage of the solar radiation abundance and with a very low environmental temperature, as the result shows the high space heating stability.

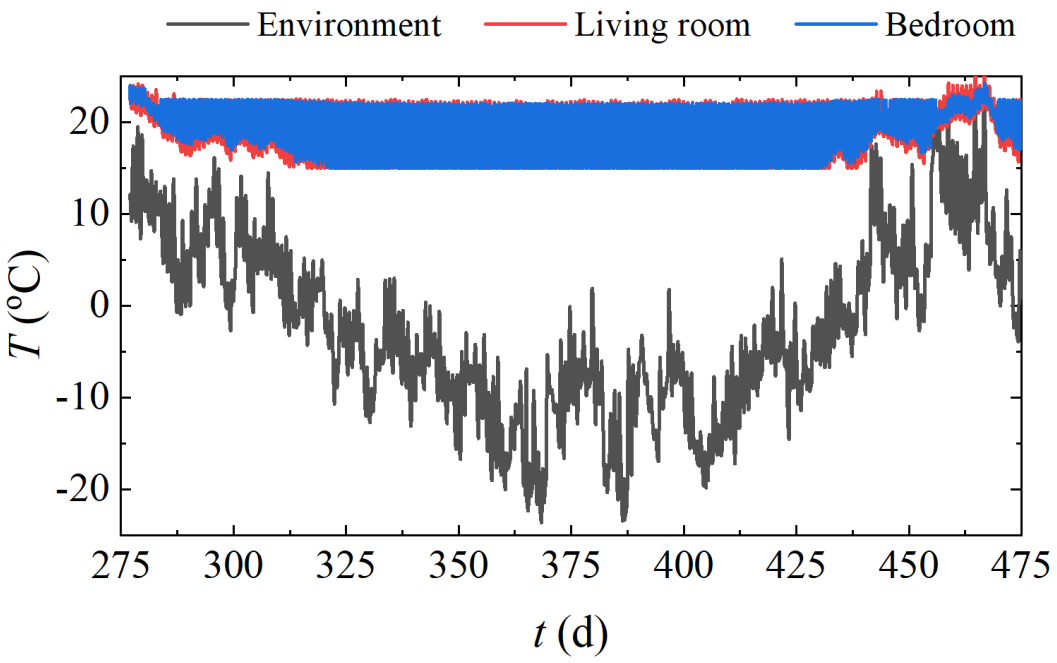


Fig. 6.11 The monitored room temperature in Urumqi in the space heating season.

Fig. 6.12 presents the heat supply in Newcastle, during the space heating season. The maximum heat supply provided by the adsorption-integrated space heating system is 8.39 kW. With the decrease of the outer temperature, the heat supply grows. Besides, the fluctuation of the heat load is quite large, which is due to the controlling temperature of the room. Similarly, if the controlling temperature is reduced, the heat supply required by the temperature range could also be cut down.

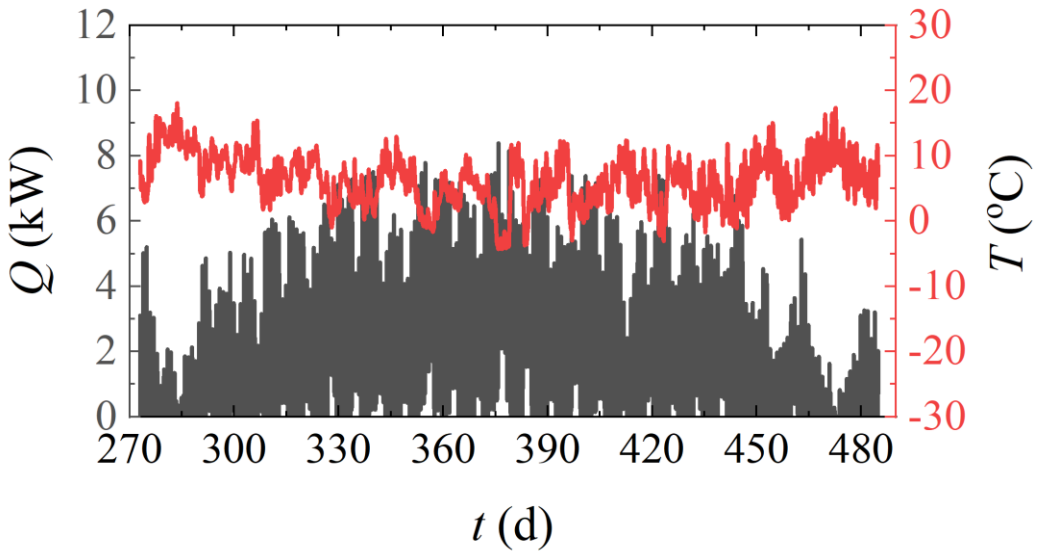


Fig. 6.12 Gross heat supply in Newcastle during the space heating season.

Tab. 6.16 exhibits the monthly heat supply in Newcastle. The minimum monthly heat supply is 428.62 kWh, in April, when the average environmental temperature is 7.7 °C. However, in October, even though the outer temperature is at its highest level, the heat supply is still higher than it is in April. The reason is that in April, the solar radiation is stronger than that in October, which provides extra thermal energy to heat the house. The accumulative heat supply in the space heating season is calculated to be 6466.39 kWh.

Tab. 6.16 Monthly heat supply in Newcastle.

| Month | Monthly heat load kWh | Monthly average temperature ℃ | Radiation density kWh/m$^2$ |
|---|---|---|---|
| October | 505.27 | 10.1 | 47.52 |
| November | 945.58 | 6.6 | 24.36 |
| December | 1319.44 | 4.5 | 14.83 |
| January | 1333.56 | 4.2 | 19.11 |
| February | 1041.59 | 4.3 | 35.90 |
| March | 892.33 | 5.6 | 74.18 |
| April | 428.62 | 7.7 | 114.91 |

Fig. 6.13 shows the temperature profile of different rooms in Newcastle, during space heating season. Obviously, the room temperature is stable in the range of the desired temperature range. It demonstrates that the adsorption-integrated space heating system is promising in the place where is cold and with normal solar radiation sources.

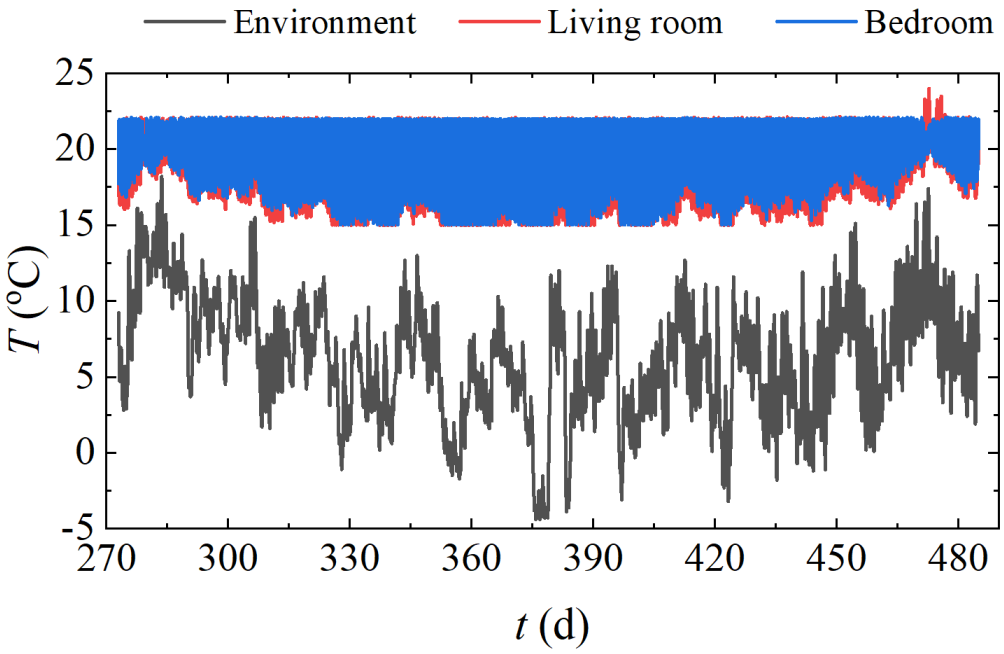


Fig. 6.13 Room temperature profile in Newcastle during space heating season.

### 6.5.2 Heat collection and heat release

Fig. 6.14 presents the heat collection/storage and heat release condition in Urumqi simulation. The results include the annual data from 21st April to 20th April (next year). With time evolution, the accumulative heat collection amount increases, as well as the heat storage percentage (versus the full storage). At 16:00 on 4th July (4432 h), the heat storage percentage is 100%. After that, the collection/storage process stops, and the accumulative heat storage amount keeps the same until the space heating season. When the space heating is required, both the accumulative heat collection amount and the heat storage percentage starts to decrease. When the heat storage percentage is less than 95% and the radiation density is higher than 100 kJ/hm$^2$, the heat storage process is switched on. Meanwhile, the accumulative heat collection amount increases. However, the environmental temperature decreases in winter, thus, the collected heat is less than the released heating effect. The heat storage percentage still decreases. On 8th March, the minimum heat storage percentage, 4%, is observed. Later, the collected heat grows larger than the released thermal energy, and the heat storage percentage is therefore enhanced. At the end of the space heating season, the residual heat storage, 2806.68 kWh, is 42.85% of the full capacity. During the full space heating period, the

accumulative heat collection amount is 15468.08 kWh.

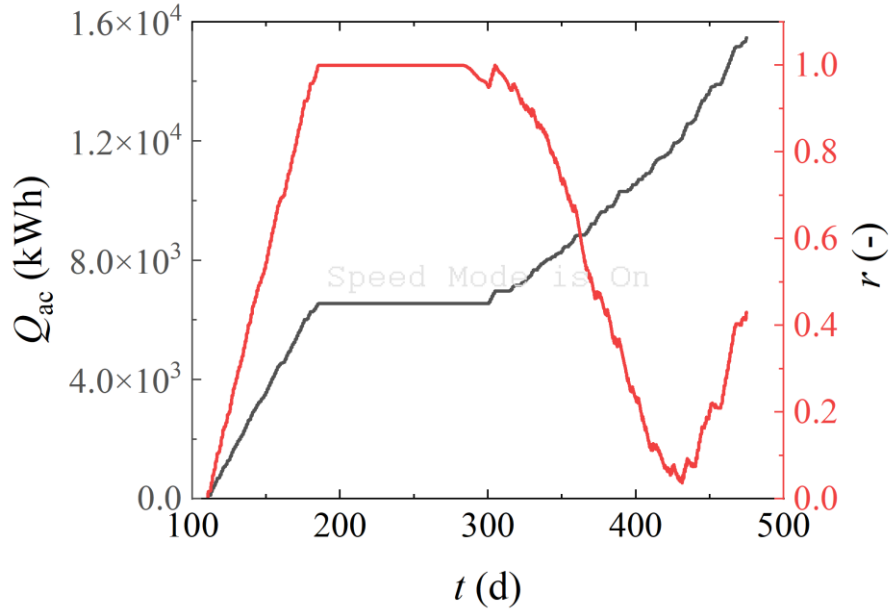


Fig. 6.14 The heat collection and heat release result in Urumqi, using the adsorption-integrated space heating system.

Tab. 6.17 is the monthly heat collection amount and efficiency. The highest heat collection is 2755.91 kWh, in April, while the lowest one is 274.68 kWh, in July. The maximum heat collection efficiency, 0.57, is found in October, while the minimum is found in February, 0.45. The average heat collection efficiency in the whole year is 0.51.

Tab. 6.17 Monthly heat collection amount and efficiency in Urumqi.

| Month | Collected heat kWh | Heat collection efficiency |
|---|---|---|
| April | 928.63 | 0.54 |
| May | 2755.91 | 0.54 |
| June | 2591.12 | 0.54 |
| July | 274.68 | 0.50 |
| August | 0.00 | 0.00 |
| September | 0.00 | 0.00 |
| October | 339.07 | 0.57 |
| November | 868.56 | 0.47 |
| December | 1085.29 | 0.46 |
| January | 1527.30 | 0.48 |
| February | 1347.97 | 0.45 |
| March | 2178.36 | 0.50 |
| April | 1571.19 | 0.51 |

Fig. 6.15 exhibits the heat collection and release amounts in Newcastle, using the adsorption-integrated space heating system. The simulation time ranges from 1st May to 30th April (next year). Similarly, the accumulation of the collected heat grows as well as the heat storage percentage with time goes. At 9:00 on 1st July (4353h), the heat storage percentage achieves 100% and the heat collection stops. At the same time, the accumulative heat collection also keeps the same until the space heating starts. The space heating season begins as the heat storage percentage is consumed. When the heat storage percentage is less than 95% and the received solar radiation is huger than 100 kJ/hm$^2$, the thermal energy collection is restarted. Even though the accumulative heat collection grows, as the environmental temperature decreases day by day in winter, the heat collection is less than the heat supply, and thus the heat storage percentage is reduced. On 10th March, the heat storage percentage is at the bottom with the value of 5%. After that date, the heat supply is reduced, and the heat collection is larger than the supply. The heat storage percentage is therefore increased. At the end of the space heating season, 57% of the gross storage capacity remains in the integrated-adsorption space heating system, which is 2052.00 kWh in value. During the whole space heating period, the gross accumulation of the collected thermal energy is 11284.44 kWh.

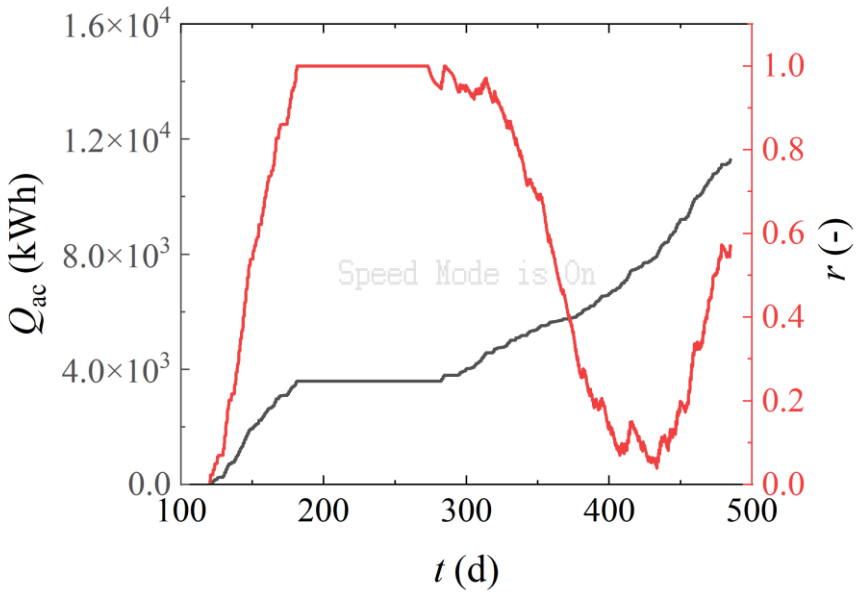


Fig. 6.15 Heat collection and release amount in Newcastle, employing the adsorption-integrated space heating system.

Monthly heat collection and release efficiency in Newcastle is listed in Tab. 6.18. The highest monthly heat collection is 2010.21 kWh, found in March, while the lowest one is 31.79 kWh in July. The maximum heat collection efficiency is discovered in November, 0.52. In February, the heat collection efficiency is 0.42, the lowest among all months. The average heat collection efficiency is 0.49, 0.2 lower than that in Urumqi.

Tab. 6.18 Monthly heat collection amount and efficiency in Newcastle.

| Month | Heat collection kWh | Heat collection efficiency |
|---|---|---|
| May | 2010.21 | 0.47 |
| June | 1558.44 | 0.42 |
| July | 31.79 | 0.54 |
| August | 0.00 | 0.00 |
| September | 0.00 | 0.00 |
| October | 466.13 | 0.50 |
| November | 960.46 | 0.52 |
| December | 671.83 | 0.50 |
| January | 853.08 | 0.52 |
| February | 1137.13 | 0.51 |
| March | 1635.79 | 0.50 |
| April | 1959.60 | 0.49 |

### 6.5.3 Energy consumption and efficiency

Tab. 6.19 Monthly energy consumption by fan and humidifier in Urumqi.

| Month | Fan kWh | Humidifier kWh | Gross kWh |
|---|---|---|---|
| April | 17.51 | 0.00 | 17.51 |
| May | 56.48 | 0.00 | 56.48 |
| June | 49.88 | 0.00 | 49.88 |
| July | 6.22 | 0.00 | 6.22 |
| August | 0.00 | 0.00 | 0.00 |
| September | 0.00 | 0.00 | 0.00 |
| October | 45.19 | 195.31 | 240.50 |
| November | 133.51 | 556.14 | 689.65 |
| December | 205.92 | 840.90 | 1046.82 |
| January | 216.52 | 873.14 | 1089.66 |
| February | 183.41 | 715.03 | 898.43 |
| March | 134.61 | 454.15 | 588.76 |
| April | 42.90 | 68.52 | 111.42 |
| Sum | 1092.16 | 3703.18 | 4795.34 |

Tab. 6.19 shows the monthly energy consumption in Urumqi. Separately, the fan cost 1092.16 kWh while the humidifier cost 3703.18 kWh per year. The gross energy consumption by the system is 4795.34 kWh for a year. The maximum energy consumption percentage is consumed by the fan, 77% of the whole cost.

The coefficient of performance (COP) is illustrated in Fig. 6.16, which is calculate by the accumulative heat supply to the room and the electricity consumption. With time going, COP of the system is improved, as the outside temperature decreases. The heat supply grows while the fixed-frequency fan has the stable power. When the environmental temperature reaches the lowest level, the maximum COP is achieved to be 1.94. The average COP among the gross space heating season is 1.85.

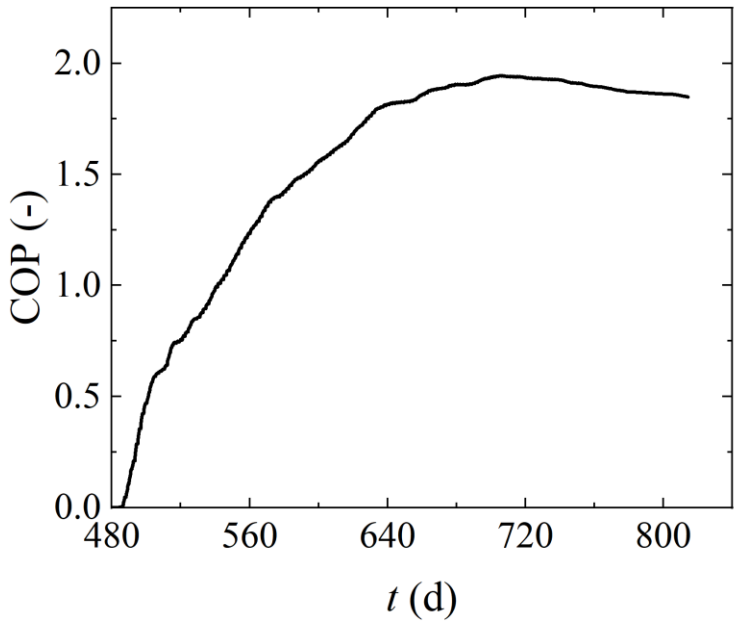


Fig. 6.16 COP of the adsorption-integrated space heating system in Urumqi.

Tab. 6. 20 presents the monthly energy consumption in Newcastle. The energy consumed by the fan is 748.74 kWh in a year, while that by the humidifier is 2163 kWh. The gross energy consumption of the adsorption-integrated space heating system is 2912.04 kWh. Different with the discovery in Urumqi simulation, the most energy consumption is by the humidifier, which constitutes 74% of the total consumption.

Tab. 6.20 Monthly energy consumption by different components in Newcastle.

| Month | Fan kWh | Humidifier kWh | Gross kWh |
|---|---|---|---|
| May | 42.60 | 0.00 | 42.60 |
| June | 36.62 | 0.00 | 36.62 |
| July | 0.74 | 0.00 | 0.74 |
| August | 0.00 | 0.00 | 0.00 |
| September | 0.00 | 0.00 | 0.00 |
| October | 61.33 | 227.75 | 289.08 |
| November | 94.04 | 317.27 | 411.30 |
| December | 109.13 | 385.96 | 495.09 |
| January | 106.55 | 370.10 | 476.65 |
| February | 100.84 | 321.28 | 422.12 |
| March | 109.34 | 327.31 | 436.65 |
| April | 87.55 | 213.65 | 301.20 |
| Sum | 748.74 | 2163.30 | 2912.04 |

The COP results calculated by the heat supply being divided by the system accumulative electricity cost is illustrated in Fig. 6.17. System COP increases after the space heating starts. The heat supply grows daily with the environmental temperature decreasing. The peak COP, 2.38, is achieved when the outside temperature reaches its lowest value. The average COP of the adsorption-integrated space heating system is 2.22 among the whole space heating season in Newcastle, which is 20% larger than that in Urumqi.

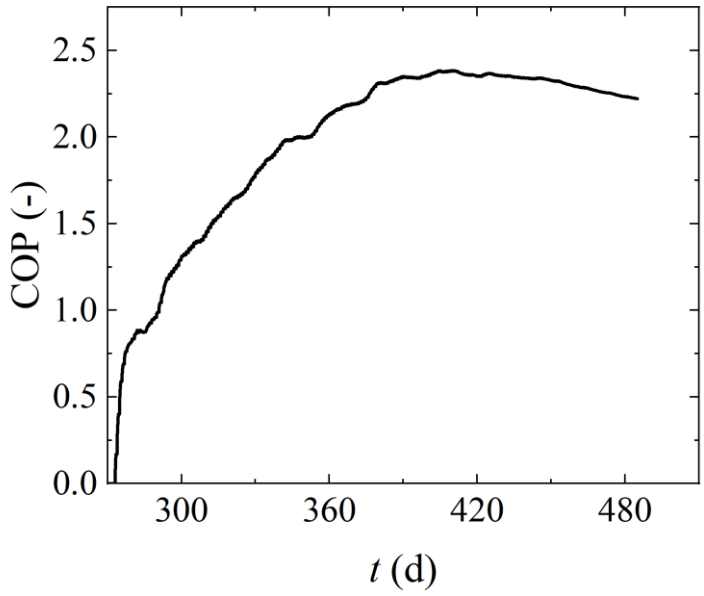


Fig. 6.17 COP of the adsorption-integrated space heating system in Newcastle.

## 6.6 Conclusion

According to the experimental investigation of the adsorption-heating performance, the adsorption-integrated space heating model is established in the software of TRNSYS. Two typical places of Newcastle, UK and Urumqi, China are selected as the background location. One represents the normal solar source and the cold weather condition, while the other is with abundant solar radiation and the cold weather. The discoveries are summarised as follows:

- With a higher required room temperature or a lower environmental temperature, the heat supply increases. Due to the room temperature controlling settings, the fluctuation of the heat supply among a day could be observed. In Urumqi, the minimum monthly heat supply is in the month when the environmental temperature is the highest among other space heating months. However, the solar radiation could provide extra heat to increase the building temperature thus in Newcastle the minimum monthly heat supply is found in April rather than in October. The gross heat supply in Urumqi and Newcastle is 8862.68 kWh and 6466.39 kWh, respectively. The results demonstrates that the required room temperature is well kept by the designed space heating system.

- The heat collection stops when the storage capacity is 100% occupied. The heat storage could be fulfilled in a year and suits the annual space heating requirement. At the end of each space heating season, the heat storage remains 42.85% and 57.00% in Urumqi and Newcastle, respectively.

- Two main energy consumers are the fan and the humidifier. 77% of the system energy consumption is cost by the fan in Urumqi, while in Newcastle, 74% of the gross consumption is by the humidifier. Moreover, the COP of the adsorption-integrated space heating system in Newcastle is 20% higher than that in Urumqi.

# Chapter 7. Conclusion and future work

## 7.1 Conclusion

The thermochemical adsorption technology is found to be feasible to seasonally store the solar energy in the days when the solar radiation is intensive. In the cold days, the stored solar thermal energy could be used for house space heating. Using the construction material of zeolite and the normal salt $MgSO_4$, LiCl, and LiBr, composite adsorbent could be formed with high water-adsorption capacity and high energy density. The composite material is then experimentally tested in the scaled house model to evaluate the practical space heating performance. After that, the model of the adsorption-integrated space heating system is established and operated to predict the seasonal storage ability and the space heating performance. The PhD project in Chapter. 2 to Chapter. 6 could be summarised as follows:

**Chapter. 2:** The thermodynamic fundamentals and material developments of inorganic salts as water sorption material for thermal energy storage is summarises. The first part introduces the mechanism of water sorption with salts for thermal energy storage, the phase equilibrium diagram, deliquescence relative humidity of different salts, the reaction enthalpy and entropy changes based on pressure-temperature diagram, as well as the heat capacity of different salt hydrates. The second part includes the research and developments of salt or salt hydrate used for water sorption thermal energy storage. The material issues and salt screening method are discussed. The usage of composite material to improve the material performance is introduced. Finally, the sorption performance of some composite materials is summarised.

**Chapter. 3:** The $MgSO_4$-zeolite composite adsorbents for the application in SSES for space heating were manufactured and characterised. These characterisations can help to explain the adsorption-heating performance difference in further applications and to discover the selection criteria for desired adsorption heat storage material. The maximum heat storage density found in the TGA-DSC desorption tests was 231.3 J/g by $MgSO_4$(20%)-4A. The maximum water adsorption capacity obtained from the tests was 0.1803 g/g by MgSO4(20%)-13X. Constant temperature-humidity adsorption results suggested that the composite adsorbents manufactured with a salt solution at concentration of 10% and the zeolite of 3A and 13X are the most promising ones for

the space heating application.

**Chapter. 4:** The composite thermochemical adsorbent materials of LiCl-zeolite, LiBr-zeolite, and LiCl-LiBr-zeolite were characterised. The higher solution concentration favours the more loadings of the salt onto the 3A zeolite, however too high solution concentration may raise the problem of blockage of mass transfer channels of water adsorption and thus limit the heat storage capacity of the adsorbent. Both SEM and BET tests results can support this finding. The framework structure of 3A zeolite remained well after impregnation. XRD results show five possible hydration bonds in the totally adsorbed composite: $LiCl{\cdot}H_2O$, $LiClO_3{\cdot}0.25H_2O$, and $LiClO_4{\cdot}3H_2O$ for LiCl impregnated samples, and $LiBr{\cdot}H_2O$, $LiBr{\cdot}2H_2O$, and $LiBrO_3{\cdot}H_2O$ for LiBr infiltrated adsorbents. The maximum heat storage density, 592.8 J/g, is found in Group 9, 5%LiCl-5%LiBr-zeolite. The most water adsorption capacity observed in the climatic chamber adsorption experiment is 0.22 g/g (5%LiCl-25%LiBr-zeolite). The highest water adsorption capacity found in TGA tests is 0.16 g/g, in Group 1, 5% LiCl-zeolite.

**Chapter. 5:** The LiCl/LiBr – zeolite composite adsorbent was experimentally investigated in 1:22.5 scaled house model to evaluate the thermochemical adsorption integrated space heating system performance. Under the same experimental conditions, sample Z15 shows the best composite adsorbent. In the pipeline-level adsorption heat storage experiments, the temperature rise rate at the outlet of the pipeline is influenced by the flow rate and humidity of the gas passing through. The studied composite adsorbent exhibited its highest heat release of 434.4 J/g at a gas flow rate of 15 $m^3$/h and an RH value of 70%, achieving an energy discharge efficiency value of 74.3%. The decrease in temperature and heat release at the pipe outlet showed a slowing down trend with the number of cycling experiments, and the composite adsorbent has good periodicity and stability.

**Chapter. 6:** The adsorption-integrated space heating model is established in the software of TRNSYS. Two typical places of Newcastle, UK and Urumqi, China are selected as the background location. One represents the normal solar source and the cold weather condition, while the other is with abundant solar radiation and the cold weather. With a higher required room temperature or a lower environmental temperature, the heat supply increases. Due to the room temperature controlling settings, the fluctuation of the heat supply among a day could be observed. The gross heat supply in Urumqi and Newcastle is 8862.68 kWh and 6466.39 kWh, respectively. The results demonstrates that the required room temperature is well kept by the designed space

heating system. The heat collection stops when the storage capacity is 100% occupied. The heat storage could be fulfilled in a year and suits the annual space heating requirement. At the end of each space heating season, the heat storage remains 42.85% and 57.00% in Urumqi and Newcastle, respectively. Moreover, the COP of the adsorption-integrated space heating system in Newcastle is 20% higher than that in Urumqi.

### 7.2 future work

The kind of composite adsorbent could be enlarged, as more novel but complex technologies are under developing to enhance the water-adsorption capacity as well as the adsorption kinetics. In the PhD project, the relatively easy manufacturing methodology is taken, considering that the practical application of the space heating and seasonal energy storage material should be cheap and easy to access.

Moreover, the space heating and SSES experiment could be conducted, rather than only utilizing the heat air by the water adsorption reactor. The composite adsorbent could be directly integrated with the wall, roof, and the floor. It could be predicted that the practical SSES experiment could take long time.

In the simulation of the thermochemical adsorption-integrated space heating system, it is found that the stored solar energy at the end of the space heating season is still quite a lot. It means that during the cold days, the collected solar energy could be used for other applications. Besides, when space heating is not required but the storage capacity is full, the solar collection device could support other user demand with extra rational settings.

# Appendix. A

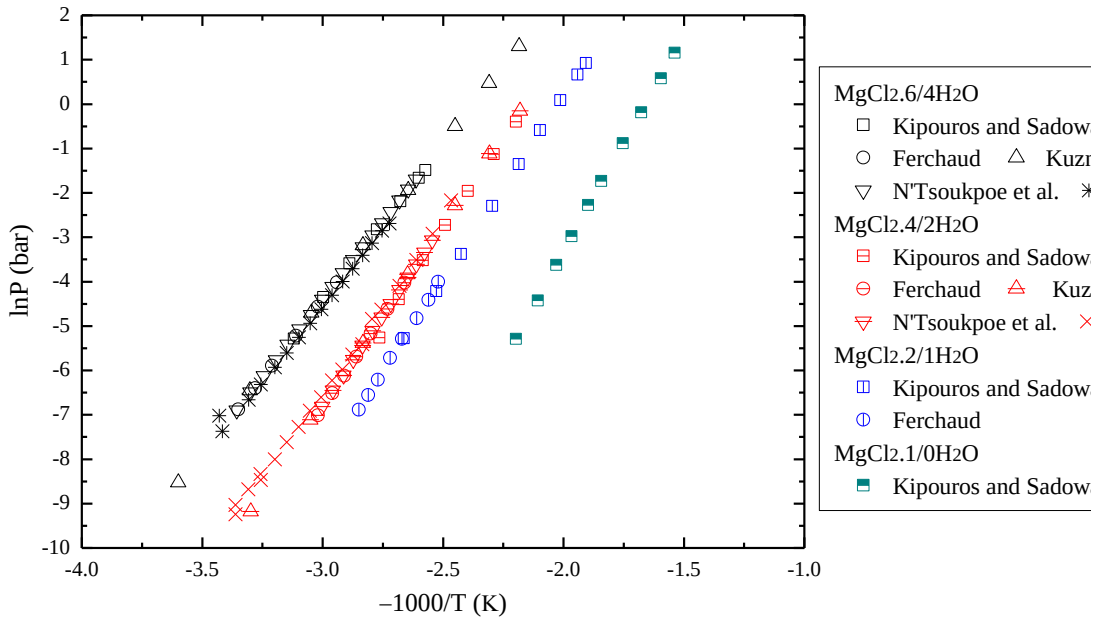


Figure A1 Equilibrium pressure-temperature of $MgCl_2$ with water vapour.

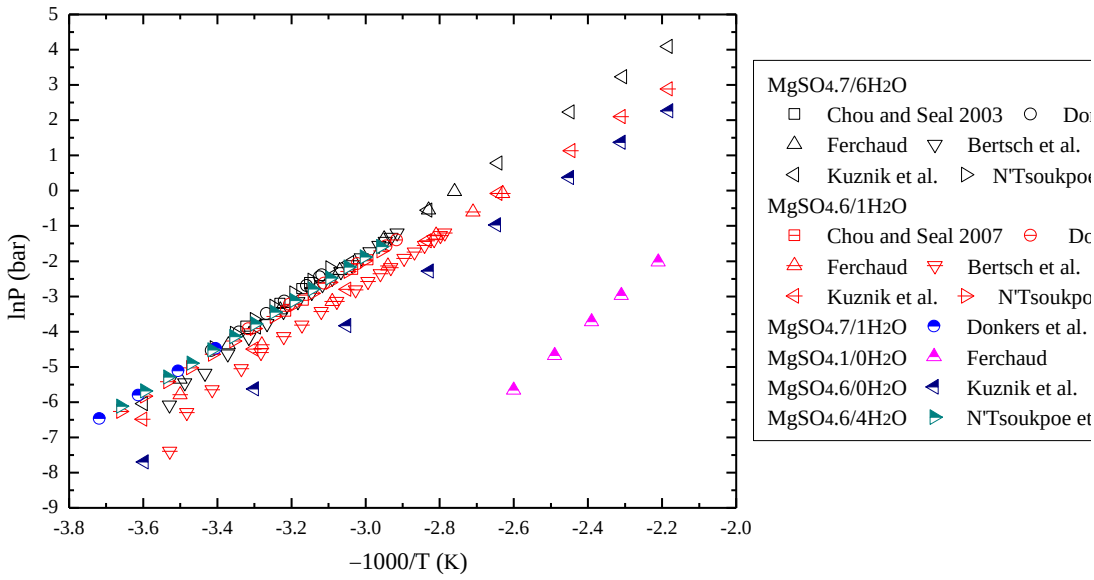


Figure A2 Equilibrium pressure-temperature of $MgSO_4$ with water vapour.

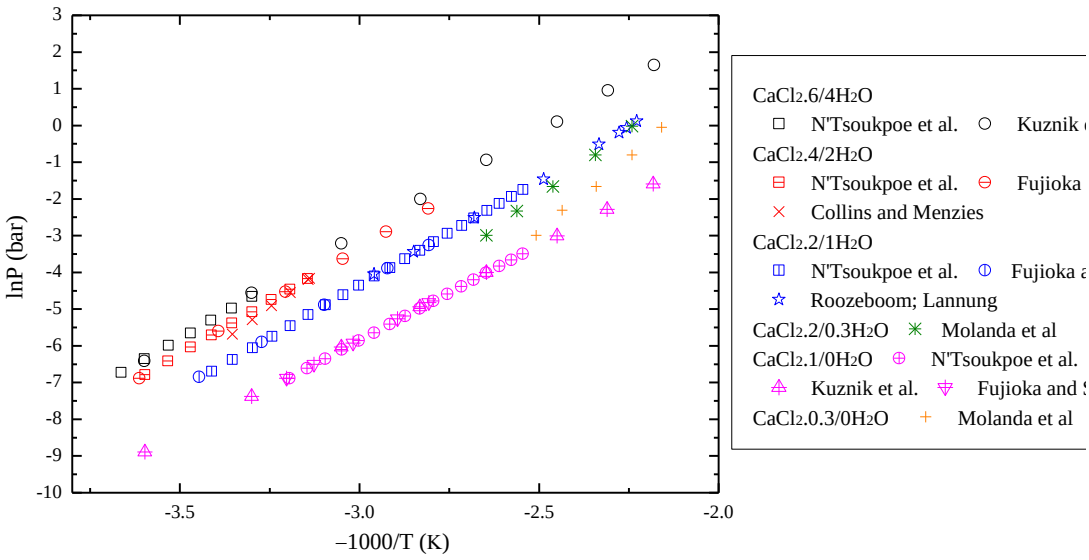


Figure A3 Equilibrium pressure-temperature of $CaCl_2$ with water vapour.

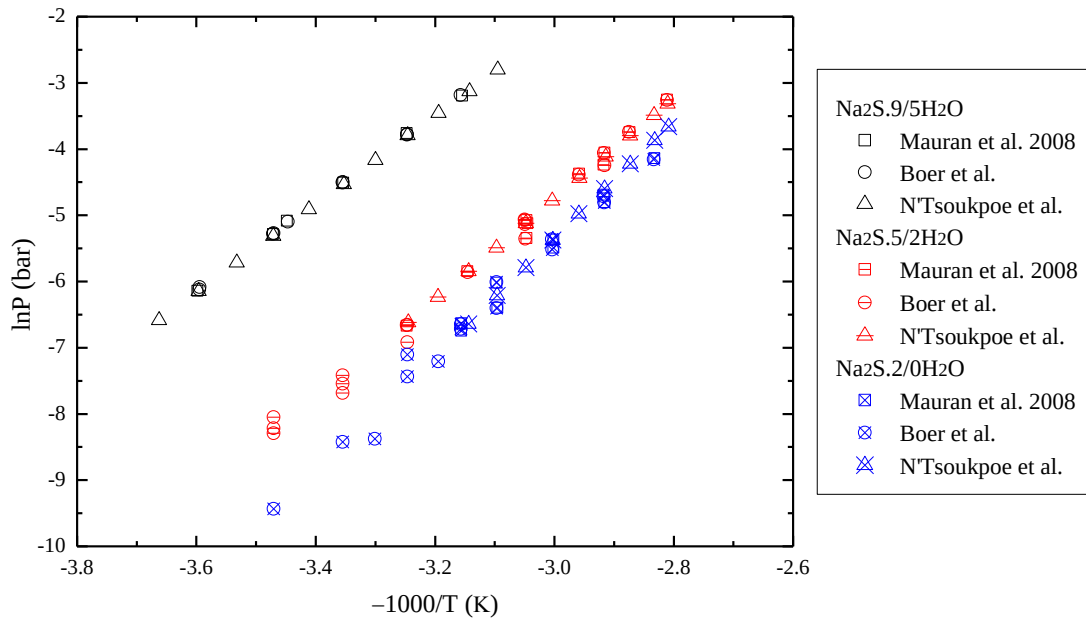


Figure A4 Equilibrium pressure-temperature of $Na_2S$ with water vapour.

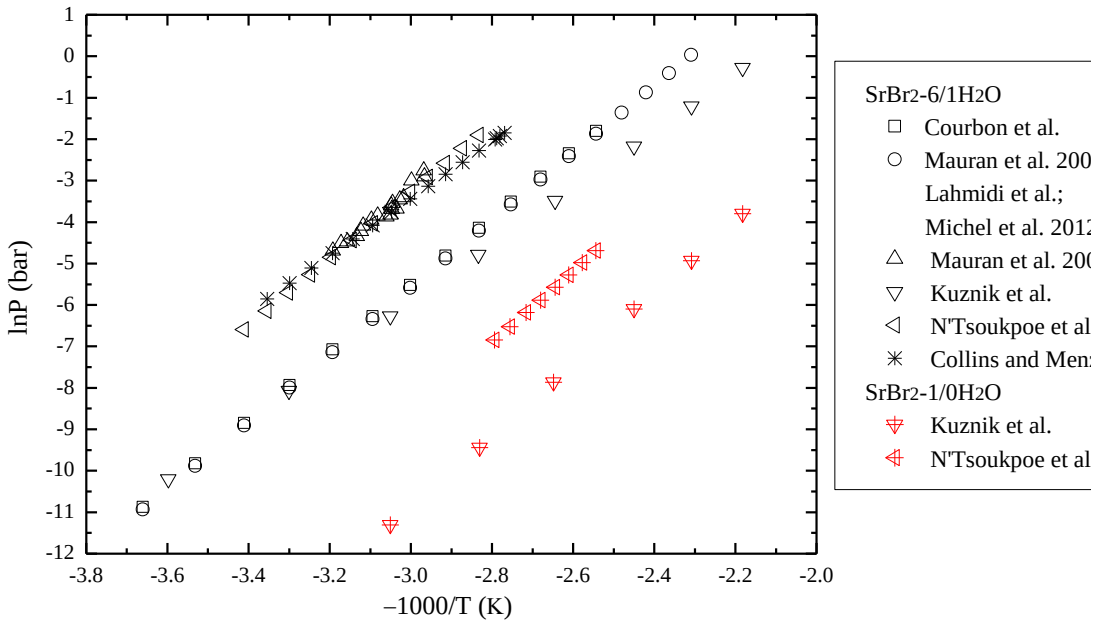


Figure A5 Equilibrium pressure-temperature of $SrBr_2$ with water vapour.

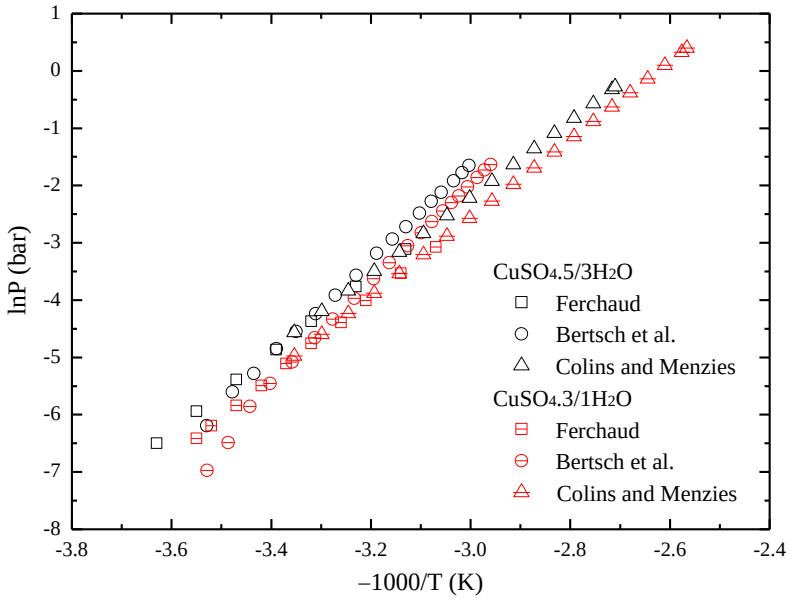


Figure A6 Equilibrium pressure-temperature of $CuSO_4$ with water vapour.

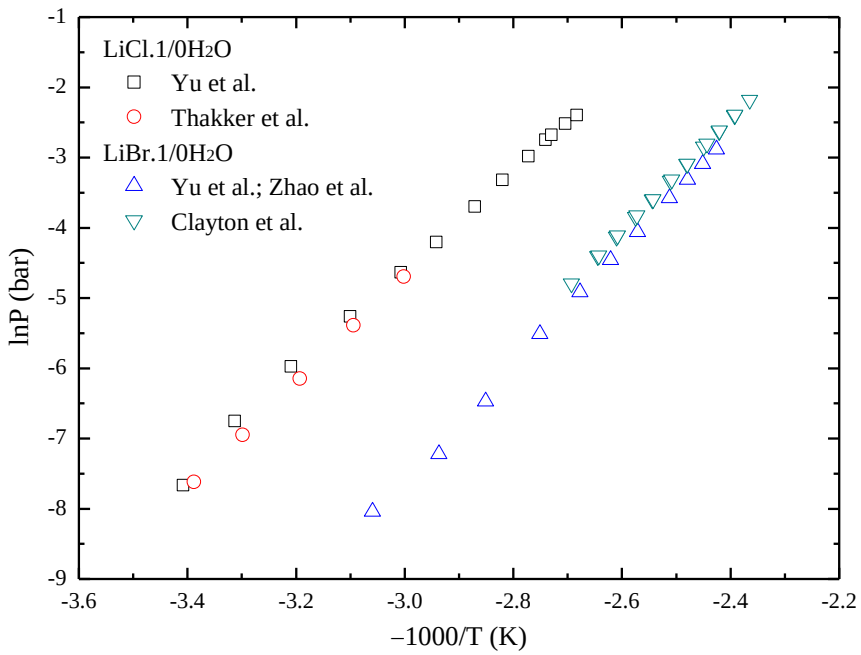


Figure A7 Equilibrium pressure-temperature of LiCl and LiBr with water vapour.

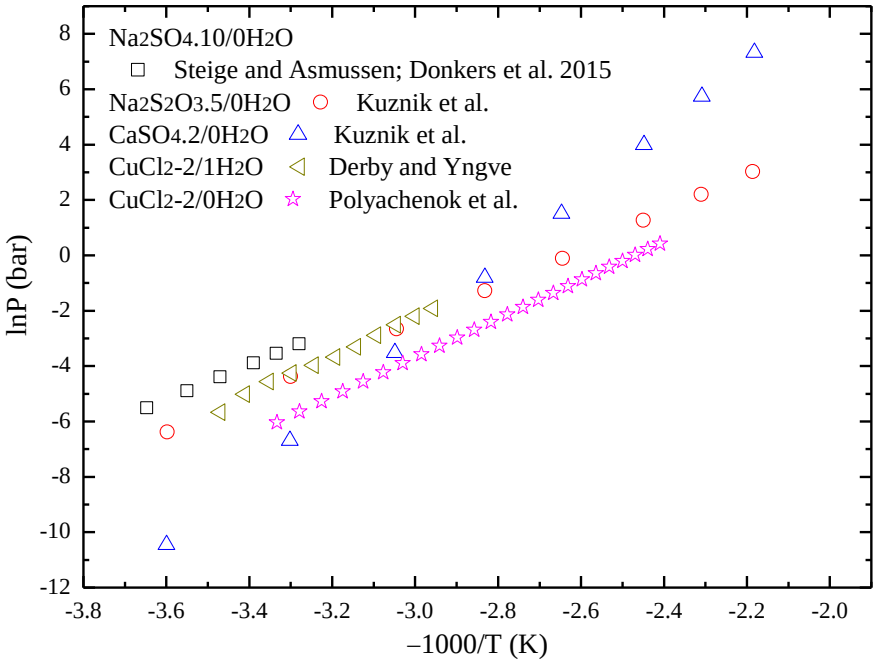


Figure A8 Equilibrium pressure-temperature of $Na_2SO_4$, $Na_2S_2O_3$, $CaSO_4$ and $CuCl_2$ with water vapour.

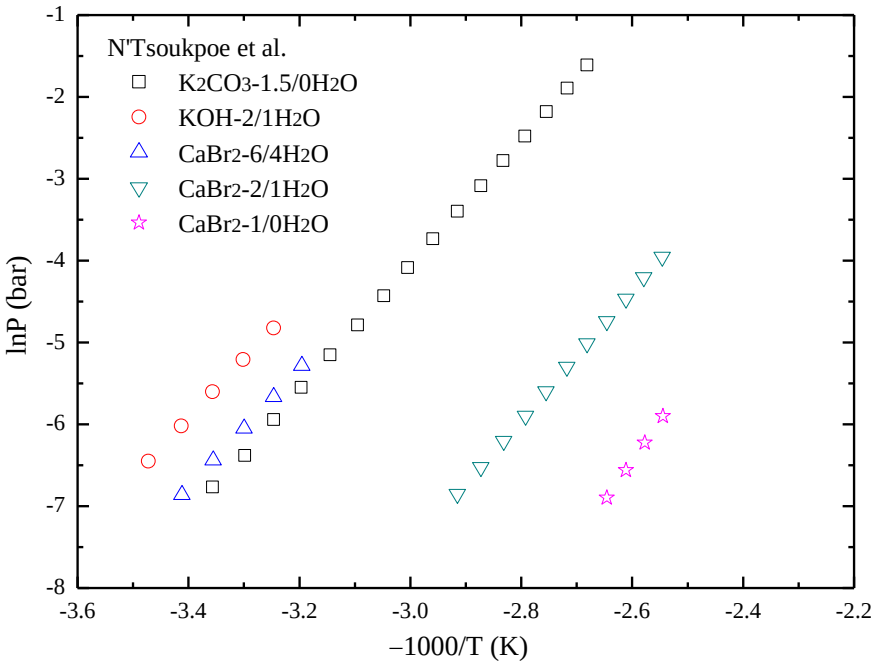


Figure A9 Equilibrium pressure-temperature of $K_2CO_3$, KOH and $CaBr_2$ with water vapour.

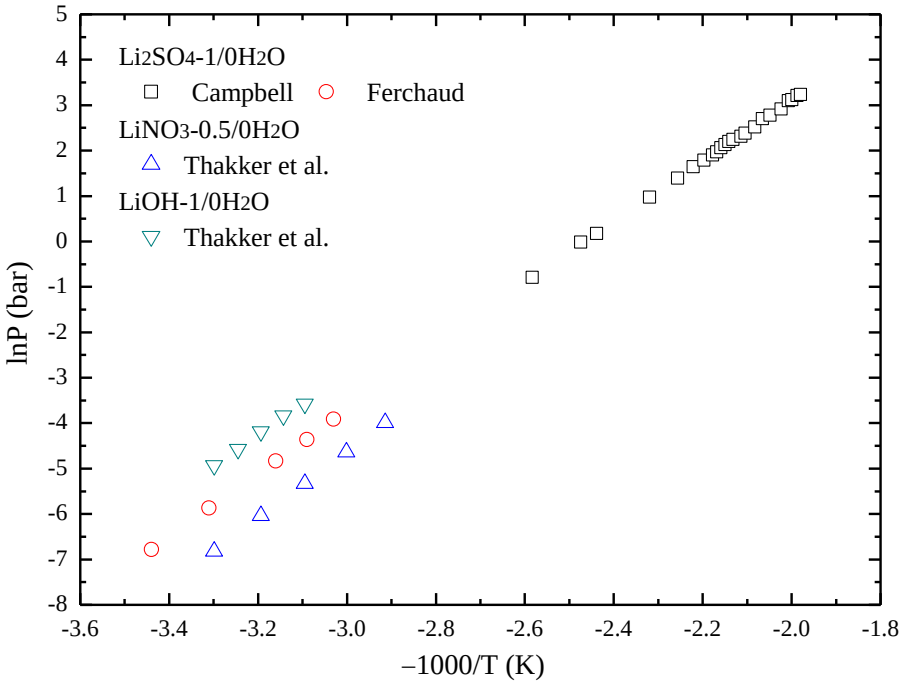


Figure A10 Equilibrium pressure-temperature of $Li_2SO_4$, $LiNO_3$ and LiOH with water vapour.

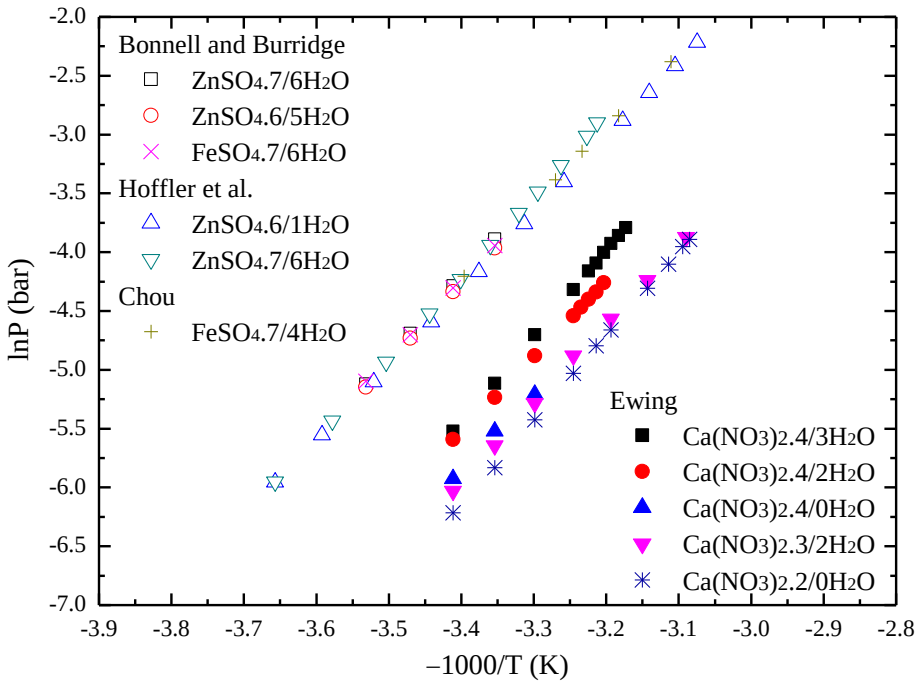


Figure A11 Equilibrium pressure-temperature of $ZnSO_4$, $FeSO_4$ and $Ca(NO_3)_2$ with water vapour.

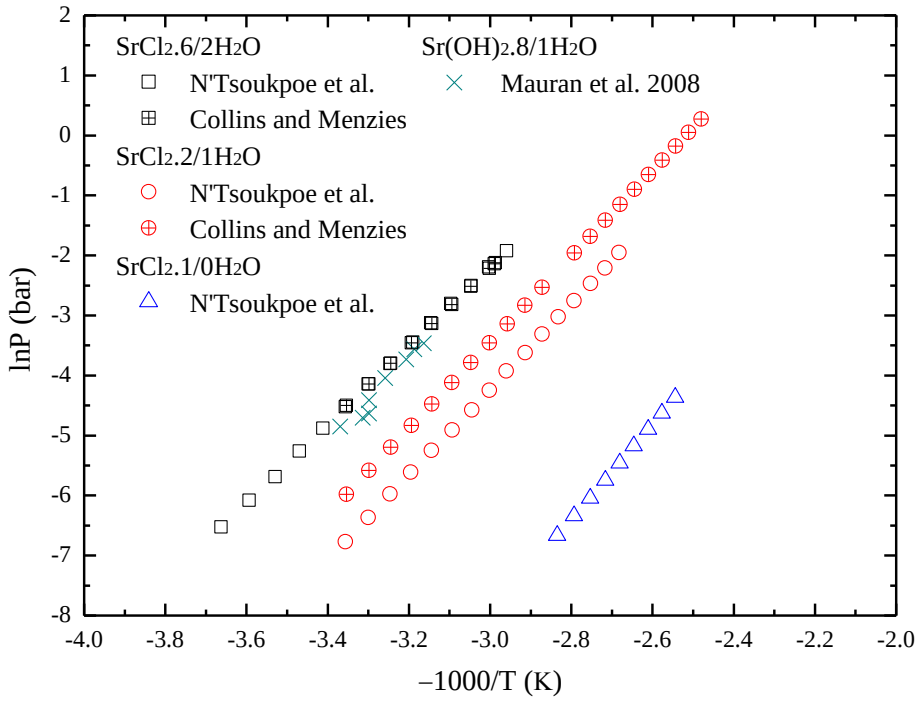


Figure A12 Equilibrium pressure-temperature of $SrCl_2$ and $Sr(OH)_2$ with water vapour.

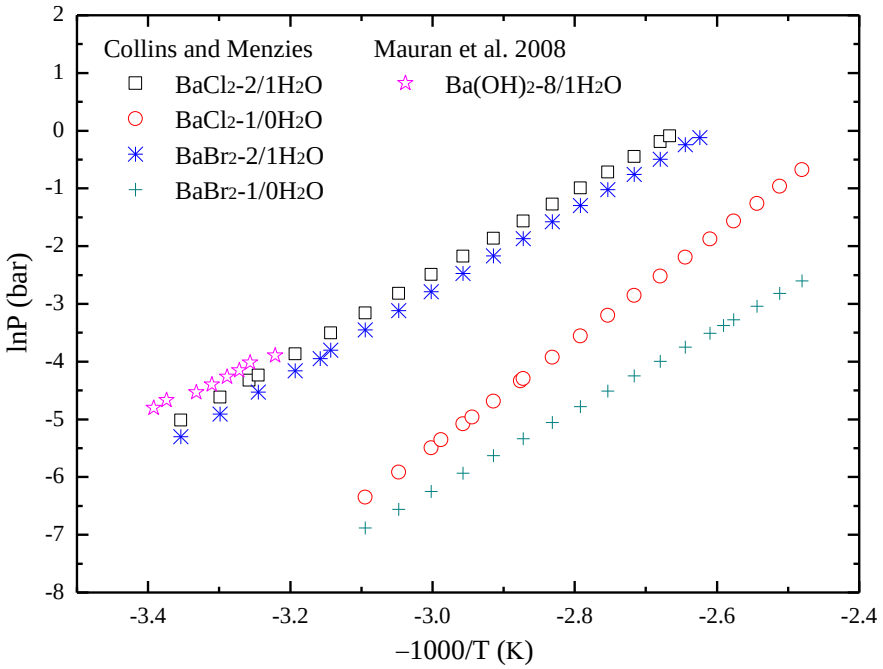


Figure A13 Equilibrium pressure-temperature of $BaCl_2$, $BaBr_2$, and $Ba(OH)_2$ with water vapour.

The corresponding references include Kipouros and Sadoway [55], Ferchaud [50], Kuznik et al. [56], N'Tsoukpoe et al. [57], Carling [54], Chou and Seal 2003 [58], Donkers et al. [53], Bertsch et al. [59], Chou and Seal 2007 [60], Fujioka and Suzuki [61], Collins and Menzies [173], Roozeboom [63], Lannung [64], Molenda et al. [65], Mauran et al. 2008 [67], de Boer et al. [66], Courbon et al. [72], Mauran et al. 2002 [68], Lahmidi et al. [69], Michel et al. 2012 [70] 2014 [71], Yu et al. [73], Thakker et al. [74], Zhao et al. [75], Clayton et al. [76], Steige and Asmussen [77], Donkers et al. 2015 [78], Derby and Yngve [80], Polyachenok et al. [79], Campbell [81], Bonnell and Burridge [82], Hoffler et al. [83], Chou et al. [84], Ewing [85].

# Appendix. B

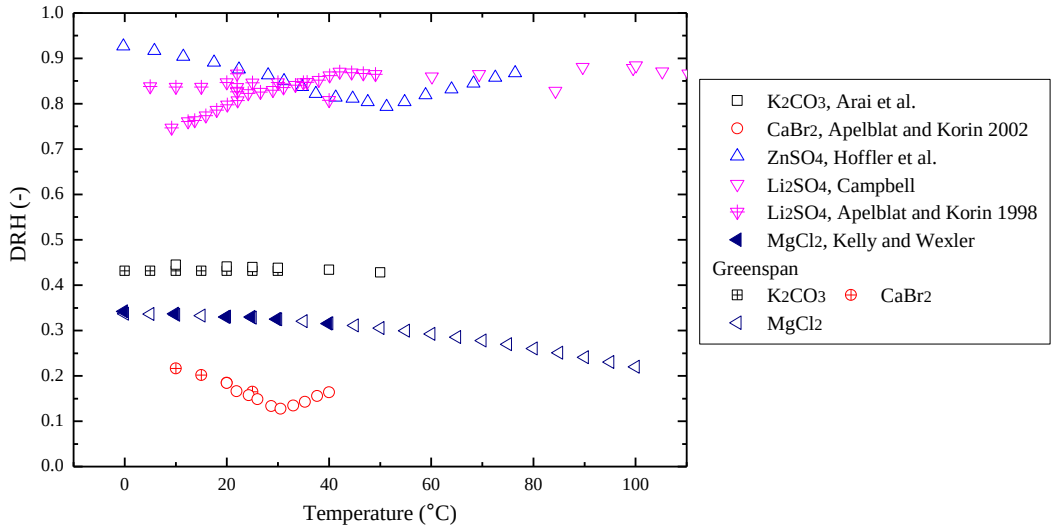


Figure B1 *DRH* with temperature of $K_2CO_3$, $CaBr_2$, $ZnSO_4$, $Li_2SO_4$, $MgCl_2$, $K_2CO_3$, $CaBr_2$, and $MgCl_2$.

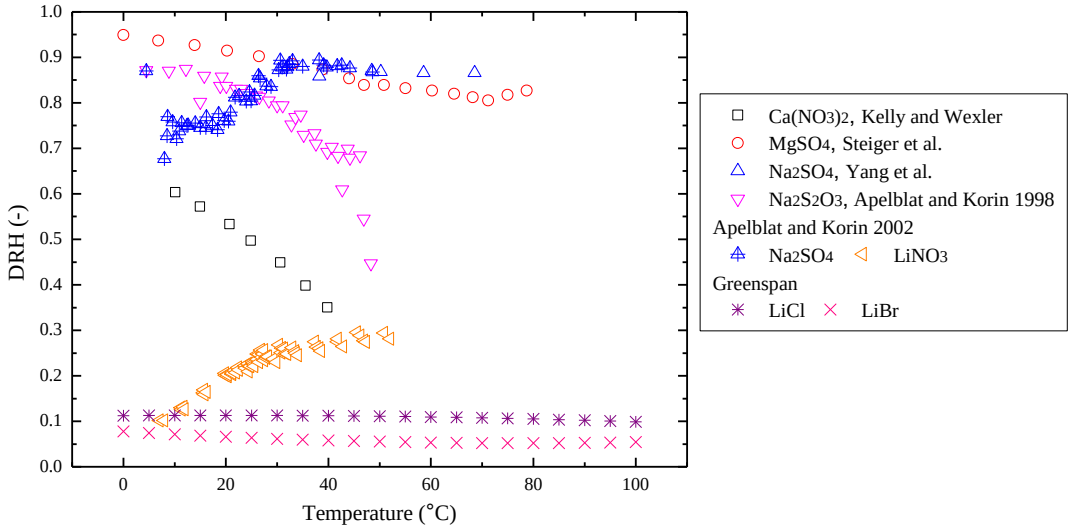


Figure B2 *DRH* with temperature of $Ca(NO_3)_2$, $MgSO_4$, $Na_2SO_4$, $Na_2S_2O_3$, $Na_2SO_4$, $LiNO_3$, LiCl, and LiBr.

They refer to the references as: Kelly and Wexler [87], Apelblat [174], Derby and Yngve [80], Collins and Menzies [62], Greespan [175], Arai et al.[176], Apelblat and Korin 2002 [177], Hoffler et al. [83], Campbell [81], Apelblat and Korin 1998 [178], Steiger et al. [179], Yang et al. [180].

# Appendix. C

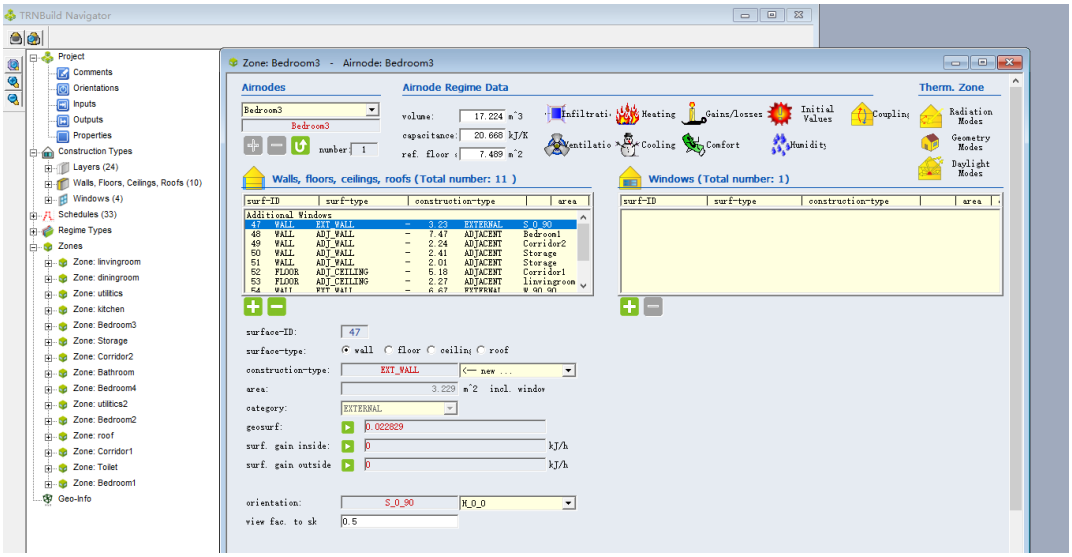


Figure C The user interface o the TRNbuild module.

# Appendix. D

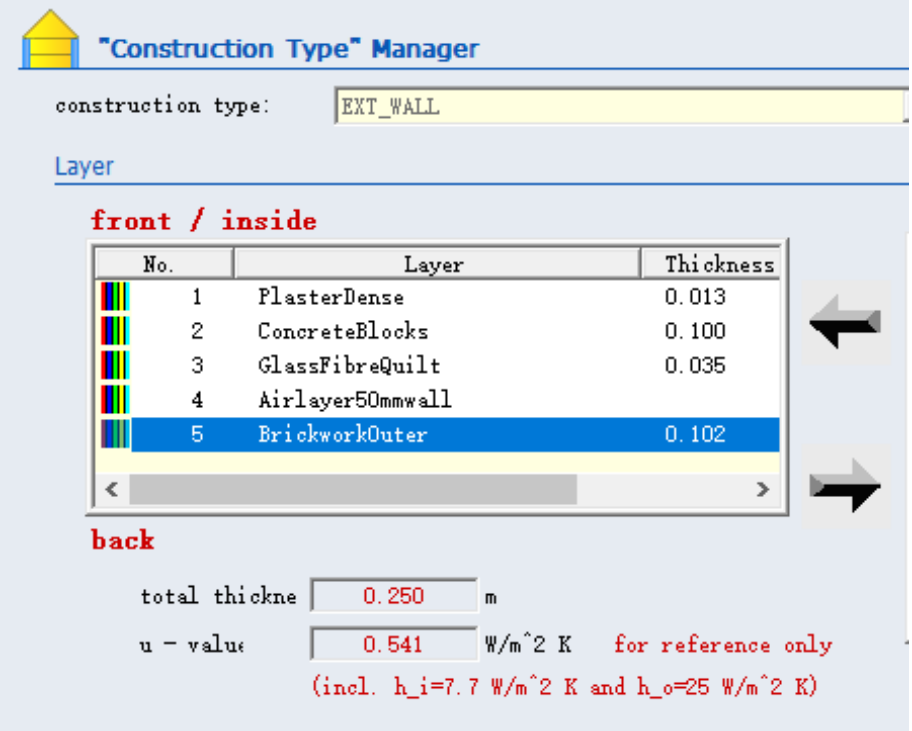


Figure D1 Example of the external wall parameters setting.

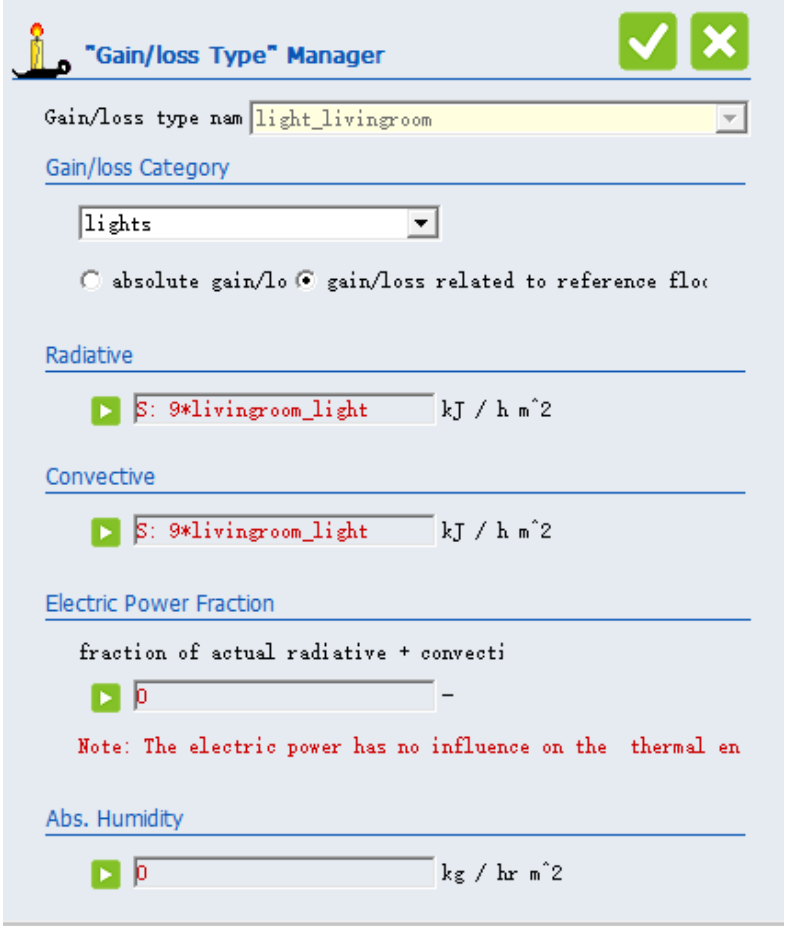


Figure D2 Example of setting inner turbulence parameters, using the illumination parameters of gain/loss.

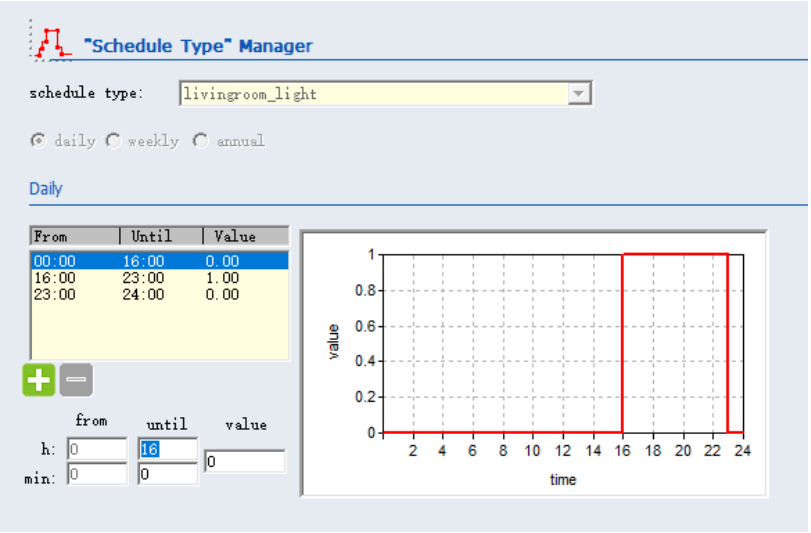


Figure D3 Example of setting internal turbulence parameters, including the

schedule type of illumination devices.

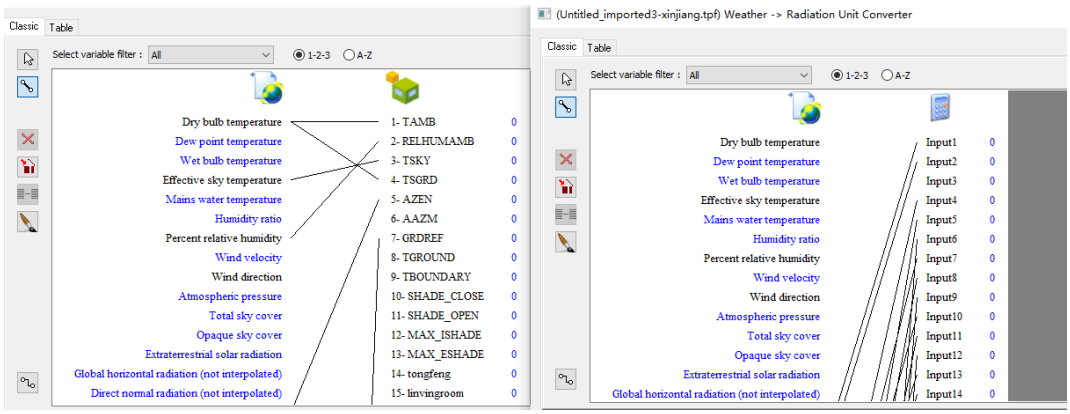


Figure D4 Example of importing the data from the weather module to the architecture module.

# Appendix. E

## E.1 Space heating system

In this study, the TRNSYS software was used to dynamically simulate the charging mode and the discharging mode. The system mainly consists of three parts. The first part is solar energy collection and energy storage; the second part is the reactor heat release as well as gas heating; the last part is the residential model as the heated unit. Fig. C.1 shows the charge mode and discharge mode for the entire operation. During the day, the sorbent is heated and dehydrated by a solar-triggered charging mode. All heat is stored, and there is no heat loss in this process (the heat conversion efficiency is 74.3%). The input heat from the solar panels regenerated the adsorbent in the reactor. At night, the discharge mode is triggered by blowing air at a certain flow rate and humidity into the reactor. All the heat of adsorption released by the reactor heats the air, which is mixed with ambient air and passed into the dwelling to heat the space. The specific content of the heat release analysis module is described in Chapter 3. The optimal heat extraction efficiency based on experimental data converts the energy stored during the day. In addition, gas is used as an auxiliary energy to supplement the insufficient power required by the house. Considering real life, assume that a simple thermostatic controller is used to maintain the indoor temperature at 22±1°C. When the indoor average area temperature is lower than 21℃, the fan starts to work, and the reactor provides heat; when it is higher than 23℃, the fan stops running. In addition, when the reaction of the adsorbent in the reactor is no longer enough to supply the indoor temperature to 20°C, no heat is provided, and the gas is started for heating work.

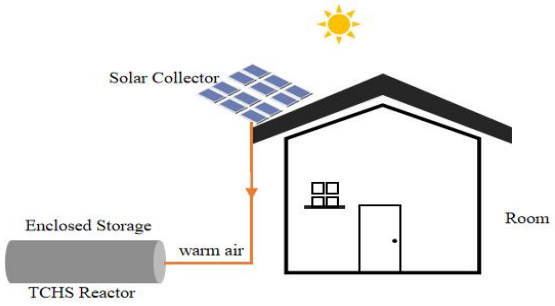

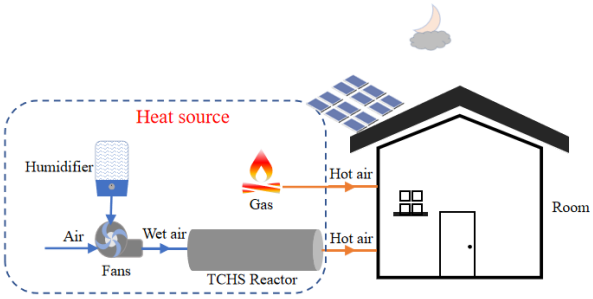


**Figure E1** Charge and discharge modes of an open TCHS system

To realize the residential model of the study, the 3D architectural design software SketchUp was used. A typical two-story residential model (actual size is 6150mm×8350mm×4550mm). As shown in Fig. C.2, the house model is then imported into TRNSYS through the TRNSYS 3d plugin. Next, transfer the module in TRNSYS Simulation Studio to build the TCHS-building simulation platform. Fig. C.3 shows the dynamic simulation flow, with controllers for each zone. Tab. C gives the structural information of the building used to determine the parameters of the walls, roof, floor and windows. The TRNSYS program generally creates a flexible environment for modelling buildings, where different building descriptions can be obtained by changing design parameters. However, this study mainly focuses on the performance research of the TCHS system. It explores the degree of its effect applied to the building, so that the parameter setting of the building itself is not changed. The system lays half-roof synchronous monocrystalline silicon solar modules and uses Type103 modules to simulate the photovoltaic power generation process. The conversion efficiency of this component can reach 21.3% under standard test condition. The climatic conditions entered refer to the climatic data of a typical weather year in Newcastle, including ambient temperature, instantaneous solar radiation on the horizontal plane, wind speed, and ambient air relative humidity. In the control module of the software, temperature control, time control and heat control are adopted. At the same time, the indoor temperature is within the range of 22±1℃, and the TCHS heating working time is from 20:00 at night to 9:00 in the morning of the next day. During this time period, when the room needs heating and the energy storage of the TCHS system is not exhausted, the system heats the room. The hot air leading to the room is distributed according to the area ratio of each room. In the analysis process of building energy consumption, the Type56 analysis module is used. The terminal calls the multi-region building model

TRNBUILD to simulate the thermal process of the room. By simulating, the domestic temperature, the data of photoelectric conversion and energy consumption are calculated. The above data are monitored by the Type65 online plotter and monthly statistical output by Type46. The simulation time step is 0.05h, and the simulation period is from October to April of the following year when heating is required.

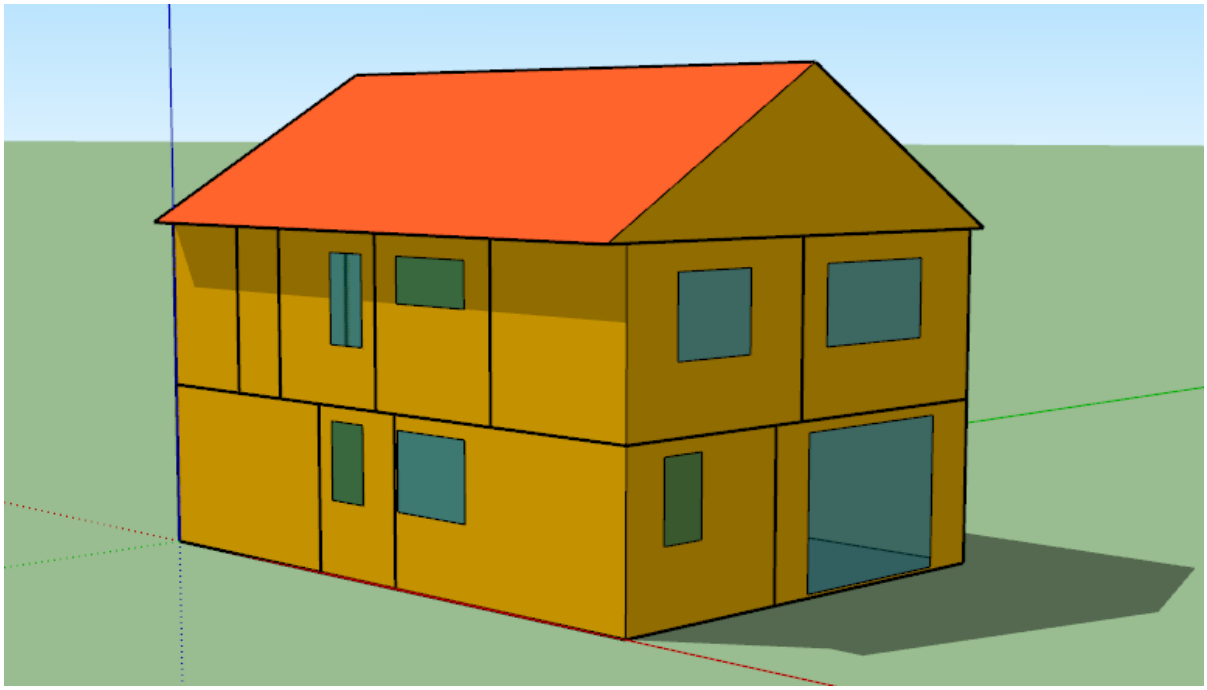

**Figure E2** 3D model of the building

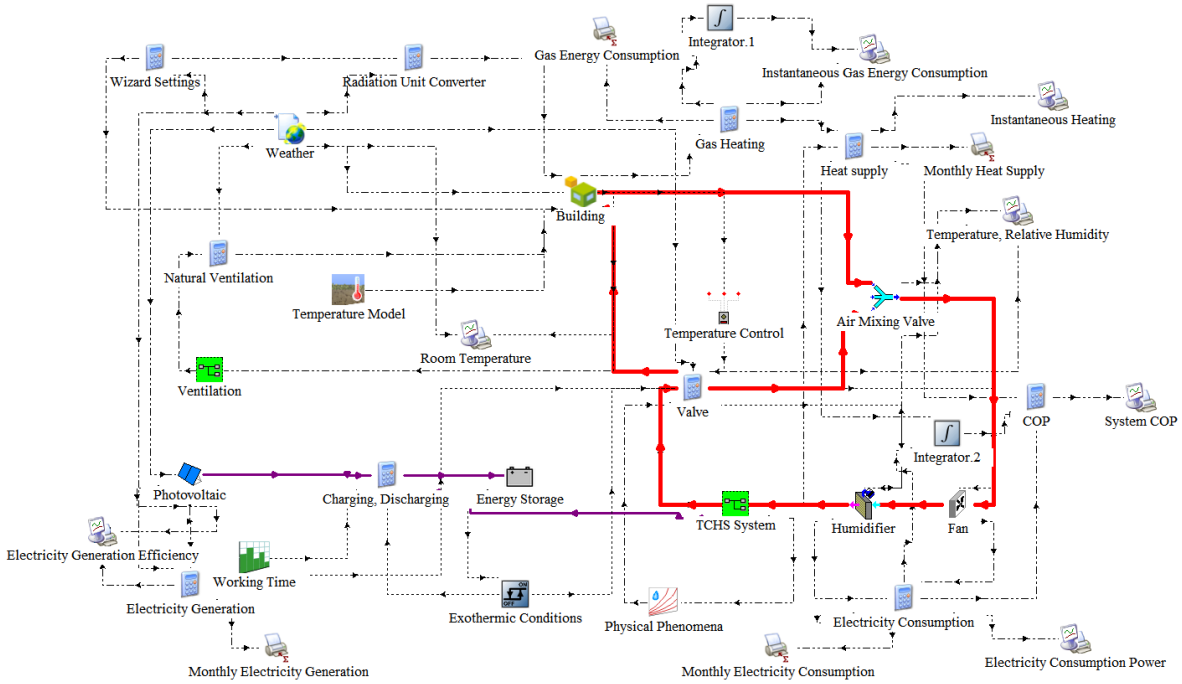

**Figure E3** TRNSYS model for building with TCHS system

**Table E** Physical and thermal properties of building materials used in modelling using TRNSYS.

| **Surfaces** | **Thermal Properties** |
|---|---|
| Doors | U=2.82 W/$m^{2}$·K |
| | Longwave emission coefficient=0.9 |
| | Convection coefficient=11 kJ/h·$m^{2}$·k(inside), |
| | 64 kJ/h·$m^{2}$·k(outside) |
| Windows | U=1.27 W/$m^{2}$·K |
| | g-value=0.74 |
| | coefficient=11 kJ/h·$m^{2}$·k(inside), |
| | 64 kJ/h·$m^{2}$·k(outside) |
| Floors | U=0.25 W/$m^{2}$·K |
| | Solar absorptance=0.8 |
| | Longwave emission coefficient=0.9 |
| | Convection coefficient=11 kJ/h·$m^{2}$·k |
| Walls | U=0.54 W/$m^{2}$·K |
| | Solar absorptance=0.7 |
| | Longwave emission coefficient=0.9 |
| | Convection coefficient=11 kJ/h·$m^{2}$·k |
| Roof | U=2.69 W/$m^{2}$·K |
| | Solar absorptance=0.8 |
| | Longwave emission coefficient=0.9 |
| | Convection coefficient=11 kJ/h·$m^{2}$·k(inside), |
| | 64kJ/h·$m^{2}$·k(outside) |

### E.2 Evaluation indicators

Compared with the energy consumption $Q_1$ of the traditional (gas) system, the energy consumption $Q_2$ achieved by the retrofitted system (TCHS and gas) is calculated according to the following Equation 6 [57].

$$Q_2=2.6\times(Q_{hum}+Q_{fan})+Q_{gas} \quad (6)$$

The heating of TCHS requires raw power from fans and humidifiers. $Q_{hum}$ and $Q_{fan}$ represent the power consumption of the humidifier and fan, respectively, and $Q_{gas}$ is the gas consumption. Among them, 2.6 is the energy conversion factor of electricity equivalent to primary energy. For TCHS systems, the average heating situation is expressed using the coefficient of performance *COP*, which is defined as [58]:

$$COP = \frac{Q_{sor}}{Q_{hum}+Q_{fan}} \quad (7)$$

Among them, $Q_{sor}$ provides heat for the TCHS system. It can be calculated from the heat capacity obtained by air flowing through the adsorbent material.

**E.3 Analysis of residential heating performance based on TCHS system**

The dynamic simulation of the charging and discharging process of the established system is carried out for a period of 7 months. The results show the operating state and performance of the system under various climatic conditions. Fig. C.4 shows the changes in ambient temperature and room temperature during the simulation cycle. Although there is temperature control to set the temperature in the range of 21±1°C, it is because that the overall trend is still affected by the ambient temperature.

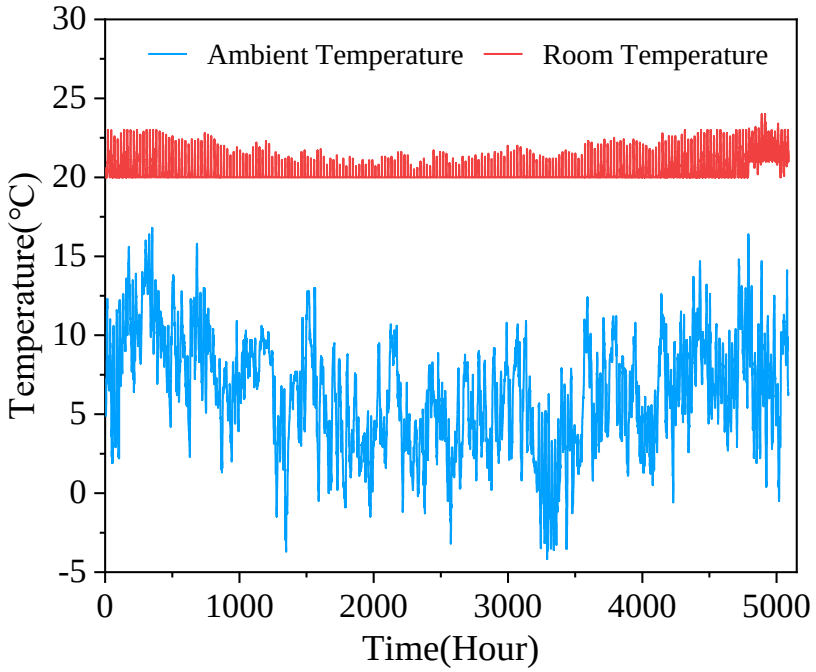


**Figure E4** Variation of ambient temperature and room temperature under simulation cycle

Fig. 4.5 shows the solar power generation, the heat of desorption $Q_{des}$ of the adsorbent and the heat of adsorption $Q_{sor}$ of the adsorption system for each month in charge mode and discharge mode. As the climate temperature rises, the better the solar heat collection effect is, the more energy can be provided to the adsorption heat storage system, and the better the effect of the adsorption heat supply. The conversion efficiency between the two follows the experimental results in Section 4.3, which is close to the optimal energy conversion efficiency of 74.3%.

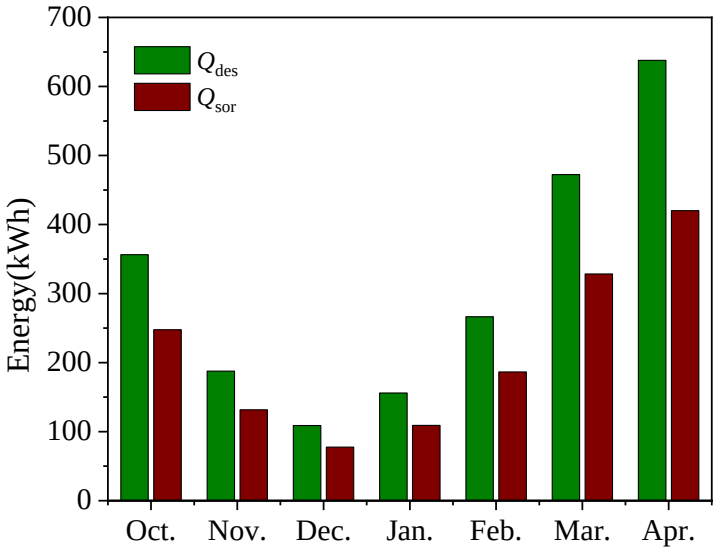


**Fig. C.5** Monthly change in thermal capacity

To evaluate the energy consumption reduction of the heating system by the heat release of TCHS. Fig. 4.6 plots the energy consumption $Q_1$ of gas heating alone, and the energy consumption $Q_2$ of the adsorption system and gas co-heating. It can be seen from the figure that the TCHS system can reduce the consumption of gas, and the total energy consumption in seven months can reduce the gas consumption by 8.8%. However, natural gas still accounts for most energy consumption, as TCHS is limited by solar energy harvesting. After the TCHS releases all the heat of adsorption, the fans and humidifiers stop working. If the ability to increase the TCHS reserve solar energy is improved, the heat release from TCHS can be increased. The power consumption of fans and humidifiers accounts for the central part, which is expected to save most of the gas.

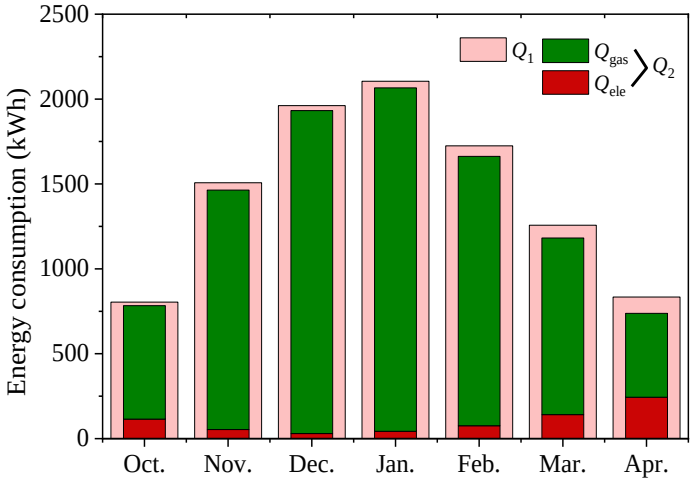


**Fig. C.6** Monthly energy consumption of the system

Fig. C.7 plots the *COP* values for TCHS for each month. The maximum was in December at 6.67. This is because the TCHS system relies on the hydration reaction of the adsorbent, which is affected by the climatic environment. Because the air humidity in Newcastle in December is relatively high, it can provide natural moisture for the reaction of the TCHS system, reducing the burden of electricity consumption of the humidifier. Similarly, the minimum value of 4.48 appeared in April. Although solar energy was abundant in April, the charging capacity reached the maximum; but the natural air was dry, which significantly increased the power consumption of the humidifier. The average monthly *COP* was calculated to be 5.56. If the investment in the TCHS system is increased, it is likely to replace most of the gas, and the heating demand of the house can be met with less power consumption.

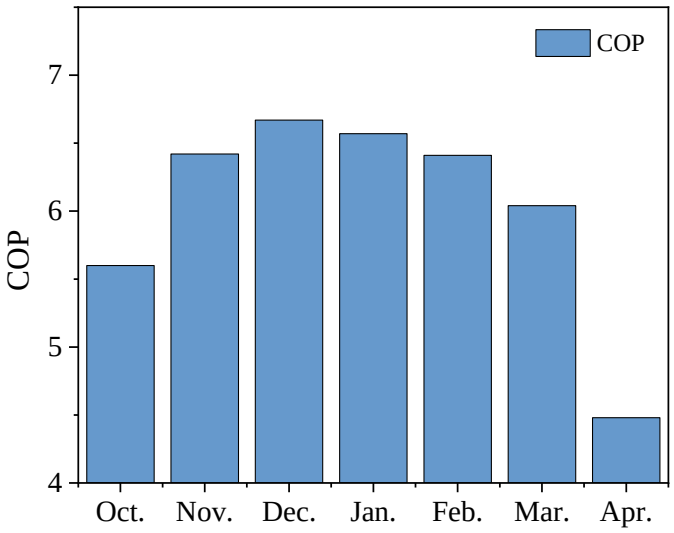


**Fig. C.7** Monthly COP of TCHS system

# Reference


[1] S. Kuravi, J. Trahan, D. Y. Goswami, M. M. Rahman, E. K. J. P. i. E. Stefanakos, and C. Science, "Thermal energy storage technologies and systems for concentrating solar power plants," vol. 39, no. 4, pp. 285-319, 2013.

[2] T. Mahlia, T. Saktisahdan, A. Jannifar, M. Hasan, H. J. R. Matseelar, and s. e. reviews, "A review of available methods and development on energy storage; technology update," vol. 33, pp. 532-545, 2014.

[3] P. Pardo *et al.*, "A review on high temperature thermochemical heat energy storage," vol. 32, pp. 591-610, 2014.

[4] T. Li, S. Wu, T. Yan, R. Wang, and J. J. E. Zhu, "Experimental investigation on a dual-mode thermochemical sorption energy storage system," vol. 140, pp. 383-394, 2017.

[5] G. Whiting, D. Grondin, S. Bennici, A. J. S. e. m. Auroux, and s. cells, "Heats of water sorption studies on zeolite–MgSO4 composites as potential thermochemical heat storage materials," vol. 112, pp. 112-119, 2013.

[6] M. Liu *et al.*, "Review on concentrating solar power plants and new developments in high temperature thermal energy storage technologies," vol. 53, pp. 1411-1432, 2016.

[7] S. Mazzoni, S. Ooi, B. Nastasi, and A. J. A. E. Romagnoli, "Energy storage technologies as techno-economic parameters for master-planning and optimal dispatch in smart multi energy systems," vol. 254, p. 113682, 2019.

[8] J.-Y. Ryu *et al.*, "A novel liquid air energy storage system using a combination of sensible and latent heat storage," vol. 203, p. 117890, 2022.

[9] S. Bellan *et al.*, "Numerical analysis of charging and discharging performance of a thermal energy storage system with encapsulated phase change material," vol. 71, no. 1, pp. 481-500, 2014.

[10] T. Yan, R. Wang, T. Li, L. Wang, I. T. J. R. Fred, and S. E. Reviews, "A review of promising candidate reactions for chemical heat storage," vol. 43, pp. 13-31, 2015.

[11] A. H Abedin and M. J. T. o. r. e. j. A Rosen, "A critical review of thermochemical energy storage systems," vol. 4, no. 1, 2011.

[12] M. Schmidt, C. Szczukowski, C. Roßkopf, M. Linder, and A. J. A. T. E. Wörner, "Experimental results of a 10 kW high temperature thermochemical storage reactor based on calcium hydroxide," vol. 62, no. 2, pp. 553-559, 2014.

[13] W. Li *et al.*, "Solar-thermal energy conversion prediction of building envelope using thermochemical sorbent based on established reaction kinetics," vol. 252, p. 115117, 2022.

[14] L. Scapino, H. A. Zondag, J. Van Bael, J. Diriken, and C. C. J. A. E. Rindt, "Sorption heat storage for long-term low-temperature applications: A review on the advancements at material and prototype scale," vol. 190, pp. 920-948, 2017.

[15] L. F. Cabeza, A. Solé, and C. J. R. E. Barreneche, "Review on sorption materials and technologies for heat pumps and thermal energy storage," vol. 110, pp. 3-39, 2017.

[16] M. Gaeini, H. Zondag, and C. J. A. T. E. Rindt, "Effect of kinetics on the thermal performance of a sorption heat storage reactor," vol. 102, pp. 520-531, 2016.

[17] F. Bertsch, B. Mette, S. Asenbeck, H. Kerskes, and H. J. P. o. E. Müller-Steinhagen, New Jersey, "Low temperature chemical heat storage–an investigation of hydration reactions," 2009.

[18] M. Molenda, M. Bouché, M. Linder, M. Blug, J. Busse, and A. Wörner,

"Thermochemical energy storage for low temperature applications: materials and first studies in a gas-solid reactor," in *Proceedings of 12th Int. Conference on Energy Storage (Innostock), Lleida, Spain*, 2012.
[19] H. Zondag, B. Kikkert, S. Smeding, R. de Boer, and M. J. A. e. Bakker, "Prototype thermochemical heat storage with open reactor system," vol. 109, pp. 360-365, 2013.
[20] N. Yu, R. Wang, Z. Lu, and L. J. C. e. s. Wang, "Development and characterization of silica gel–LiCl composite sorbents for thermal energy storage," vol. 111, pp. 73-84, 2014.
[21] E. Piperopoulos *et al.*, "Morphological and structural evaluation of hydration/dehydration stages of MgSO4 filled composite silicone foam for thermal energy storage applications," vol. 10, no. 2, p. 453, 2020.
[22] H. Zhao *et al.*, "Water sorption on composite material “zeolite 13X modified by LiCl and CaCl2”," vol. 299, p. 110109, 2020.
[23] R. Macriss, J. Gutraj, and T. Zawacki, "Absorption fluids data survey: final report on worldwide data," Oak Ridge National Lab., TN (USA); Institute of Gas Technology, Chicago, IL …1988.
[24] L. G. Gordeeva, A. D. Grekova, T. A. Krieger, Y. I. J. M. Aristov, and m. materials, "Adsorption properties of composite materials (LiCl+ LiBr)/silica," vol. 126, no. 3, pp. 262-267, 2009.
[25] A. Entezari, T. Ge, and R. J. E. Wang, "Water adsorption on the coated aluminum sheets by composite materials (LiCl+ LiBr)/silica gel," vol. 160, pp. 64-71, 2018.
[26] M.-M. Druske *et al.*, "Developed materials for thermal energy storage: synthesis and characterization," vol. 61, pp. 96-99, 2014.
[27] D. Mohapatra and J. J. M. T. P. Nandanavanam, "Salt in matrix for thermochemical energy storage-A review," vol. 72, pp. 27-33, 2023.
[28] K. Lim, J. Che, and J. J. A. T. E. Lee, "Experimental study on adsorption characteristics of a water and silica-gel based thermal energy storage (TES) system," vol. 110, pp. 80-88, 2017.
[29] R. de Boer, S. Smeding, H. Zondag, and G. Krol, *Development of a prototype system for seasonal solar heat storage using an open sorption process*. Petten: ECN, 2014.
[30] A. P. Singh, S. Khanna, S. Paneliya, H. Hinsu, Y. Patel, and B. J. M. T. P. Mehta, "Preparation and characterization of solid-state neopentyl glycol/expanded graphite micro composite for thermal energy storage applications," vol. 47, pp. 621-625, 2021.
[31] C. Xu, Z. Yu, Y. Xie, Y. Ren, F. Ye, and X. J. A. T. E. Ju, "Study of the hydration behavior of zeolite-MgSO4 composites for long-term heat storage," vol. 129, pp. 250-259, 2018.
[32] T. Nonnen, H. Preißler, S. Kött, S. Beckert, R. J. M. Gläser, and M. Materials, "Salt inclusion and deliquescence in salt/zeolite X composites for thermochemical heat storage," vol. 303, p. 110239, 2020.
[33] Y. Zhang, R. Wang, Y. Zhao, T. Li, S. Riffat, and N. J. E. Wajid, "Development and thermochemical characterizations of vermiculite/SrBr2 composite sorbents for low-temperature heat storage," vol. 115, pp. 120-128, 2016.
[34] Q. Wang *et al.*, "Structure and hydration state characterizations of MgSO4-zeolite 13x composite materials for long-term thermochemical heat storage," vol. 200, p. 110047, 2019.
[35] S. Wei *et al.*, "Influence of minerals with different porous structures on

thermochemical heat storage performance of CaCl2-based composite sorbents," vol. 243, p. 111769, 2022.
[36] Y. Ge, Y. Zhao, and C. J. R. E. Zhao, "Transient simulation and thermodynamic analysis of pumped thermal electricity storage based on packed-bed latent heat/cold stores," vol. 174, pp. 939-951, 2021.
[37] L. Calabrese, S. De Antonellis, S. Vasta, V. Brancato, and A. J. A. S. Freni, "Modified silicone-SAPO34 composite materials for adsorption thermal energy storage systems," vol. 10, no. 23, p. 8715, 2020.
[38] C. Xu, Y. Xie, Z. Liao, Y. Ren, and F. J. A. T. E. Ye, "Numerical study on the desorption process of a thermochemical reactor filled with MgCl2· 6H2O for seasonal heat storage," vol. 146, pp. 785-794, 2019.
[39] W. Li, J. J. Klemeš, Q. Wang, and M. J. R. E. Zeng, "Development and characteristics analysis of salt-hydrate based composite sorbent for low-grade thermochemical energy storage," vol. 157, pp. 920-940, 2020.
[40] H. Zondag, B. Kikkert, S. Smeding, R. d. Boer, and M. Bakker, "Prototype thermochemical heat storage with open reactor system," *Applied Energy,* vol. 109, pp. 360-365, 2013/09/01/ 2013.
[41] A. A. Safa, A. S. Fung, and R. Kumar, "Heating and cooling performance characterisation of ground source heat pump system by testing and TRNSYS simulation," *Renewable Energy,* vol. 83, pp. 565-575, 2015/11/01/ 2015.
[42] D. Sakellari, M. Forsén, and P. Lundqvist, "Investigating control strategies for a domestic low-temperature heat pump heating system," *International Journal of Refrigeration,* vol. 29, no. 4, pp. 547-555, 2006/06/01/ 2006.
[43] E. I. S. Department of Business, "Energy consumption in the UK 2020 - End uses data tables," 2020.
[44] E. I. S. D. o. Business, "Energy consumption in the UK 2022 - end uses data tables," 2022.
[45] L. Calderone, "2021 Top Article - Solar Wind Could Replace Solar Energy," *Solar Power,* 2021.
[46] T. Pauschinger, "Solar district heating with seasonal thermal energy storage in germany," *Steinbeis Res. Inst. Sol. Sustain. Therm. Energy Syst,* 2012.
[47] E. Courbon *et al.*, "Further improvement of the synthesis of silica gel and $CaCl_2$ composites: Enhancement of energy storage density and stability over cycles for solar heat storage coupled with space heating applications," *Solar Energy,* vol. 157, pp. 532-541, 2017.
[48] N. Yu, R. Z. Wang, and L. W. Wang, "Sorption thermal storage for solar energy," *Progress in Energy and Combustion Science,* vol. 39, no. 5, pp. 489-514, 2013.
[49] P. A. J. Donkers, L. C. Sogutoglu, H. P. Huinink, H. R. Fischer, and O. C. G. Adan, "A review of salt hydrates for seasonal heat storage in domestic applications," (in English), *Applied Energy,* vol. 199, pp. 45-68, Aug 1 2017.
[50] C. J. Ferchaud, "Experimental study of salt hydrates for thermochemical seasonal heat storage," PhD, Eindhoven University of Technology, 2016.
[51] P. A. J. Donkers, L. Pel, and O. C. G. Adan, "Hydration / dehydration cycles of salt hydrates – studied with NMR," presented at the International Solar Energy Society Conference, Aix-lex-Bains, France 2014.
[52] H. DeVoe, *Thermodynamics and chemistry*. Upper Saddle River, NJ: Prentice Hall ; London : Prentice Hall International, 2015.
[53] P. A. J. Donkers, S. Beckert, L. Pel, F. Stallmach, M. Steiger, and O. C. G. Adan, "Water transport in $MgSO_4{\cdot}7H_2O$ during dehydration in view of thermal

storage," *The Journal of Physical Chemistry C,* vol. 119, no. 52, pp. 28711-28720, 2015.

[54] R. W. Carling, "Dissociation pressures and enthalpies of reaction in $MgCl_2.nH_2O$ and $CaCl_2.nNH_3$," (in English), *Journal of Chemical Thermodynamics,* vol. 13, no. 6, pp. 503-512, 1981.

[55] G. J. Kipouros and D. R. Sadoway, "The chemistry and electrochemistry of magnesium production," *Advances in molten salt chemistry,* vol. 6, pp. 127-209, 1987.

[56] F. Kuznik, K. Johannes, and C. Obrecht, "Chemisorption heat storage in buildings: State-of-the-art and outlook," *Energy and Buildings,* vol. 106, pp. 183-191, 2015.

[57] K. E. N'Tsoukpoe, T. Osterland, O. Opel, and W. K. L. Ruck, "Cascade thermochemical storage with internal condensation heat recovery for better energy and exergy efficiencies," *Applied Energy,* vol. 181, pp. 562-574, 2016.

[58] I. M. Chou and R. R. Seal, "Determination of epsomite-hexahydrite equilibria by the humidity-buffer technique at 0.1 MPa with implications for phase equilibria in the system $MgSO_4$-$H_2O$," (in English), *Astrobiology,* vol. 3, no. 3, pp. 619-630, Fal 2003.

[59] F. M. Bertsch, B.; Asenbeck, S.; Kerskes, H.; Muller-Steinhagen, H., "Low temperature chemical heat storageean investigation of hydration reactions," in *Effstock 2009-Thermal Energy Storage for Efficiency and Sustainability*, Stockholm, Schweden, 2009.

[60] I. M. Chou and R. R. Seal, "Magnesium and calcium sulfate stabilities and the water budget of Mars," (in English), *Journal of Geophysical Research-Planets,* vol. 112, no. E11, Nov 8 2007.

[61] K. Fujioka and H. Suzuki, "Thermophysical properties and reaction rate of composite reactant of calcium chloride and expanded graphite," *Applied Thermal Engineering,* vol. 50, no. 2, pp. 1627-1632, 2013.

[62] T. Xu, Z. P. Zhang, and L. T. Qu, "Graphene-Based Fibers: Recent Advances in Preparation and Application," (in English), *Advanced Materials,* Article; Early Access p. 16, 2019, Art. no. 1901979.

[63] H. W. B. Roozeboom, "Experimentelle und theoretische studien über die gleichgewichtsbedingungen zwischen festen und flüssigen verbindungen von wasser mit salzen, besonders mit dem chlorcalcium," *Zeitschrift für Physikalische Chemie,* vol. 4U, no. 1, pp. 31-65, 1889.

[64] A. Lannung, "Dampfdruckmessungen des systems calciumchlorid-wasser," *Zeitschrift für anorganische und allgemeine Chemie,* vol. 228, no. 1, pp. 1-18, 1936.

[65] M. Molenda, J. Stengler, M. Linder, and A. Wörner, "Reversible hydration behavior of $CaCl_2$ at high $H_2O$ partial pressures for thermochemical energy storage," *Thermochimica Acta,* vol. 560, pp. 76-81, 2013.

[66] R. de Boer, W. G. Haije, and J. B. J. Veldhuis, "Determination of structural, thermodynamic and phase properties in the $Na_2S$-$H_2O$ system for application in a chemical heat pump," (in English), *Thermochimica Acta,* vol. 395, no. 1-2, pp. 3-19, Jan 3 2003.

[67] S. Mauran, H. Lahmidi, and V. Goetz, "Solar heating and cooling by a thermochemical process. First experiments of a prototype storing 60kWh by a solid/gas reaction," *Solar Energy,* vol. 82, no. 7, pp. 623-636, 2008.

[68] S. L. Mauran, H.; Goetz, V., "3rd intermediate report, European project no NNE5-2000-00385," 2002.

[69] H. Lahmidi, S. Mauran, and V. Goetz, "Definition, test and simulation of a thermochemical storage process adapted to solar thermal systems," *Solar Energy,* vol. 80, no. 7, pp. 883-893, 2006.
[70] B. Michel, N. Mazet, S. Mauran, D. Stitou, and J. Xu, "Thermochemical process for seasonal storage of solar energy: Characterization and modeling of a high density reactive bed," *Energy,* vol. 47, no. 1, pp. 553-563, 2012.
[71] B. Michel, N. Mazet, and P. Neveu, "Experimental investigation of an innovative thermochemical process operating with a hydrate salt and moist air for thermal storage of solar energy: Global performance," (in English), *Applied Energy,* vol. 129, pp. 177-186, Sep 15 2014.
[72] E. Courbon *et al.*, "A new composite sorbent based on $SrBr_2$ and silica gel for solar energy storage application with high energy storage density and stability," *Applied Energy,* vol. 190, pp. 1184-1194, 2017.
[73] N. Yu, R. Z. Wang, Z. S. Lu, L. W. Wang, and T. F. Ishugah, "Evaluation of a three-phase sorption cycle for thermal energy storage," *Energy,* vol. 67, pp. 468-478, 2014.
[74] M. Thakker, C. W. Chi, R. Peck, and D. T. Wasan, "Vapor pressure measurements of hygroscopic salts," *Journal of Chemical & Engineering Data,* vol. 13, no. 4, pp. 553-558, 1968.
[75] Y. J. Zhao, R. Z. Wang, T. X. Li, and Y. Nomura, "Investigation of a 10 kWh sorption heat storage device for effective utilization of low-grade thermal energy," *Energy,* vol. 113, pp. 739-747, 2016.
[76] P. R. Clayton, A. G. Dunn, S. Holt, and L. A. Staveley, "Thermodynamic study of disorder in lithium bromide monohydrate," *Journal of the Chemical Society, Faraday Transactions 1: Physical Chemistry in Condensed Phases,* vol. 76, pp. 2362-2373, 1980.
[77] M. Steiger and S. Asmussen, "Crystallization of sodium sulfate phases in porous materials: The phase diagram $Na_2SO_4$–$H_2O$ and the generation of stress," *Geochimica et Cosmochimica Acta,* vol. 72, no. 17, pp. 4291-4306, 2008.
[78] P. A. J. Donkers, K. Linnow, L. Pel, M. Steiger, and O. C. G. Adan, "$Na_2SO_4 \cdot 10H_2O$ dehydration in view of thermal storage," *Chemical Engineering Science,* vol. 134, pp. 360-366, 2015.
[79] O. Polyachenok, E. Dudkina, and L. Polyachenok, "Thermal stability and thermodynamics of copper (II) chloride dihydrate," *The Journal of Chemical Thermodynamics,* vol. 41, no. 1, pp. 74-79, 2009.
[80] I. H. Derby and V. Yngve, "The Dissociation Tensions of Certain Hydrated Chlorides and the Vapor Pressures of Their Saturated Solutions," *Journal of the American Chemical Society,* vol. 38, no. 8, pp. 1439-1451, 1916.
[81] A. Campbell, "The System $Li_2SO_4$-$H_2O$," *Journal of the American Chemical Society,* vol. 65, no. 12, pp. 2268-2271, 1943.
[82] D. Bonnell and L. Burridge, "The dissociation pressures of some salt hydrates," *Transactions of the Faraday Society,* vol. 31, pp. 473-478, 1935.
[83] F. Höffler, I. Müller, and M. Steiger, "Thermodynamic properties of $ZnSO_4$ (aq) and phase equilibria in the $ZnSO_4$–$H_2O$ system from 268 K to 373 K," *The Journal of Chemical Thermodynamics,* vol. 116, pp. 279-288, 2018.
[84] I.-M. Chou, R. Seal, and B. Hemingway, "Determination of melanterite-rozenite and chalcanthite-bonattite equilibria by humidity measurements at 0.1 MPa," *American Mineralogist,* vol. 87, no. 1, pp. 108-114, 2002.
[85] W. W. Ewing, "Calcium nitrate. II. The vapor pressure-temperature relations of the binary system calcium nitrate-water," *Journal of the American Chemical*

*Society*, vol. 49, no. 8, pp. 1963-1973, 1927.
[86] K. G. Denbigh, *The principles of chemical equilibrium with applications in chemistry and chemical engineering*, 4th ed. Cambrige University Press, 1981.
[87] J. T. Kelly and A. S. Wexler, "Thermodynamics of carbonates and hydrates related to heterogeneous reactions involving mineral aerosol," (in English), *Journal of Geophysical Research-Atmospheres*, vol. 110, no. D11, Jun 1 2005.
[88] D. D. Wagman *et al.*, "The Nbs Tables of Chemical Thermodynamic Properties - Selected Values for Inorganic and C-1 and C-2 Organic-Substances in Si Units," (in English), *Journal of Physical and Chemical Reference Data*, vol. 11, pp. 1-392, 1982.
[89] L. Glasser and H. D. B. Jenkins, "The thermodynamic solvate difference rule: Solvation parameters and their sse in interpretation of the role of bound solvent in condensed-phase solvates," *Inorganic Chemistry*, vol. 46, no. 23, pp. 9768-9778, 2007.
[90] L. Scapino, H. A. Zondag, J. Van Bael, J. Diriken, and C. C. M. Rindt, "Sorption heat storage for long-term low-temperature applications: A review on the advancements at material and prototype scale," (in English), *Applied Energy*, vol. 190, pp. 920-948, Mar 15 2017.
[91] K. E. N'Tsoukpoe, T. Schmidt, H. U. Rammelberg, B. A. Watts, and W. K. L. Ruck, "A systematic multi-step screening of numerous salt hydrates for low temperature thermochemical energy storage," (in English), *Applied Energy*, vol. 124, pp. 1-16, Jul 1 2014.
[92] M. M. Farid, A. M. Khudhair, S. A. K. Razack, and S. Al-Hallaj, "A review on phase change energy storage: materials and applications," (in English), *Energy Conversion and Management*, vol. 45, no. 9-10, pp. 1597-1615, Jun 2004.
[93] W. Chen, W. Li, and Y. Zhang, "Analysis of thermal deposition of $MgCl_2 \cdot 6H_2O$ hydrated salt in the sieve-plate reactor for heat storage," *Applied Thermal Engineering*, vol. 135, pp. 95-108, 2018.
[94] C. J. Ferchaud, H. A. Zondag, J. B. J. Veldhuis, and R. d. Boer, "Study of the reversible water vapour sorption process of $MgSO_4.7H_2O$ and $MgCl_2.6H_2O$ under the conditions of seasonal solar heat storage," *Journal of Physics: Conference Series*, vol. 395, p. 012069, 2012.
[95] Z. Zhao, S. Wang, F. Wan, Z. Tie, and Z. Niu, "Scalable 3D Self‐Assembly of MXene Films for Flexible Sandwich and Microsized Supercapacitors," *Advanced Functional Materials*, 2021.
[96] D. R. Lide, *CRC handbook of chemistry and physics*. CRC press, 2004.
[97] D. W. Green and M. Z. Southard, *Perry's chemical engineers' handbook*. McGraw-Hill Education, 2019.
[98] E. Courbon, M. Frere, N. Heymans, and P. D'ans, "Hygroscopic composite material," United States, 2017. Available: http://www.freepatentsonline.com/y2017/0167801.html.
[99] Y. I. Aristov, "New family of solid sorbents for adsorptive cooling: Material scientist approach," *Journal of Engineering Thermophysics*, vol. 16, no. 2, pp. 63-72, 2007.
[100] Y. Zhang, R. Wang, T. Li, and Y. Zhao, "Thermochemical characterizations of novel vermiculite-LiCl composite sorbents for low-temperature heat storage," *Energies*, vol. 9, no. 10, p. 854, 2016.
[101] L. G. Gordeeva and Y. I. Aristov, "Composites ‘salt inside porous matrix’ for adsorption heat transformation: a current state-of-the-art and new trends," *International Journal of Low-Carbon Technologies*, vol. 7, no. 4, pp. 288-302,

2012.
[102] A. Jabbari-Hichri, S. Bennici, and A. Auroux, "$CaCl_2$-containing composites as thermochemical heat storage materials," (in English), *Solar Energy Materials and Solar Cells,* vol. 172, pp. 177-185, Dec 2017.
[103] H. Ye, Z. Yuan, S. Li, and L. Zhang, "Activated carbon fiber cloth and $CaCl_2$ composite sorbents for a water vapor sorption cooling system," *Applied Thermal Engineering,* vol. 62, no. 2, pp. 690-696, 2014.
[104] S. P. Casey, J. Elvins, S. Riffat, and A. Robinson, "Salt impregnated desiccant matrices for 'open' thermochemical energy storage—Selection, synthesis and characterisation of candidate materials," *Energy and Buildings,* vol. 84, pp. 412-425, 2014.
[105] F. B. Cortes, F. Chejne, F. Carrasco-Marin, A. F. Perez-Cadenas, and C. Moreno-Castilla, "Water sorption on silica- and zeolite-supported hygroscopic salts for cooling system applications," (in English), *Energy Conversion and Management,* vol. 53, no. 1, pp. 219-223, Jan 2012.
[106] Y. I. Aristov, G. Restuccia, M. M. Tokarev, and G. Cacciola, "Selective water sorbents for multiple applications, 10. Energy storage ability," (in English), *Reaction Kinetics and Catalysis Letters,* vol. 69, no. 2, pp. 345-353, Mar 2000.
[107] A. Permyakova *et al.*, "Design of salt–metal organic framework composites for seasonal heat storage applications," *Journal of materials chemistry A,* vol. 5, no. 25, pp. 12889-12898, 2017.
[108] M. Gaeini, A. L. Rouws, J. W. O. Salari, H. A. Zondag, and C. C. M. Rindt, "Characterization of microencapsulated and impregnated porous host materials based on calcium chloride for thermochemical energy storage," (in English), *Applied Energy,* vol. 212, pp. 1165-1177, Feb 15 2018.
[109] A. Shkatulov, R. Joosten, H. Fischer, and H. Huinink, "Core–Shell Encapsulation of Salt Hydrates into Mesoporous Silica Shells for Thermochemical Energy Storage," *ACS Applied Energy Materials,* vol. 3, no. 7, pp. 6860-6869, 2020.
[110] S. Wei *et al.*, "Development of pomegranate-type CaCl2@ C composites via a scalable one-pot pyrolysis strategy for solar-driven thermochemical heat storage," *Energy Conversion and Management,* vol. 212, p. 112694, 2020.
[111] K. E. N'Tsoukpoe *et al.*, "A review on the use of calcium chloride in applied thermal engineering," *Applied Thermal Engineering,* vol. 75, pp. 513-531, 2015.
[112] A. Jabbari-Hichri, S. Bennici, and A. Auroux, "Enhancing the heat storage density of silica-alumina by addition of hygroscopic salts ($CaCl_2$, $Ba(OH)_2$, and $LiNO_3$)," (in English), *Solar Energy Materials and Solar Cells,* vol. 140, pp. 351-360, Sep 2015.
[113] Y. I. Aristov, M. Tokarev, G. Cacciola, and G. Restuccia, "Selective water sorbents for multiple applications .1. $CaCl_2$ confined in mesopores of silica gel: Sorption properties," (in English), *Reaction Kinetics and Catalysis Letters,* vol. 59, no. 2, pp. 325-333, Nov 1996.
[114] J. Jänchen, D. Ackermann, E. Weiler, H. Stach, and W. Brösicke, "Calorimetric investigation on zeolites, AlPO4's and $CaCl_2$ impregnated attapulgite for thermochemical storage of heat," *Thermochimica Acta,* vol. 434, no. 1-2, pp. 37-41, 2005.
[115] Y. I. Aristov, G. Restuccia, M. M. Tokarev, H. D. Buerger, and A. Freni, "Selective water sorbents for multiple applications. 11. $CaCl_2$ confined to expanded vermiculite," (in English), *Reaction Kinetics and Catalysis Letters,* vol. 71, no. 2, pp. 377-384, Nov 2000.

[116] A. Ristić, D. Maučec, S. K. Henninger, and V. Kaučič, "New two-component water sorbent $CaCl_2$-FeKIL2 for solar thermal energy storage," *Microporous and Mesoporous Materials,* vol. 164, pp. 266-272, 2012.
[117] H. Liu, K. Nagano, D. Sugiyama, J. Togawa, and M. Nakamura, "Honeycomb filters made from mesoporous composite material for an open sorption thermal energy storage system to store low-temperature industrial waste heat," *International Journal of Heat and Mass Transfer,* vol. 65, pp. 471-480, 2013.
[118] Y. I. Aristov, M. M. Tokarev, G. Restuccia, and G. Cacciola, "Selective water sorbents for multiple applications .2. $CaCl_2$ confined in micropores of silica gel: Sorption properties," (in English), *Reaction Kinetics and Catalysis Letters,* vol. 59, no. 2, pp. 335-342, Nov 1996.
[119] D. Zhu, H. Wu, and S. Wang, "Experimental study on composite silica gel supported $CaCl_2$ sorbent for low grade heat storage," *International Journal of Thermal Sciences,* vol. 45, no. 8, pp. 804-813, 2006.
[120] O. Skrylnyk, E. Courbon, N. Heymans, M. Frere, J. Bougard, and G. Descy, "Performance characterization of salt-in-silica composite materials for seasonal energy storage design," (in English), *Journal of Energy Storage,* vol. 19, pp. 320-336, Oct 2018.
[121] K. Korhammer *et al.,* "Sorption and thermal characterization of composite materials based on chlorides for thermal energy storage," *Applied energy,* vol. 162, pp. 1462-1472, 2016.
[122] J. Mrowiec-Bialon, A. B. Jarzebski, A. J. Lachowski, J. J. Malinowski, and Y. I. Aristov, "Effective inorganic hybrid adsorbents of water vapor by the sol-gel method," (in English), *Chemistry of Materials,* vol. 9, no. 11, pp. 2486-2490, Nov 1997.
[123] M. Tokarev, L. Gordeeva, V. Romannikov, I. Glaznev, and Y. Aristov, "New composite sorbent $CaCl_2$ in mesopores for sorption cooling/heating," (in English), *International Journal of Thermal Sciences,* vol. 41, no. 5, pp. 470-474, May 2002.
[124] A. Ristic and N. Z. Logar, "New Composite Water Sorbents $CaCl_2$-PHTS for Low-Temperature Sorption Heat Storage: Determination of Structural Properties," (in English), *Nanomaterials,* vol. 9, no. 1, Jan 2019.
[125] A. Grekova, L. Gordeeva, and Y. Aristov, "Composite sorbents "Li/Ca halogenides inside multi-wall carbon nano-tubes" for thermal energy storage," *Solar Energy Materials and Solar Cells,* vol. 155, pp. 176-183, 2016.
[126] A. Giampieri, Z. Ma, A. Smallbone, and A. P. Roskilly, "Thermodynamics and economics of liquid desiccants for heating, ventilation and air-conditioning–An overview," *Applied Energy,* vol. 220, pp. 455-479, 2018.
[127] J. Burch, J. Woods, E. Kozubal, and A. Boranian, "Zero energy communities with central solar plants using liquid desiccants and local storage," *Energy Procedia,* vol. 30, pp. 55-64, 2012.
[128] N. Yu, R. Z. Wang, Z. S. Lu, and L. W. Wang, "Development and characterization of silica gel–LiCl composite sorbents for thermal energy storage," *Chemical Engineering Science,* vol. 111, pp. 73-84, 2014.
[129] X. Zheng, T. Ge, R. Wang, and L. Hu, "Performance study of composite silica gels with different pore sizes and different impregnating hygroscopic salts," *Chemical Engineering Science,* vol. 120, pp. 1-9, 2014.
[130] X. Zheng, T. Ge, L. Hu, and R. Wang, "Development and characterization of mesoporous silicate–LICL composite desiccants for solid desiccant cooling systems," *Industrial & Engineering Chemistry Research,* vol. 54, no. 11, pp.

2966-2973, 2015.
[131] A. Shkatulov, L. G. Gordeeva, I. S. Girnik, H. Huinink, and Y. I. Aristov, "Novel adsorption method for moisture and heat recuperation in ventilation: Composites “LiCl/matrix” tailored for cold climate," *Energy,* p. 117595, 2020.
[132] J. Xu *et al.*, "Efficient Solar‐driven Water Harvesting from Arid Air with Metal‐organic Frameworks Modified by Hygroscopic Salt," *Angewandte Chemie International Edition,* vol. 59, 2020.
[133] J. Cheng *et al.*, "Two-Dimensional Black Phosphorus Nanomaterials: Emerging Advances in Electrochemical Energy Storage Science," *Nano-Micro Letters,* vol. 12, no. 1, 2020.
[134] Y. Luo *et al.*, "Investigation on water vapor adsorption performance of LiCl@ MIL‐100 (Fe) composite adsorbent for adsorption heat pumps," *International Journal of Energy Research,* 2020.
[135] A. D. Grekova, L. G. Gordeeva, and Y. I. Aristov, "Composite “LiCl/vermiculite” as advanced water sorbent for thermal energy storage," *Applied Thermal Engineering,* vol. 124, pp. 1401-1408, 2017.
[136] H.-j. Chen, Q. Cui, Y. Tang, X.-j. Chen, and H.-q. Yao, "Attapulgite based LiCl composite adsorbents for cooling and air conditioning applications," *Applied Thermal Engineering,* vol. 28, no. 17-18, pp. 2187-2193, 2008.
[137] V. Brancato *et al.*, "Experimental characterization of the LiCl/vermiculite composite for sorption heat storage applications," *International Journal of Refrigeration,* vol. 105, pp. 92-100, 2019.
[138] A. D. Grekova, L. G. Gordeeva, Z. Lu, R. Wang, and Y. I. Aristov, "Composite “LiCl/MWCNT” as advanced water sorbent for thermal energy storage: Sorption dynamics," *Solar Energy Materials and Solar Cells,* vol. 176, pp. 273-279, 2018.
[139] V. Brancato *et al.*, "Water adsorption equilibrium and dynamics of LICL/MWCNT/PVA composite for adsorptive heat storage," *Solar Energy Materials and Solar Cells,* vol. 193, pp. 133-140, 2019.
[140] K.-D. Grevel and J. Majzlan, "Internally consistent thermodynamic data for magnesium sulfate hydrates," *Geochimica et Cosmochimica Acta,* vol. 73, no. 22, pp. 6805-6815, 2009.
[141] M. Steiger, K. Linnow, D. Ehrhardt, and M. Rohde, "Decomposition reactions of magnesium sulfate hydrates and phase equilibria in the $MgSO_4$–$H_2O$ and $Na^+$–$Mg^{2+}$–$Cl^-$–$SO_4^{2-}$–$H_2O$ systems with implications for Mars," *Geochimica et Cosmochimica Acta,* vol. 75, no. 12, pp. 3600-3626, 2011.
[142] K. Linnow, M. Niermann, D. Bonatz, K. Posern, and M. Steiger, "Experimental studies of the mechanism and kinetics of hydration reactions," *Energy Procedia,* vol. 48, pp. 394-404, 2014.
[143] S. Hongois, F. Kuznik, P. Stevens, and J.-J. Roux, "Development and characterisation of a new $MgSO_4$–zeolite composite for long-term thermal energy storage," *Solar Energy Materials and Solar Cells,* vol. 95, no. 7, pp. 1831-1837, 2011.
[144] S. Z. Xu, Lemington, R. Z. Wang, L. W. Wang, and J. Zhu, "A zeolite 13X/magnesium sulfate–water sorption thermal energy storage device for domestic heating," *Energy Conversion and Management,* vol. 171, pp. 98-109, 2018.
[145] C. Xu, Z. Yu, Y. Xie, Y. Ren, F. Ye, and X. Ju, "Study of the hydration behavior of zeolite-$MgSO_4$ composites for long-term heat storage," *Applied Thermal Engineering,* vol. 129, pp. 250-259, 2018.

[146] G. Whiting, D. Grondin, S. Bennici, and A. Auroux, "Heats of water sorption studies on zeolite–$MgSO_4$ composites as potential thermochemical heat storage materials," *Solar Energy Materials and Solar Cells,* vol. 112, pp. 112-119, 2013.
[147] D. Mahon, G. Claudio, and P. C. Eames, "An experimental investigation to assess the potential of using MgSO4 impregnation and Mg2+ ion exchange to enhance the performance of 13X molecular sieves for interseasonal domestic thermochemical energy storage," *Energy Conversion and Management,* vol. 150, pp. 870-877, 2017.
[148] Q. Wang, Y. Xie, B. Ding, G. Yu, F. Ye, and C. Xu, "Structure and hydration state characterizations of MgSO4-zeolite 13x composite materials for long-term thermochemical heat storage," *Solar Energy Materials and Solar Cells,* vol. 200, p. 110047, 2019.
[149] K. Posern, K. Linnow, M. Niermann, C. Kaps, and M. Steiger, "Thermochemical investigation of the water uptake behavior of $MgSO_4$ hydrates in host materials with different pore size," *Thermochimica Acta,* vol. 611, pp. 1-9, 2015.
[150] P. A. Kallenberger, F. J. Brieler, K. Posern, and M. Fröba, "Magnesium Sulfate/Polymer Composites for Seasonal, Thermochemical Energy Storage," *Chemie Ingenieur Technik,* vol. 88, no. 3, pp. 379-384, 2016.
[151] P. A. Kallenberger, K. Posern, K. Linnow, F. J. Brieler, M. Steiger, and M. Fröba, "Alginate‐Derived Salt/Polymer Composites for Thermochemical Heat Storage," *Advanced Sustainable Systems,* p. 1700160, 2018.
[152] V. Brancato *et al.*, "$MgSO_4{\cdot}7H_2O$ filled macro cellular foams: An innovative composite sorbent for thermo-chemical energy storage applications for solar buildings," *Solar Energy,* vol. 173, pp. 1278-1286, 2018.
[153] E. Piperopoulos *et al.*, "Morphological and Structural Evaluation of Hydration/Dehydration Stages of $MgSO_4$ Filled Composite Silicone Foam for Thermal Energy Storage Applications," *Applied Sciences,* vol. 10, no. 2, p. 453, 2020.
[154] V. M. van Essen *et al.*, "Characterization of $MgSO_4$ hydrate for thermochemical seasonal heat storage," *Journal of Solar Energy Engineering,* vol. 131, no. 4, p. 041014, 2009.
[155] H. A. Ousaleh, S. Said, A. Zaki, A. Faik, and A. El Bouari, "Silica gel/inorganic salts composites for thermochemical heat storage: Improvement of energy storage density and assessment of cycling stability," *Materials Today: Proceedings,* 2020.
[156] S. Xu, R. Wang, L. Wang, and J. Zhu, "Performance characterizations and thermodynamic analysis of magnesium sulfate-impregnated zeolite 13X and activated alumina composite sorbents for thermal energy storage," *Energy,* vol. 167, pp. 889-901, 2019.
[157] K. Posern and A. Osburg, "Determination of the heat storage performance of thermochemical heat storage materials based on $SrCl_2$ and $MgSO_4$," *Journal of Thermal Analysis and Calorimetry,* vol. 131, no. 3, pp. 2769-2773, 2018.
[158] S. C. Akcaoglu, Z. Sun, S. C. Moratti, and G. Martinopoulos, "Investigation of Novel Composite Materials for Thermochemical Heat Storage Systems," *Energies,* vol. 13, no. 5, p. 1042, 2020.
[159] R. Pilar, L. Svoboda, P. Honcova, and L. Oravova, "Study of magnesium chloride hexahydrate as heat storage material," *Thermochimica acta,* vol. 546, pp. 81-86, 2012.
[160] P. F. Weck and E. Kim, "Solar energy storage in phase change materials: first-

principles thermodynamic modeling of magnesium chloride hydrates," *The Journal of Physical Chemistry C*, vol. 118, no. 9, pp. 4618-4625, 2014.
[161] B. Smeets, E. Iype, S. V. Nedea, H. A. Zondag, and C. C. M. Rindt, "A DFT based equilibrium study on the hydrolysis and the dehydration reactions of MgCl2 hydrates," *The Journal of chemical physics*, vol. 139, no. 12, p. 124312, 2013.
[162] H. A. Zondag, V. M. Van Essen, L. P. J. Bleijendaal, B. W. J. Kikkert, and M. Bakker, "Application of MgCl2· 6H2O for thermochemical seasonal solar heat storage," in *Proceedings IRES 2010 conference, Berlin*, 2010.
[163] G. T. Whiting, D. Grondin, D. Stosic, S. Bennici, and A. Auroux, "Zeolite–$MgCl_2$ composites as potential long-term heat storage materials: Influence of zeolite properties on heats of water sorption," *Solar Energy Materials and Solar Cells*, vol. 128, pp. 289-295, 2014.
[164] J. Xu, T. Li, J. Chao, T. Yan, and R. Wang, "High energy-density multi-form thermochemical energy storage based on multi-step sorption processes," *Energy*, vol. 185, pp. 1131-1142, 2019.
[165] L. Shere, S. Trivedi, S. Roberts, A. Sciacovelli, and Y. Ding, "Synthesis and characterization of thermochemical storage material combining porous zeolite and inorganic salts," *Heat Transfer Engineering*, pp. 1-6, 2018.
[166] T. Yan, T. Li, J. Xu, and R. Wang, "Water sorption properties, diffusion and kinetics of zeolite NaX modified by ion-exchange and salt impregnation," *International Journal of Heat and Mass Transfer*, vol. 139, pp. 990-999, 2019.
[167] A. A. Hawwash, H. Hassan, and K. E. feky, "Impact of reactor design on the thermal energy storage of thermochemical materials," *Applied Thermal Engineering*, vol. 168, p. 114776, 2020/03/05/ 2020.
[168] K. Kant, A. Shukla, D. M. J. Smeulders, and C. C. M. Rindt, "Performance analysis of a K2CO3-based thermochemical energy storage system using a honeycomb structured heat exchanger," *Journal of Energy Storage*, vol. 38, p. 102563, 2021/06/01/ 2021.
[169] H. Liu, K. Nagano, and J. Togawa, "A composite material made of mesoporous siliceous shale impregnated with lithium chloride for an open sorption thermal energy storage system," *Solar Energy*, vol. 111, pp. 186-200, 2015/01/01/ 2015.
[170] T. I. S. Kondo, I. Abe, "Adsorption Science," *Chemical Industry Press, Beijing*, 2006.
[171] K. Johannes, F. Kuznik, J.-L. Hubert, F. Durier, and C. Obrecht, "Design and characterisation of a high powered energy dense zeolite thermal energy storage system for buildings," *Applied Energy*, vol. 159, pp. 80-86, 2015/12/01/ 2015.
[172] x. liang, "Household energy demand management using retrofitting and passive energy saving methods," *PhD Thesis*, 2019.
[173] E. M. Collins and A. W. C. Menzies, "A comparative method for measuring aqueous vapor and dissociation pressures with some of its applications," *The Journal of Physical Chemistry*, vol. 40, no. 3, pp. 379-397, 1936.
[174] A. Apelblat, "The vapour pressures of saturated aqueous solutions of potassium bromide, ammonium sulfate, copper (II) sulfate, iron (II) sulfate, and manganese (II) dichloride, at temperatures from 283 K to 308 K," *The Journal of Chemical Thermodynamics*, vol. 25, no. 12, pp. 1513-1520, 1993.
[175] L. Greenspan, "Humidity fixed points of binary saturated aqueous solutions," *Journal of Research of National Bureau of Standards - A. Physical and Chemistry*, vol. 81, no. 1, pp. 89-96, 1977.
[176] C. Arai, S. Hosaka, K. Murase, and Y. Sano, "Measurements of the relative

humidity of saturated aqueous salt solutions," *Journal of Chemical Engineering of Japan*, vol. 9, no. 4, pp. 328-330, 1976.

[177] A. Apelblat and E. Korin, "The vapour pressure of water over saturated solutions of sodium sulfate, calcium bromide, ferric chloride, zinc nitrate, calcium nitrate, and lithium nitrate at temperatures from 278.15 K to 323.15 K," *The Journal of Chemical Thermodynamics*, vol. 34, no. 10, pp. 1621-1637, 2002.

[178] A. Apelblat and E. Korin, "Vapour pressures of saturated aqueous solutions of ammonium iodide, potassium iodide, potassium nitrate, strontium chloride, lithium sulphate, sodium thiosulphate, magnesium nitrate, and uranyl nitrate from T=(278 to 323) K," *The Journal of Chemical Thermodynamics*, vol. 30, no. 4, pp. 459-471, 1998.

[179] M. Steiger *et al.*, "Hydration of $MgSO_4$ center dot $H_2O$ and generation of stress in porous materials," (in English), *Crystal Growth & Design*, vol. 8, no. 1, pp. 336-343, Jan 2008.

[180] L. Yang, R. T. Pabalan, and M. R. Juckett, "Deliquescence relative humidity measurements using an eectrical conductivity method," *Journal of Solution Chemistry*, vol. 35, no. 4, pp. 583-604, 2006.

[181] Rodrigues, V.C. et al. (2010) 'A correct enthalpy relationship as thermal comfort index for Livestock', International Journal of Biometeorology, 55(3), pp. 455–459. doi:10.1007/s00484-010-0344-y.

[182] Liang, X., Wang, Y. and Roskilly, T. (2015) 'Reduce household energy consumption using passive methods', Energy Procedia, 75, pp. 1335–1340. doi:10.1016/j.egypro.2015.07.203.